ROYAUME DU MAROC
Université Mohammed V - RABAT -
جامعة محمد الخامس – الرباط –
Faculté des sciences
كلية العلوم
CENTRE D'ÉTUDES DOCTORALES - SCIENCES ET TECHNOLOGIES

N° d'ordre : **3544**

THÈSE

En vue de l'obtention du : ***DOCTORAT***

Structure de Recherche : Laboratoire de la Matière Condensée et des Sciences Interdisciplinaires (LaMCScI)

Discipline : Sciences de la Matière Physique

Spécialité : Matière Condensée et Modélisation des Systèmes

Présentée et soutenue le : 30/10/2021
Par :

Ismail BENABDALLAH

Optical and electronic properties of exfoliated black phosphorus and quantum dots

JURY

El Hassan SAIDI	PES, Faculté des Sciences, Université Mohammed V de Rabat	Président
Lalla Btissam DRISSI	PH, Faculté des Sciences, Université Mohammed V de Rabat	Rapporteur /Examinateur
Bouchaib HARTITI	PES, Faculté des Sciences et Techniques de Mohammedia, Université Hassan II de Casablanca	Rapporteur /Examinateur
El Mustapha FEDDI	PES, École Nationale Supérieure des Arts et Métiers, Université Mohammed V de Rabat	Rapporteur/Examinateur
Abdelkader KARA	PES, College of Sciences, Université de Floride Centrale, USA	Examinateur
Mathieu KOCIAK	DR, Centre National de la Recherche Scientifique (CNRS), Université Paris-Saclay – France.	Examinateur
Abdallah EL KENZ	PES, Faculté des Sciences, Université Mohammed V de Rabat	Examinateur
Mohammed BENAISSA	PES, Faculté des Sciences, Université Mohammed V de Rabat	Directeur de thèse

Année Universitaire: 2020/2021

Acknowledgments

This thesis was carried out at the Laboratory of Condensed matter and Interdisciplinary Sciences (**LaMCScI**) at the Faculty of Sciences – Mohammed V University in Rabat, under the supervision of Professor **Mohammed BENAISSA**, PES at Mohammed V University in Rabat.

First of all, I would like to express my deepest thanks and appreciations to my supervisor Professor **Mohammed BENAISSA**, PES at Mohammed V University in Rabat. Looking back, I notice that my personality has changed a lot since the start of this adventure, all this thanks to my supervisor as he has passed on to me values that I would never want to let go of. Among these I can note his tact and patience, but also his sense of sensing the atmosphere and reacting to group dynamics and embracing paradigms from different fields and building an intuitive understanding.

I am grateful to the thesis committee for examining my work and providing informative and relevant feedback in the completion of this modest project. It is a tremendous honor for me that they consented to review this work. My sincere thanks are first addressed to Professor **El Hassan SAIDI,** PES at Mohammed V University in Rabat. for the interest he has shown for this work and by giving us the honor of being president of the jury members of this thesis.

I would also like to offer my thanks to the reviewers of this thesis, namely; Professor **Lalla Btissam DRISSI**, PH at Mohammed V University in Rabat, for having agreed to examine and report this thesis.

My deepest gratitude for Professor **Bouchaib HARTITI,** PES at Hassan II University in Casablanca, for having accepted to examine and report this thesis work.

I also would like to thank Professor **El Mustapha FEDDI,** PES at Mohammed V University in Rabat, for his pertinent remarks and for having also agreed to examine and report this thesis.

Many thanks to Professor **Abdelkader KARA**, PES at University of Central Florida in USA, for his time toward examining my thesis.

My deepest thank to Professor **Mathieu KOCIAK,** RD (Research Director) at Paris-Saclay University in France, for his time toward examining my thesis and for his heartwarming welcome at the Laboratoire de physique du solide (LPS) in Orsay.

My deepest gratitude to Professor **Abdallah EL KENZ** (Faculty of Sciences, Rabat) PES at Mohammed V University in Rabat, for having accepted to examine my thesis work. Many thanks to all the jury members for your help and insight in our work.

I would like to acknowledge the financial support during the thesis preparation period, in the frame of the R& D Initiative - Appel à projets autour des phosphates APPHOS – sponsored by OCP (OCP Foundation, R&D OCP, Mohammed VI Polytechnic University, National Centre of Scientific and Technical Research CNRST, Ministry of Higher Education, Scientific Research and Professional Training of Morocco MESRSFC) under the project entitled: Le potential du phosphorene pour le stockage et la conversion de l'énergie, under the project ID *MAT-MOU 01/2017*. We thank our sponsors who provided insight, expertise and follow-up that greatly assisted this research.

My warmful thanks are also directed to my dearest Professor **Abdelilah BENYOUSSEF** for all his teachings, guidance and help during my scholar career at the University. I am also very thankful to Professor **Omar MOUNKACHI,** Dr. **Khadija LAMAALAM** and Dr. **Ghassane TIOUITCHI** for their nice collaboration and for providing the black phosphorus samples.

I would also like to express special thanks to Professor **Jaber BOUJEMÂA** and Professor **Rabie FATHALLAH** from the UATRS division at the Centre National pour la Recherche Scientifique et Technique (CNRST, Rabat) for giving me the chance to use their transmission electron microscopes. These special thanks also go to all the UATRS members, for their unconditional help and support.

Particular thanks to my dear friend Yves Auad for his welcome at the Laboratoire de physique du solide (LPS) at Université Paris-Saclay in Orsay, France. I would like to thank all the LPS them for their patience, availability and the pedagogy with which they were able to teach me the electron energy loss spectroscopy. Also, a big thank to all the STEM team including Professor Odile Stephane, Christian Colliex, Marcel Tencé and everyone else for their welcome and fruitful discussions.

My deepest thanks are warmly expressed to all my friends of the LaMCscI Lab, old and new, particularly: Niama Ennassiri, Hind El Massaoudi, Anass Sibari, Wafaa Azzouzi, Ayoub Samie, Zineb Kerrami, Lahcen Boudad, Essajai Rida and everyone else. Special thanks to my friends, El Mehdi Benzekri, Karim Saber, Mohammed El-Bouji and Ayman Bakhella for their support.

Finally, I would like to thank all my relatives and in particular my mom and my dad, for having always been by my side from the first moments in my life to this special moment and for having endowed me with an extremely fulfilling manners and education, to my brother Taha (as well as my friend Yassine Ahallat) for welcoming me during my stay in Paris as well as helping me with high computational resources and to my little sister Kawtar, for continuing to support me all along. And last but definitely not least, an additional thanks to my parents and my whole family, including my uncles, aunts and all my cousins for their motivation. Now is the time to continue carving out our way into the future with resolve and optimism, hoping the next few years will be at least as good, and bringing back a multitude of good memories.

Abstract

This thesis work is dedicated to the study of the electronic and optical properties of exfoliated black phosphorus and quantum dots synthesized from commercialized black phosphorus. For that purpose, this work was divided into three main parts. The first one consists to investigate the structural and optical properties of the commercialized black phosphorus used in our work. The results obtained by electronic microscopy proved the high purity of the commercialized Black phosphorus used. While the Electron Energy-loss Spectroscopy allowed a direct measurement of the narrow bandgap ~0.3eV, as well as intraband electronic and excitonic transitions.

After that first study, the focus was on the investigation of the effect of solvent properties in the exfoliation/reaggregation of black phosphorus by molecular dynamics. This study showed that for an efficient exfoliation/reaggregation planar molecules with a high interaction energy with phosphorene are the most suitable for a smooth exfoliation as well as a better prevention against reaggregation.

Finally, the quantum confinement effect in phosphorene and black phosphorus quantum dots (BPQD) is extensively studied. Benzonitrile solvent is found to be the best candidate for exfoliation of BP and for synthesis of BPQD, as well as preventing oxidation. Furthermore, optical properties characterization showed a significant increase in the bandgap value of both structures. Such an increase was supported by theoretical calculations using density functional theory and a modified-effective mass approximation. Thus, revealing that the bandgap variation exhibits a size dependence of ($1/d^n$) rather than ($1/d^2$), with n being confinement dimensionality.

Keywords : Black phosphorus, Phosphorene, Quantum dots, Liquid Phase Exfoliation, Quantum confinement, ab-initio calculations.

Résumé

Ce travail de thèse est dédié à l'étude des propriétés électroniques et optiques du phosphore noir exfolié et des boîtes quantiques synthétisés à partir du phosphore noir commercialisé. Pour cela, ce travail a été divisé en trois parties. La première consiste à étudier les propriétés structurales et optiques du phosphore noir commercialisé. Les résultats obtenus par microscopie électronique montrent la pureté du phosphore noir commercialisé. Tandis que la spectroscopie de perte d'énergie électronique a permis une mesure directe du gap ~ 0,3 eV, ainsi que des transitions intrabande électroniques et excitoniques.

Après cette première étude, l'accent a été mis sur l'étude de l'effet des propriétés des solvants dans l'exfoliation/réagrégation du phosphore noir par dynamique moléculaire. Cette étude a montré que pour une exfoliation/réagrégation efficace, les molécules planes ayant une haute énergie d'interaction avec le phosphorene sont les plus adaptées pour exfolier et protéger contre la réagrégation.

Enfin, l'effet de confinement quantique dans les boîtes quantiques de phosphore et de phosphore noir (BPQD) est étudié. Le Benzonitrile s'avère être le meilleur solvant pour l'exfoliation du BP et la synthèse des BPQD, ainsi que pour la prévention de l'oxydation. De plus, la caractérisation des propriétés optiques a montré une augmentation significative de la valeur du gap des deux structures. Une étude par la théorie de la fonctionnelle de la densité et une approximation de la masse effective modifiée a permis de révéler que variation de la bande interdite présente une dépendance de taille de ($1/d^n$) plutôt que ($1/d^2$), n étant la dimensionnalité du confinement.

Mots-clés : Phosphore noir, Phosphorene, Boîtes quantiques, Exfoliation en phase liquide, Confinement quantique, Calculs ab-initio.

ملخص

هذه الرسالة مخصصة لدراسة الخصائص الإلكترونية والبصرية للفوسفور الأسود المقشر والنقاط الكمومية المصنّعة من الفسفور الأسود التجاري. لهذا، تم تقسيم هذا العمل إلى ثلاثة أجزاء. الأول هو دراسة الخصائص التركيبية والبصرية للفوسفور الأسود. أظهرت النتائج التي تم الحصول عليها بالمجهر الإلكتروني نقاء الفسفور الأسود. بينما سمح التحليل الطيفي لفقدان طاقة الإلكترون بقياس مباشر للفجوة ~ 0.3 فولت، بالإضافة إلى التحولات الإلكترونية والإكسيتونية داخل النطاق.

بعد هذه الدراسة الأولى، تم التركيز على دراسة تأثير خصائص المذيبات في تقشير / إعادة تجميع الفسفور الأسود بواسطة الديناميكيات الجزيئية. أظهرت هذه الدراسة أنه من أجل التقشير الفعال / إعادة التجميع، فإن الجزيئات المستوية ذات الطاقة العالية للتفاعل مع الفوسفور هي الأنسب للتقشير والحماية من إعادة التجميع.

أخيرًا، تم دراسة تأثير الحبس الكمي في الفسفور والنقاط الكمومية للفسفور الأسود. تم العثور على مذيب بنزونتريلليكون أفضل مذيب لتقشير الفسفور الأسود وتوليف والنقاط الكمومية للفسفور الأسود، وكذلك لمنع الأكسدة. بالإضافة إلى ذلك، أظهر توصيف الخصائص البصرية زيادة كبيرة في قيمة الفجوة بين الهيكلين. كشفت دراسة عن طريق نظرية الكثافة الوظيفية وتقريب الكتلة الفعال المعدل أن تباين فجوة النطاق يعتمد على الحجم ($1/d^n$) بدلاً من ($1/d^2$), n هي أبعاد الاحتواء.

الكلمات المفتاحية: الفسفور الأسود، الفوسفوريين، النقاط الكمومية، التقشير السائل، حسابات منذ البدء (ab-initio).

Résumé détaillé

Ce travail de thèse s'inscrit dans le cadre de l'Initiative R&D - Appel à projets autour des phosphates APPHOS – financé par la fondation OCP dans le cadre du projet intitulé : Le potentiel du phosphoréne pour le stockage et la conversion de l'énergie.

L'objectif de ce travail de thèse est : d'étudier les propriétés structurales, électronique et optique du phosphore noir sous forme massif et d'autre part, obtenir une bonne exfoliation et une bonne stabilité en solution du phosphore noir exfolié (phosphorene) et des boîtes quantiques de phosphore noir afin d'évaluer leurs propriétés électroniques et optiques. Dans ce but, nous avons utilisé plusieurs méthodes expérimentales tels que la spectroscopie de perte d'énergie en microscopie électronique à transmission, la spectroscopie UV-VIS, Raman et autres. En plus de méthodes de calcul théorique comme la dynamique moléculaire et les calculs ab-initio.

Pour la première partie de notre travail de thèse, une étude structurale, électronique et optique détaillée de phosphore noir (BP) a été réalisée dans la région faible infrarouge en utilisant la spectroscopie monochromatique de pertes d'énergie (EELS) couplé à un microscope électronique en transmission (TEM). Les images par microscopie (TEM) ont montré la bonne cristallinité et la non-oxydation du phosphore noir. En utilisant le spectroscope de perte d'énergie de cœur, les pics caractéristiques P-$L_{2,3}$ et P-L_1 du phosphore noir ont été clairement identifiées et attribuées à différentes transitions électroniques. Dans la zone EELS à faibles pertes, le plasmon de volume a aussi été détecté avec une énergie concordant avec celle de nos calculs théoriques. En plus de ces résultats et grâce à la monochromation du faisceau d'électrons et à l'aide d'un spectromètre avec une résolution en énergie de 20 meV, nous avons pu obtenir la valeur de la bande interdite du BP ayant une énergie de 0,33 ± 0,02 eV et d'une transition intrabande à 0,75 eV. En outre, deux autres excitations détectées se sont avérées être de nature excitoniques. Tous ces résultats démontrent l'utilité de la spectroscopie monochromatiques EELS à mesurer les propriétés électroniques de semi-conducteurs à faible bande interdite.

Dans la seconde partie de notre travail, nous avons utilisé la dynamique moléculaire pour élucider le rôle de nombreux paramètres qui contribuent au mécanisme d'exfoliation/réagrégation du phosphore noir. Huit solvants ont été testés à cette fin. Un paramètre de planarité a d'abord été désigné pour classer ces molécules. Notre modélisation du processus d'exfoliation BP a montré qu'en termes de facilité d'exfoliation, les molécules semblent nécessiter moins d'énergie que les non-planaires. De plus, nous avons remarqué que

chaque phosphorene exfolié s'est avéré être entouré d'une couche moléculaire dense, signe d'une interaction significative entre la feuille de phosphorene et les molécules de solvant. En calculant l'énergie d'interaction et la diffusion entre la surface de la couche de phosphorene avec les molécules alentour, nous avons remarqué que les molécules planaires interagissent le plus comparé à des molécules non-planaires. En effet, plus l'interaction du phosphorene avec les molécules de surface était forte, plus l'autodiffusion était élevée et plus le processus d'exfoliation était facile. En ce qui concerne la réagrégation, le processus semble être favorisé par la formation d'une couche moléculaire confinée entre les feuillets de phosphorene en raison de l'énergie de cohésion des molécules de solvant. En ce sens, les molécules non planes ne se sont révélées défavorables ni pour une suspension stable de phosphorène ni pour un processus d'exfoliation facile. Plus l'énergie d'interaction surface-molécules est faible, plus le processus de réagrégation est prononcé.

Pour la dernière partie de notre travail, nous avons démontré les performances du solvant Benzonitrile (BN) pour synthétiser du phosphorene et des boites quantiques de phosphore noir bien dispersés et bien protégés. À partir de la caractérisation vibrationnelle, nous avons constaté que le solvant BN a tendance à protéger le phosphorène et les boites quantique de l'oxydation, car aucun pic d'oxygène autour n'a été détecté. La spectroscopie Raman a montré un changement dans le mode des phonons B_2g et A_2g à la fois dans le phosphorène et pour les boites quantiques. Ce décalage Raman confirme encore que des couches de phosphorene sont bien dispersée dans la solution. À partir de la caractérisation optique, du phosphorène et des boites quantiques une bonne dispersion avec une grande cristallinité a été observé par la microscopie en transmission et la diffraction électronique. La caractérisation optique par UV-VIS a montré que la bande interdite expérimentale augmentait en fonction du confinement pour le phosphorène et pour les boites quantiques. En outre, des études théoriques approfondies, par la DFT et l'approximation de la masse effective modifié ont été réalisé révélant que la variation de la bande interdite présente une dépendance en fonction du régime de confinements.

Ces résultats obtenus démontrent le grand potentiel de nanomatériaux à base de phosphore noir pour des applications optoélectroniques telles que les cellules solaires et les lasers grâce à leur structure atomique et leur flexibilité dans l'ingénierie de leurs propriétés optiques et électroniques.

SUMMARY

Table of figures

List of tables

List of abbreviations

BP: Black Phosphorus

TEM: Transmission electron microcopy

HRTEM: High-resolution Transmission electron microcopy

EELS: Electron energy loss spectroscopy

DFT: Density Functional theory

QC: Quantum Confinement

BPQD: Black Phosphorus quantum dots

BN or BZ: Benzonitrile

DMF: Dimethyl formamide

NVP: N-Vinylpyrrolidone

EMA : Effective mass approximation

MSD: Mean square displacement

2D: two dimensional

0D: zero dimensional

MD: Molecular Dynamics

DMSO : Dimethyl sulfoxide

NMP : N-methyl-2-pyrrolidone

CHP : N-cyclohexyl-2-pyrrolidone

IPA: Isopropyl alcohol

DMI: 1,3-Dimethyl-2-imidazolidinone

PMF: Potential of mean force

Chapter I.

General Introduction and State of the art

The discovery of two-dimensional materials (2D) in materials science, has drew worldwide attention and had a significant impact in a variety of sectors. In recent years, the understanding of layered 2D materials has improved significantly. Many kinds of 2D materials can be isolated from their bulk counterparts such as Graphene,[1] Stanene,[2] Germanene,[3] MoS_2[4] and black phosphorus (BP).[5] While the chemical composition of these materials varies depending on their atomic arrangement, they all have one thing in common: they are made up of separate atomic-thick layers with weak van der Waals interlayer bonding. The study of this family of materials is without doubt at the cutting edge of materials science, due to their unique properties originated from quantum-confinement effects such as a tunable band gap, a high Young's modulus, high strength, excellent carrier mobility, and high anisotropic properties between their in-plane and out-of-plane structure.[6-7-8-9-10] Owing to these outstanding properties, 2D materials are nowadays promising candidates for a wide range of applications in different fields including electronics, spintronics, energy conversion, optoelectronics, medical, etc.[11-12-13-14]

BP is currently considered a pioneering material due to its broadband optical response, from visible to mid-infrared, due the tunability of its band-gap energy ranging from 0.3 eV for bulk state, ~0.8 eV for triple layers, ~1.3 eV for bilayer and 1.7 eV for a monolayer.[15] . Besides, BP also exhibits a mobility as high as 10000 $cm^2V^{-1}s^{-1}$,[16] a large on/off ratio (10^5)[17] and unique linear and nonlinear optical features. The anisotropic optical response,[18] saturable absorption effect,[19] and Kerr effect[20] are some examples of the optical properties of BP. The nonlinear saturable absorption coefficients of BP are superior to those of other 2D known materials like graphene, MoS_2 and WS_2. All these features suggest that it could be employed for a large plethora of optical applications such as solar cells,[21] bioimaging,[22] and cancer therapy.[23] In fact, it was found that BP could allow photodetection over a broad spectral region, thanks to its tunable bandgap making it suitable as a photoacoustic imaging agent for bioimaging.[22] In addition, exfoliated BP nanosheets were reported to be effective photosensitizers for the generation of singlet oxygen that can be applied in photodynamic cancer therapy.[24] BP has also shown a superior performance for gas sensing, which can be applied to detect environmental hazardous gases as the adsorption of gas molecules was found to be stronger than other 2D materials, which leads to an enhancement of the electric properties of BP and subsequently enabling the construction of highly sensitive gas sensors.

For all the above-mentioned applications, it is of central importance to provide BP with high purity and quality. It is then very critical to control its fabrication at a laboratory scale and

beyond. Early in 1914, BP was first discovered by accident in an attempt to convert white phosphorus into red phosphorus (both are phosphorus allotropes).[25] It was produced by applying high hydrostatic pressure to white phosphorus. Under kerosene, white phosphorus was inserted in a high-pressure cylinder. At room temperature, a high pressure of up to 0.6 GPa was applied. After that, the cylinder was heated to 200°C and the pressure was increased to 1.2 GPa. Under these conditions, the shift from white phosphorus to BP took between 5-30 minutes. After cooling the cylinder and releasing the pressure, a little amount of BP was discovered. Subsequently, many methods to synthesize BP followed. Among these methods, RP was heated at 1000°C followed by slow cooling rate at 100°C per hour under a constant pressure of 10 kbar, giving yield to high purity BP crystals.[26] A few attempts were also made to create BP single crystals with 5 mm in length and 10–100 μm in thickness using different processes such as mercury catalysis or recrystallization of liquid Bismuth.[27-28] However, those procedures are quite harmful to nature and experimentally time consuming. The Chemical Vapor Transport (CVT) approach has been identified as a possible method for manufacturing BP crystals.[29-30] A short way transport reaction from red phosphorus with Sn/SnI_4 as a mineralization additive and Au as a catalyst can be used to grow BP. Along with BP crystals, byproducts such as Au_3SnP_7, AuSn, Au_2P_3, and others are formed in this CVT process. By using excess Sn and as a mineral additive, Köpf et al. attempted to optimize the reaction conditions in such a way that the main product and unwanted phases are well separated from each other, allowing for a more efficient and quick synthesis of BP.[31] It is worth to mention that Tiouitchi et al. has successfully synthesized high-quality and impurity-free BP by CVT by using a cheap, abundant and non-toxic catalyst Cu (Copper).[32]

As already said, BP is basically made of ordered and packed phosphorus atomic sheets. When separated, these sheets are individually called Phosphorene layers. Producing these 2D layered nanomaterials can be performed in a variety of ways. These techniques can be divided into two categories: top-down and bottom-up approaches. Self-assembly or, more typically, chemical vapor deposition (CVD) are examples of bottom-up techniques, while, mechanical cleavage to liquid-based approaches are all examples of top-down techniques. Mechanical cleavage is considered amongst the earliest methods to produces layered materials, while this approach yields high-quality monolayers, it takes a long time and has a low throughput.[33] In contrast, Li-ion intercalations, which involves inserting Li ions into bulk crystals to split the layers and produce individual layers in solution, is one example of a liquid-based approach. Although this approach creates a significant number of monolayers, the nanosheets produced

contain a lot of defects. On the other hand, Liquid Phase Exfoliation (LPE) is a straightforward process based on solubility characteristics; allow for the production of nanosheets in organic solvents. Coleman et al. invented this process, which is utilized to make defect-free mono- and few-layered nanosheets in solution.[34] For LPE, BP is immersed in a suitable solvent; the latter is chosen to match the nanomaterial's surface energy. To counteract the van der Waals cohesive force between the stacked sheets, an energy is given to the system in the form of sonication between the layers of the bulk BP. Despite the fact that diverse variety of exfoliation media were used, there is still a significant lack of understanding about how to design the optimal solvent for an efficient exfoliation and stabilization of a given 2D nanomaterial.

Most recently, BP quantum dots (BPQDs), the new derivative of BP nanomaterials, have gotten a lot of attention since their first preparation by solution-based method in 2015.[35] Owing to the quantum confinement and edge effect, these zero-dimensional materials have shown unique electronic and optical features as compared to standard 2D-BP nanosheets.[35] However, preparation approaches suffer from long processing times and yields some structural defects in the product, impeding their development and applications. Exfoliation in liquid media was extensively used to produce BPQDs.[35,36,37] First synthesized BPQD were obtained by using both a bath and a probe sonicator, to provide additional energy to the exfoliated sheets; thus, breaking them from the edges allowing formation of small size BPQD.[38] Unusual methods based on solvents were also used to obtain BPQD such as mixing with a kitchen blender giving QD of consistent sizes of about ~5 nm.[39] Solvothermal assisted LPE was also used, which consists of providing an additional energy to the exfoliated sheets after ultrasound to exfoliated the thin sheets from the edges.[40] These formed BPQDs were found to have exceptional properties such as a high memory performance,[41] a high UV/VIS absorption spectroscopy,[42] interesting photothermal conversion and nonlinear optical properties.[37] They also have a high extinction coefficient of 14.8 $Lg^{-1}cm^{-1}$ at 808 nm, a high conversion efficiency of 28.4% and good photostability in the near-infrared.[37] Due to their properties, BPQD were used and suggested for a broad range of applications, especially, nonlinear optical absorbers, sensors, cancer therapy, optoelectronic devices and others.[43-44-45]

Hence, by deeply understanding the exfoliation process of BP, a solution to produce exfoliated BP and BPQD in a large-scale could be conceived, thus, leading to a better investigation and understanding of their electronic and optical properties for potential applications. This is exactly the purpose of the present thesis which is part of a project funded by OCP Foundation, ID: MAT-MOU 01/2017.

Our motivation was to combine theoretical and experimental methods to investigate the optical and electronic properties of BP and BP nanomaterials (nanosheets and quantum dots) for electronic and optical applications. However, due to the reduced size of the material under study, nano-sheets and quantum dots, the need for adequate characterization tools is of fundamental importance. In the present thesis, BP properties were deeply investigated by transmission electron microscopy (TEM), a technique that allows a fast and direct probing of the material's properties (structural, electronic, optical and chemical) at a nanometer scale, especially when coupled to electron energy loss spectroscopy (EELS) and cathodoluminescence. A reason why TEM-EELS was extensively used to reveal the intrinsic properties of BP, particularly the electronic properties since bulk-BP exhibits a narrow bandgap and excitonic transitions in the near infrared region. Highly resolved EELS was then needed and the results of which were permanently confronted to those of ab-initio calculations. So, the outline of the present thesis is as follows:

In ***Chapter I,*** a succinct overview of the state of the art of black phosphorus material's synthesis, properties and applications was detailed, to emphasize the main goals of our research.

In ***Chapter II,*** theoretical and experimental methods were fully described, namely; the Density of Functional Theory, Molecular dynamics, TEM, EELS, Raman, FTIR and UV/VIS spectroscopy. Finally, the black phosphorus powder, solvents and exfoliation methods were thoroughly described.

Chapter III *is dedicated to* an experimental study by electron energy loss spectroscopy in a TEM was performed on black phosphorus flakes, and then confronted to ab-initio calculation results to better describe and investigate their electronic and optical properties. Contrary to other spectroscopic techniques, monochromated low-loss EELS allowed elucidate the low bandgap of black phosphorus as well as excitonic features and intra-band transitions. Additionally, DFT allowed assign each of these optical transitions. This study showed the efficiency of a monochromated EELS coupled to a STEM to perform direct measurements on materials with narrow band-gap such as black phosphorus.

In ***Chapter IV***, we focused on the theoretical study of the liquid phase exfoliation of black phosphorus. This study, we performed a molecular dynamics simulation of the LPE of BP in different solvents to survey each solvent molecule effect on the exfoliation and reaggregation as well as to understand the mechanism of LPE. This study helped choose the

most promising solvent for the exfoliation task, which is benzonitrile, to successfully prepare quantum structures (phosphorene and BPQDs).

Finally, ***Chapter V*** describes the preparation of stable phosphorene suspensions and synthesize black phosphorus quantum dots on the basis of the aforementioned results from previous chapters. By using Benzonitrile solvent, which was found to be the best candidate for liquid phase exfoliation from molecular dynamics, we managed to successfully synthesize our 2D and 0D BP nanomaterials. We then extensively studied the quantum confinement effect on BP materials using theoretical and experimental approaches. Structural characterization via high-resolution transmission electron microscopy imaging and electron diffraction patterns allowed to investigate the structural characterization of our materials. While, Raman and Fourier-transform infrared spectroscopy were used to observe the vibrational properties of BP, phosphorene and BPQD. Furthermore, optical properties were investigated by UV-VIS spectroscopy. All the experimental results were supported by theoretical calculations including density functional theory and a modified-effective mass approximation, thus giving a description of the bandgap and effective mass dependence as a function of the confinement regime.

Chapter II.

Theoretical and experimental techniques

II.1. Theoretical methods

II.1.1. Density functional Theory

Density functional theory (DFT) is a theoretical method extensively used in our thesis with the main purpose of investigating structural, electronic and optical properties of black phosphorus, exfoliated black phosphorus and quantum dots. The DFT method allowed us to understand the physical properties of BP in details by comparing the results obtained in theory with those obtained experimentally. However, to get results in accord with reality, several factors are to be considered, such as the approximation used and the interactions taken into account. In the next section, a brief description of the DFT method along with the approximations and approaches used in our calculations are presented.

II.1.1.1. Introduction

In 1924, Louis de Broglie[46] hypothesized that for any particle of energy and given momentum, it is possible to associate a wave frequency and a given wavelength, called a "wave function". This theory expresses the wave-particle duality of matter. Schrödinger then proposed a time-dependent equation,[47] with $\hat{H}$ the Hamiltonian operator, $\psi_k(\vec{r},t)$ the wave function describing the system in a quantum state *k* at time *t* and at a point in space *r*. The temporal and spatial evolution of this system is described by:

$$\hat{H}\psi_k(\vec{r},t) = i\hbar\frac{\partial}{\partial t}\psi_k(\vec{r},t) \qquad (1)$$

This equation is simplified, by considering the terms E_k which are the eigenvalues of $\hat{H}$ associated with the eigenvectors ψ_k. These eigenvalues correspond to the energies of the different states, the system's equation becomes:

$$\hat{H}\psi_k(\vec{r},t) = E_k\,\psi_k(r) \qquad (2)$$

The quantum study of the system aims to determine the wave functions by solving the equation. However, the exact solution of this equation is impossible for systems with three particles and more, which forces us to work with approximate solutions.

Density Functional Theory (DFT) is based on the description of the electron density (ρ_r) which is an observable (unlike the wave function). This theory, introduced in the 1960s by Kohn, Hohenberg and Sham, is based on two theorems.[48]

- The first theorem states that the energy of a polyelectronic system is a unique functional of the electron density in its ground state corresponding to a unique external potential V_{ext}.

$$\rho(r) = \sum_{i=1}^{N} \psi_i(r)\psi_i^*(r) \qquad (3)$$

- The second theorem states that the total electronic energy E is a function of the electron density, $E = E[\rho(r)]$. The ground state of the system ρ_0 is therefore characterized by a minimum energy $E[\rho_0]$. However, the exact expression of energy as a functional density is unknown, it is therefore necessary to introduce approximations.

In 1965, Kohn and Sham[49] proposed a framework based on an iterative procedure of self-consistent type with the expression of the density established on monoelectronic wavefunctions ϕ_i^{KS}, called Kohn-Sham orbitals. This approach describes a set of electrons without interactions but with an electronic density similar to that of the studied system, which amounts to expressing the eigenvalues equation as follows:

$$\hat{F}_i^{KS}\phi_i(r) = \varepsilon_i\phi_i \qquad (4)$$

With $\hat{F}_i^{KS}$ monoelectronic operator of Kohn-Sham, ε_i and ϕ_i, are the eigenvalues and eigenfunctions, respectively.

As electrons are independent, their wavefunctions are orthogonal and the Hamiltonian is symmetric. The total energy of the functional Kohn-Sham is given by:

$$E_{KS}[r] = \int V_{ext}(r)\rho(r)dr + T_{KS}[\rho] + E_H[\rho] + E_{XC}[\rho] \qquad (5)$$

Where the first term corresponds to the potential energy between electrons and particles or external fields, $T_{KS}[\rho]$ is the kinetic energy of N electrons without interaction and $E_H[\rho]$ is the Hartree energy. However, while this energy of Hartree must describe an electron-electron interaction, it only takes into account the repulsion between two electrons. For a better description of this interaction complex, the exchange-correlation term $E_{XC}[\rho]$ is added.

If all the Kohn-Sham terms of functional are exactly known, however, this is not the case with the exchange and correlation part. To get close to the exact energy of exchange and correlation, many approximations were used. The quality of description of the electronic structure depends on the choice of its approximation and its ability to describe a real system. The most common approximations are the local density approximation (LDA) and the gradient approximation generalized (GGA) as well as Hybrid functional approximation.

II.1.1.2. Local density approximation

This approximation consists in considering the density as locally uniform. The exchange correlation energy $V_{xc}^{LDA}[\rho(r)]$ for each r position is assumed to be the same as for a uniform electron gas having the same density. The exchange correlation energy is a function of $\varepsilon_{xc}^{hom}[\rho(r)]$, which is the exchange-correlation energy per homogeneous gas particle electron density $\rho(r)$.[50] This energy can be split into the sum of two contributions: The exchange energy ε_x^{hom} and the correlation energy ε_c^{hom}, such that:

$$V_{xc}^{LDA}[\rho(r)] = \int \rho(r)\varepsilon_{xc}^{hom}[\rho(r)dr] = \int (\varepsilon_x^{hom}[\rho(r)] + \varepsilon_c^{hom}[\rho(r)])dr \quad (6)$$

If the exchange part is known for a uniform gas, this is not the case for the correlation which is parameterized from numerical solutions from databases data.

Generally, the LDA approach is suitable for electronic systems having relatively homogeneous densities. This concept allows to achieve relatively good results by compensating for errors. Indeed, this method tends to underestimate the exchange energy while it overestimates the correlation energy, which makes it possible to achieve a fairly good value for the energy of exchange and correlation.

II.1.1.3. Generalized gradient approximation

One way to improve the description of the inhomogeneous local electronic density, is to take into account the gradient of the electron density $\nabla\rho(r)$:

$$V_{xc}^{GGA}[\rho(r)] = \int f[\rho(r), \nabla\rho(r)]dr \quad (7)$$

Unlike the LDA, the GGA[51] is no longer just a local function of density but also depends on the amplitude of its gradient. It's important to note that GGA methods are not non-local methods. Moreover, there are several empirically parameterized versions of GGA, more or less well suited depending on the systems studied, and the choice of method and parameters are made according to the agreement with experience. Anyway, these methods offer real advantages through the precision they achieve, on quantities that the LDA tended to describe less precisely. The GGA leads in particular to a significant increase in the mesh parameters of certain materials containing heavy elements (transition metals). In fact, in our results we found a clear underestimation of the results obtained by the use of LDA and GGA approximation such as the bandgap energy. As such, to remedy to this discrepancy, another family of functionals had to be considered, which are the hybrid functionals.

II.1.1.4. Hybrid functionals

New generation of functionals appeared since the 90s, called hybrid functionals.[52] Becke suggested the combination of a part of the exchange energy of the Hartree Fock type and the density functional. The complete description of the electronic exchange and correlation is obtained by combining an exchange functional and a correlation functional.[53] The use of HF exchange part associated with GGA functionalities provides results comparable to those of the generalized gradient approximation. The conversion of a reference system "without interaction" into an interacting system is the origin of the adiabatic term connection. We can show that the exchange correlation energy can be determined as:

$$E_{xc} = \int_0^1 \langle \psi(\lambda) | V_{xc} | \psi(\lambda) \rangle \, d\lambda \qquad (8)$$

Where λ describes the extent of the electronic interaction, which is the strength of the electronic coupling that varies between two borderline cases. When λ = 0, the equation corresponds to the value of the HF exchange energy of the system without any interaction between the electrons, but calculated with the Kohn-Sham orbitals (this is often referred to as the "exact" exchange term). For λ = 1, we have a real system in complete interaction. The entire exchange-correlation is described by a DFT functional. Integration comes down to introducing part of the exact exchange into the energy functional, in order to remedy to the defect of the GGA correction of the uniform gas model electrons. The integration between the two boundary systems takes place at constant density and electronic configuration, which is at the origin of the so-called hybrid functionals. Different kind of hybrid functionals exist, from which we can cite B3LYP, B1PW91, PBE0, HSE06…[54-55-56]

In our thesis work we used the HSE06. This functional allows to combine an exact exchange part of Hartree Fock (α) and a well-defined exchange part (w), as shown by the following expression:

$$E_{XC}^{HSE} = \alpha E_X^{HF,SR}(w) + (1-\alpha) E_X^{PBE,SR}(w) + E_x^{PBE,LR}(w) + E_C^{PBE}(w) \qquad (9)$$
$$(\alpha = 0.25, w = 0.2)$$

With α is the mixing parameter and w is an adjustable parameter controlling the short range of the interaction. $E_X^{PBE,SR}$ and $E_C^{PBE,LR}$ are the short-range and long-range components of the PBE exchange functional.

II.1.1.5. Van der Waals interaction

Due to the 2-dimensional nature of BP which consists of layers separated by vdW interactions, some long-distance interactions (d > 3 Å) may be over or underestimated via the previously cited approximations, as is the case for the weak van der Waals interactions (vdW), also called dispersion forces. So, a term representing this E_{disp} scattering energy is added to the total energy:

$$E_{DFT-disp} = E_{KS-DFT} + E_{disp} \qquad (10)$$

Subsequently, Van der Waals functional (vdW-DF) was developed to include these interactions.[57-58-59] This van der Waals implementation is found to be successful for large systems calculations. Currently, the vdW-DF implementation has negligible time difference with calculations using only standard GGA calculations. In this thesis, the vdW-optB88 method was used.[60] This method applies the optB88 exchange functional which was proven suitable to obtain accurate results such as lattice parameters and energy of solids.

II.1.2. Molecular Dynamics

The second computational method used in our thesis is Molecular Dynamics. The aim of this method was to analyse the effect of different solvent molecules on the exfoliation and reaggregation of BP. We used molecular dynamics as it is a simulation method dedicated to the analysis of physical movement of atoms and molecules. These atoms and molecules are allowed to interact with one another for a fixed period of time, hence allowing investigation of their properties imparted by their interactions. One major point to be concerned about is the choice of a suitable potential (Force Field) for the interactions in our system. In the following section, we will describe the principle of molecular dynamics and the potential used to describe the system used in this thesis.

II.1.2.1. Introduction

From the appearance of the first computers in the 1950s, molecular dynamics laid down its first milestones. The first article reporting a simulation of molecular dynamics was written by Alder and Wainwright in 1957.[61] The aim of this article was to find the phase diagram of a system of hard spheres, and in particular that of the phases of liquids and solids. The article by G. B. Gibson, which appeared in 1960,[61] is probably the first example of a molecular dynamics calculation with

a continuous potential based on a finite difference time integration method. Annesur Rahman of Argonne laboratory was one of the most famous pioneers in molecular dynamics. In his article in 1964,[62] he studied the properties of liquid argon using a Lennard-Jones potential on a system containing 864 atoms. Loup Verlet found in 1967[63-64] the phase diagram of argon using the Lennard-Jones potential and calculated correlation functions to test the theories of the liquid state. The famous counting method known as Verlet's neighborhood list was introduced in his papers as well as "Verlet's time integration algorithm". Phase transitions in the same system were investigated by Hansen and Verlet a few years later.[65]

In 1971, the molecular dynamics method never ceased to experience rapid developments, both from the point of view of algorithmic developments and of applications to the most diverse complex systems (molecular fluid, "giant" polyatomic systems, solids and interfaces ...). A wide variety of molecular dynamics simulation studies have been carried out on water[66-67-68] and on biological systems (charged proteins, membranes, etc.) in which ions appear.[69]

II.1.2.2. Molecular Dynamics theory

Classical molecular dynamics corresponds to the integration of Newton's equations of motion to calculate the atomic positions from the forces acting on each atom. These forces are defined by the force field; it is therefore crucial to have a force field adapted to the interactions that exist in reality for the molecules under study.

$$F_i = m_i a_i = m_i \frac{\partial^2 r_i}{\partial t^2} = -\frac{\partial V}{dr_i} \qquad (11)$$

With F_i is the force applied to atom i, m_i is its mass, a_i its acceleration, r_i its vector position, t time and V is the potential. We can therefore see how starting from a potential (Force field), we can calculate the forces applied to an atom, therefore its acceleration a_i and its position. The integration step is the time interval used to digitally integrate these equations. In molecular dynamics, when all atoms are represented explicitly, this integration step is equal to one tenth of the fastest movement, to represent it correctly. The vibration of a carbon-hydrogen bond is the fastest movement, and corresponds to approximately 10 fs (10.10^{-15} s). The chosen integration step is therefore 1 fs. A variant of Verlet's algorithm is used to update the positions as a function of time.[63]

In any simulation, it is necessary to define a simulation cell which represents a portion of the system in the study. Given the small number of simulated molecules, this cell is quite small: of the order from 1 to 10 nm^3. The surfaces therefore represent a significant percentage of the system.

While in laboratory, surface effects are often negligible compared to the sample volume. To limit these significant surface effects in simulation, periodic boundary conditions are used (Figure 1). As soon as an atom leaves the simulation cell from one side, it goes back from the other way. The surfaces are thus eliminated and the simulated system is pseudo-infinite.

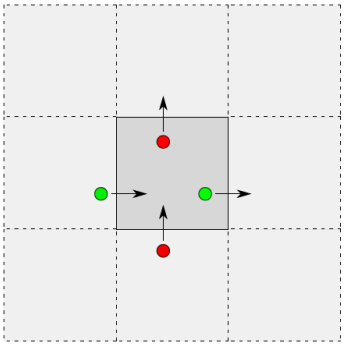

Figure 1. Periodic boundary conditions

II.1.2.3. Atomistic models

Atomistic methods use classical mechanics to describe matter at the level of the atom. Each atom is represented by a rigid sphere having a mass and a charge. These spheres interact with each other either through binding or non-binding terms. The function giving the energy of a molecule (Eq. 12) is therefore written as a sum of these two terms. Binding terms include potential energy terms describing the deformation chemical bonds (stretching, shearing, dihedral), while non-binding interactions takes into consideration atoms that are separated by more than three bonds to interact, to represent potential energy describing electrostatic interactions for example.

$$V = V_{bonds} + V_{angles} + V_{dihedrals} + V_{non-bonded\ interaction} \quad (12)$$

The different energy terms are schematized in figure 2 and described in the sub-sections following.

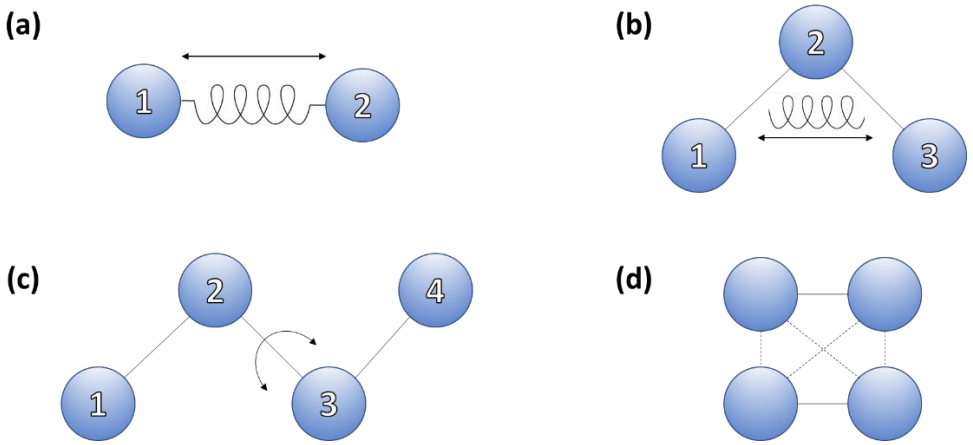

Figure 2. Interactions in molecular mechanics. (a) Vibration of the connections. (b) Change in angles. (c) Variation of dihedral angles. (d) Non-covalent interactions between two diatomic molecules.

II.1.2.4. Force fields

All the equations used to describe the interactions between atoms, as well as the parameters used in these equations form what is called a force field. The choice of forces fields in molecular dynamics is a crucial step. Indeed, each force field is parameterized for specific classes of molecules and validations of these potentials' interactions are made by comparing different properties measured experimentally or calculated theoretically. To choose a suitable force field suited to the problem required, it is therefore necessary to learn about the type of molecules used for parameterization as well as the properties used for validation. If these properties are determined by molecular interactions playing an important role in the problem under study, then the field corresponding forces can serve as a reasonable basis as an interaction potential for the simulations.

The OPLS-AA (Optimized Potential for Liquid Solutions - All Atom) force field[70] has been developed using a set of pure organic liquids including for example alkanes, ketones, amides or ethers. The parameters used are optimized to reproduce structural and thermodynamic data such as liquid density and enthalpy of vaporization. These properties strongly depend on inter-molecular interactions. Now it turns out that these interactions play a primary role in the behavior of mesophases.[71] In this phD thesis, the OPLS-AA force field is therefore used. The equations and their parameters used in this force field are described below.

II.1.2.4.1. Bonds and angles

The bonds and angles between atoms are represented by a harmonic potential (Eq. 13). Such a potential requires two parameters: a position of equilibrium or an angle of equilibrium (x_0) and a

force constant (k). The equilibrium value represents the minimum energy: any deviation from this position of equilibrium results in an increase in potential energy. The force constant represents the ease with which the bond or angle can be moved away from this position of balance.

$$V_{bond/angle} = k(x - x_0)^2 \qquad (13)$$

II.1.2.4.2. Dihedrals

A dihedral angle is an angle between two planes. In Figure 2, these are the planes formed by the atoms 1-2-3 and 2-3-4. A variation of this angle is therefore equivalent to a rotation around the bonds between atoms 2 and 3. Mathematically, such a rotation is represented by a sum of cosine functions, as shown in Eq. 14, where ϕ is the dihedral angle and the coefficients k_i are the coefficients of torsion, revealing the relative importance of each cosine function.

$$V_{dihedral} = k_1[1 + \cos(\phi)] + k_2[1 - \cos(2\phi)] + k_3[1 + \cos(3\phi)] \quad (14)$$

II.1.2.4.3. Non-bonded interactions

The OPLS-AA force field has two types of non-bonded interactions: the van der Waals and the Coulomb interaction.[25] The van der Waals interaction allows interactions between all atoms, whether they are charged or not, because it depends only on the distance between two atoms. It represents a sum of the forces of Keesom, the forces of Debye and the forces of London. Its expression is given by a Lennard-Jones potential (Eq. 15).

$$V_{vdW} = 4\epsilon[(\frac{\sigma}{r})^{12} - (\frac{\sigma}{r})^{6}] \qquad (15)$$

The parameter ϵ determines the depth of the potential well and the parameter σ represents the distance from which the potential changes from attractive to repulsive.

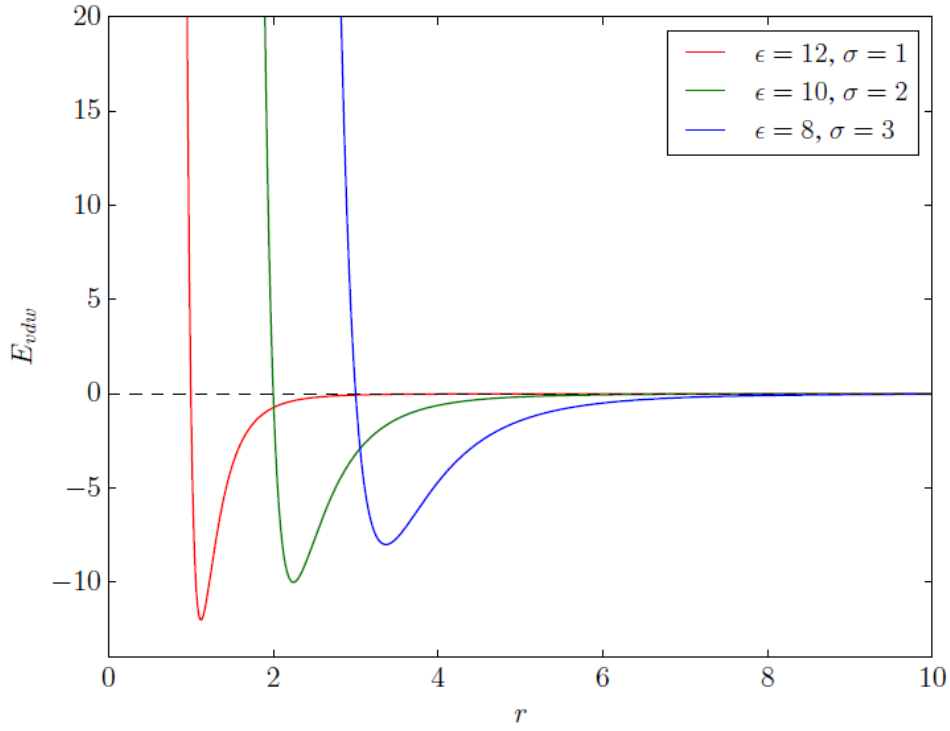

Figure 3. Lennard-Jones potential and effect of ϵ and σ

Figure 3 is a representation graph of the Lennard-Jones potential and shows the influence of the parameters ϵ and σ. Unlike the van der Waals forces, the Coulomb interaction describes the forces acting on charged species (atoms which carry a partial charge).

$$V_{Coulomb} = k_e \frac{q_i q_j}{r_{ij}} \qquad (16)$$

where k_e is the Coulomb's constant ($\frac{1}{4\pi\varepsilon_0}$) , q_i is the partial charge of atom i and r_{ij} is the distance which separates the two atoms i and j. Once the force field has been chosen, we determine the approximations describing the interactions between atoms. From initial conditions (positions and speeds of each atom), we can then generate the coordinates of the atoms as a function of time by integrating the equations of Newton's motion: this is the principle of classical molecular dynamics.

Figure 4 below summarizes the molecular dynamics process.

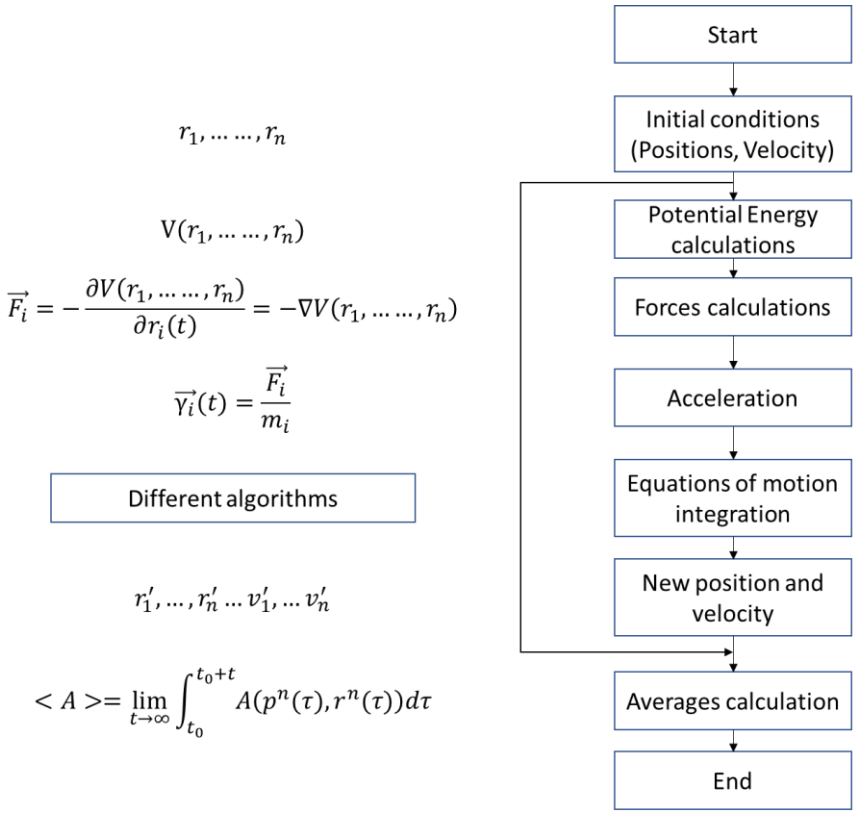

Figure 4. Schematic representation of a molecular dynamics program. $p^n(\tau)$ and $r^n(\tau)$ represents the set of positions and moment of particle of a system in time

II.2. Characterization methods

II.2.1. Transmission Electron Microscopy (TEM)

II.2.1.1. Introduction

Regarding the main experimental technique used in this work, we have devoted this part of the chapter to describe the transmission electron microscopy technique and its main operating modes. First of all, it should be mentioned that this technique coupled with other techniques such as Energy-dispersive X-ray spectroscopy X (EDX) and electron energy loss spectroscopy (EELS) was considerably used in our work as it provides a precise and local observation of the crystallographic and chemical information in our samples on a nanometric or even atomic scale. The following section describes the working principle of a transmission electron microscope and the other techniques coupled to it, as well as the specificities of the microscopes used in our thesis work.

II.2.1.2. Working principle of the transmission electron microscope

Electron microscopy allows to obtain an image of the microstructure of materials with a magnification and resolution much higher than the conventional optical microscope. Transmission electron microscopy is one of two types of electronic microscopy and it is this technique that was the mostly used in this thesis. This type of microscope generally uses an energy range varying from 100 to 400 keV. In order to accelerate the electrons to such a speed, a complex system is put in in motion. Obviously, this technique is particularly expensive. These impressive costs are, however, justified by the TEM's ability to provide a multitude of information about the study sample.

Prior to describing the electron path in a TEM, the occurring electron-matter interactions in the microscope are described. In a transmission electron microscopy experiment, fast electrons, typically of the order of 100 to 200 keV, or about half the speed of light, are sent on the sample of interest. After interaction, the characteristics of the electrons will be modified, and a number of particles and radiations will be produced. The signals thus obtained will provide access to information on structural, electronic and optical properties, among others, of the material, and will thus be used in TEM. The different interaction processes are summarized in the Figure 5 below. The most useful particles are of course the electrons themselves. Thus, the majority (typically 80%) of the electrons will not interact inelastically with the sample, and will either be directly transmitted, either diffracted and / or elastically diffused. The contrasts obtained in conventional imaging, high-resolution imaging, diffraction, all come from a different use of these electrons. The remaining 20% energy is therefore lost through interaction with the sample by creating plasmons, inter-band transitions and transitions from the valence to the conduction band. The study of this lost energy is the basis of electronic energy loss spectroscopy (EELS), as will be further described.

The excitations described can be de-excited according to different modes, some of which are very useful. This is the case with de-excitations from unoccupied levels to heart states, in the form of X rays. The technique is used to perform quantitative chemical analyzes on nanoscale volumes, and is known as the term Energy Dispersive X-Ray Spectroscopy. This is also the case for the de-excitations of states of the conduction band to the valence band in the form of visible UV and infrared photons. The associated technique, called cathodoluminescence, is also available in a TEM. During de-excitation, secondary electrons can be emitted. In addition, incident electrons can be backscattered. Although practically unused in TEM, these two types of electrons are the basis of contrast formation of Scanning Electron Microscopy images.

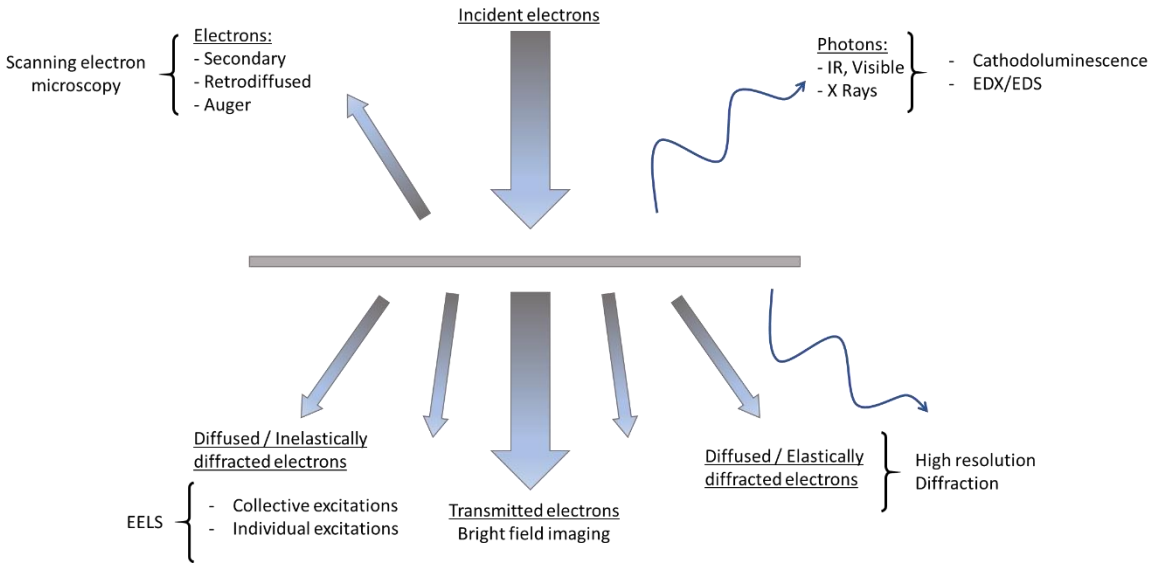

Figure 5. The different electron-matter interaction processes and their link with the different TEM techniques.

For the electron beam trajectory, Figure 6 illustrates the operation of a MET. An electron gun is responsible of a beam generation. This beam then passes through a series of condenser lenses, the role of which is to be able to adjust the size and angle of incidence of the beam. The latter then reaches the sample. A first image is then produced by the objective lens. It should be noted that the latter is the most important element, because its quality will depend on the resolution of the image. In addition, the objective lens hardly enlarges ($\approx \times 10$), this role being devolved to the projector lenses. After passing through the objective lens, the intermediate lens will either form a second image, if its object plane coincides with the image plane of the objective lens, either form an image of the diffraction cliché, if its object plane coincides with the focal plane of the objective lens. We thus see obvious advantages of transmission electron microscopy: by modifying the value of the focal length of the intermediate lens (in practice, a simple button to press modifying the current in the intermediate coils), we easily obtain the image or diffraction image of the same zone. Finally, the projector lenses will enlarge the image or diffraction pattern and project it onto a detector, which is a fluorescent screen, a photo plate or more commonly a scintillator coupled to a CCD camera.

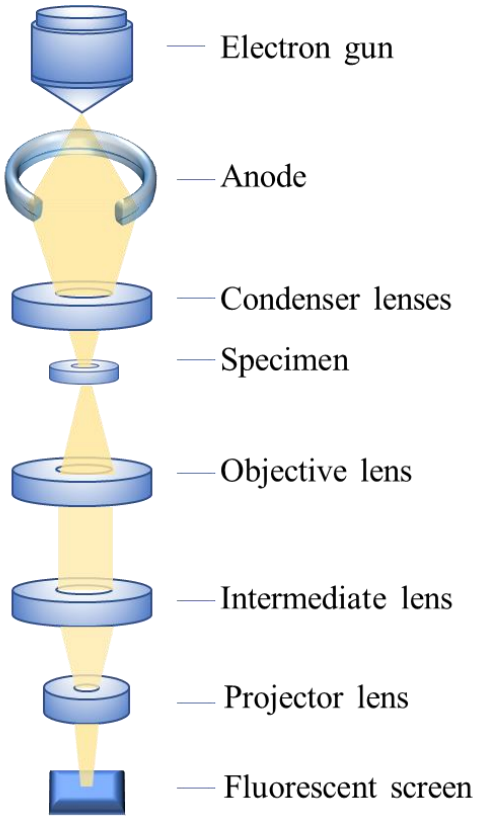

Figure 6. A generalized cut-away diagram of the internal structure of a transmission electron microscope

II.2.1.3. Observation modes of TEM

II.2.1.3.1. Imaging mode

a. Conventional imaging

The image is produced by selecting a wave through the aperture objective and orienting the crystal so that there is only an intense diffracted wave in addition to the incident wave. The other low intensity waves are neglected. If the transmitted wave is selected, (Figure 7a) the image formed is said to be in a bright field where the dark parts correspond to areas of the sample that have diffracted a significant part of the incident electrons. If the diffracted beam is selected (Figure 7b) (the beam is moved to the zone axis by tilting the incident beam) we obtain a so-called dark field image where only the regions of the sample having crystallographic planes in the diffraction condition, are visible. The conventional imaging in a TEM was used to a great extent in observing our BP sample as it allowed clear observation of the prepared samples.

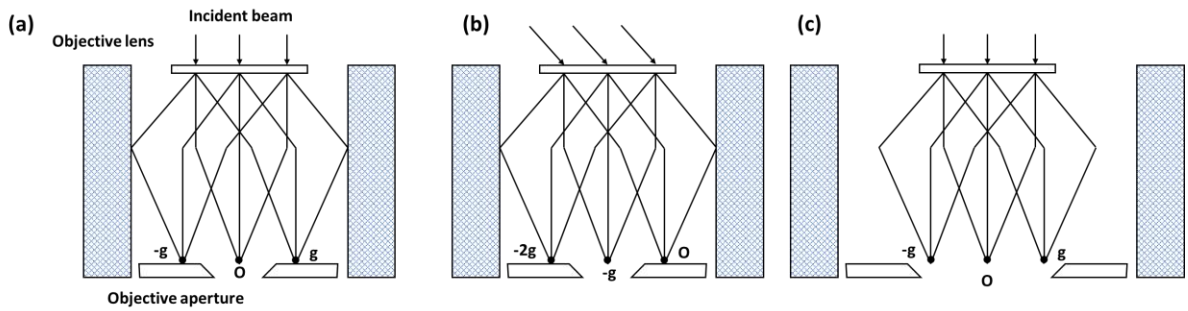

Figure 7. Different imaging mode (a) Bright field (b) Dark field (c) High-resolution imaging

b. High-Resolution imaging

High resolution microscopy is a remarkable technique for 'seeing' directly atoms or groups of atoms. It is based on the principle of interference between the transmitted beam and one or more beams diffracted by the different reticular planes participating in the formation of the image (Figure 7c). However, the microscope is not a perfect optical system and induces aberrations in the formation of the image interference, in particular the spherical aberration *Cs* which is more troublesome than the chromatic aberration *Cc*. In addition, a slight change in the focal length of the lens shifts the object plane of this lens of a quantity Δz called defocus at the exit face of the object. The quality of the images can be improved by acting on this defocus. The best setting is the one for which the transfer function of the microscope has the minimum of zeros with the first zero as far as possible from the origin. This is a priori achievable for a so-called Scherzer sub-focusing which is:

$$\Delta z_{Sch} = -1.2\ (\lambda . C_S)^{1/2} \qquad (16)$$

However, with simple structures it is sometimes preferable to choose a suitable defocus which visualizes the atomic columns in the form of white dots.

c. Diffraction mode

After interacting with the sample, the electrons in the primary beam are diffracted by the atomic planes of the crystal according to Bragg's law:

$$2 . d . sin\ \theta = n . \lambda \qquad (17)$$

The diffracted rays parallel to each other exit the object at an angle $2.\theta_B$ (θ_B: Bragg angle associated with each of the reticular planes of the object) with respect to the optical axis and form a diffraction pattern in the focal plane of the objective lens. Electronic diffraction operates in different modes.

The most used mode in this work is the S.A.E.D (Selected Area Electronic Diffraction). This type of diagram is obtained by introducing an area selection aperture in the plane of an intermediate image (the foreground image of the objective lens) in order to select an area of the sample. The essential relationship to the analysis of diffraction images is given by the formula:

$$d.D = L.\lambda = K \qquad (18)$$

By measuring the distance *D* between the transmitted central spot and the diffracted spots and knowing the constant *K* of the microscope for the length of camera *L* used, we can determine the inter-reticular distances d_{hkl} of the crystallographic structure of the sample. Electronic diffraction on a TEM was also used in our work, to observe the crystallinity, orientation and also the thickness (number of layers) of BP samples.

II.2.2. Energy-dispersive X-Ray Spectroscopy (EDX)

Energy-dispersive X-ray spectroscopy (also referred to as EDS, EDX, or EDXA) is an effective technique for determining the elemental composition of a given sample. The ability of high-energy electromagnetic radiation (X-rays) to eject 'heart' electrons (electrons in the inner shell) from an atom is the main operating principle that enables EDX to work. This theory is known as Moseley's Law, which establishes a direct relationship between the frequency of light emitted and the atomic number of an atom. When these electrons are removed from the system, a hole is left behind that a higher-energy electron will fill, thus releasing energy as it relaxes. Since the energy emitted during this relaxation process is specific to each element on the periodic table, bombarding a sample with electrons can be used to determine which elements are present and in what proportions. An example of how EDX works is shown in figure 8 below. The letters K, L, and M denote the *n* value of electrons in that shell (*K* electrons, nearest to the nucleus, have *n*=1 electrons), while α and β denote the transition size. The relaxation from *M* to *L* or *L* to *K* is thus referred to as *L* or *K*, respectively. While the transition from *M* to *K* is referred to as a K transition. In our work, the EDX spectroscopy was used for the detection of the oxidation of BP and the exfoliated BP.

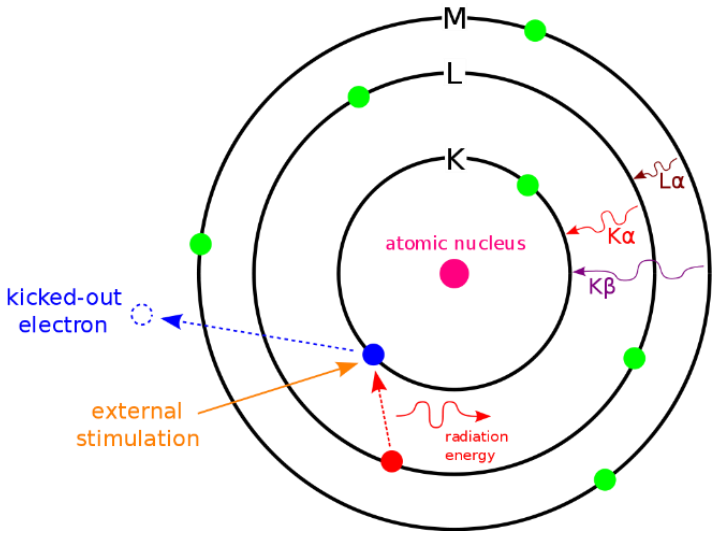

Figure 8. Energy dispersive X-Ray Spectroscopy (EDX).

II.2.3. Electron Energy-Loss Spectroscopy (EELS)

II.2.3.1. Experimental setup and theory

The EELS technique coupled to a monochromated scanning electron microscope is shown to be a very suitable method for studying BP materials as it allows a fast and direct probe of our material's bandgap on an atomic scale. It not only allows the identification and quantification of chemical elements presented in the sample but also to have information on the electronic structure, chemical bonds and the local crystallographic environment of the interacting atom. It is based on the principle of analyzing the energy losses of electrons diffused inelastically by the atoms in the sample. The quantification of energy ΔE lost by the incident electron is equivalent to the energy required for an electron extraction from a level *N* increased by its kinetic energy, allows the recognition of this level and therefore of the element. The fundamental principle of EELS spectroscopy is that an electron beam transmits through a sample, losing energy by producing excitations, and then the transmitted beam is dispersed by a magnetic prism to produce a spectrum of the sample's energy loss events. Figure. 9 depicts a STEM schematic and the process that the electron beam goes through before being collected in the EELS detector. The magnetic fields in the various lenses and the aberration corrector after the gun only change the shape of the beam, but not its energy. The spread of the energies of the electrons coming out of the gun limits the final energy resolution of any EELS measurement.

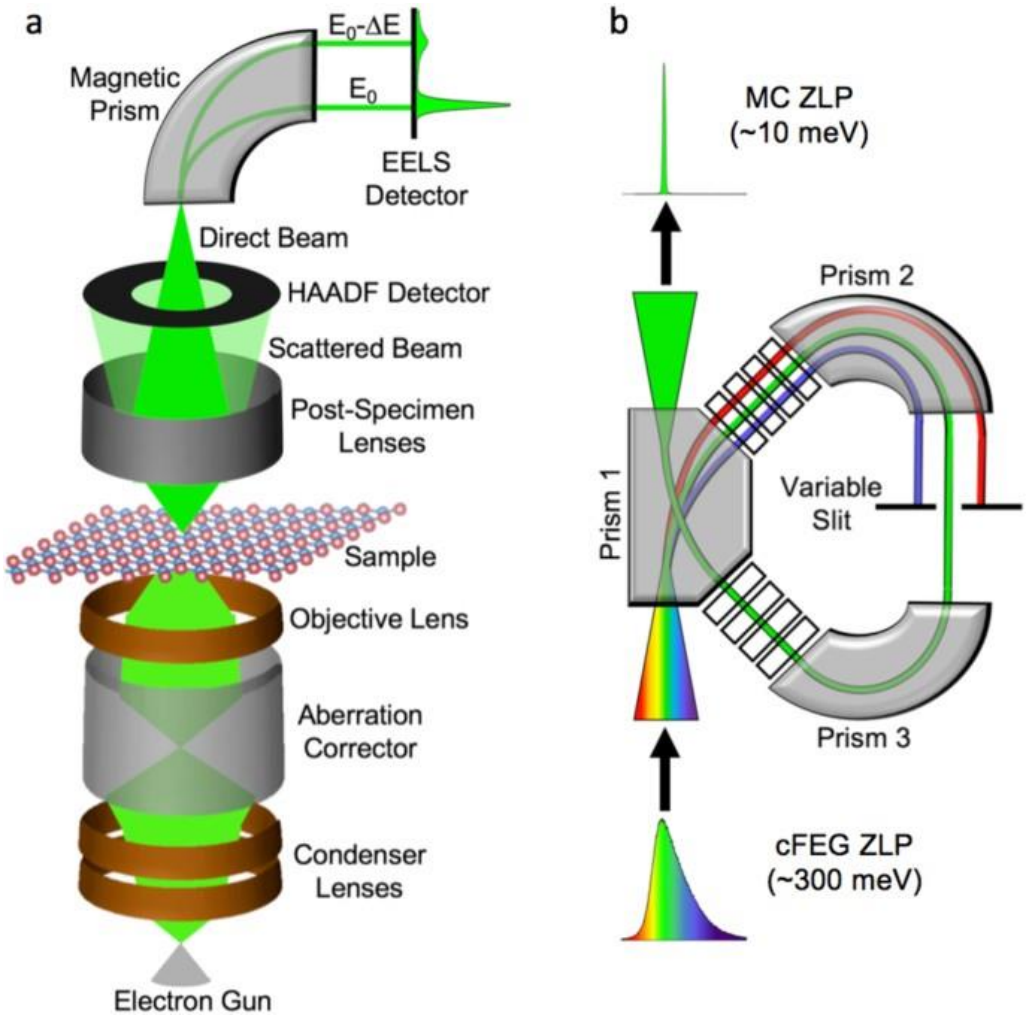

Figure 9. (a) Schematic of electron energy-loss spectroscopy (EELS) in a scanning transmission electron microscope (b) Schematic of monochromation electron beam (occurring between the electron gun and the condenser lenses).[72]

It is impossible to retrieve all of the electrons dispersed by the sample in EELS experiments. These restrictions are primarily due to geometrical constraints. there are two important angles to consider if one wants to understand which scattered electrons have been collected in the spectrometer.

- α is called the convergence semi-angle and is determined by the microscope's settings, especially the condenser lens and aperture. The α angles corresponding to the different configuration of the TEM are be provided by the TEM manufacturer or measured using a known diffraction pattern.
- The second important experimental parameter is the collection semi-angle β fixed by the entrance diaphragm of the spectrometer (of diameter d) and the camera length L with a geometric factor.

With:

$$\beta = \frac{d}{2L} \times \text{geometric factor}$$

It is necessary to be sure that L is not too large in order to have $\beta > \theta_e$ where θ_e is a characteristic angle of the studied threshold being worth: $\theta_e = E_{threshold}/2E_0$. With E_0 being the primary beam energy.

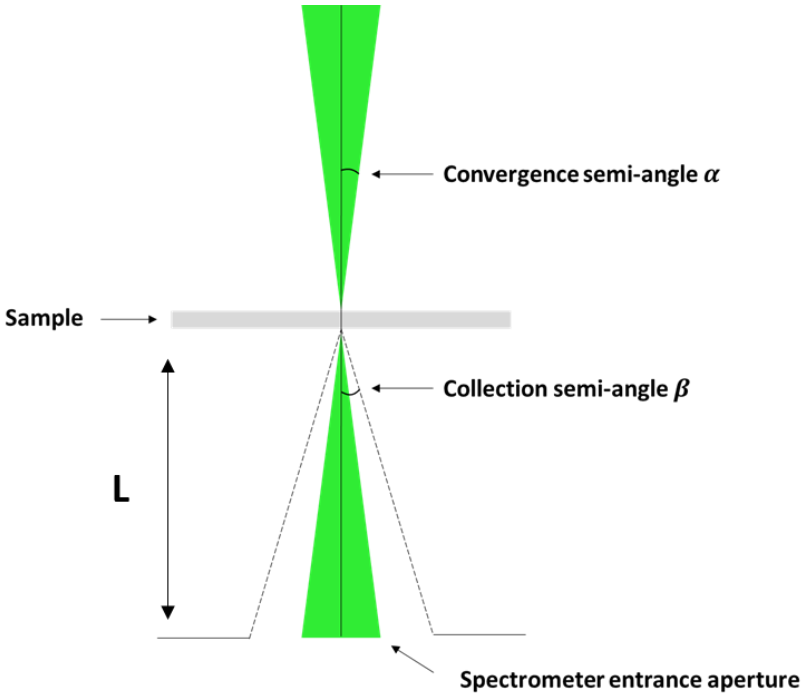

Figure 10. Definition of α and β in a (S)TEM

II.2.3.2. EELS spectrum

An energy loss spectrum represents the variation in the intensity of the scattered electrons as a function of the energy loss (Figure. 11). On this spectrum we can distinguish three different regions which essentially reflect the response of the electrons of the solid to the perturbation induced by the incident electrons:

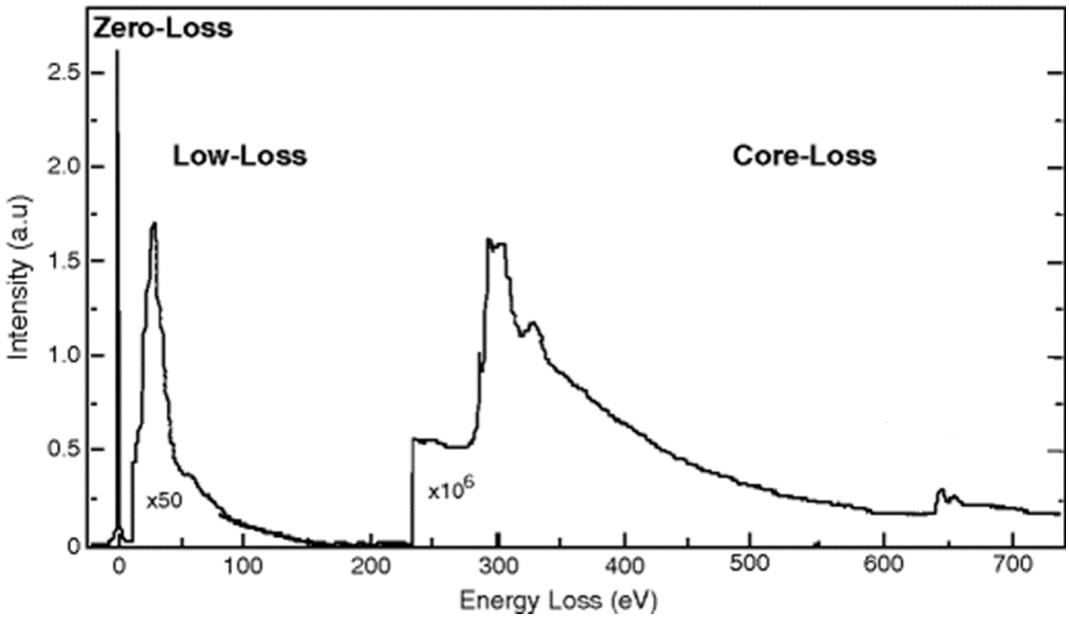

Figure 11. Example of an EELS spectrum

1. The region of zero losses or the Zero-Loss peak (ZLP): represented by a very intense peak called elastic peak (Zero Loss) which contains all elastic and quasi-elastic events, i.e., this area includes energy loss lower than the energy resolution of the microscope spectrometer such as the excitation of phonons for example.
2. The region of low losses: it extends over a domain of about 50 eV from the elastic peak and corresponds to the collective excitation of conduction and valence electrons, also known as plasmons, and also contains inter- and intra-band transitions.
3. The region of high losses: It extends from 50 eV to several thousands of eV and corresponds to the excitations of electrons from well-localized atomic orbitals towards Bloch states or towards the continuum (ionization).

II.2.3.3. Main characteristics of the used microscopes

To carry out our study, three transmission electron microscopes were used as shown in Figure 12. Two of these microscopes belongs to at the UATRS (Unité d'Appui Technique à la Recherche Scientifique) in CNRST (Centre Nationale pour la Recherche Scientifique et Technique) – Rabat, Morocco. On one hand, the FEI-TECNAI G² microscope was used for training and for conventional imaging. On the other hand, the FEI Talos F200X S/TEM field emission microscope was used for high-end imaging resolution, electronic diffraction, EDS analysis and nano-analysis. The first microscope is said to be conventional with an LaB6 electron source,

insofar its resolution is limited to 0.35 nm at 120 kV with the possibility of tilting the object on two axes (very useful for crystallographic analyzes). The second microscope is a very high-resolution analytical microscope as it is equipped with a Schottky-type field-emission cannon. Compared to a classical LaB6 electron source type, the field emission gun guarantees a very high brightness (104 times brighter), a high resolution (0.12 nm at 200 kV) with a very good coherence, very low energy dispersion (0.4 to 1eV) and a cross-over diameter of 104 to 105 weaker (2 to 30 nm). The third microscope used in our study is a Nion Hermes-S200 (CHROMATEM). It belongs to the Solid States Physics Laboratory-Université Paris-Saclay in Orsay, France. This high-end microscope was mainly used for EELS measurements. The CHROMATEM machine is dedicated to ultra-High-resolution spectroscopy. It features in particular HREELS (down to 5 meV @ 30 keV) with high current (typically 20 pA for 7 meV spectral resolution in a probe of 0.5 nm at 100 keV), the capability to perform cathodoluminescence and a stage entry allowing for liquid nitrogen temperature and in-situ biasing and heating experiments. These characteristics give it remarkable performances.

Figure 12 Transmission Electron Microscopes (a) Tecnai G² Twin (UATRS-CNRST) (b) FEI Talos 200X S/TEM (UATRS-CNRST) (c) Nion Hermes-S200 (LPS-CNRS) used in our work.

II.2.4. Fourier Transform Infrared Spectroscopy (FT-IR)

Fourier Transform Infrared spectroscopy (FTIR) is an advanced method using infrared light to obtain an infrared spectrum of absorption or emission of a solid, liquid or gas. Near infrared light (13000-4000cm^{-1}), mid-infrared light (4000-400 cm^{-1}) and far-infrared light (4000-400 cm^{-1}) are the three types of infrared light (400-10 cm^{-1}). Infrared light does not have enough energy to cause electronic transitions in a material, but it can cause vibrational and rotational changes. A

material's vibrational rotational motions can be classified as symmetric/asymmetric stretching, scissoring (symmetric in-plane bending), rocking (asymmetric in-plane bending), wagging (out-of-plane bending), and twisting (out of plane bending). The equation below can be used to express the vibration frequency of a molecule excited by infrared light.

$$V = \frac{1}{2\pi}\sqrt{\frac{k}{\mu}}$$

With V being the frequency in cm^{-1}, k represents the force constants in $N.cm^{-1}$, μ is the reduced mass of the molecule, respectively. An infrared spectrum is created by passing infrared light through a sample and measuring the transmittance or absorbance at each frequency of light. FTIR obtained peaks correspond to the vibrational frequencies of functional groups in the sample. The vibrational properties of functional groups are one-of-a-kind. A schematic summarizing the working principle of FTIR is shown in Fig. 13.

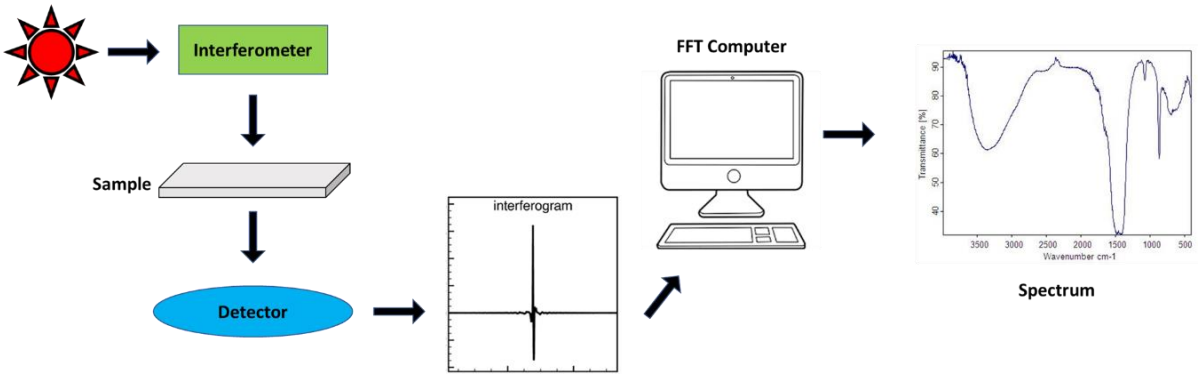

Figure 13. Working principle of an FTIR spectroscope.

FTIR will be useful in analyzing the structure of black phosphorus and functional groups caused by solvents contribution, the spectrometer used for black phosphorus's sample characterization is shown in the figure below.

Figure 14. PerkinElmer Spectrum version 10.4.3 spectrometer (UATRS-CNRST)

II.2.5. Raman Spectroscopy

Infrared absorption and Raman scattering are the two most common spectroscopies used to study molecular vibrations. They're widely used to extract valuable information about a substance's chemical structure by analyzing its spectral patterns. Raman and Krishnan were the first to observe inelastic scattering experimentally in 1928. Raman scattering has been named after this phenomenon, and Raman spectroscopy has been developed since then.

In Raman spectroscopy, a single frequency of radiation (typically 514 nm, 633 nm, or 785 nm) is used, and the scattered radiation is detected. When vibrations cause changes in the polarizability of the electron cloud around the molecule, intense Raman scattering occurs, and when vibrations cause changes in the dipole moment of the molecule, intense infrared absorption occurs. As a result, Raman and infrared spectroscopy are complementary and are often combined to provide a better understanding of molecular structure. Hence its use to investigate Black phosphorus materials vibrations.

dd

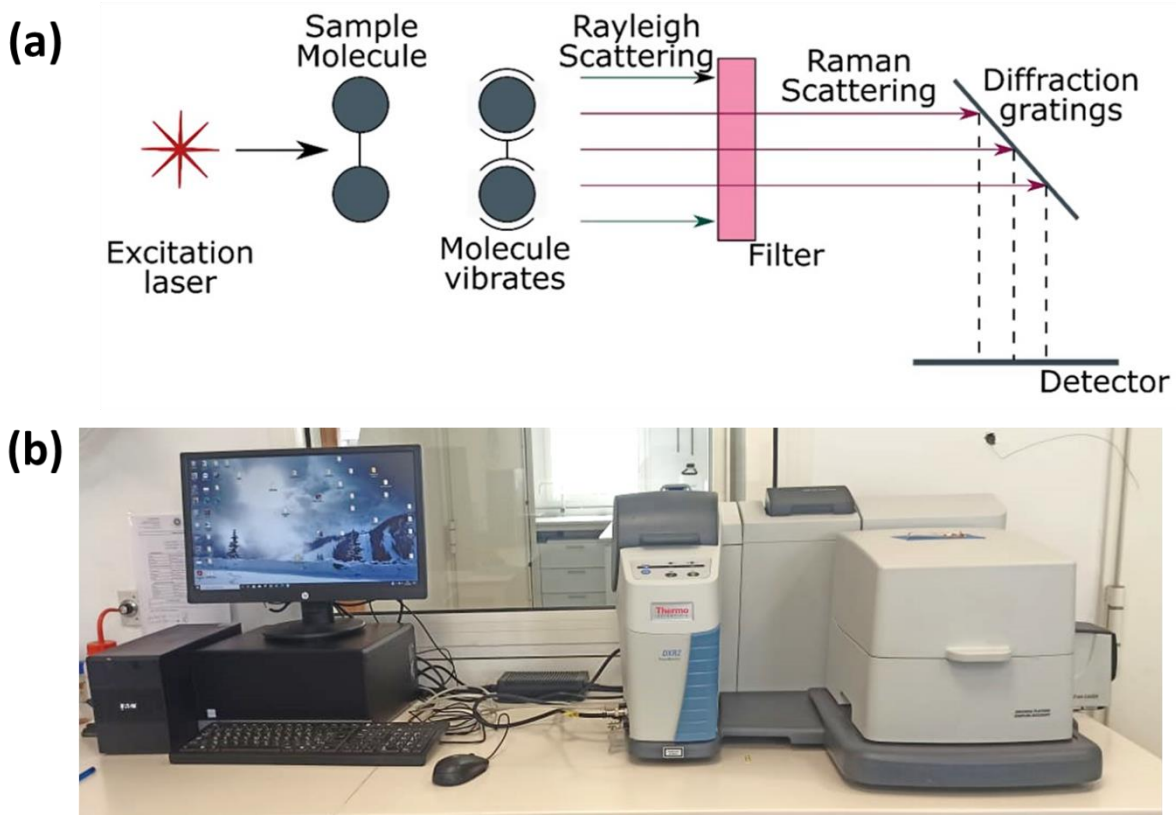

Figure 15. Working principle of Raman spectroscopy (b) DXR2 Smart Raman Spectrometer used for characterization (UATRS-CNRST)

II.2.6. UltraViolet-Visible Spectroscopy (UV-VIS)

UV-Visible spectroscopy is a simple and fast method, which provides information on the chemical nature, the physico-structural properties, and the optical characteristics of materials. It is particularly well suited for the identification, study and of species in liquid solution and as solids. Hence its use in tracking electronic properties in black phosphorus, exfoliated BP and BP quantum dots.

The UV-Visible Spectroscopy principle is based on chemical compounds absorption of ultraviolet or visible light, which results in the formation of different spectra. The interaction of light and matter is the basis of spectroscopy. Excitation and de-excitation occur as matter absorbs light, resulting in the formation of a spectrum. When matter absorbs ultraviolet light, the electrons inside it become excited. This leads them to leap from a ground state (an energy state having a little amount of energy connected with it) to an excited state (an energy state with a relatively large amount of energy associated with it). It's worth noting that the difference between the energies of

the electron's ground and excited states is always equal to the quantity of ultraviolet or visible energy it absorbs.

As mentioned, when light of intensity I_0 passes through a solution, part of it is absorbed by the solute. The intensity I of the transmitted light is therefore less than I_0. We define the absorbance A of the solution as: $A = \log_{10}(\frac{I}{I_0})$

The Absorbance A is a positive value, without a unit. Its value increases the lower the intensity is transmitted. The Beer-Lambert relationship describes that, at a given wavelength λ, the absorbance of a solution is proportional to the concentration of the species in the solution and to the length of the optical path (distance over which light passes through the solution). Thus, for a solution containing a single absorbent species: $A_\lambda = \varepsilon_\lambda . c . l$

A_λ is the absorbance of the solution for a wavelength λ, ε_λ (in $mol^{-1}.L.cm^{-1}$) is the molar extinction coefficient of the absorbent species in a solution. c (in mol. L^{-1}) is the concentration of the absorbent species and l (in cm) is the length of the optical path.

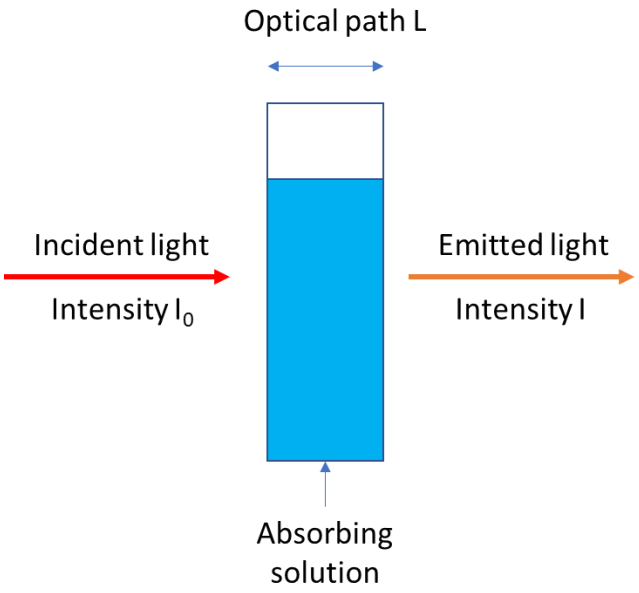

Figure 16. Schematic representation for the Beer-Lambert law

The figure below shows the instrumentation used for UV-VIS spectroscopy.

Figure 17. UV-Vis LAMBDA 52 Perkin Elmer (UATRS-CNRST)

II.3. Experimental procedure

For the realization of the suspensions there are three important parameters to control. The first is the choice of the black phosphorus powder. A bad powder will create a bad sheet. The second parameter is the choice of solvents, because they are the ones that will make it possible to achieve a suspension. Finally, the last parameter is the energy input required to separate the sheets.

In order to experimentally prepare single BP sheets and BPQDs, Liquid Phase Exfoliation (LPE) is very useful with the help a variety of organic solvents such as dimethylformamide (DMF), dimethyl sulfoxide (DMSO), N-cyclohexyl-2-pyrrolidone (CHP), Isopropanol alcohol (IPA) and N-methyl pyrrolidone (NMP).[73,74,75,76] Due to its easiness and controllable production on a large scale, LPE and solvothermal-assisted LPE were respectively used to prepare our phosphorene and BPQDs solutions. An initial BP solution was first prepared from milled commercial BP powders (from Smart elements Co.) dispersed in one of the given solvents used (from Honeywell, 99%, BN). The obtained dispersion was then subjected to stirring until solution homogenization in a magnetic stirrer. Exfoliation of the initial BP solution was afterwards obtained through bath ultrasonication in a Branson 8000 for about 1h30, before being subjected to centrifugation at 13000 rpm in a HERMLE Z32 for 15 min, in order to only keep BP monolayers (phosphorene) in the upper part of the solution. These sonication and centrifugation parameters were chosen based on trial test as will be shown further.

In the case of BPQDs, a solvothermal-assisted LPE method is needed to obtain poly-dispersed QD suspensions.[77,78,79] Preparation of the BPQDs solution was subjected to the same protocol as for phosphorene, with the addition of a heat treatment at 150°C for 6 hours in an oven, after ultrasonication and prior to centrifugation.

II.3.1. Black phosphorus powder

Black phosphorus powder (99.998% purity) was provided by Smart elements Company. This commercialized black phosphorus was produced by gas phase transport in an argon filled vacuum chamber. Prior to its use the black phosphorus was kept in a sealed and aluminum enrolled flask under total vacuum, so that no oxidation would interfere. Figure 18 shows the black phosphorus used in our research directly after opening the flask seal. We should also mention that the time black phosphorus was used under ambient temperature was kept at a minimum, before being added to the solvent in order to minimize the oxidation.

Figure 18. Image of the commercialized Black Phosphorus powder used in our study

II.3.2. Solvents

In the previous chapter we saw the specificities of the solvent's requirements for exfoliation of black phosphorus. The main condition being to have a solvent with a surface tension close to 21 mJ/m² (black phosphorus's surface tension), In Table 1 below we summarized the values of the solvents used in this thesis along with the images of the used solvents Figure 19 which were also bought thanks to the APPHOS project from Honeywell and VWR.

Table 1. Solvent's used surface tensions and boiling temperature

Solvents	**Surface tension (mJ/m²)**	**Boiling temperature (°C)**
Benzonitrile (BN)	22.5	191
Dimethylformamide (DMF)	24.9	153
N-Vinylpyrrolidone (NVP)	19.8	148
N-Methyl-2-Pyrrolidone (NMP)	23	202
1,3-Dimethyl-2-imidazolidinone (DMI)	23	225
Isopropyl Alcohol (IPA)	26.7	82.5
Dimethyl sulfoxide	26.4	189
N-Cyclohexyl-2-pyrrolidone (CHP)	23.6	284

Table 1 shows the values of the surface tensions of the solvents as well as their boiling temperatures. It is clear that from a logical point of view to exfoliate graphene under the best conditions, all these solvents satisfy the surface tension being close to that of black phosphorus.

Figure 19. All the solvents used in our study.

II.3.3. Sample preparation

II.3.3.1. Ultrasonication

In the previous chapter we saw that it was necessary to supply energy to the suspension to separate the sheets.

There are several methods for this:

- Ultrasound (in a bath or with a tip) / Boiling

These are two techniques for obtaining black phosphorus sheets. The best known and most studied is the ultrasound method. The advantage of ultrasound is that its power and frequency can influence exfoliation. From the moment that there is an energy supply the majority of the sheets separate. The downside is the size of the ultrasonic baths; they are small in size and therefore cannot process a large amount of suspension. This problem could be solved by the use of ultrasonic tips. Still, in

our thesis we used the baths sonication as shown in Figure 20. Boiling is one of the possible routes for the production of phosphorene; it has a major advantage, because the exfoliation of the leaflets is carried out gently and allows to obtain less defect. However, there are two problems: the use of certain solvents, such as NMP, DMF or CHP, causes the boiling temperature to be higher which adds an energy cost. In addition, this manufacturing method requires equipment and more important manufacturing conditions than for ultrasound or mixer. Hence the use of ultrasound for separating black phosphorus sheets.

Figure 20. Ultrasonication baths used in our thesis.

II.3.3.2. Centrifugation

The centrifugation separates constituents of different size and mass contained in a liquid, from molecules to whole cells. All of the constituents in a sample are subjected to gravity, a force exerted from top to bottom, and Archimedes' thrust, a force exerted from bottom to top. Apart from the particular case in which these two forces are perfectly balanced, one could therefore expect that over time all the constituents end up falling to the bottom of the container in which they are found (sedimentation) or rise to the surface. By rotating the sample, a new force is produced, the centrifugal force, which is an acceleration that exerts radially outward from the axis of rotation. For a given constituent, by correctly choosing the speed of rotation, the acceleration obtained can become preponderant in relation to molecular agitation, which leads to its sedimentation towards the bottom.

The centrifugation was extensively used for all BP solutions preparation as it separates the thick BP flakes from the thin ones. A high-speed centrifuge (13 000rpm) was employed as it allowed better separation between the precipitate and the surnatant. The figure below shows the centrifuge employed for that matter.

Figure 21. High speed centrifuges used in our thesis.

II.3.3.3. Heat treatment

For BP-QD synthesis a heat treatment was applied on the obtained centrifuged solution after surnatant recollection. The process of quantum dots synthesis by solvothermal method is as follows. In fact, when the temperature of a mixture containing the solvent and black phosphorus is elevated above the boiling point of the solvent under a solvothermal condition, black phosphorus starts to be exfoliated from the edges of its exfoliated sheets by vapor pressure of the intercalated solvent and is consequently converted to BP quantum dots.

Figure 22. Nabertherm oven used for heat-treatment.

Chapter III.

Optical properties of Black phosphorus

III.1. Introduction

Black phosphorus (BP), the most stable form among phosphorus allotropes, is an elemental narrow-gap semiconductor with an anisotropic layered structure. Such a structural property has created a great deal of research interest mainly focused on tuning the BP bandgap as a function of sheets number (0.3 – 2eV),[80] on exploiting its high carrier mobility[81], and on exploring their excitonic nature and anisotropic nonlinear optical properties.[82,83] These investigations have given rise to various applications based on BP, namely photo-detectors,[84] gas sensors,[85] thermo-optical modulators,[86] ultrafast lasers[87] and solar cells.[88] Despite its various interesting properties and applications, additional thorough research studies on BP electronic properties in the low infrared region are still needed.

So far, experimental bandgap measurements of BP have been performed using techniques with a limited spatial-resolution such as reflectance spectroscopy (0.35 eV),[89] angle-resolved photoemission spectroscopy (≈0.3 eV),[90] scanning tunneling spectroscopy (0.32 eV, 0.4 eV)[91,92] and infrared spectroscopy (0.3 eV).[93] Therefore, these spectroscopic methods only allow indirect probing and provide an averaged value of the bandgap over a macroscopic area. To provide nanometric measurements, local low-loss electron energy-loss spectroscopy (EELS), in a monochromated scanning transmission electron microscope, is proven to be a very suitable method as it allows a fast and direct probe of the material's bandgap on a nanometer scale.[94] Indeed, low-loss EELS concerns low energy losses, where optical characteristics can be revealed and explored.[95,96] For narrow bandgap materials, such as BP, the monochromation becomes an important issue, as the background tail of the zero-loss peak (ZLP) in the low-loss spectrum can extend in the visible range, which would lead to the concealment of the bandgap both in the visible and infrared region.[97] Monochromated low-loss EELS also improves many aspects of the spectrum analysis, such as balancing the required total signal with the desired energy resolution, reducing the background noise and increasing the excitation sensitivity.[15]

In the present chapter, monochromated low-loss EELS-STEM, confronted with *ab-initio* calculations, is used to investigate the bandgap and excitons energies of black phosphorus flakes in the near infrared region. A direct measurement of the BP narrow bandgap energy will be performed along with excitonic transitions.

III.2. Black phosphorus

Phosphorus was discovered in 1669 by the alchemist Hennig Brand.[98] It is part of the group of pnictogens with 5 valence electrons and is classified as a nonmetal. Elemental phosphorus has several allotropic forms including white phosphorus, red phosphorus and black phosphorus. White (or yellow) phosphorus is formed from P_4 molecules with a tetrahedral arrangement. Each atom of the molecule is linked to the other three by simple P-P covalent bonds and the molecules are linked together by van der Waals forces in three possible arrangements (, or). It is the least stable allotrope, igniting at 30°C. Red phosphorus is an amorphous structure which is formed by heating white phosphorus above 250°C. It is used in the match scraper. The red phosphorus in the scraper reacts with the potassium chloride in the match head and ignites it. Black phosphorus is the most stable allotrope showing no pyrophoric characteristics unlike white and red phosphorus. It was discovered by Bridgman in 1914[99] by applying hydrostatic pressure of 1.2 GPa at 200 °C on white or red phosphorus. In 1935, its lamellar structure of orthorhombic symmetry and its space group Cmca were determined by the powder diffraction technique.[100] The dimensions were refined in 1965 by powder diffraction to arrive at accepted public values.[101] Its band structure, calculated in 1981 with the tight binding model, is that of a direct narrow gap semiconductor at 0.33 eV (3.5 μm).[102] Recent advances have predicted blue phosphorus, which is an allotrope similar to black phosphorus, but with a wider and indirect gap. Although blue phosphorus exhibits interesting characteristics, it still remains at the theoretical stage with only growth by molecular beam epitaxy (MBE) has been reported by Zhang et al.[103]

III.2.1. Properties of Black phosphorus

III.2.1.1. Structural properties

Bulk BP is made up of stacked hexagonal honeycombs, similar to graphite, and a single layer of BP can also be created through mechanical exfoliation. The BP structure is orthorhombic with space group Cmca under normal conditions. A phase transition was discovered under high pressure, transforming from an orthorhombic to a rhombohedral structure at ~5 GPa, then to a basic cubic structure at ~10 GPa.[104] The atomic structure of BP is seen in Fig. 23 Because phosphorus has only three valence electrons, each atom is connected to three neighboring atoms, forming a honeycomb puckered network through sp^3 hybridization between phosphorus atoms. As shown in Fig. 23, the monolayer or few-layer BP is dubbed phosphorene, similar to graphene. Weak van der Waals forces hold the individual layers of phosphorus atoms together, and van der

Waals interactions are strong in the crystallographic y direction.[105] The single-layer is shown to be made up of two atomic layers, with the bond distance between the nearest atoms d_1 being 2.224 Å and the length of the link between the top and bottom atoms d_2 being 2.244.[23] The covalent bonds produced from phosphorus 3p orbitals are attributed to the near values of d_1 and d_2. Additionally, computational research projected various additional phosphorene polymorphs with buckling honeycomb structure or non-honeycomb structure, enriching the phosphorene family with varied members.[106,107] In the BP structure, the x and y directions correspond to the armchair (AM) and zigzag (ZZ) directions, respectively, and it should be observed that the in-plane anisotropy arising from these two directions is quite distinctive. Other 2D materials, for example, do not have a large degree of effective mass anisotropy.[108]

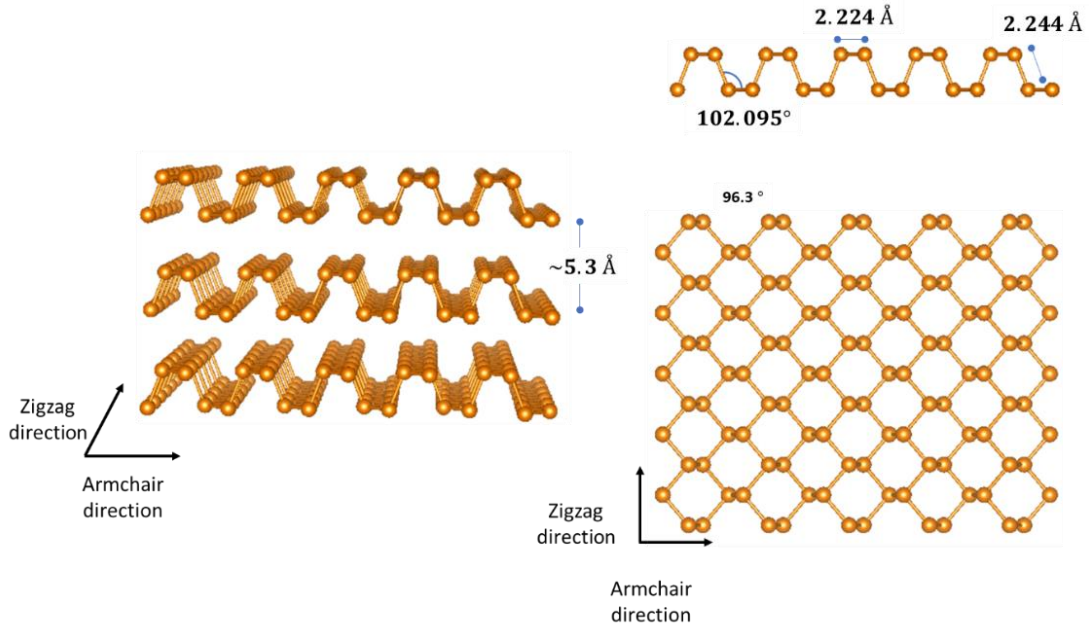

Figure 23. Atomic structure of multi-layer black phosphorus and (b) monolayer phosphorene.

III.2.1.2. Optoelectronic properties

Bulk BP is a semiconductor with a direct band gap of 0.3 eV, as determined by first principles calculations (G_0W_0)80 and angle-resolved photoemission spectroscopy (ARPES).[109,93] The band gap gradually increases due to quantum confinement as the thickness decreases, reaching 2 eV for monolayer phosphorene, according to the formula $A/N^{0.7}+B$ (N is the layer number), which decays much slower than the conventional $1/N^2$ scaling expected by the normal quantum confinement effect. Unlike transition metal dichalcogenides (TMDCs), where the band topology changes with thickness, all few-layer phosphorene samples are direct semiconductors with the conduction band minimum at the Γ point.[110] For its prospective photonics and optoelectronics

applications, phosphorene's thickness independent band topology is critical. The gap value (0.3-2 eV) is typically smaller than that of TMDC compounds (1.1-2.5 eV), but larger than that of semi-metallic graphene, allowing phosphorene to have a moderate on/off ratio (10^4-10^5) while maintaining a sufficient carrier mobility (around 1000 $cm^2/V.S$) suitable for many applications.[90] Photoluminescence measurements carried out in the infrared made it possible to check the BP optical band gap value.[30] These measurements are based on the phenomenon of photoconductivity. So, to participate in current generation, an electron requires an energy equal to that of the bond with a hole plus that of the prohibited band optics. This distinction is important for materials with a large binding energy (> 0.5 eV). In BP, it is less than 0.5 eV. It has little influence but allows to explain the difference often observed between the electronic bandgap calculated and the observed optical bandgap.

The layer-dependent direct band gap of black phosphorus is its most appealing attribute. The band gap for BP monolayer is ~2.0 eV, ~1.3 eV for double layers, and ~0.8 eV for triple layers, while the band gap for bulk BP is 0.3 eV. The unique band structure and puckered honeycomb lattice of BP will result in thickness and polarization dependent linear optical responses. The linear absorption and reflection spectra for few layers black phosphorus shows a dependent bandgap as a function of the thickness as found by Qiao et al.[111] The cut-off light energy decreases as you progress from monolayer to bulk, indicating that the bandgap is inversely proportional to the thickness of black phosphorus. This tunable bandgap property in BP is a key element in fabricating broadband optical systems ranging from ultraviolet to mid-infrared. Additionally, as discussed above, BP exhibits an anisotropic structure, hence an anisotropy-dependent properties. In fact, it was found that the absorption of BP from monolayer to bulk is strongly anisotropic.[112] Absorption in the armchair direction is stronger than in the zigzag direction. This anisotropic optical response of BP might benefit polarization dependent applications.

III.3. Experimental and theoretical details:

III.3.1. Experimental details:

III.3.1.1. Preparation of TEM samples

BP powders were prepared from amorphous red phosphorus by chemical vapor transport as previously reported.[113] The BP powder was then encapsulated and protected from air and from light. Few milligrams were ground in a mortar and dispersed in ethanol for 1-hour sonication using

a 300 W bath sonicator. 10 µL of the BP dispersion was drop-cast onto a 300-mesh copper TEM grid coated with holey carbon and put immediately in the TEM after ethanol evaporation.

III.3.1.2. TEM setup for imaging and EELS

Bright-field TEM and high-resolution TEM were performed using a FEI Talos F200X S/TEM, operated at 200 kV accelerating voltage and a point-to-point resolution of 1.2 Å. Core-loss EELS experiments were performed on a probe corrected JEOL ARM200F operated at 200 kV accelerating voltage using a convergence semi-angle of 28 mrad and a collection semi-angle of 111 mrad. Low-loss EELS experiments, on the other hand, were carried out on a Nion Hermes 200-S aberration-corrected high energy-resolution monochromated EELS-STEM, operated at 100 kV accelerating voltage. Two different EELS settings were used. For plasmon analyses, spectra were recorded using convergence and collection semi-angles of 25 mrad, and an energy resolution as given by the FWHM of the zero-loss peak (ZLP) of about 240 meV. While for the bandgap measurement, the convergence and the collection semi-angles were set at 10 mrad, and an energy-resolution of about 20 meV.

III.3.1.3. Kramers-Kronig analysis

BP dielectric function was extracted from the low-loss spectrum using the Kramer-Kronig analysis method implemented in digital micrograph (Gatan, inc., USA). To avoid errors during transformation, all spectra were recorded up to 70 eV (where intensity is almost approaching zero). Both the plural scattering and ZLP contributions were removed using the Fourier-Log method, giving rise to an inelastic single scattered distribution (SSD). The single scattered intensity is closely related to the energy-loss function $\mathrm{Im}[{}^{-1}/_{\varepsilon(E)}]$ via the relation:[129] $S(E) = K\,\mathrm{Im}[\frac{-1}{\varepsilon(E)}]\ln[1+\frac{\beta^2}{\theta_E^2}]$, where S(E) is the single scattering distribution, K is a proportionality constant and β and θ_E are the effective collection and characteristic scattering angles respectively. Hence, the energy-loss function can be extracted from the SSD. Since the dielectric function is causal, the real part $\mathrm{Re}[{}^{1}/_{\varepsilon(E)}]$ can be derived from the aforementioned $\mathrm{Im}[{}^{-1}/_{\varepsilon(E)}]$ using the Kramers-Kronig transformation as shown in the equation: $\mathrm{Re}\left[{}^{1}/_{\varepsilon(E)}\right] = 1 - \frac{2}{\pi}P\int_0^\infty \mathrm{Im}[{}^{-1}/_{\varepsilon(E)}]\,\frac{E'dE'}{E'^2-E^{2\prime}}$, where P indicates the Cauchy principal of the integral. Once

$\mathrm{Re}\left[1/\varepsilon(E)\right]$ was retrieved, the real and imaginary parts of the dielectric function can be calculated via: $\varepsilon(E) = \varepsilon_1(E) + i\varepsilon_2(E) = \frac{\mathrm{Re}\left[1/\varepsilon(E)\right] + i\left\{\mathrm{Im}\left[-1/\varepsilon(E)\right]\right\}}{\left\{\mathrm{Re}\left[1/\varepsilon(E)\right]\right\}^2 + \left\{\mathrm{Im}\left[-1/\varepsilon(E)\right]\right\}^2}$.

III.3.2. Computational details:

First-principles calculations were performed within the framework of density functional theory (DFT), implemented in the full-potential Wien2k code.[114] The Perdew–Burke–Ernzerhof (PBE-GGA) functional[115] was applied to take into account electron–ion interactions, in addition to the screened hybrid YS-PBE0 functional,[116] which is very similar to the hybrid functional Heyd-Scuseria-Ernzerhof approach (HSE)[117] known to yield results in good agreement with experimental gaps. The used hybrid functional includes a fraction of the screened short-range Hartree-Fock exchange term, which takes into consideration electron-electron (e-e) interaction, resulting in an accurate prediction of bandgaps in several semi-conductors. Effects of van der Waals (vdW) interactions were taken into account in the form of optimized B88 correction (also known as optB88-vdW).[118] Prior to electronic properties calculations, the atomic positions and the lattice parameters were fully optimized to obtain the relaxed configuration. Atomic relaxation was performed with an energy convergence of 10^{-5} Ry and a force convergence of 10^{-4} Ry per Bohr. In order to achieve energy and charge convergence, the RMT*K_{max} value was set to 7 (RMT refers to the small atomic radius in the unit cell, while K_{max} is the size of the largest vector in the plane-wave expansion), which is more than enough to achieve convergence. The wave function was iteratively updated until self-consistency was reached. A mesh of 12×12×12 *K*-points was applied, and the tetrahedral method was used for Brillouin-zone integration.[119]

III.4. Results and discussion:

III.4.1. Structural properties of bulk black phosphorus:

To better elucidate the structural properties of bulk black phosphorus, transmission electron microscopy, scanning electron microscopy and electronic diffraction were intensively used. As could be seen from Fig. 24 and Fig. 25, all the TEM images show a layered structure, with weak oxidation at the surface as could be seen from the EDX and STEM/Mapping image. The two peaks at around 0.15eV and 0.9eV are related to the carbon, which is coming from the carbon film TEM grid.

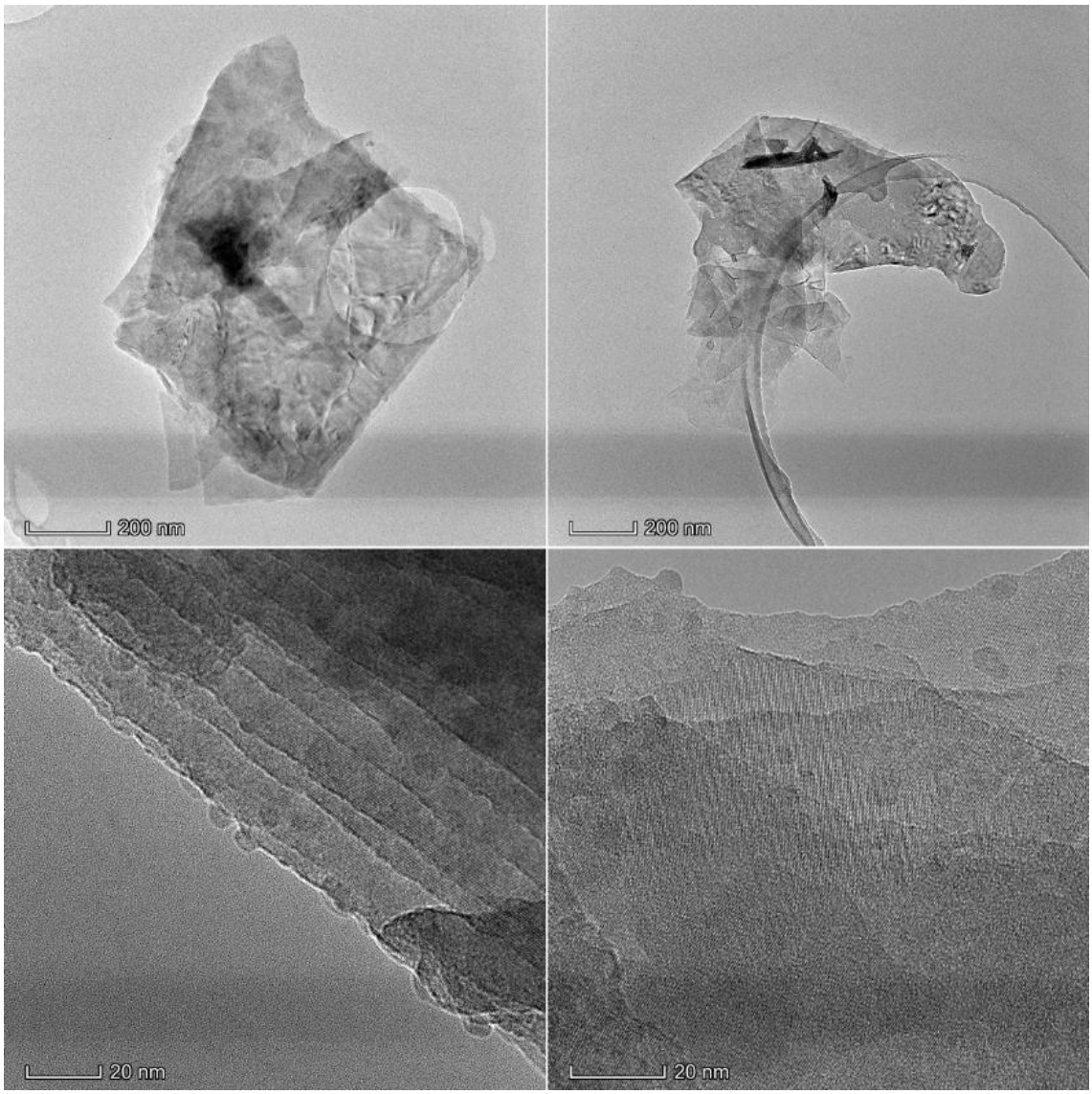

Figure 24. TEM images of bulk BP powder.

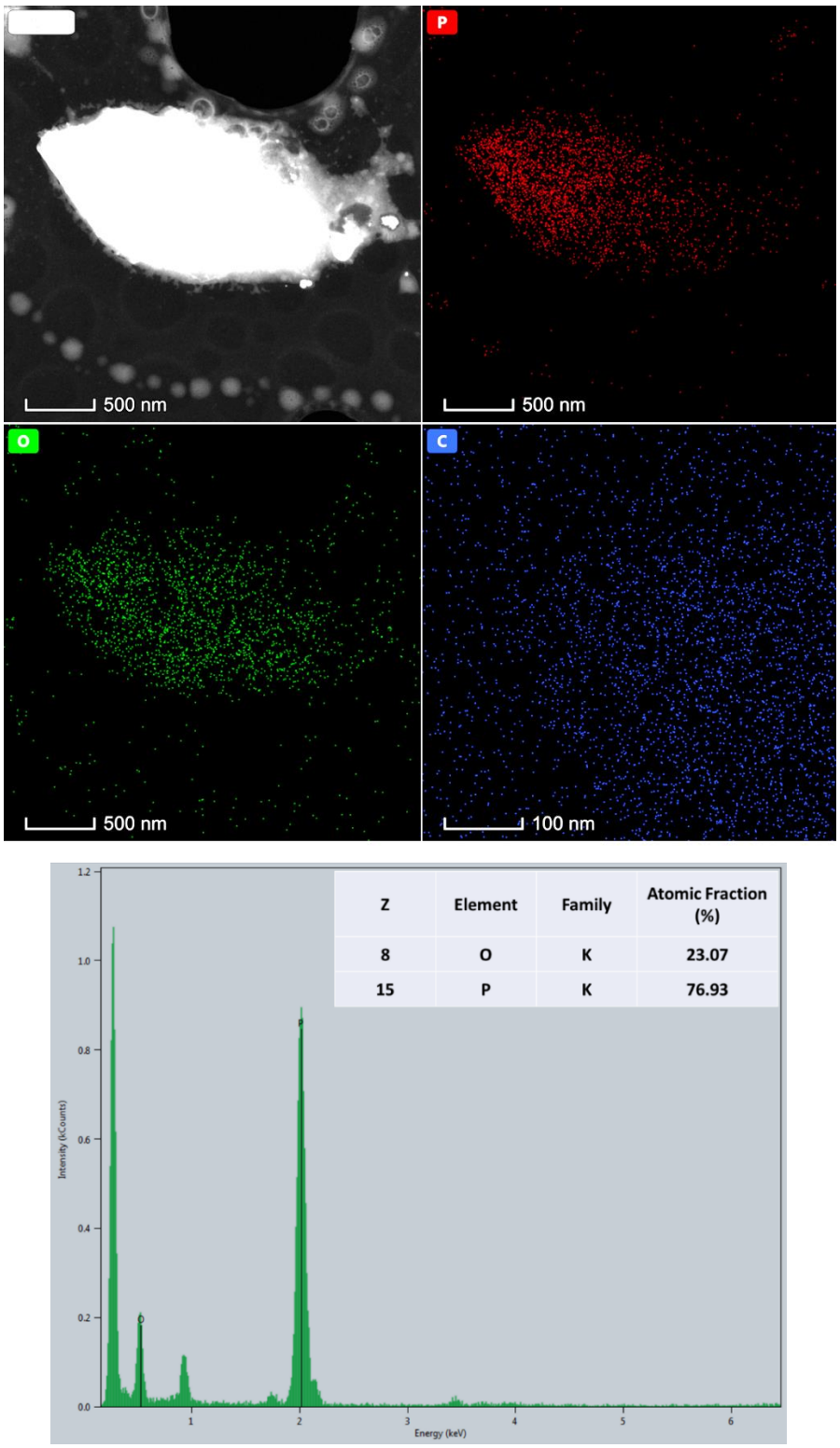

Figure 25. HAADF and mapping images of a bulk black phosphorus fake along with its EDX.

Fig. 26a shows a typical TEM image of the BP powder, mainly constituted of multi-sheet flakes of about 1.5 μm in size. To elucidate the single-crystalline character of such BP flakes, a selected-area electron diffraction (SAED) pattern is shown in Fig. 26b. The SAED reveals a pattern along the [001] zone axis of the known BP orthorhombic crystalline structure (space group Cmca), where

BP flakes are considered perpendicularly oriented with respect to such an axis. Indexing of the SAED pattern showed indeed the presence of diffraction spots corresponding to the expected (200) and (020) planes of the BP unit cell. High-resolution TEM imaging of our BP flakes is presented in Fig. 1c. The as-measured fringe distances confirm the known BP lattice parameters ***a*** = 3.31 Å and ***b*** = 4.32 Å. These measured in-plane parameters are in good agreement with previously reported X-ray powder diffraction measurements of the BP orthorhombic structure.[120,101]

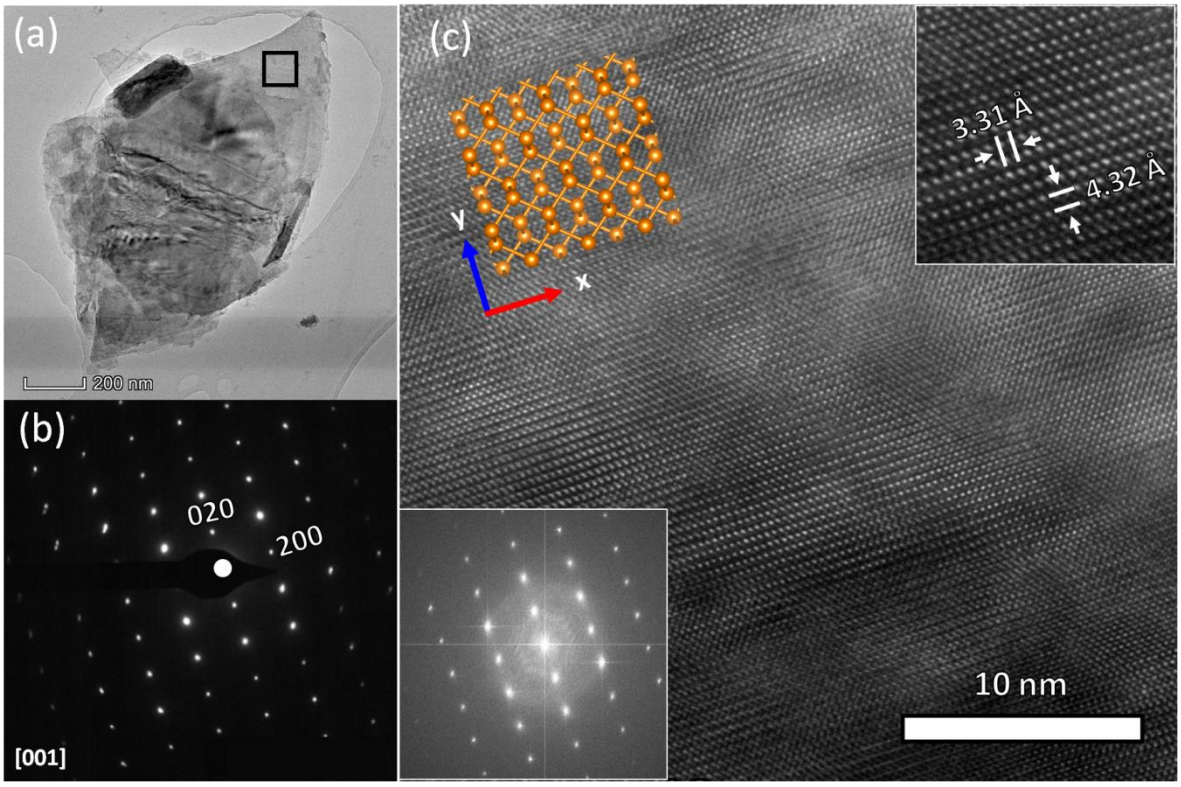

Figure 26. (a) Transmission electron microscopy (TEM) image of a black phosphorous flake. (b) SAED pattern from the flake of Fig. 1(a) showing an orientation along the [001] direction and confirming its single-crystalline character. (c) HRTEM image of the squared area.

III.4.2. Electronic and optical properties of bulk black phosphorus

III.4.2.1. Core-loss EELS of bulk BP

To describe the electronic structure of the above-characterized BP flakes, core-loss EELS was first performed. Such an analysis has the advantage to provide an idea on the purity of our BP. First, measurements recorded from a BP flake do not reveal any oxygen peak at 530 eV as could be seen from the red spectrum in Fig. 27. A BP flake on a TEM grid was left under ambient air and temperature to oxidize it to observe the oxygen peak contribution.

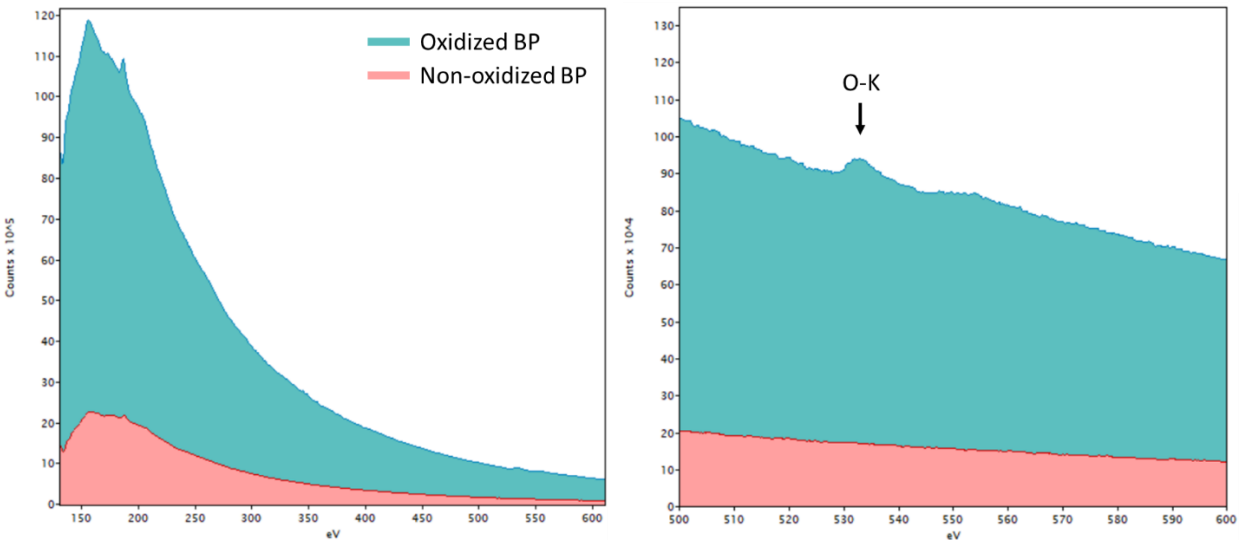

Figure 27. Core-loss spectra of a non-oxidized and an oxidized BP.

Fig. 28 shows a core-loss EELS, which can be compared with the electronic local density of states, as it represents the direct electronic transitions from core-levels to empty states above the Fermi level.[121] Such a core-loss edge is characterized by a main sharp edge with two components located at 130 and 131 eV, respectively, which are characteristic of the known P-$L_{2,3}$ lines. The splitting of the pre-edge components corresponds to the intense spin-orbit pair arising from the single particle transition P(2*p*) → 1e* of the P_4 molecule, a result that is in agreement with reported XANES measurements.[122]

Comparison with DFT calculated density of states (DOS) of projected *s*- and *d*- orbitals shows that the observed $L_{2,3}$-lines are mainly due to $2p^{3/2} \rightarrow 3s$ and $2p^{1/2} \rightarrow 3d$ electronic transitions, respectively. Furthermore, the two additional contributions, showing up at 136.5 eV and 140.75 eV, are due to the excitation from 2*p* core levels to the admixture of 3*s* and 3*d* conduction states,[123] while the broad peak at ~157 eV corresponds to transitions from 2*p* core levels to *d*-state levels.[124] At 187 eV, the P-L_1 line is characteristic of 2*s* core level electronic transition to 3*s* and 3*d* hybridized levels.[125,126]

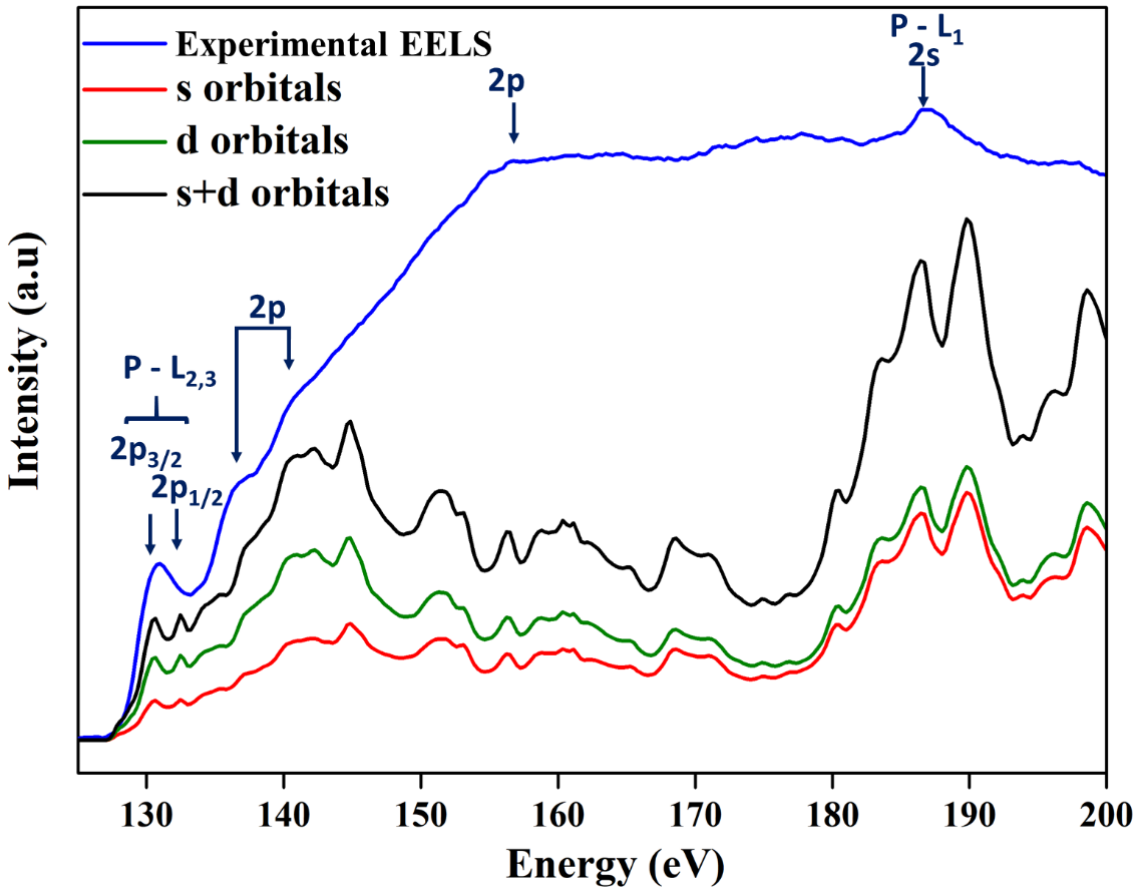

Figure 28. Core-loss EELS compared to DOS as predicted by DFT. See text for a full description.

III.4.2.2. BP volume plasmon

In order to assess the optical bandgap of the BP flakes, monochromated low-loss EELS was used. Spectral images were first acquired in STEM mode to extract EELS spectra.

Fig. 29a shows a High-Angle Annular Dark-Field (HAADF) image of a typical BP flake used for low-loss EELS measurement. For the sake of comparison, three different locations (white squares in Fig. 3a) having different *apparent* thicknesses were characterized. On one hand, the BP volume plasmon energy is seen to occur at E_p = 19.6 ± 0.1eV. Comparison with a DFT calculated loss function (Fig. 29b) shows an $E_p \approx 19.60$ eV, a value that is in very good agreement with the experiment. Our calculated and experimental values are also in good agreement with reported values.[127,128] On the other hand, the thickness effect can straightforwardly be observed from the signal intensity in the non-deconvoluted low-loss EELS spectra (Fig. 29b), where no apparent energy-shift in the recorded volume plasmon peaks is noted, which is a clear indication that we are not dealing with a thickness dependence.

III.4.2.3. Thickness assessment

To better elucidate such a point, the thickness of the three areas was estimated from the EELS log-ratio method[129] via the following equation: $t = \lambda \ln(I_t / I_0)$, where ***t*** corresponds to the thickness of the characterized area, λ to the BP inelastic mean free path (IMFP), I_t to the total intensity of the EELS spectrum and I_0 to the intensity of the ZLP. The IMFP for BP was predicted using the parameterized formula.[130-131] $\lambda = \frac{106\ F\ (E_0/E_m)}{\ln\ (2\beta E_0/E_m)}$, with E_0 being the incident energy in keV (100 keV in our case), E_m the mean energy loss in eV ($E_m \approx 7.6\ Z^{0.36}$; Z : atomic number), β the collection semi-angle in mrad, and F the relativistic factor ($F = \frac{1+E_0/1022}{(1+E_0/511)^2}$). The thickness was also estimated by the Kramers-Kronig method, which requires the refractive index of the BP for normalization.[132]

For the two methods used, we found very close values (± 2 nm). From the above, the calculated thicknesses corresponding to the three areas are ~30 nm, ~51 nm and ~90 nm, which are respectively equivalent to ~55 ML, ~93 ML and ~150 ML (ML: BP monolayer). This high number of MLs corresponds therefore to bulk BP, a reason why no size effect or energy-shift was noticed in the volume plasmon energy.

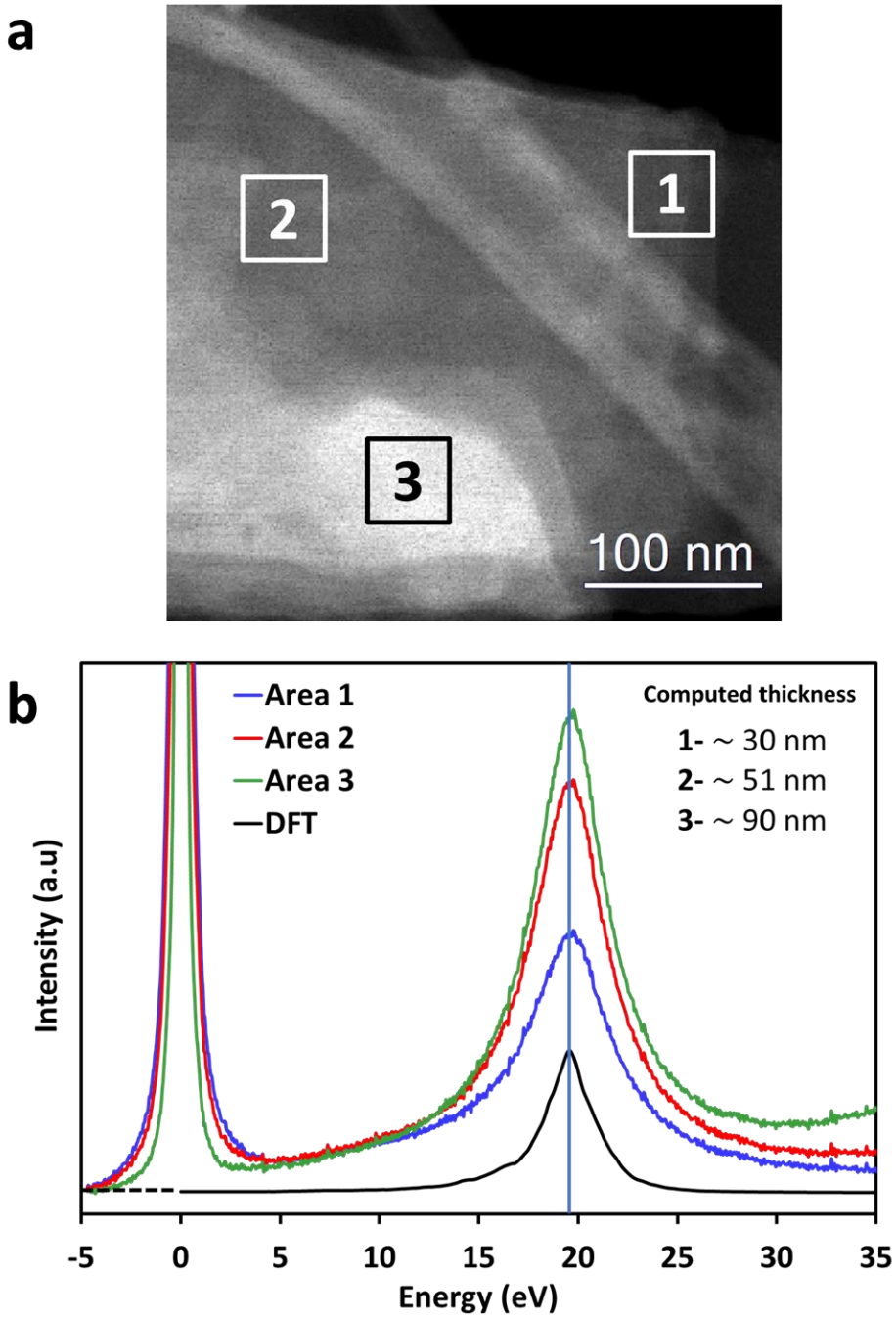

Figure 29. (a) HAADF image of a BP flake. The numbered squares indicate regions with different thickness (b) Low-Loss EEL spectra from the BP flake with a strong plasmon peak at 19.60 eV, along with the calculated DFT energy-loss spectrum.

III.4.2.4 Low-loss EELS

a. Bandgap and excitons from EELS

Due to the narrow bandgap of BP, E_g = 0.35 eV,[133] monochromated low-loss EELS analyses in the low infrared (< 1eV) region were required as the background tail of the ZLP can extend in the visible range, which would lead to concealment of the bandgap. Fig. 31a depicts raw low-loss

EELS spectra showing a characteristic absorption peak due to the BP bandgap energy along with the spectral image, from which low-loss spectra were extracted. Analyses were then performed on areas 1 (thin) and 2 (thick). For a better assessment, zero-loss and plural scattering contributions were removed using the Fourier-log method and a corresponding Lorentz fit (multiple peak fit) was applied, giving rise to the deconvoluted low-loss EELS spectra shown in Fig. 30b. Close inspection, within ±0.02 eV errors, reveals two major electronic transitions, noted as E_0 and E_1, respectively at ~0.33 and 0.75 eV. Besides these transitions, additional features are also observed at 0.42 eV and 0.55 eV, denoted as A and B, respectively.

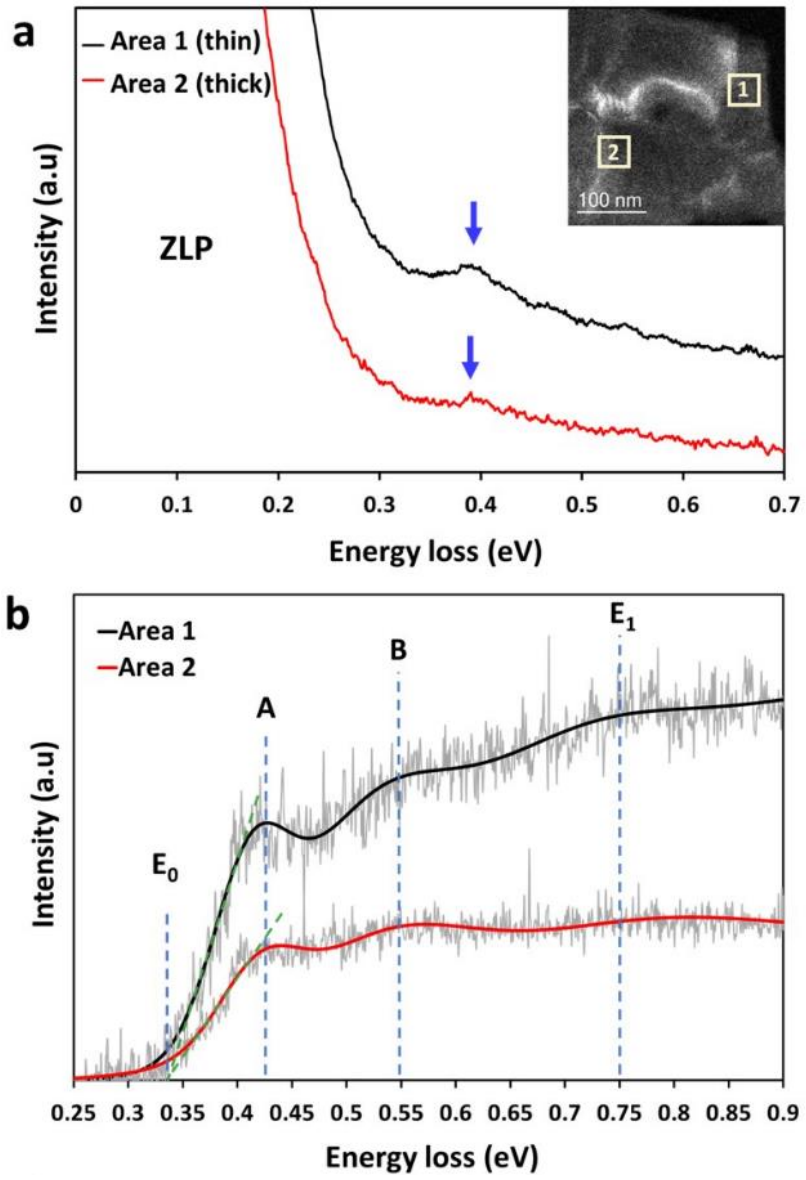

Figure 30. (a) BP bandgap absorption edges (marked by an arrow) clearly visible in the near infrared spectral region of the low-loss spectra. (b) Bandgap edge after ZLP removal. Red and dark lines are smoothed curves. Green dashed lines are bandgap sloops

b. Bandgap and excitons from EELS

To assign these transitions, DFT band-structure calculations were performed using the GGA+YS-PBE0 hybrid functional,[134] as presented in Fig. 31. It can clearly be observed from the calculated band structure that BP has a direct bandgap along the high symmetry point Z. According to our DFT calculation, E_0 corresponds to the transition between the highest valence band Z_2^+ ($3p_y$ orbital) and the lowest conduction band Z_4^- ($3s$ orbital) having an energy gap of about $E_0 = 0.33$ eV, which is in very good agreement with our experiment and reported calculated bandgaps.[135] Such a finding clearly demonstrates the powerfulness of our local and direct measurement of a narrow bandgap as that of a single BP flake. It is worth mentioning that both areas (thin and thick) are giving rise to the same bandgap energy value, which is consistent with our above bulk-plasmon energy statement. On the other hand, E_1 seems to correspond to an intraband transition along the highest valence band Z_2^+ ($3p_y$ orbital) and the lowest conduction band Z_2^- ($3s$ orbital) as indicated in the calculated band-structure of Fig. 31.

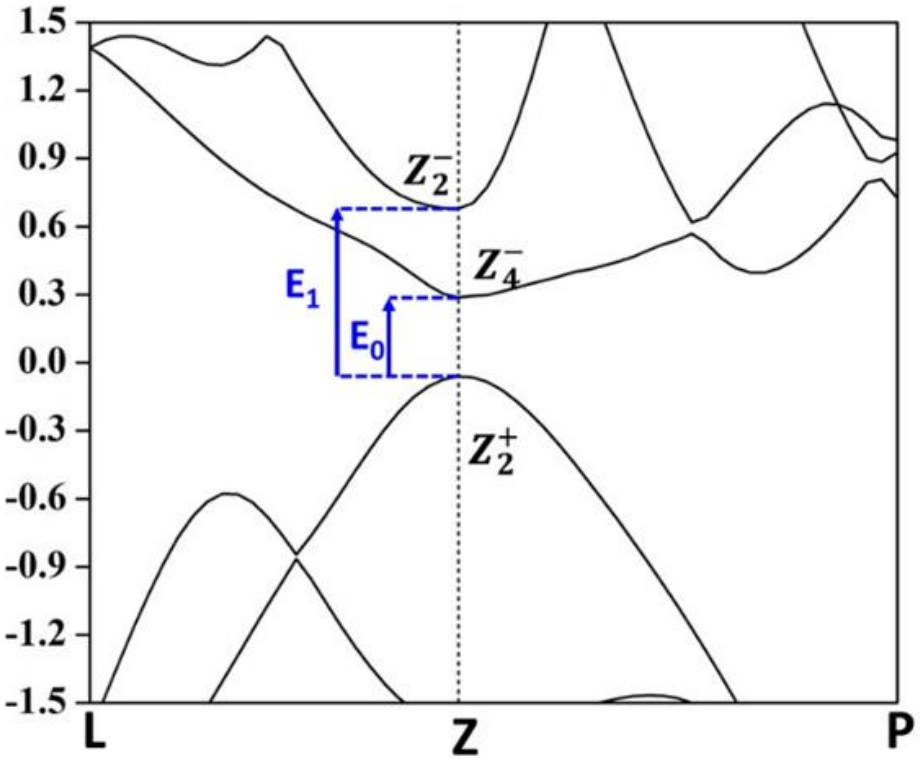

Figure 31. Calculated band structure of BP along high symmetry points indicating E_0 and E_1 electronic transitions.

Regarding the low-energy mode (A) that resides slightly above the bandgap edge, we believe it is excitonic in nature.[136] As a consequence, the as-extracted exciton binding energy (difference between electronic and optical bandgap) results in an energy value of around 70 meV. This value is consistent with the linear scaling law that predicts that the exciton binding energy is

approximately a quarter of the quasi-particle bandgap.[137] Interestingly, the intensity of the energy-loss peak increases when the thickness decreases in spite of the reduced amount of material. Such a finding is indeed consistent with reported photoluminescence data that strongly argue in favor of layer-dependent excitonic absorption,[138] due to the enhanced screening effect in thick areas.[139] In addition, the second mode resonance (B) is very similar to that observed around 0.6 eV along the Γ_X (armchair) direction, which gradually shifts to lower energy and loses strength when changing the polarization direction from the Γ_X to the Γ_Y (zigzag) direction.[136] Table 2 shows the bandgap of black phosphorus as deduced from other experimental methods as well as ours.

Table 2. Comparison of measured bandgap energies of black phosphorus

Method used	**Bandgap (eV)**	**Reference**
Reflectance Spectroscopy	0.35	[89]
Angle resolved photoemission Spectroscopy	~ 0.3	[90]
Scanning tunneling Spectroscopy	0.32	[91] – [92]
Infrared Spectroscopy	0.3	[93]
Monochromated Low-loss EELS	0.33 (± 0.02)	This work

III.4.3. Optical transitions

To investigate the optical transitions of our black phosphorus material, the dipole selection rule was applied. The optical response of BP is essentially a single-particle property. This single-particle (non-interacting) optical absorption spectrum is calculated in the dipole-transition approximation as:[140]

$$\alpha(\omega) \cong \frac{1}{\omega}\sum_{vc\vec{k}}\left|\langle v\vec{k}|\vec{d}|c\vec{k}\rangle\right|^2 \delta(\omega - E_{c\vec{k}} + E_{v\vec{k}})$$

Where $\vec{d}$ is the dipole operator, δ is a function that sums the number of transitions with the required energy ω. The dipole matrix in the above-mentioned equation may be written as $\langle v\vec{k}|\vec{d}|c\vec{k}\rangle = \langle v\vec{k}|\vec{e}.\vec{r}|c\vec{k}\rangle$, where $\vec{e}$ is the direction of polarization of the incident light. This leads to the well-known dipole selection rules, which state whether a transition is allowed or forbidden based on the symmetry of the valence and conduction wave functions. The dipole selection rules have two parts;

since the $\vec{r}$ operator has an odd parity; the matrix element will be zero unless the two wavefunctions involved have opposite parity in the direction of $\vec{e}$, and the same parity in the other direction. Secondly, for the atomic orbitals, the angular momentum number l must differ by one ± 1. The resulting allowed transitions between atomic orbitals for polarization along each direction is shown in Table 3 below, with *y* being for light polarized along zigzag and *x* for light polarized along the armchair direction of BP.

Table 3. Selection rules for optical transitions black phosphorus

	s	**d_{zx}**	**d_{zy}**	**d_{z^2}**	**$d_{x^2-y^2}$**	**d_{xy}**
Px	x			x	x	y
Py	y			y	y	x
Pz		x	y			

After assessing the selection rules for optical transitions, a full analysis of the Bandstructure and density of states transitions was performed along the *Z* and *Γ* points as shown in Fig. 32 and 33. The band-structure was used to acknowledge all the transitions along theses points, while the density of states was used to calculate the contribution percentage of each sub-orbitals responsible for the transition. The reason for choosing only the *Z* and *Γ* points is due to the fact that the transition energies found afterward from the EELS-KKA analysis were found to be related to these two orientations.

The transition energy, along with the assigned point symmetry, orbitals and contribution percentage are summarized in Table. 4.

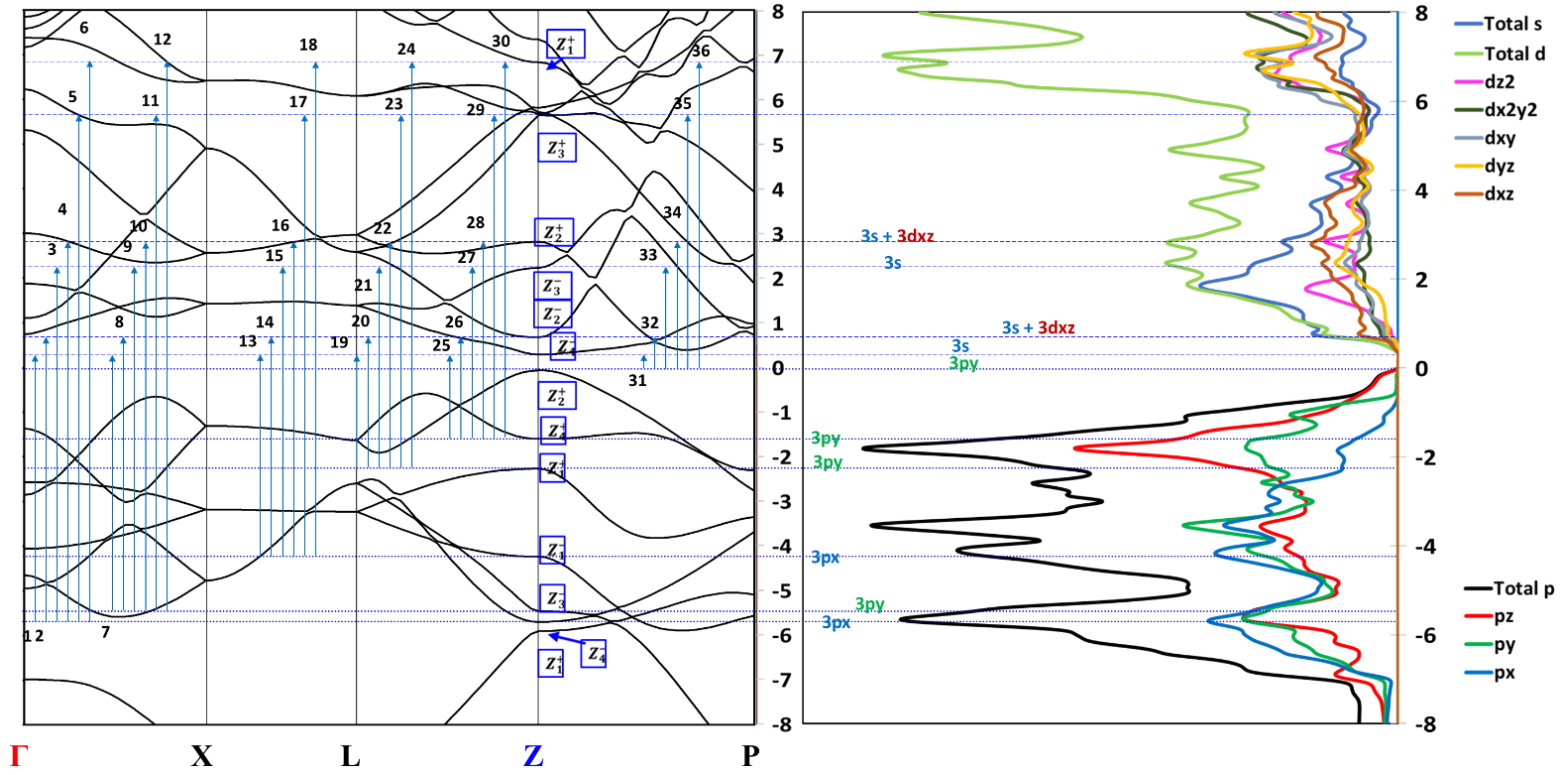

Figure 33. Optical transitions along Z k-point

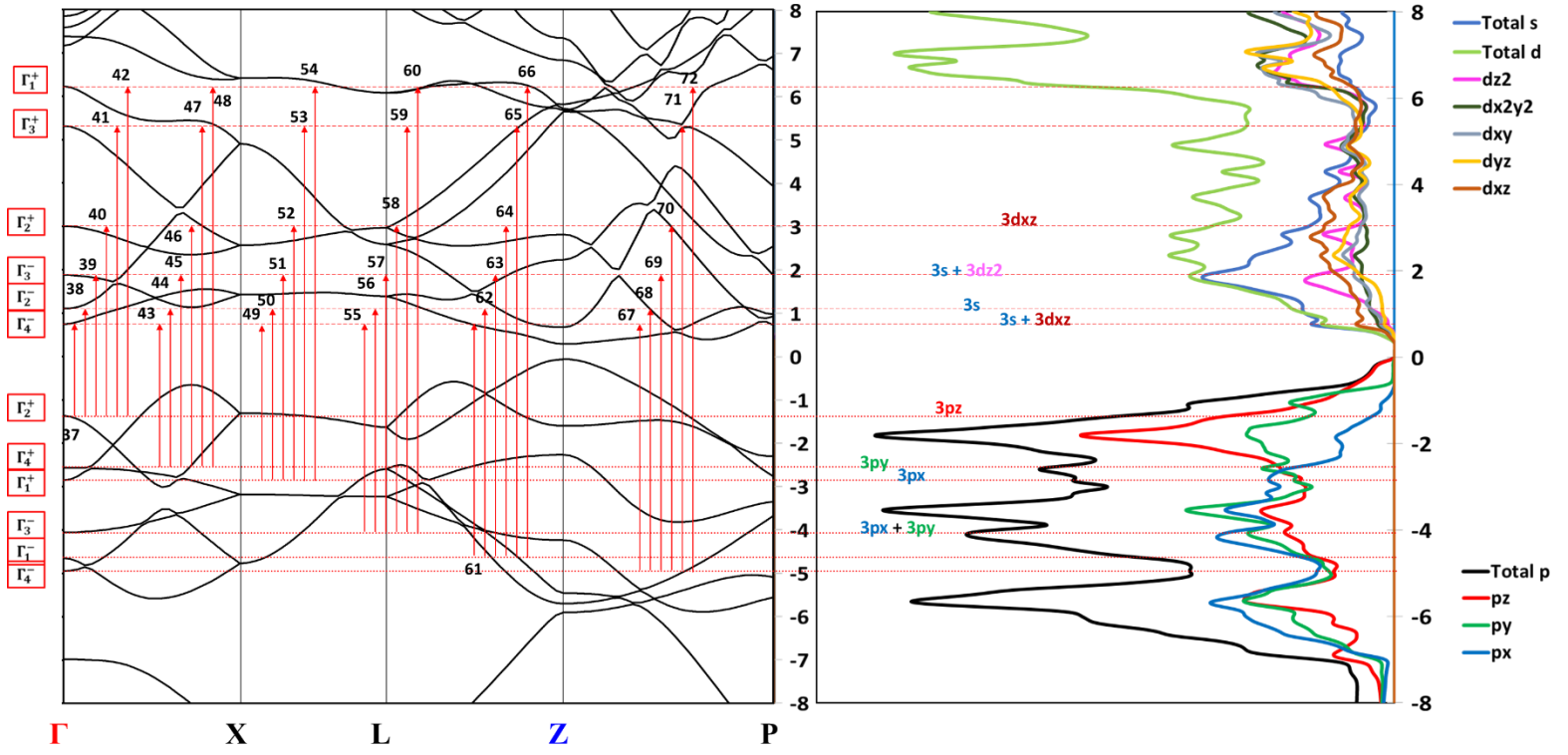

Figure 32. Optical transitions along the Γ k-point

Table 4. All possible optical transitions along the Z and Γ points

Transition number	DFT energy	Assignation point symmetry	Assignation orbitals	Percentage
31	0.347	$Z_2^+ \rightarrow Z_4^-$	3py → 3s	46% s, 3.72% dz^2, 15.98% dx^2y^2, 8.46% dxy, 4.74% dyz, 20.76% dxz
32	0.738	$Z_2^+ \rightarrow Z_2^-$	3py → 3s	48.91% s, 4.05% dz^2, 10% dx^2y^2, 8.21% dxy, 6.09% dyz, 22.71% dxz
25	1.877	$Z_4^+ \rightarrow Z_4^-$	3py → 3s	46% s, 3.72% dz^2, 15.98% dx^2y^2, 8.46% dxy, 4.74% dyz, 20.76% dxz
37	2.109	$\Gamma_2^+ \rightarrow \Gamma_4^-$	3pz → 3s	48.71%s, 4.16% dz^2, 10.13% dx^2y^2, 8.36% dxy, 6.13% dyz, 22.48% dxz
26	2.268	$Z_4^+ \rightarrow Z_2^-$	3py → 3s	48.91% s, 4.05% dz^2, 10% dx^2y^2, 8.21% dxy, 6.09% dyz, 22.71% dxz
33	2.292	$Z_2^+ \rightarrow Z_3^-$	3py → 3s	36.52% s, 10.74% dz^2, 9.26% dx^2y^2, 11.90% dxy, 13.93% dyz, 17.63% dxz
38	2.471	$\Gamma_2^+ \rightarrow \Gamma_2^-$	3pz → 3s	43.05% s, 10.85 dz^2, 11.76% dx^2y^2, 11.08% dxyz, 5.89% dyz, 17.35 dxz
19	2.528	$Z_1^+ \rightarrow Z_4^-$	3py → 3s	46% s, 3.72% dz^2, 15.98% dx^2y^2, 8.46% dxy, 4.74% dyz, 20.76% dxz
34	2.87	$Z_2^+ \rightarrow Z_2^+$	3py → 3s+3dz^2	29.72% s, 18.93% dz^2, 7.44% dx^2y^2, 9.8% dxy, 12.81% dyz, 21.27% dxz
20	2.938	$Z_1^+ \rightarrow Z_2^-$	3py → 3s	48.91% s, 4.05% dz^2, 10% dx^2y^2, 8.21% dxy, 6.09% dyz, 22.71% dxz
39	3.234	$\Gamma_2^+ \rightarrow \Gamma_3^-$	3pz → 3s + 3dz^2	43.86% s, 19.09% dz^2, 7.63% dx^2y^2, 9.26% dxy, 7.60% dyz, 12.54 dxz
43	3.311	$\Gamma_4^+ \rightarrow \Gamma_4^-$	3py → 3s	48.71%s, 4.16% dz^2, 10.13% dx^2y^2, 8.36% dxy, 6.13% dyz, 22.48% dxz
49	3.596	$\Gamma_1^+ \rightarrow \Gamma_4^-$	3px → 3s	48.71%s, 4.16% dz^2, 10.13% dx^2y^2, 8.36% dxy, 6.13% dyz, 22.48% dxz
44	3.673	$\Gamma_4^+ \rightarrow \Gamma_2^-$	3py → 3s	43.05% s, 10.85 dz^2, 11.76% dx^2y^2, 11.08% dxyz, 5.89% dyz, 17.35 dxz
27	3.822	$Z_4^+ \rightarrow Z_3^-$	3py → 3s	36.52% s, 10.74% dz^2, 9.26% dx^2y^2, 11.90% dxy, 13.93% dyz, 17.63% dxz
50	3.958	$\Gamma_1^+ \rightarrow \Gamma_2^-$	3px → 3s	43.05% s, 10.85 dz^2, 11.76% dx^2y^2, 11.08% dxyz, 5.89% dyz, 17.35 dxz

40	4.364	$\Gamma_2^+ \rightarrow \Gamma_2^+$	3pz → 3dxy	28.22% s, 13.68% dz^2, 9.40% dx^2y^2, 11.09% dxy, 14.81% dyz, 22.77% dxz
28	4.4	$Z_4^+ \rightarrow Z_2^+$	3py → 3s+3dz^2	29.72% s, 18.93% dz^2, 7.44% dx^2y^2, 9.8% dxy, 12.81% dyz, 21.27% dxz
45	4.443	$\Gamma_4^+ \rightarrow \Gamma_3^-$	3py → 3s + 3dz^2	43.86% s, 19.09% dz^2, 7.63% dx^2y^2, 9.26% dxy, 7.60% dyz, 12.54 dxz
21	4.492	$Z_1^+ \rightarrow Z_3^-$	3py → 3s	36.52% s, 10.74% dz^2, 9.26% dx^2y^2, 11.90% dxy, 13.93% dyz, 17.63% dxz
13	4.5	$Z_1^- \rightarrow Z_4^-$	3px → 3s	46% s, 3.72% dz^2, 15.98% dx^2y^2, 8.46% dxy, 4.74% dyz, 20.76% dxz
51	4.728	$\Gamma_1^+ \rightarrow \Gamma_3^-$	3px → 3s + 3dz^2	43.86% s, 19.09% dz^2, 7.63% dx^2y^2, 9.26% dxy, 7.60% dyz, 12.54 dxz
55	4.795	$\Gamma_3^- \rightarrow \Gamma_4^-$	3px + 3py → 3s	48.71%s, 4.16% dz^2, 10.13% dx^2y^2, 8.36% dxy, 6.13% dyz, 22.48% dxz
14	4.91	$Z_1^- \rightarrow Z_2^-$	3px → 3s	48.91% s, 4.05% dz^2, 10% dx^2y^2, 8.21% dxy, 6.09% dyz, 22.71% dxz
22	5.07	$Z_1^+ \rightarrow Z_2^+$	3py → 3s+3dz^2	29.72% s, 18.93% dz^2, 7.44% dx^2y^2, 9.8% dxy, 12.81% dyz, 21.27% dxz
56	5.157	$\Gamma_3^- \rightarrow \Gamma_2^-$	3px + 3py → 3s	43.05% s, 10.85 dz^2, 11.76% dx^2y^2, 11.08% dxyz, 5.89% dyz, 17.35 dxz
61	5.392	$\Gamma_1^- \rightarrow \Gamma_4^-$	3py → 3s	48.71%s, 4.16% dz^2, 10.13% dx^2y^2, 8.36% dxy, 6.13% dyz, 22.48% dxz
46	5.566	$\Gamma_4^+ \rightarrow \Gamma_2^+$	3py → 3dxy	28.22% s, 13.68% dz^2, 9.40% dx^2y^2, 11.09% dxy, 14.81% dyz, 22.77% dxz
67	5.689	$\Gamma_4^- \rightarrow \Gamma_4^-$	3px + 3py → 3s	48.71%s, 4.16% dz^2, 10.13% dx^2y^2, 8.36% dxy, 6.13% dyz, 22.48% dxz
7	5.72	$Z_3^- \rightarrow Z_4^-$	3py → 3s	46% s, 3.72% dz^2, 15.98% dx^2y^2, 8.46% dxy, 4.74% dyz, 20.76% dxz
35	5.73	$Z_2^+ \rightarrow Z_3^+$	3py → 3dxy	10.59% s, 15.46% dz^2, 15.21% dx^2y^2, 21.4% dxy, 19.69% dyz, 17.62% dxz
62	5.754	$\Gamma_1^- \rightarrow \Gamma_2^-$	3py → 3s	43.05% s, 10.85dz^2, 11.76% dx^2y^2, 11.08% dxyz, 5.89% dyz, 17.35 dxz
52	5.851	$\Gamma_1^+ \rightarrow \Gamma_2^+$	3px → 3dxy	28.22% s, 13.68% dz^2, 9.40% dx^2y^2, 11.09% dxy, 14.81% dyz, 22.77% dxz
57	5.927	$\Gamma_3^- \rightarrow \Gamma_3^-$	3px + 3py → 3s + 3dz^2	43.86% s, 19.09% dz^2, 7.63% dx^2y^2, 9.26% dxy, 7.60% dyz, 12.54 dxz

1	5.962	$Z_4^- \rightarrow Z_4^-$	3px → 3s	46% s, 3.72% dz^2, 15.98% dx^2y^2, 8.46% dxy, 4.74% dyz, 20.76% dxz
68	6.051	$\Gamma_4^- \rightarrow \Gamma_2^-$	3px + 3py → 3s	43.05% s, 10.85 dz^2, 11.76% dx^2y^2, 11.08% dxyz, 5.89% dyz, 17.35 dxz
8	6.13	$Z_3^- \rightarrow Z_2^-$	3py → 3s	48.91% s, 4.05% dz^2, 10% dx^2y^2, 8.21% dxy, 6.09% dyz, 22.71% dxz
2	6.372	$Z_4^- \rightarrow Z_2^-$	3px → 3s	48.91% s, 4.05% dz^2, 10% dx^2y^2, 8.21% dxy, 6.09% dyz, 22.71% dxz
15	6.464	$Z_1^- \rightarrow Z_3^-$	3px → 3s	36.52% s, 10.74% dz^2, 9.26% dx^2y^2, 11.90% dxy, 13.93% dyz, 17.63% dxz
63	6.524	$\Gamma_1^- \rightarrow \Gamma_3^-$	3py → 3s + $3dz^2$	43.86% s, 19.09% dz^2, 7.63% dx^2y^2, 9.26% dxy, 7.60% dyz, 12.54 dxz
41	6.68	$\Gamma_2^+ \rightarrow \Gamma_3^+$	3pz → 3dxy + 3dyz	12.88% s, 15.49% dz^2, 15.81% dx^2y^2, 19.48% dxy, 16.89% dyz, 19.41% dxz
69	6.821	$\Gamma_4^- \rightarrow \Gamma_3^-$	3px + 3py → 3s + $3dz^2$	43.86% s, 19.09% dz^2, 7.63% dx^2y^2, 9.26% dxy, 7.60% dyz, 12.54 dxz
36	6.89	$Z_2^+ \rightarrow Z_1^+$	3py → $3dx^2y^2$	9.14% s, 17.61% dz^2, 22.11% dx^2y^2, 20.18% dxy, 18.29% dyz, 12.65% dxz
16	7.042	$Z_1^- \rightarrow Z_2^+$	3px → 3s+$3dz^2$	29.72% s, 18.93% dz^2, 7.44% dx^2y^2, 9.8% dxy, 12.81% dyz, 21.27% dxz
58	7.05	$\Gamma_3^- \rightarrow \Gamma_2^+$	3px + 3py → 3dxy	28.22% s, 13.68% dz^2, 9.40% dx^2y^2, 11.09% dxy, 14.81% dyz, 22.77% dxz
29	7.26	$Z_4^+ \rightarrow Z_3^+$	3py → 3dxy	10.59% s, 15.46% dz^2, 15.21% dx^2y^2, 21.4% dxy, 19.69% dyz, 17.62% dxz
64	7.647	$\Gamma_1^- \rightarrow \Gamma_2^+$	3py → 3dxy	28.22% s, 13.68% dz^2, 9.40% dx^2y^2, 11.09% dxy, 14.81% dyz, 22.77% dxz
9	7.684	$Z_3^- \rightarrow Z_3^-$	3py → 3s	36.52% s, 10.74% dz^2, 9.26% dx^2y^2, 11.90% dxy, 13.93% dyz, 17.63% dxz
42	7.684	$\Gamma_2^+ \rightarrow \Gamma_1^+$	3pz → 3dxy + 3dx2y2	9.50% s, 19.65% dz^2, 21.39% dx^2y^2, 24.35% dxy, 15.15% dyz, 9.94% dxz
47	7.882	$\Gamma_4^+ \rightarrow \Gamma_3^+$	3py → 3dxy + 3dyz	12.88% s, 15.49% dz^2, 15.81% dx^2y^2, 19.48% dxy, 16.89% dyz, 19.41% dxz
3	7.926	$Z_4^- \rightarrow Z_3^-$	3px → 3s	36.52% s, 10.74% dz^2, 9.26% dx^2y^2, 11.90% dxy, 13.93% dyz, 17.63% dxz
23	7.93	$Z_1^+ \rightarrow Z_3^+$	3py → 3dxy	10.59% s, 15.46% dz^2, 15.21% dx^2y^2, 21.4% dxy, 19.69% dyz, 17.62% dxz

70	7.944	$\Gamma_4^- \rightarrow \Gamma_2^+$	3px + 3py → 3dxy	28.22% s, 13.68% dz^2, 9.40% dx^2y^2, 11.09% dxy, 14.81% dyz, 22.77% dxz
53	8.167	$\Gamma_1^+ \rightarrow \Gamma_3^+$	3px → 3dxy + 3dyz	12.88% s, 15.49% dz^2, 15.81% dx^2y^2, 19.48% dxy, 16.89% dyz, 19.41% dxz
10	8.262	$Z_3^- \rightarrow Z_2^+$	3py → 3s+3dz^2	29.72% s, 18.93% dz^2, 7.44% dx^2y^2, 9.8% dxy, 12.81% dyz, 21.27% dxz
30	8.42	$Z_4^+ \rightarrow Z_1^+$	3py → 3dx^2y^2	9.14% s, 17.61% dz^2, 22.11% dx^2y^2, 20.18% dxy, 18.29% dyz, 12.65% dxz
4	8.504	$Z_4^- \rightarrow Z_2^+$	3px → 3s+3dz^2	29.72% s, 18.93% dz^2, 7.44% dx^2y^2, 9.8% dxy, 12.81% dyz, 21.27% dxz
48	8.798	$\Gamma_4^+ \rightarrow \Gamma_1^+$	3py → 3dxy + 3dx2y2	9.50% s, 19.65% dz^2, 21.39% dx^2y^2, 24.35% dxy, 15.15% dyz, 9.94% dxz
54	9.083	$\Gamma_1^+ \rightarrow \Gamma_1^+$	3px → 3dxy + 3dx2y2	9.50% s, 19.65% dz^2, 21.39% dx^2y^2, 24.35% dxy, 15.15% dyz, 9.94% dxz
24	9.09	$Z_1^+ \rightarrow Z_1^+$	3py → 3dx^2y^2	9.14% s, 17.61% dz^2, 22.11% dx^2y^2, 20.18% dxy, 18.29% dyz, 12.65% dxz
59	9.366	$\Gamma_3^- \rightarrow \Gamma_3^+$	3px + 3py → 3dxy + 3dyz	12.88% s, 15.49% dz^2, 15.81% dx^2y^2, 19.48% dxy, 16.89% dyz, 19.41% dxz
17	9.902	$Z_1^- \rightarrow Z_3^+$	3px → 3dxy	10.59% s, 15.46% dz^2, 15.21% dx^2y^2, 21.4% dxy, 19.69% dyz, 17.62% dxz
65	9.963	$\Gamma_1^- \rightarrow \Gamma_3^+$	3py → 3dxy + 3dyz	12.88% s, 15.49% dz^2, 15.81% dx^2y^2, 19.48% dxy, 16.89% dyz, 19.41% dxz
71	10.26	$\Gamma_4^- \rightarrow \Gamma_3^+$	3px + 3py → 3dxy + 3dyz	12.88% s, 15.49% dz^2, 15.81% dx^2y^2, 19.48% dxy, 16.89% dyz, 19.41% dxz
60	10.282	$\Gamma_3^- \rightarrow \Gamma_1^+$	3px + 3py → 3dxy + 3dx2y2	9.50% s, 19.65% dz^2, 21.39% dx^2y^2, 24.35% dxy, 15.15% dyz, 9.94% dxz
66	10.879	$\Gamma_1^- \rightarrow \Gamma_1^+$	3py → 3dxy + 3dx2y2	9.50% s, 19.65% dz^2, 21.39% dx^2y^2, 24.35% dxy, 15.15% dyz, 9.94% dxz
18	11.062	$Z_1^- \rightarrow Z_1^+$	3px → 3dx^2y^2	9.14% s, 17.61% dz^2, 22.11% dx^2y^2, 20.18% dxy, 18.29% dyz, 12.65% dxz
11	11.122	$Z_3^- \rightarrow Z_3^+$	3py → 3dxy	10.59% s, 15.46% dz^2, 15.21% dx^2y^2, 21.4% dxy, 19.69% dyz, 17.62% dxz
72	11.176	$\Gamma_4^- \rightarrow \Gamma_1^+$	3px + 3py → 3dxy + 3dx2y2	9.50% s, 19.65% dz^2, 21.39% dx^2y^2, 24.35% dxy, 15.15% dyz, 9.94% dxz
5	11.364	$Z_4^- \rightarrow Z_3^+$	3px → 3dxy	10.59% s, 15.46% dz^2, 15.21% dx^2y^2, 21.4% dxy, 19.69% dyz, 17.62% dxz

12	12.28 2	$Z_3^- \rightarrow Z_1^+$	$3py \rightarrow 3dx^2y^2$	9.14% s, 17.61% dz^2, 22.11% dx^2y^2, 20.18% dxy, 18.29% dyz, 12.65% dxz
6	12.52 4	$Z_4^- \rightarrow Z_1^+$	$3px \rightarrow 3dx^2y^2$	9.14% s, 17.61% dz^2, 22.11% dx^2y^2, 20.18% dxy, 18.29% dyz, 12.65% dxz

In addition to the bandgap edge, clearly visible at 0.322 eV, a series of additional absorption peaks, or inter-band (IB) transitions, in the lower eV range of the loss function are also observed proving that our measured EEL spectrum contains the complete characteristic of the complex dielectric function **ε**. To describe such a dielectric function, a Kramers–Kronig Analysis (KKA) was first applied to extract the imaginary part ($\boldsymbol{\varepsilon}_2$) which would better illustrate the IB transitions. At this stage, it is interesting to underline that our low-loss EELS spectra were recorded with the BP $\vec{c}$-axis oriented normal to the transferred momentum $\vec{q}$ ($\vec{q} \perp \vec{c}$), which means that our measurements were not sensitive to contributions from the $\vec{c}$ component. The as-extracted imaginary part ($\boldsymbol{\varepsilon}_2$) from KKA is presented in Fig. 34, and compared to the armchair (*y*) and zigzag (*x*) components of the DFT calculated $\boldsymbol{\varepsilon}_2$.

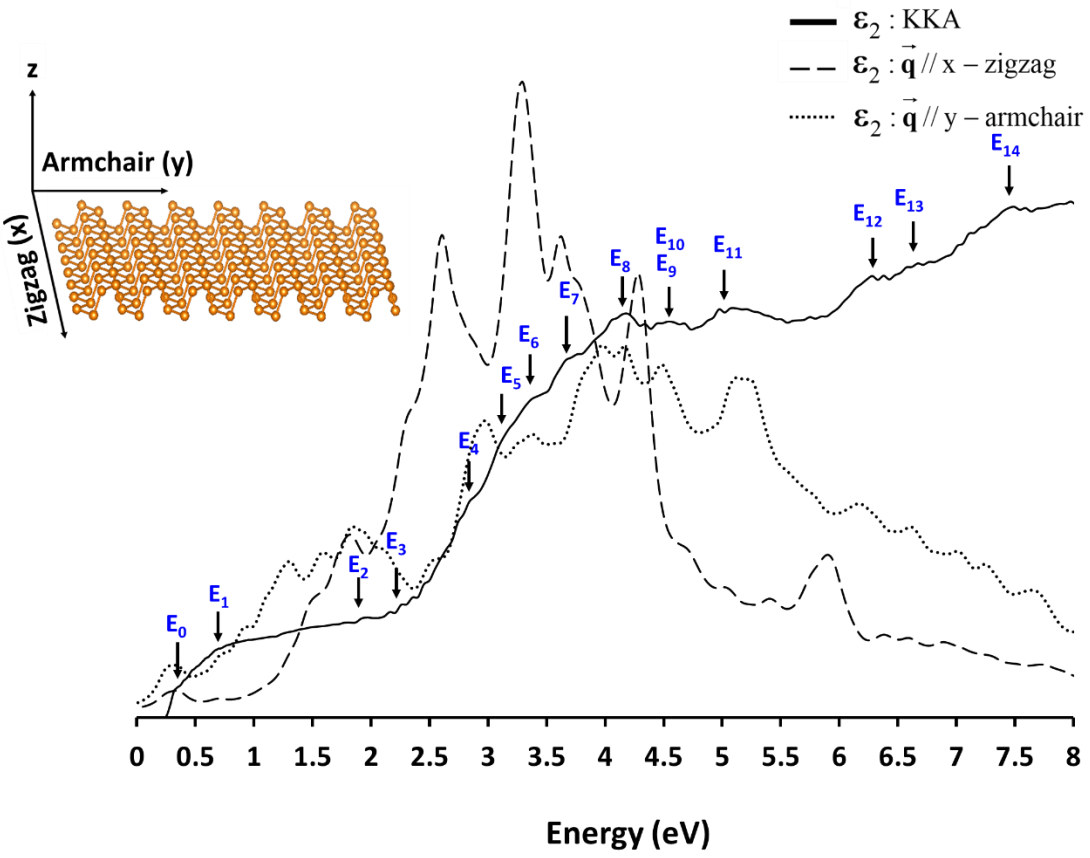

Figure 34. Imaginary part of the dielectric function ε2 extracted from VEELS spectrum with the help of KK analysis, and compared to x- and y-components of DFT calculated ε2

Strong similarities between experimental and calculated spectra are observed, especially along the armchair direction (*y*) where almost all the features are identified. This suggests that our

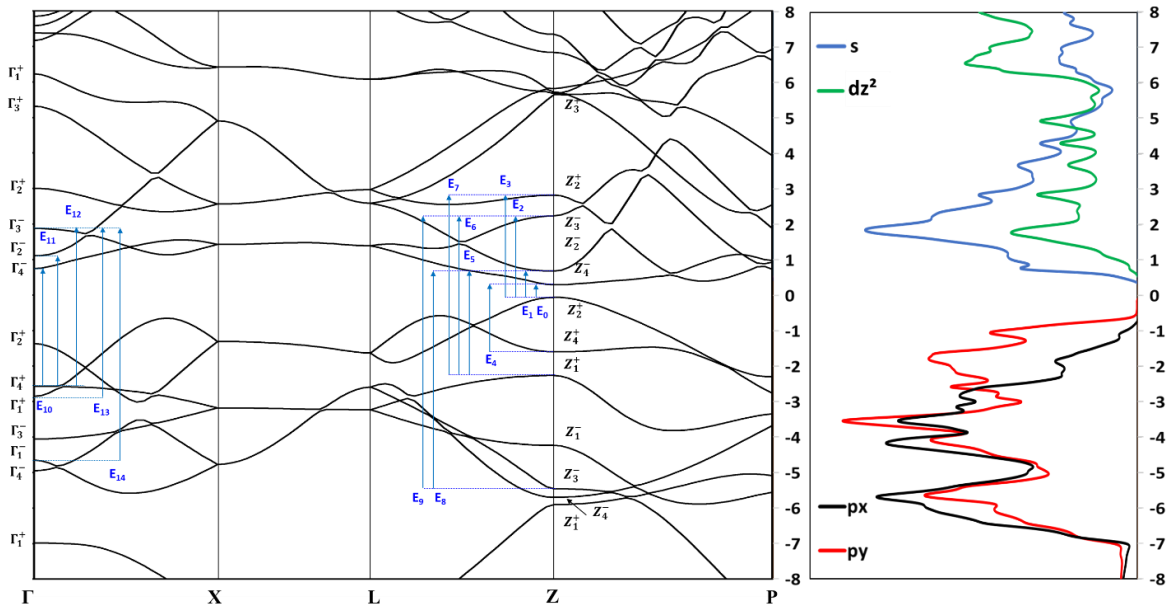

measured low-loss EELS spectrum was most probably recorded with $\vec{q}$ being close to the $\vec{b}$-axis. The dominant features, or critical points, found in our KKA-$\boldsymbol{\varepsilon}_2$ spectrum (for $\vec{q} \perp \vec{c}$) are labeled

Figure 35. Density of states of black phosphorus and (c) its corresponding electronic band structure. The arrows in (a) indicate the interband transitions assigned in the band structure at Z and Γ symmetry points.

from E_0 to E_{14}, and were assigned to specific IB transitions at high symmetry points in the Brillouin zone (BZ) since the low-loss EEL region of the spectrum is described in terms of the energy-loss function.[141] To assign these critical points, DFT DOS and band structure were calculated and respectively presented in Fig. 35. For the sake of clarity, only orbitals responsible for allowed IB transitions were presented (optical selection rules were applied). From Fig. 35, it can be seen that the valence bands are mainly comprised of $3p_x$ and $3p_y$ sub-orbitals, while $3p_z$ was removed as the transferred momentum $\vec{q}$ is perpendicular to z. While the conduction bands are mainly comprised of an admixture of 3*s* and 3*d* orbitals. In this figure case, only 3*s* and $3d_{z^2}$ orbitals were presented, where $3d_{x^2+y^2}$ and $3d_{xy}$ sub-orbitals were neglected due to their low contribution into the DOS, even though they are allowed by optical selection rules. Again, $3d_{xz}$ and $3d_{yz}$ sub-orbitals were removed as $\vec{q} \perp \vec{c}$.

In Table 5 are summarized suggested IB transitions (point symmetry and orbitals) as deduced from our KKA-$\boldsymbol{\varepsilon}_2$ and DFT calculations, where all transitions were assigned along Z and

Γ high-symmetry points, in agreement with previous reports.[142,102] It is worth mentioning that most of the transitions are originating from $3p_y$ sub-orbitals, which is consistent with KKA-$\boldsymbol{\varepsilon}_2$ recorded close to the armchair direction (*y*). From Fig. 35, we also notice that IB transitions below 4 eV in energy are predominantly towards 3*s* conduction band states, while those having higher energies are towards the admixture of $3d_{z^2}$+3*s*, with a high contribution to $3d_{z^2}$. These transitions energies are in good agreement with results obtained from Hard X-Ray Photoelectron Spectra (HAXPES).[143] All these results clearly demonstrate the powerfulness of monochromated VEELS in describing the dielectric function of narrow-bandgap semiconductors.

Table 5. Comparison of critical points energies as obtained from the imaginary part of the dielectric function with energies from DFT calculations

	EELS energy (eV)	DFT energy (eV)	Suggested point-symmetry assignation	Suggested orbitals assignation
E_0	0.32	0.35	$Z_2^+ \rightarrow Z_4^-$	3py → 3s
E_1	0.74	0.74	$Z_2^+ \rightarrow Z_2^-$	3py → 3s
E_2	1.87	1.88	$Z_4^+ \rightarrow Z_4^-$	3py → 3s
E_3	2.25	2.29	$Z_2^+ \rightarrow Z_3^-$	3py → 3s
E_4	2.84	2.87	$Z_2^+ \rightarrow Z_2^+$	3py → 3s + 3dz²
E_5	3.08	2.94	$Z_1^+ \rightarrow Z_2^-$	3py → 3s
E_6	3.32	3.31	$\Gamma_4^+ \rightarrow \Gamma_4^-$	3py → 3s
E_7	3.71	3.67	$\Gamma_4^+ \rightarrow \Gamma_2^-$	3py → 3s
E_8	4.14	4.44	$\Gamma_4^+ \rightarrow \Gamma_3^-$	3py → 3s + 3dz²
E_9	4.53	4.49	$Z_1^+ \rightarrow Z_3^-$	3py → 3s
E_{10}		4.73	$\Gamma_1^+ \rightarrow \Gamma_3^-$	3px → 3s + 3dz²
E_{11}	5.12	5.07	$Z_1^+ \rightarrow Z_2^+$	3py → 3s + 3dz²
E_{12}	6.23	6.13	$Z_3^- \rightarrow Z_2^-$	3py → 3s
E_{13}	6.62	6.52	$\Gamma_1^- \rightarrow \Gamma_3^-$	3py → 3s + 3dz²
E_{14}	7.49	7.68	$Z_3^- \rightarrow Z_3^-$	3py → 3s

III.5. Conclusion

In conclusion, a detailed structural and electronic study of BP flakes has been carried out in the low infrared region using monochromated EELS. These BP flakes were perpendicular to the analysis axis in core- and low-loss EELS modes. Using core-loss EELS, the characteristic P-$L_{2,3}$ and P-L_1 lines of BP were clearly identified and respectively assigned to $2p^{3/2} \rightarrow 3s$, $2p^{1/2} \rightarrow 3d$ and $2s \rightarrow 3(s+d)$ electronic transitions. In the low-loss EELS zone, the volume plasmon was detected at an energy E_p = 19.6 ± 0.1 eV, while in the low infrared monochromated EELS was very crucial allowing a fast and direct "lecture" of electronic transitions close to the gap area. With the help of DFT band structure calculations, two transitions were respectively assigned along the high symmetry point Z, as the bandgap with an energy of 0.33 ± 0.02 eV and an intraband transition at 0.75 eV. Two more excitations were found to be excitonic in nature as confirmed by the increase of the energy-loss peak intensity with decreasing thickness due to the enhanced screening effect in thick areas. A full description of the imaginary part ($\boldsymbol{\varepsilon}_2$) of the dielectric function was achieved and the dominant critical points assigned to specific IB transitions ($3p \rightarrow 3s$ and $3p \rightarrow 3d_{z^2}$) along Z and Γ high-symmetry points of the Brillouin zone. We finally note that the optical quality of the studied BP flakes may pave the way for optoelectronic and photonic applications. All these findings demonstrate the usefulness of monochromated low-loss EELS in measuring electronic properties of narrow-bandgap semiconductors.

Chapter IV.

Theoretical studies on Exfoliation and re-aggregation mechanisms of black phosphorus

IV.1. Introduction

Two-dimensional (2D) materials are consisting of monoatomic sheets with weak van der Waals (vdW) interactions. Phosphorene, the two-dimensional variant of the layered black phosphorus (BP) allotrope, is one of the last born in the family[144-145-146] with promising applications in fields such as electronics,[146] optics,[147] catalysis[148] and biosensors.[149] Taking advantage of its sheet-like structure, exfoliation of BP is mainly inspired from methods used to exfoliate graphene from graphite,[150,151] such as micromechanical cleavage,[146] plasma assisted thinning treatment[152] and Liquid Phase Exfoliation (LPE).[153-154] Among these methods, LPE has shown promising results, due to its ability to produce nanosheets in large quantities, its ease of use, as well as the efficiency in preparing stable solutions of phosphorene suspensions.[154-155]

In fact, the efficiency of the LPE method is mainly dependent on the solvent physical properties. Even after a successful exfoliation, re-aggregation events remain nevertheless a major obstacle for preparing a limpid and stable suspension of single phosphorene sheets.[156] Many parameters are *a fortiori* involved in the exfoliation/re-aggregation mechanism where the solvent intrinsic properties play a crucial role during exfoliation and re-aggregation phenomena. Among these parameters, one can cite the Hildebrand solubility parameter (related to the cohesive energy of the solvent),[157,158,159] in addition to the size/planarity[160] and polarity[153,161] of the solvent's molecule. On this basis, many attempts were carried out to exfoliate BP into phosphorene monoatomic sheets using a variety of solvents. For instance, exfoliation of BP in N-Cyclohexyl-2-pyrrolidone (CHP) resulted in BP flakes of about 10 sheets in thickness.[153,162] Although less stable than that obtained from CHP, N-methyl pyrrolidone (NMP) also provided a BP flakes solution with a thickness around 6 to 10 nm (10 to 16 sheets).[154] Isopropanol (IPA), however, has shown a high efficiency during BP exfoliation,[163] but gave a non-stable suspension as compared to those obtained from CHP and NMP. In the case of Dimethyl-based solvents (Dimethyl sulfoxide, DMSO, and Dimethyl formamide, DMF), exfoliation always resulted in BP flakes with a slight advantage for DMF in terms of flakes thickness (5 nm for DMF versus 15 nm for DMSO).[153] So far, solvents giving the highest suspension stability (several weeks) as compared to the above mentioned solvents are Benzonitrile (BZ), 1,3-dimethyl-2-imidazolidinone (DMI) and 1-vinyl-2-pyrrolidinone (NVP).[158] From the above, one can notice that a good solvent for BP exfoliation does not necessarily guarantee the suspension stability. Many questions may then arise not only regarding the driving force for a re-aggregation phenomenon, that directly affects the suspension stability, but also on the parameters that truly controls the exfoliation process.

Selection of the adequate solvent for the purpose of exfoliation is usually performed on one

main criterion; that is the solubility parameter of the solvent as compared to that of phosphorene.[164,165] This solubility issue is controlled by the interaction between the phosphorene and the solvent molecules where surface tension and Hildebrand solubility parameters are *a priori* governing the exfoliation/re-aggregation mechanism. In fact, the exfoliation and/or the re-aggregation phenomena should also be influenced by the ability of the molecule to diffuse into BP during the LPE process. Indeed, the motion of solvent molecules is a crucial step towards molecules intercalation, as this movement is related to the amount of energy responsible of the peeling process. Consequently, the self-diffusion properties combined with the Hildebrand solubility parameter are expected to collectively contribute to the exfoliation/re-aggregation mechanism where the weight of each is yet not clearly understood. In the present chapter, classical molecular dynamics (MD) simulations will be extensively used to gain better insights into such a collective contribution, since it has already been successfully applied for studying the liquid phase exfoliation and for the generation of other two-dimensional nanosheets, such as hexagonal Boron nitride (h-BN),[161] graphite[166] and C_2N.[167] Indeed, MD simulation is the technique of choice to explore force attractions between molecules which are dominated by interatomic potentials and molecular force fields. The influence of the solvent molecule's self-diffusion, morphology and size on the BP exfoliation/re-aggregation mechanism is deeply studied and presented in the following.

IV.2. Exfoliation of Black phosphorus

BP nanosheets were often made from bulk BP using a mechanical or solvent-assisted exfoliation process, whereas bulk BP was mostly made via a phase-transformation reaction using white or red phosphorus as the P source. Bulk BP crystals were initially produced in 1914 using white phosphorus as the phosphorus source at high hydrostatic pressure (0.6–1.2 GPa) at a temperature below the phase transformation run. Until recently, bulk BP could be made from red phosphorus at low pressure using a modified chemical vapor transport process, which involved the interaction of red phosphorus, Sn, Au, and SnI_4. The modified chemical vapor transport method using red phosphorus as a precursor is currently the most common method for producing bulk BP as was described in the previous section. Meanwhile, various unique methods for transferring bulk BP crystal to BP nanosheets have been devised, including mechanical exfoliation,[168] liquid exfoliation,[162] electrochemical expansion,[169] and solvothermal technique.[170]

IV.2.1. Micromechanical cleavage

It is well known that graphene may be obtained from mechanical cleaving of bulk graphite using a sticky-tape method,[171] and same method can also be used to make single-layer BP. Ye et al. demonstrated in 2014 that Scotch-tape-based microcleavage of commercially available multilayer bulk BP crystals can produce atomically thin monolayer and few-layer BP nanosheets.146 The thickness of the exfoliated BP nanosheets has size less than 1 μm, which is close to the theoretical value of 0.6 nm, indicating the presence of monolayer BP. Despite the fact that sticky-tape mechanical exfoliation of bulk BP crystals can produce high-quality monolayer BP, the yield is still poor and the surface has a sticky adhesive. Jin and colleagues also proposed an experimental approach for fabricating monolayer BP that combined mechanical cleavage and plasma thinning.152 Few-layer BP nanosheets were first produced on a Si substrate, and subsequently the layer number of the BP nanosheets was reduced using an Ar^+ plasma thinning technique. To date, sticky-tape-prepared few-layer BP has mostly been used in the domains of field effect transistors and photodetectors. Recently, a ball-milled mechanical exfoliation approach was used to prepare few-layer BP nanosheets in an Ar environment using LiOH as an additive.[172] Notably, during the high-energy ball milling process, BP is very reactive and unstable, and in the absence of LiOH, it can be converted to red phosphorus. The BP sample is significantly smaller (300–500 nm) and the thickness is decreased to tens of nanometers after ball-milling. Although a huge quantity of BP nanosheets may be created quickly using the mechanical exfoliation approach, one disadvantage is that the exfoliated BP will permanently breakdown and oxidize when exposed to the environment. This preparation process faces a significant problem in developing an effective technique to prevent BP oxidation. Fig. 36 below shows an example of a mechanical exfoliation of black phosphorus using PDMS stamps.

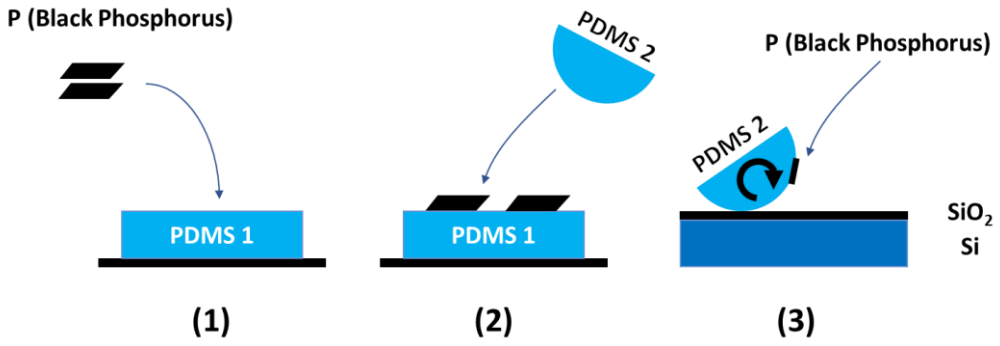

Figure 36. Three step exfoliation procedure of BP via mechanical exfoliation. (1) Exfoliation done on the flat PDMS-1. (2) The flakes were reported on semi-spherical PDMS-2 stamp. (3) the stamp was rolled on the substrate (SiO_2 on Si) with an estimated speed of 0.1 cm/s.[173]

IV.2.2. Liquid Phase Exfoliation

Liquid-phase exfoliation refers to breaking a layered crystal into 2D materials by suspending the crystal in a "solvent" and blasting the crystal with ultrasonic energy. The general process for preparing ultrathin BP flakes by liquid-phase exfoliation involves three steps: (i) dispersion of the starting material in a liquid medium, (ii) exfoliation via sonication and (iii) centrifugation. When ultrasonic waves (usually 20–50 kHz) pass through a liquid, they create alternating high- and low-pressure cycles. Small cavities form in low-pressure areas, which later collapse under compression, resulting in the localized development of high temperatures and pressures,[174] a phenomenon known as cavitation. Ultrasonication of liquids can be done with either a bath or a probe; both experimental setups have been successful in exfoliating BP. The position of the sample in the bath can have a substantial impact on the sonication intensity, limiting reproducibility.[175,176] Because ultrasonic probes are immediately submerged in the solution to be sonicated, the power delivered is often higher than that of an ultrasonic bath, resulting in shorter sonication durations. In summary, during the sonication process, shear forces and cavitation can be induced due to the propagation of high amplitude sonication waves acting on the surface of bulk materials, and hence shears the crystal apart.[177,178] As a result, utilizing ultrasonication to exfoliate multilayer materials is an effective and scalable process. To stabilize the as-prepared 2D flakes, the interfacial tension between the materials being exfoliated and the liquid medium should be decreased, recognizing the existence of favorable contacts. Afterwards, the sonicated solution is subjected to ultracentrifugation to separate thick BP layers from thin BP layers. The schematic below shows the process of liquid phase exfoliation used in our work to exfoliate BP.

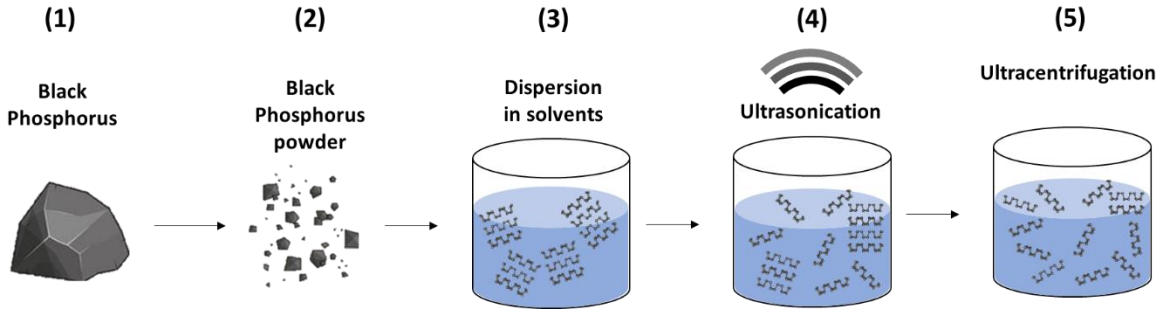

Figure 37. (1) Black phosphorus crystal (2) Crushed Black phosphorus (3) Dispersion containing black phosphorus powder (4) Ultrasonication of the solution (5) Ultracentrifugation

As a result, how to choose a mild liquid system for dispersion of the target materials is a critical component in the methodology's efficacy. Before we arrive at an efficient and scalable sonication

system, numerous aspects such as sonication time and surface tension should be addressed. More details into the matter are discussed in the next section (Solubility theory).

Brent et al.[155] were the first to generate liquid-exfoliated BP flakes in NMP solution, where BP flakes with more than two layers can be generated using a one-step ultrasonication technique. Since then, BP flakes have been made in a variety of solvents, including hexane, IPA, methanol, ethanol, acetone, THF, chloroform, NMF, DCB, CHP, NVP, DMSO, formamide, and water.[162,179,180,181,182,183] Drop-casting BP solution onto a transmission electron microscopy (TEM) copper grid can be used to determine the thickness of liquid-exfoliated BP flakes down to 0.52 nm.[184] Formamide has been reported to have the greatest known BP exfoliation yield in solvents, reaching 38% efficiency, and the concentration of BP flakes in each solvent can be ranked in the following descending order: Formamide > DMSO > DMF-NMP-IPA > ethanol-methanol > acetone-THF-DI water.

According to Beer-Lambert law $A/l = \alpha C$, where A is the absorbance intensity, l is the cell length, α is the extinction coefficient, and C is the concentration, (A scales linearly with C for minor dispersions in ethanol). The concentration of BP in solvents may be estimated by extracting information from UV–vis–NIR absorption spectra. When comparing the surface tension of different solvents with the concentration of BP, it was found that the BP exfoliation yield increases monotonically with the increase in surface tension, which is comparable to the situation in graphene and TMD exfoliation.[185,186]

Conventional organic solvents, on the other hand, are hazardous to the environment, and it's difficult to entirely separate the synthesized chemicals from the solvents. As a result, green ionic liquids were developed as organic solvent alternatives.[187,188,189] Exfoliated BP in water or water-dispersed solvents are more sensitive to ambient O_2 and H_2O than anhydrous organic solvents or ionic liquids; deoxygenated water must be used in conjunction with ultrapure inert-gas-evacuated vacuum-based chambers to prevent BP deterioration. Furthermore, surfactant-mediated liquid-phase exfoliation can successfully prevent the flakes from oxidizing, resulting in monolayer BPNSs that are stable for several weeks.[183] The success of an exfoliation treatment is determined by a variety of other elements, many of which are application-specific. The thickness, lateral dimensions, size dispersity, crystal quality, and stability of the nanosheets produced must all be taken into account, as well as the solvent's compatibility with the intended production processes and applications. Furthermore, the solvent's cost and toxicity are crucial considerations to consider.

Using techniques like AFM and XPS, it has been discovered that LPE of BP is significantly more stable than mechanically exfoliated material. Exfoliation solvents and ligands are expected to play a role in preserving exfoliated flakes. The fact that LPE flakes are coated in a layer of organic molecules is not entirely advantageous, because current must pass across flake boundaries, which is hampered by insulating organic; ligands, for example, in situations requiring high electron mobility, LPE material is likely to perform worse than mechanically exfoliated material. However, LPE flakes appear to be well suited for a variety of additional applications, including sensors and polymer composites.

IV.2.3. Solvothermal assisted Liquid phase exfoliation

Exfoliation procedures such as mechanical and liquid exfoliation, as discussed above, are now the most extensively utilized "top-down" ways for the preparation of few-layer BP nanosheets.[170,190, 191] In fact, the fabrication of BP nanosheets is complex since it requires a two-step synthesis procedure in which bulk BP crystals are generated first, followed by exfoliation of bulk BP to BP nanosheets. Furthermore, by exfoliation procedures, scalable manufacture of few-layer BP nanosheets with acceptable durability remains a difficulty, limiting the widespread research and applications of few-layer BP nanosheets. Furthermore, by exfoliation procedures, scalable manufacture of few-layer BP nanosheets with acceptable durability remains a difficulty, limiting the widespread research and applications of few-layer BP nanosheets. Tian and colleagues recently reported the wet-chemical preparation of few-layer BP nanosheets in gray-scale quantities using a "bottom-up" solvothermal synthesis approach at 140 °C, achieving the direct transformation of white phosphorus to BP nanosheets via a one-step synthesis process under mild conditions.[170] The solvent component as well as the reaction temperature are important parameters in determining the thickness of BP nanosheets. The as-prepared BP nanosheets had a typical 2D structure with a size of 800–1000 nm, which is advantageous for photocatalysis, electrocatalysis, and photoelectronic devices. Furthermore, the findings revealed that partial oxidation of the surface of BP nanosheets improves their stability, while the mechanism for this improvement is still unknown. This method allows for the creation of few-layer BP nanosheets in a simple, scalable, and low-cost manner, which is particularly useful for the study and practical application of BP nanosheets. In addition to that, the solvothermal assisted LPE was also found to be efficient to prepare QD of BP with a uniform size distribution and exhibiting excellent biocompatibility and conversion of NIR light into heat, hence its suitability for cancer treatment applications.[192] The

solvothermal LPE used to synthesize BPQD is described by the schematic below (Further details are given in Chapter V).

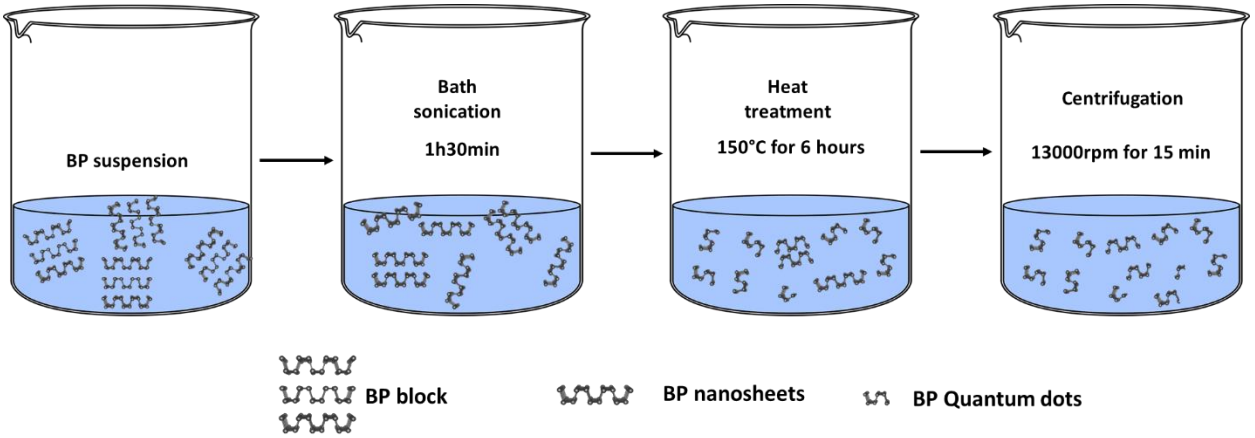

Figure 38. Schematic of the synthesis process to prepare. A batch sonication is initially performed to separate the BP flakes into nanosheets, followed by a heat treatment used to break the sheets borders, thus giving BPQD's. Finally, centrifugation is used to separate the BP flakes into nanosheets, followed by a heat treatment used to break the sheets borders, thus giving BPQD's. Finally, centrifugation is used to separate BP nanosheets from BPQD.

IV.2.4. Solubility theory

For a better understanding of the solvent parameters used in liquid phase exfoliation and solvothermal exfoliation, a theoretical study of the solvent's parameters is to be considered. A solid, liquid, or gas has a property called solubility. There has been a lot of study done on polymer solubility theory, particularly on the development of solubility parameters. Solubility parameters are based on a thermodynamic model that uses vaporization energy to account for molecular interactions. To capture the chemistry of mixing using a solubility parameter, Hildebrand and Hansen created two theories,[193,194] the first of which was developed by Hildebrand and the second by Hansen. From solubility screening to chemical resistance, solubility parameters are employed in a variety of applications. Solubility criteria have previously been used to examine the solubility of nanomaterials in various solvents, and not all solvents, for example, can produce a stable dispersion.[195,196] The surface energies of the nanomaterial and the solvent must be properly matched. A mismatch of parameters might cause rapid aggregation and, eventually, sedimentation of the nanomaterial. As a result, it's critical to comprehend the chemical interaction between the solvent and the nanosheets. In terms of solubility parameters and surface energies, the following subsections examine the interaction between solvents and nanosheets.[197]

a. Solution thermodynamics

Mechanical exfoliation is a well-known method for generating nanosheets, although it is a time-consuming and labor-intensive procedure. Nanomaterials are used in applications such as mechanical reinforcement and batteries, and this necessitates a technology that can manufacture huge amounts of material. Liquid-based production technologies appear to be the most promising for meeting these stringent requirements. Liquid phase exfoliation (LPE) is a sonication-based solution-based technique for exfoliating multilayer materials. Organic solvents are commonly used for sonication. Solubility theory is examined in order to create a stable dispersion of nanosheets in a solvent. Solution thermodynamics governs the change in entropy ($\Delta\bar{S}_{mix}$) and enthalpy ($\Delta\bar{H}_{mix}$) of a system when two or more chemical substances are mixed. The fundamental principle of Gibbs free energy, as shown below, can be used to characterize this interaction:[198]

$$\Delta\bar{G}_{mix} = \Delta\bar{H}_{mix} - \mathrm{T}\Delta\bar{S}_{mix} \qquad (19)$$

Enthalpy ($\Delta\bar{H}_{mix}$), temperature (T), and entropy ($\Delta\bar{S}_{mix}$) all affect the Gibbs free energy of mixing ($\Delta\bar{G}_{mix}$). The Gibbs free energy must be negative in order to achieve a viable dispersion, i.e., dissolution. Large (positive) amounts of entropy are advantageous in an ideal situation for ensuring stability. However, because two-dimensional nanosheets like graphene and phosphorene are large and rigid, their entropy is low.[165] As a result, minimizing $\Delta\bar{H}_{mix}$ is favorable for producing a feasible dispersion. It is not sufficient to consider solely the interaction between the solute and the solvent when studying the thermodynamics of mixing; the solute-solute and solvent-solvent interactions are equally relevant.

"Like dissolves like" is a frequent rule of thumb in chemical solubility. There is a chemical contact between atoms and molecules in a liquid or solid. The bonds between nearest neighbors must be disrupted to obtain solubility of a solid in a liquid. Energy must be provided in order to accomplish this. The vaporization energy is the entire amount of energy required to fully separate these molecules. The van der Waals energy that holds the molecules together is represented by this energy. The vaporization energy is used to calculate solubility parameters, which are related to the solvent's cohesive energy. By extension, the cohesive energy represents the van der Waals energy between molecules in a solvent. In order to adequately describe the system, Hildebrand proposed a solubility parameter. This parameter is defined as the square root of the cohesive energy density and is represented by the symbol $\delta = \sqrt{E/V}$ (where E is the energy and V is the solvent molar

volume). The Hildebrand-Scratchard equation can be calculated for small compounds using these solubility constants as follows:

$$\frac{\Delta \bar{H}_{mix}}{V_{mix}} \approx \phi(1-\phi).(\delta_a - \delta_b)^2 \quad (20)$$

The enthalpy of mixing ($\Delta \bar{H}_{mix}$) is calculated using Hildebrand solubility parameters (a, b for the solvent and solute, respectively) and the solvent volume fraction. Although this is an approximate statement due to the approximations used in its derivation, it does not negate the equation's underlying power. The expression clearly demonstrates that matching the solubility parameters, *a* and *b*, reduces the mixing enthalpy.

We get an expression that accounts for intermolecular pairwise interactions by relating the Flory-Huggins parameter to $\Delta \bar{H}_{mix}$.[199]

$$\frac{\Delta \bar{H}_{mix}}{V_{mix}} = \frac{\chi \phi(1-\phi)kT}{\mathrm{v}_0} \quad (21)$$

Where, v_0 is the solvent molecular volume and ϕ is the solvent volume fraction. The Flory-Huggins parameter was designed for polymer systems, but it may be used to govern the dispersion of our nanomaterial as well. A high value suggests a repulsive solute-solvent interaction and, as a result, a high positive enthalpy of mixing, which might delay the solution process if it is large enough. A negative also signifies an attractive interaction, which results in a negative enthalpy of mixing, which ensures disintegration. The Flory-Huggins parameter (χ) has been used to account for intermolecular pairwise interactions. It's possible to express it in terms of the system's cohesive energy interactions. The Flory-Huggins parameter can be expressed as follows for non-polar solvents:

$$\chi \approx \frac{\mathrm{v}_0}{kT}(\delta_a - \delta_b) \quad (22)$$

When using polar solvents, a correction term is required; however, it is obvious that matching the solvent and nanosheet solubility characteristics reduces the mixing enthalpy. These nanosheet/solvent interactions can be better understood using Flory-Huggins theory.

The interaction of a particle in a solvent may be accurately described using this thermodynamic solubility theory. As previously demonstrated, careful matching of solubility parameters can be employed to generate a stable dispersion devoid of aggregation effects. This theory's application to CNT or 2D nanosheets has been entirely empirical.

An equation that appropriately reflect the enthalpy of mixing for 2D nanosheet was developed in this group's previous work.[159,164,196] The aforementioned theory, which accounts for pairwise interactions as well as the surface energy parameters for solutes and solvents, is included in this derivation. The energy necessary to separate all of the nanomaterial layers and solvent molecules was calculated. This formula yields an expression that describes the energy cost of mixing per unit volume. The aforementioned theory, which accounts for pairwise interactions as well as the surface energy parameters for solutes and solvents, is included in this derivation. The energy necessary to separate all of the nanomaterial layers and solvent molecules was calculated. This formula yields an equation that describes the energy cost of mixing per unit volume.[193]

$$\frac{\Delta \bar{H}_{mix}}{V_{mix}} = \frac{2}{T_{flake}} . (\partial_{nanosheet} - \partial_{solvent})^2 \qquad (23)$$

T_{flake} is the thickness of a nanosheet, $\partial_a = \sqrt{E_{sur}^a}$ is the square root of the surface energy related to phase "*a*," and $\phi = V_{nanosheet}/V_{mix}$ is the volume fraction of nanosheets. As a result of equation (13), solvents with a surface energy similar to that of a nanomaterial have a high likelihood of solubility.

b. Solvent solubility parameters

The interactions between solvent molecules and solutes (nanosheets) can be described using Hildebrand solubility parameters above. However, Charles Hansen identified some short comings with the approach, only dispersive forces are considered. There are several types of interactions between solvent molecules and nanosheets. The most important interactions can be described using the dispersive force (non-polar, E_D), polar cohesive energy (E_P) and hydrogen bonding (E_H). The sum of these interactions represents the total cohesive energy (E),

$$E = E_D + E_P + E_H \quad (24)$$

Cohesive energies of larger molecules are higher; hence they must be scaled by volume (V). A Hansen solubility parameter (HSP) is defined as the square root of the corresponding cohesion energy divided by the molecular volume ($\delta = \sqrt{E/V}$).[197] The sum of the squares of each separate Hansen solubility parameter is the Hildebrand solubility parameter.

$$\delta^2 = \delta_D^2 + \delta_P^2 + \delta_H^2 \qquad (25)$$

The Flory-Huggins parameters can be expressed as:

$$\chi \approx \frac{v_0}{kT}\left[(\delta_{D,A} - \delta_{D,B})^2 + (\delta_{P,A} - \delta_{P,B})^2 + (\delta_{H,A} - \delta_{H,B})^2\right] \qquad (26)$$

HSPs are well-known for a variety of solvents and are crucial when determining solubility. It is obvious that matching this solvent and nanosheet properties selectively will reduce $(\delta_a - \delta_b)^2$. The greater the possibility of solubility, the closer a solvent and nanosheet are in terms of their dispersive, polar, and hydrogen bonding energies. The application of solubility parameters is appealing; unfortunately, it is not always successful. Complete solubility is attained when the energies of two substances are perfectly matched. Nonetheless, this method gives a reliable model for predicting nanomaterial solubility in various solvents; as such it will be used to evaluate a series of solvents used to exfoliate black phosphorus.

IV.3. Simulation details

IV.3.1. Molecular dynamics simulation:

In the present thesis, all calculations were performed using LAMMPS molecular dynamics[200] and COLVARS packages.[201] Our models constructed using PACKMOL code[202] and visualized with OVITO,[203] consist of BP layers impregnated in a box filled with a given solvent. For the force field representing the inter-atomic interactions, we manually included the solvent's interatomic potential using the OPLS-AA force field,[204] while for the phosphorene's potential we used a Lennard-Jones (L-J) force field.**[160]** The advantage of the (L-J) potential is the built in ($1/r^3$) long range interaction necessary to represent the BP inter-layers interactions.

For the exfoliation process, BP (a stack of four phosphorene sheets) was first placed in a solvent molecules box. In this simulation, we "peeled off" the first top layer of BP. The potential of mean force (PMF) of exfoliation (related to the amount of reversible work required to exfoliate)[205-160] was calculated using the umbrella sampling and the weighed histogram analysis method (WHAM)[206] with a convergence tolerance of 10^{-5} kcal/mol. The coordinates related to the inter-sheet separation were sampled between 4Å and 16Å with steps of 0.25Å. At each step the system was allowed to relax in the NPT ensemble for 100ps for a total of 5 ns, this allowed good sampling of the histogram at each step. The cut-off used for both L-J and Coulomb potential was 12nm with a timestep of 2fs. Coulombic interactions were handled by the PPPM method (particle-particle particle-mesh) with a 10^{-5} Kcal/mole tolerance.[207] Hydrogen bonds were constrained by SHAKE algorithm also implemented in LAMMPS. These configurations were first equilibrated at constant temperature of 300K in the canonical ensemble NVT (N: constant number of atoms, V: volume and T: temperature) with a relaxation time of 1ps for a total simulation time of 1 ns. Followed by a total of 4 ns in the NPT (P: pressure) ensemble for each simulation. Temperature of

300 K and pressure of 1 bar was maintained constant with a Nose-Hoover thermostat with 2 ps time constant and a barostat with 5 ps time constant.

For the molecular behavior at the interface with phosphorene, one phosphorene sheet was first impregnated in a simulation box filled with molecules of a given solvent. The time step used during this simulation is 2 fs and the cut-off energy used was 12 nm. The calculation was run for 5ns in the canonical NVT ensemble.

For the re-aggregation process calculations, we simulated a two parallel phosphorene sheets box, surrounded by solvent molecules. During this simulation the two phosphorene sheets were attracted toward each other in similar conditions as those used for the above exfoliation process.

IV.3.2. OPLS-AA Potential parameters for molecules:

In this section, we will summarize the potential parameters (L-J parameters, charges, bonds and angles parameters) extracted and calculated from the OPLS-AA data file, which were used afterwards for all the upcoming results.

IV.3.2.1. Benzonitrile

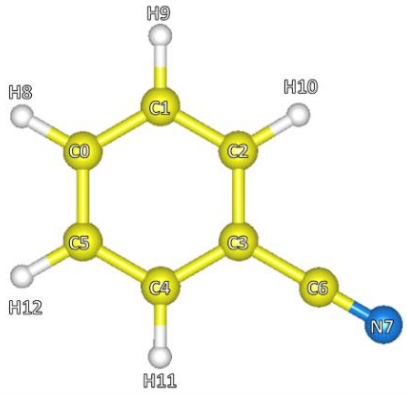

Lennard-Jones parameters and partial charges for BN.

Atom	q (e^-)	σ (Å)	ε (kCal/mol)
C0	-0.115	3.55	0.070
C1	-0.115	3.55	0.070
C2	-0.115	3.55	0.070
C3	0.135	3.55	0.070
C4	-0.115	3.55	0.070
C5	-0.115	3.55	0.070
C6	0.395	3.65	0.150
N7	-0.430	3.20	0.170
H8	0.115	2.42	0.030
H9	0.115	2.42	0.030
H10	0.115	2.42	0.030

H11	0.115	2.42	0.030
H12	0.115	2.42	0.030

Bond Stretching Parameters for BN.

Atom		K_r (kCal/mol. Å^{-2})	r_{eq} (Å)
C0	C1	469.0	1.4000
C0	C5	469.0	1.4000
C0	H8	367.0	1.0800
C1	C2	469.0	1.4000
C1	H9	367.0	1.0800
C2	C3	469.0	1.4000
C2	H10	367.0	1.0800
C3	C4	469.0	1.4000
C3	C6	400.0	1.4510
C4	C5	469.0	1.4000
C4	H11	367.0	1.0800
C5	H12	367.0	1.0800
C6	N7	650.0	1.1570

Angle Bending Parameters for BN.

Atom			K_θ (kCal/mol.rad^{-2})	θ_{eq}
C0	C1	C2	63.00	120.00
C0	C1	H9	35.00	120.00
C0	C5	C4	63.00	120.00
C0	C5	H1	35.00	120.00
C1	C0	C5	63.00	120.00
C1	C0	H8	35.00	120.00
C1	C2	C3	63.00	120.00
C1	C0	H1	35.00	120.00
C2	C3	C4	63.00	120.00
C2	C3	C6	70.00	120.00
C3	C2	H1	35.00	120.00
C3	C4	C5	63.00	120.00
C3	C4	H1	35.00	120.00
C3	C6	N7	150.00	180.00
C4	C3	C6	70.00	120.00
C4	C5	H1	35.00	120.00
C5	C0	H8	35.00	120.00
C5	C4	H1	35.00	120.00
C2	C3	H1	37.50	110.70

IV.3.2.2. Dimethyl Formamide (DMF)

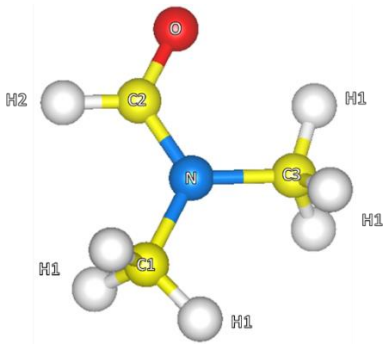

Lennard-Jones parameters and partial charges for DMF.

Atom	q (e^-)	σ (Å)	ε (kCal/mol)
C1	-0.11	3.50	0.0660
C2	0.50	3.75	0.1049
H1	0.06	2.50	0.0300
H2	0.00	2.42	0.0150
N	-0.14	3.25	0.1700
O	-0.50	2.96	0.2100

Bond Stretching Parameters for DMF.

Atom	K_r (kCal/mol. $Å^{-2}$)	r_{eq} (Å)
C0 C5 H12	35.00	120.00
C1 C0 C5	63.00	120.00
C1 C0 H8	35.00	120.00
C1 C2 C3	63.00	120.00
C1 C0 H10	35.00	120.00
C2 C3 C4	63.00	120.00
C2 C3 C6	70.00	120.00
C3 C2 H10	35.00	120.00
C3 C4 C5	63.00	120.00
C3 C4 H11	35.00	120.00
C3 C6 N7	150.00	180.00
C4 C3 C6	70.00	120.00
C4 C5 H12	35.00	120.00
C5 C0 H8	35.00	120.00
C5 C4 H11	35.00	120.00
C2 C3 H12	37.50	110.70

Angle Bending Parameters for DMF.

Atom	K_θ (kCal/mol.rad^{-2})	θ_{eq}
C1 N C1	50.00	118.00

C1	N	C2	50.00	121.90
H1	C1	H1	33.00	107.80
H1	C1	N	35.00	109.50
H2	C2	N	40.00	114.00
H2	C2	O	35.00	123.00
N	C2	O	80.00	122.90

IV.3.2.3. 1-Vinyl-2-pyrrolidinone (NVP)

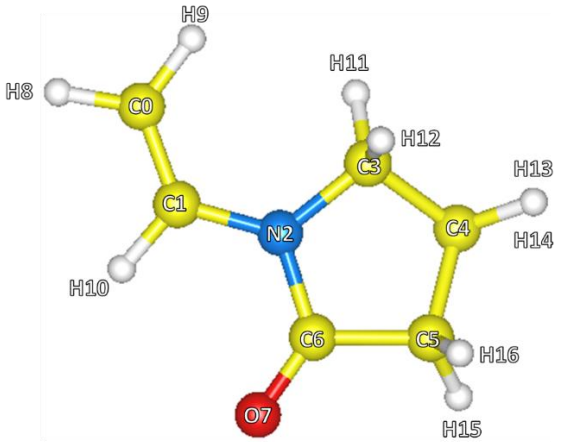

Lennard-Jones parameters and partial charges for NVP.

Atom	q (e^-)	σ (Å)	ε (kCal/mol)
C0	-0.060	3.50	0.066
C1	-0.050	3.50	0.066
N2	-0.140	3.50	0.066
C3	-0.050	3.50	0.066
C4	-0.120	3.50	0.066
C5	-0.120	3.50	0.066
C6	0.500	3.75	0.105
O7	-0.500	2.96	0.210
H8	0.060	2.50	0.030
H9	0.060	2.50	0.030
H10	0.060	2.50	0.030
H11	0.060	2.50	0.030
H12	0.060	2.50	0.030
H13	0.060	2.50	0.030
H14	0.060	2.50	0.030
H15	0.060	2.50	0.030
H16	0.060	2.50	0.030

Bond Stretching Parameters for NVP.

Atom		K_r (kCal/mol. $Å^{-2}$)	r_{eq} (Å)
C0	C1	549.0	1.3400
C0	H8	340.0	1.0800
C0	H9	340.0	1.0800
C1	H10	340.0	1.0800

C1	N2	448.0	1.3650
C3	C4	268.0	1.5290
C3	H11	340.0	1.0900
C3	H12	340.0	1.0900
C4	H13	340.0	1.0900
C4	H14	340.0	1.0900
C5	C6	317.0	1.5220
C5	H15	340.0	1.0900
C5	H16	340.0	1.0900
C6	N2	418.0	1.3880
C6	O7	570.0	1.2290

Angle Bending Parameters for NVP.

Atom			K_θ (kCal/mol.rad^{-2})	θ_{eq}
C0	C1	H10	35.00	120.00
C0	C1	N2	70.00	121.00
C1	C0	H8	35.00	120.00
C1	C0	H9	35.00	120.00
C1	N2	C3	63.00	112.40
C1	N2	C6	70.00	121.60
C3	C4	C5	58.35	112.70
C3	C4	H13	37.50	110.70
C3	C4	H14	37.50	110.70
C3	N2	C6	63.00	112.40
C4	C3	H11	37.50	110.70
C4	C3	H12	37.50	110.70
C4	C3	N2	51.65	110.58
C4	C5	C6	63.00	111.10
C4	C5	H15	37.50	110.70
C4	C5	H16	37.50	110.70
C5	C4	H13	37.50	110.70
C5	C4	H14	37.50	110.70
C5	C6	N2	69.90	118.18
C5	C6	O7	80.00	120.40
C6	C5	H15	35.00	109.50
C6	C5	H16	35.00	109.50
H8	C0	H9	35.00	117.00
H10	C3	H12	35.00	119.10
H11	C3	H14	33.00	107.80
H11	C3	N2	35.00	109.50
H12	C3	N2	35.00	109.50
H13	C4	H14	33.00	107.80
H15	C5	H16	33.00	108.80
N2	C6	O7	80.00	120.60

IV.3.2.4. N-Methyl-pyrrolidinone (NMP)

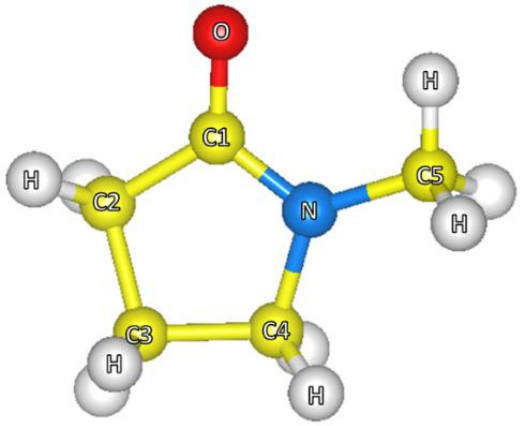

Lennard-Jones parameters and partial charges for NMP.

Atom	q (e^-)	σ (Å)	ε (kCal/mol)
C1	-0.05	3.50	0.066
C2	-0.12	3.50	0.066
C3	-0.12	3.50	0.066
C4	0.5	3.75	0.105
N	-0.14	3.25	0.170
C5	-0.11	3.50	0.066
O	-0.5	2.96	0.210
H	0.06	2.50	0.030

Bond Stretching Parameters for NMP.

Atom		K_r (kCal/mol. $Å^{-2}$)	r_{eq} (Å)
C1	C2	268.0	1.5290
C2	C3	268.0	1.5290
C1	N	337.0	1.4490
N	C5	337.0	1.4490
C	H	340.0	1.0900
C3	C4	317.0	1.5220
C4	N	490.0	1.3350
C4	O	570.0	1.2290

Angle Bending Parameters for NMP.

Atom			K_θ (kCal/mol.rad^{-2})	θ_{eq}
C2	C1	N	80.00	109.70
N	C1	H	35.00	109.50
H	C1	H	33.00	107.80
C1	C2	C3	58.35	112.70
C2	C3	C4	63.00	111.10
C4	C3	H	35.00	109.50

C4	C3	H	35.00	109.50
C3	C4	N	70.00	116.60
C3	C4	O	80.00	120.40
N	C4	O	80.00	122.90
C4	N	C5	50.00	121.90
C2	C3	H	37.50	110.70

IV.3.2.5. 1,3-dimethyl-2-imidazolidinone (DMI)

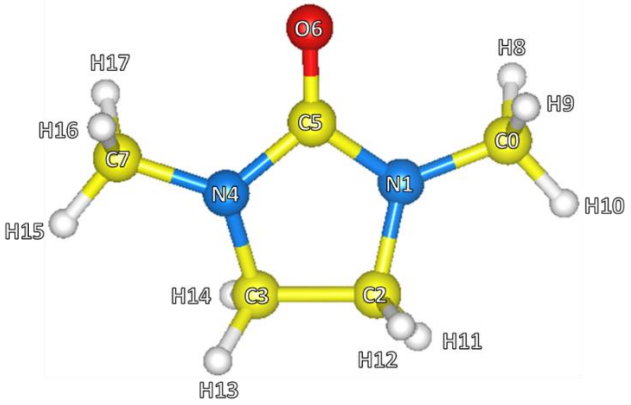

Lennard-Jones parameters and partial charges for DMI.

Atom	q (e^-)	σ (Å)	ε (kCal/mol)
C0	-0.110	3.50	0.066
N1	-0.140	3.25	0.170
C2	-0.050	3.50	0.066
C3	-0.050	3.50	0.066
N4	-0.140	3.25	0.170
C5	0.500	3.75	0.105
O6	-0.500	2.96	0.210
C7	-0.110	3.50	0.066
H8	0.060	2.50	0.030
H9	0.060	2.50	0.030
H10	0.060	2.50	0.030
H11	0.060	2.50	0.030
H12	0.060	2.50	0.030
H13	0.060	2.50	0.030
H14	0.060	2.50	0.030
H15	0.060	2.50	0.030
H16	0.060	2.50	0.030
H17	0.060	2.50	0.030

Bond Stretching Parameters for DMI.

Atom		K_r (kCal/mol. $Å^{-2}$)	r_{eq} (Å)
C0	H8	340.0	1.0900
C0	H9	340.0	1.0900
C0	H10	340.0	1.0900
C0	N1	337.0	1.4490

C2	C3	268.0	1.5290
C2	H11	340.0	1.0900
C2	H12	340.0	1.0900
C2	N1	337.0	1.4490
C3	H13	340.0	1.0900
C3	H14	340.0	1.0900
C3	N4	337.0	1.4490
C5	N1	490.0	1.3350
C5	N4	490.0	1.3350
C5	O6	570.0	1.2290
C7	H15	340.0	1.0900
C7	H16	340.0	1.0900
C7	H17	340.0	1.0900
C7	N4	337.0	1.4490

Angle Bending Parameters for DMI.

Atom			K_θ (kCal/mol.rad^{-2})	θ_{eq}
C0	N1	C1	50.00	118.00
C0	N1	C5	50.00	121.90
C2	C3	H13	37.50	110.70
C2	C3	H14	37.50	110.70
C2	C3	N4	80.00	109.70
C2	N1	C5	50.00	121.90
C3	C2	H11	37.50	110.70
C3	C2	H12	37.50	110.70
C3	C2	N1	80.00	109.70
C3	N4	C5	50.00	121.90
C3	N4	C7	50.00	118.00
C5	N4	C7	50.00	121.90
H8	C0	H9	33.00	107.80
H8	C0	H10	33.00	107.80
H8	C0	N1	35.00	109.50
H9	C0	H10	33.00	107.80
H9	C0	N1	35.00	109.50
H10	C0	N1	35.00	109.50
H11	C2	H12	33.00	107.80
H11	C2	N1	35.00	109.50
H12	C2	N1	35.00	109.50
H13	C3	H14	33.00	107.80
H13	C3	N4	35.00	109.50
H14	C3	N4	35.00	109.50
H15	C7	H16	33.00	107.80
H15	C7	H17	33.00	107.80
H15	C4	N4	35.00	109.50
H16	C7	H17	33.00	107.80
H16	C7	N4	35.00	109.50
H17	C7	N4	35.00	109.50
N1	C5	N4	70.00	114.20
N1	C5	O6	80.00	122.90
N4	C5	O6	80.00	122.90

IV.3.2.6. Isopropanol (IPA)

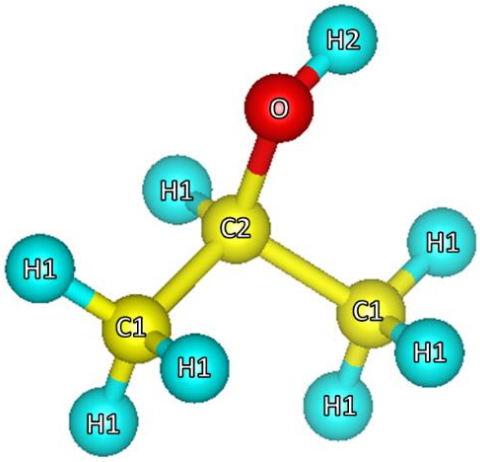

Lennard-Jones parameters and partial charges for IPA.

Atom	q (e^-)	σ (Å)	ε (kCal/mol)
C1	-0.180	3.50	0.066
C2	-0.205	3.50	0.066
H1	0.060	2.50	0.030
H2	0.418	0.00	0.000
O	-0.683	3.12	0.170

Bond Stretching Parameters for IPA.

Atom		K_r (kCal/mol. $Å^{-2}$)	r_{eq} (Å)
C1	C2	268.0	1.5290
C1	H1	340.0	1.0900
C2	H1	340.0	1.0900
C2	O	320.0	1.4100
H2	O	553.0	0.9450

Angle Bending Parameters for IPA.

Atom			K_θ (kCal/mol.rad^{-2})	θ_{eq}
C1	C2	C1	58.35	112.70
C1	C2	H1	37.50	110.70
C1	C2	O	50.00	109.50
C2	C1	H1	37.00	110.70
C2	O	H2	55.00	108.50
H1	C1	H1	33.00	107.80
C1	C2	O	35.00	109.50

IV.3.2.7. Dimethyl sulfoxide (DMSO)

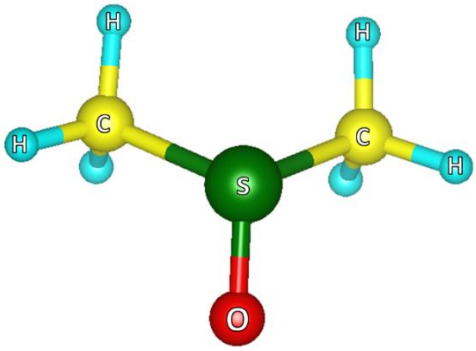

Lennard-Jones parameters and partial charges for DMSO.

Atom	σ (Å)	ε (kCal/mol)	q (e^-)
S	3.4	0.23	0.139
O	2.8	0.07	-0.459
CH_3	3.8	0.29	0.160

Bond stretching and angle-bending parameters for DMSO

Atom numbers		K_r (kcal/mol. $Å^{-2}$)	r_{eq} (Å)
S	O	600.0	1.5290
S	CH_3	399.1	1.800

Atom numbers		K_θ (kCal/mol.rad^{-2})	θ_{eq} (Å)
S	O	200.7	97.4
S	CH_3	95.3	106.75

IV.3.2.8. N-Cyclohexyl-2-Pyrrolidone (CHP)

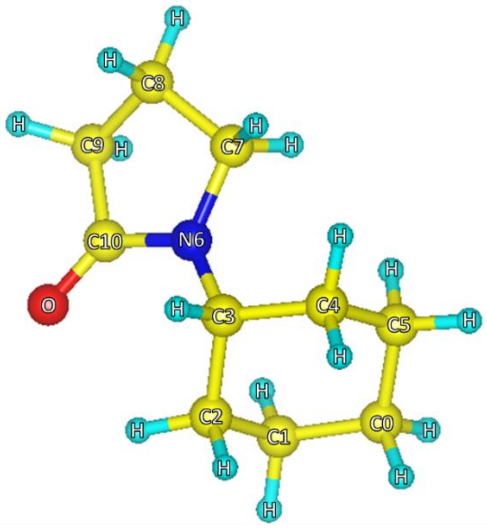

Lennard-Jones parameters and partial charges for CHP.

Atom	q (e^-)	σ (Å)	ε (kCal/mol)
C0	-0.12	3.50	0.066
C1	-0.12	3.50	0.066
C2	-0.12	3.50	0.066
C3	0.01	3.50	0.066
C4	-0.12	3.50	0.066
C5	-0.12	3.50	0.066
N6	-0.14	3.25	0.170
C7	-0.05	3.50	0.066
C8	-0.12	3.50	0.066
C9	-0.12	3.50	0.066
C10	0.50	3.55	0.070
O	-0.50	2.96	0.210
H	0.06	2.50	0.030

Bond Stretching Parameters

Atom		K_r (kCal/mol. $Å^{-2}$)	r_{eq} (Å)
C0	C1	268.0	1.5290
C0	C5	268.0	1.5290
C0	H	340.0	1.0900
C1	C2	268.0	1.5290
C1	H	340.0	1.0900
C2	C3	268.0	1.5290
C2	H	340.0	1.0900
C3	C4	268.0	1.5290
C3	H	340.0	1.0900
C3	N6	337.0	1.4490
C4	C5	268.0	1.5290
C4	H	340.0	1.0900

C5	H	340.0	1.0900
C7	C8	268.0	1.5290
C7	H	340.0	1.0900
C7	N6	337.0	1.4490
C8	C9	268.0	1.5290
C8	H	340.0	1.0900
C9	C10	317.0	1.5520
C9	H	340.0	1.0900
C10	N6	490.0	1.3350
C10	O	570.0	1.2290

Angle Bending Parameters for CHP.

Atom			K_θ (kCal/mol.rad^{-2})	θ_{eq}
C0	C1	C2	58.350	112.70
C0	C1	H	37.500	110.70
C0	C5	C4	58.350	112.70
C0	C5	H	37.500	110.70
C1	C0	C5	58.350	112.70
C1	C0	H	37.500	110.70
C1	C2	C3	58.350	112.70
C1	C2	H	37.500	110.70
C2	C1	H	37.500	110.70
C2	C3	C4	58.350	112.70
C2	C3	H	37.500	110.70
C2	C3	N6	80.000	109.70
C3	C2	H	37.500	110.70
C3	C4	C5	58.350	112.70
C3	C4	H	37.500	110.70
C3	N6	C7	50.000	118.00
C3	N6	C10	50.000	121.90
C4	C3	H	37.500	110.70
C4	C3	N6	80.000	109.70
C4	C5	H	37.500	110.70
C5	C0	H	37.500	110.70
C5	C4	H	37.500	110.70
C7	C8	N9	58.350	112.70
C7	C8	H	37.500	110.70
C7	N6	C10	50.000	121.90
C8	C7	H	37.500	110.70
C8	C9	C10	63.000	111.10
C8	C9	H	37.500	110.70
C9	C8	H	37.500	110.70
C9	C10	N6	70.000	116.60
C9	C10	O	80.000	120.40

IV.3.3. Lennard-Jones potential for black phosphorus:

For Black phosphorus and phosphorene, a simple Lennard-Jones potential was used, as it was found to well agree with experimental lattice dimensions as well as experimental elastic constants.[160] The parameters used for BP potential are shown in the table below.

Parameter	Value
q	0.0
σ (Å)	3.33
ε (kCal/mol)	0.50
K_r (kCal/mol. $Å^{-2}$)	411.09
r_{eq} (Å)	2.225
K_θ (kCal/mol.rad^{-2})	112.52
θ_{eq}	96.4

Furthermore, a combining rule was used in order to calculate the potential parameter between solvent atoms and between solvent atoms and the phosphorus. These interactions were calculated by employing the geometric averaging rule: $\varepsilon_{ij} = \sqrt{\varepsilon_{ii}\varepsilon_{jj}}$ and $\sigma_{ij} = \frac{\sigma_{ii}+\sigma_{jj}}{2}$.

IV.4. Results and discussion:

IV.4.1. Solvent intrinsic process:

In the present study, MD simulations are focused on understanding the parameters that govern the BP exfoliation/re-aggregation mechanism. For such a purpose, eight solvents were used, the intrinsic physical properties, namely: Hildebrand solubility parameter, polarity and morphology, of which are presented in Table 6. The choice of these different solvents was primarily based on the closeness of their Hildebrand solubility parameter to that of BP (~21 $MPa^{1/2}$).[158] As noticed, all solvents are polar aprotic (lack O-H or N-H bond to avoid participation in hydrogen bonding) except for IPA which is polar protic (the latter was selected to check the role of hydrogen bonding during the LPE process as it was recently stated that degradation of BP is enhanced in polar protic solvents).[208]

Table 6. Intrinsic properties of molecules. Color scheme: yellow, carbon; red, oxygen; Blue, nitrogen; cyan, hydrogen; Green, sulfur.

Solvent	Hildebrand solubility parameter ($MPa^{1/2}$)	Size (Number of atoms)	Polarity	Morphology
BZ	22.5	13	Polar aprotic	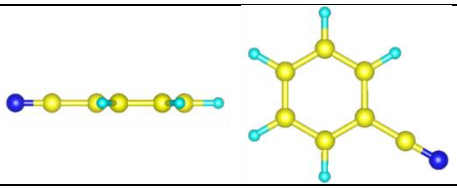
DMF	24.9	12	Polar aprotic	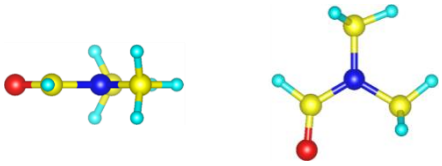
NVP	19.8	17	Polar aprotic	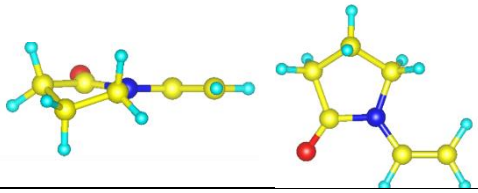
NMP	23	16	Polar aprotic	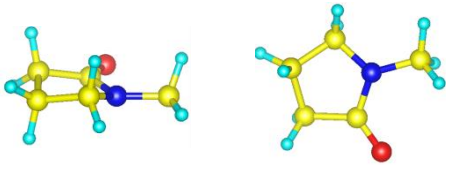
DMI	23	18	Polar aprotic	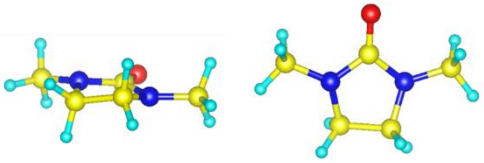
DMSO	26.7	10	Polar aprotic	
IPA	23.6	12	Polar protic	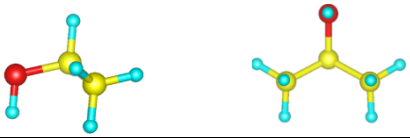
CHP	20.5	29	Polar aprotic	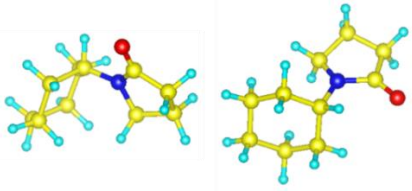

In order to classify these solvents, a planarity parameter denoted as ‘δ’ was first measured considering the *thickness* of the molecule when crashed between two flat surfaces. Fig. 39 gives an overview of such a δ parameter resulting in a classification from a zero-value corresponding to BZ (a fully planar molecule) to a value of 2.14 Å corresponding to the CHP molecule where the δ parameter has significantly increased because of the presence of two perpendicular aromatic cycles in its structure. This classification will be very useful to better understand our MD simulations of the BP exfoliation/re-aggregation mechanism that are divided in two parts. Modelling of BP exfoliation process is treated first, followed by that of re-aggregation.

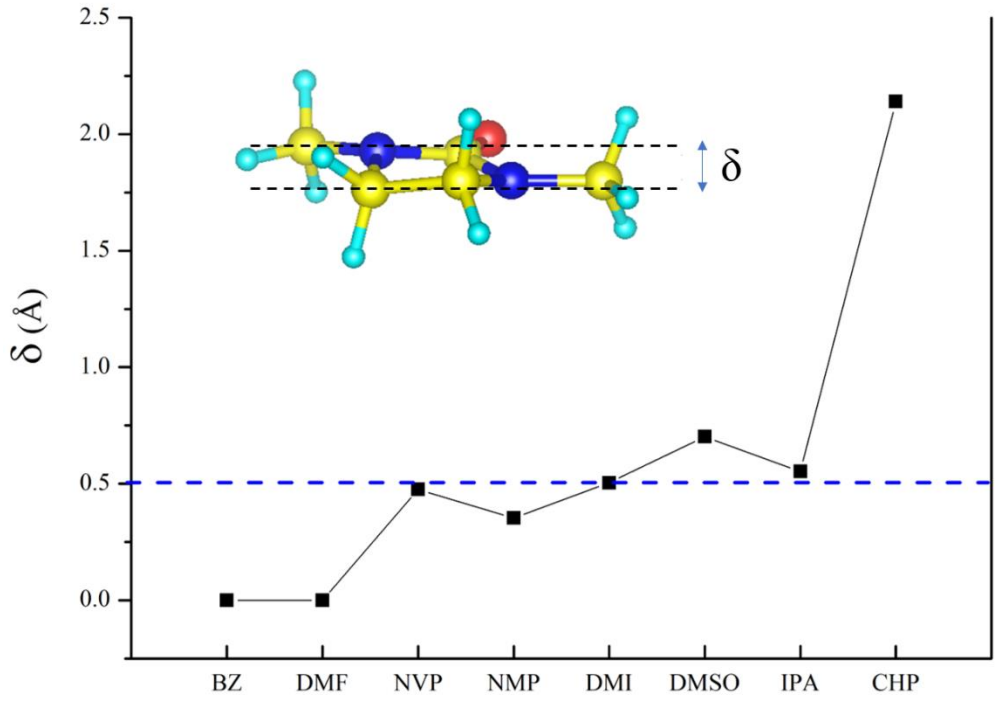

Figure 39. The “δ” parameter measured for all molecules showing a departure from a full planarity (δ=0) corresponding to the BZ molecule. The dashed line at 0.5 Å separates planar from non-planar molecules.

IV.4.2. Exfoliation process:

IV.4.2.1. Potential of Mean Force (PMF)

Modelling of BP exfoliation process was carried out by simulating a stack of four layers of BP with dimensions of about 3.3 nm × 4.2 nm in the xy plane, inside a box with dimensions of 6 nm × 6 nm × 6 nm, while immersed in solvents. The number of a solvent molecules used in this simulation is 1500 for BZ, 1356 for NVP, 1500 for NMP, 1300 for DMI, 1860 for DMF, 2050 for DMSO, 800 for CHP and 1850 for IPA. After equilibrium, the distances between adjacent replicas of phosphorene layers along ‘x’ and ‘y’ are about 3.4 nm of solvent space, and about 4.8 nm along

'z'. To simulate the exfoliation process, a perpendicular harmonic biasing potential of 100 Kcal/mol (this parameter was converged as lower forces resulted in no-exfoliation) was applied along the 'z' direction on one edge of the BP top-layer (phosphorene sheet), as illustrated in Fig. 40a. The vertical distance along the peeling between two phosphorene sheets was denoted 'd'. All the other sheets edges were kept fixed to their positions by a harmonic potential to avoid any sliding. The potential of mean force (PMF) calculated from this simulation was generated to compare the phosphorene exfoliation energetics of different solvent molecules at different separations. To elucidate in more details the exfoliation process, we present in Fig. 40b the PMF for all molecules. Low PMF values means less energy is required to exfoliate. As can be noticed, we have two distinct regions separated by an inflection point at d~7.8Å. In the first region, only very small differences are observed between the curves, meaning that there is not enough room between two phosphorene layers to allow molecules infiltration. We can see that those solvents having the smaller δ planarity parameter are the first to intercalate, namely BZ and DMF followed by NVP, DMI and NMP presenting larger δ parameter. At interlayer openings above ~7.8Å, a difference in the PMF curve is discerned, in addition to a series of inflection points namely at ~9Å and ~12Å. These points represent opening values at which more molecules are able to gradually intercalate, as the top layer is constantly peeled-off away from the BP stack. In terms of exfoliation ease, planar molecules (δ < 0.5 Å) seem to require less energy than non-planar ones (δ > 0.5 Å) which is fully consistent with experimental reports where BZ was found to give the highest yield in BP flakes concentration as compared to other solvents.[158] Same remark is noted with DMF which was found to be a better exfoliating agent than NMP prior to centrifugation.155 For non-planar molecules, despite the fact that IPA and DMSO have a smaller size than that of DMF, we can now state that their non-planarity is responsible for their low performance (low exfoliation yield). In addition, IPA's polar protic character is at the origin of its high PMF value as the vdW interactions between the molecules and the phosphorene are weaker as compared to intra-molecular hydrogen bonding. In this context, it was indeed reported that the polar protic methanol solvent, yielded the lowest concentration of exfoliated flakes in arsenene.[209] The CHP molecule is found to be the least favorable, as it requires the highest energy to exfoliate due to its very high δ parameter requiring a high interlayer opening to intercalate. Our findings clearly show that the δ parameter and the PMF value have the same trend, which proves that the δ parameter is a key parameter for an efficient exfoliation. Our findings are very consistent with experimental results where BZ, NVP and DMI were found to provide the highest concentrations of phosphorene sheets followed by DMF.[158]

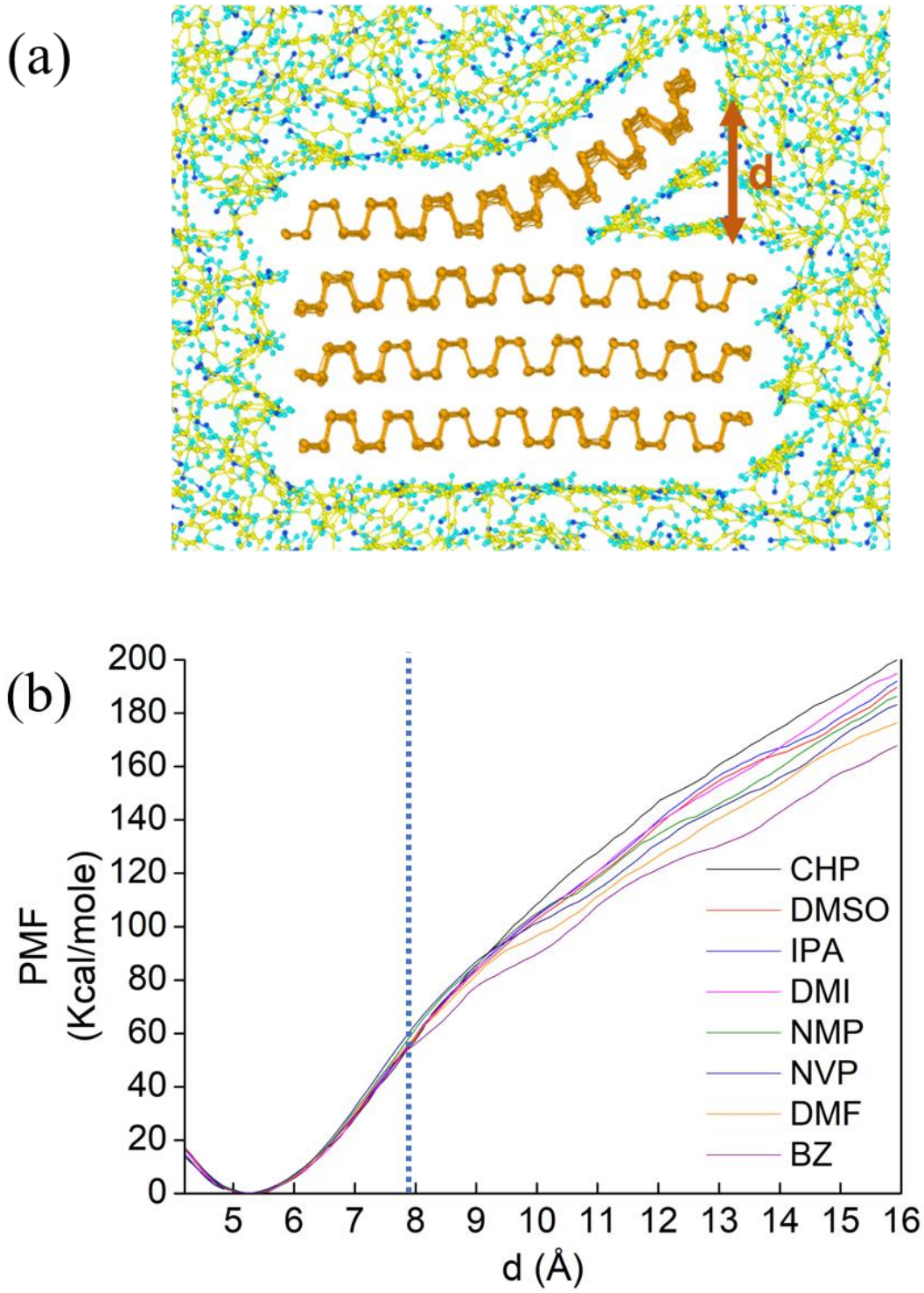

Figure 40. (a) Snapshot of the exfoliation simulation (b) PMF curve evolution for each solvent as a function of the sheet-opening 'd'.

IV.4.2.2. Solvent density profile

After a successful exfoliation, the exfoliated phosphorene sheet becomes surrounded by a dense molecular layer as presented in Fig. 41a, the density profile of which is presented in Fig. 41b. The latter shows an oscillating density where the height of each peak corresponds to a

maximum molecule's density at a precise distance from the phosphorene sheet, while its width is associated with the molecule's rotational freedom. Two main peaks (around 5Å and 9Å respectively) can be observed close to the two sides of the phosphorene sheet. Far from the molecules/phosphorene interface, the density profile shows small fluctuations which indicates that the previously noticed order is vanished and the molecules are acting as in the bulk phase. The formation of these dense molecular layers is therefore an indication of a significant interaction between the phosphorene sheet and the solvent molecules. The molecular ordering at the interface is found to always be preceded by an adsorption on the BP surface in a favorable geometry.[210] Again, the as-measured distance Δ between these surface-molecules and phosphorene increases with increasing δ, as shown in Fig. 41c. The higher is the δ parameter the higher Δ becomes. In terms of interaction energy between these surface-molecules and phosphorene, Fig. 41c shows an opposite trend as compared to the one observed in the case of Δ, which means that it is also opposite to that of **δ**. The smaller is the **δ** parameter, the stronger the surface-molecules interaction energy is.

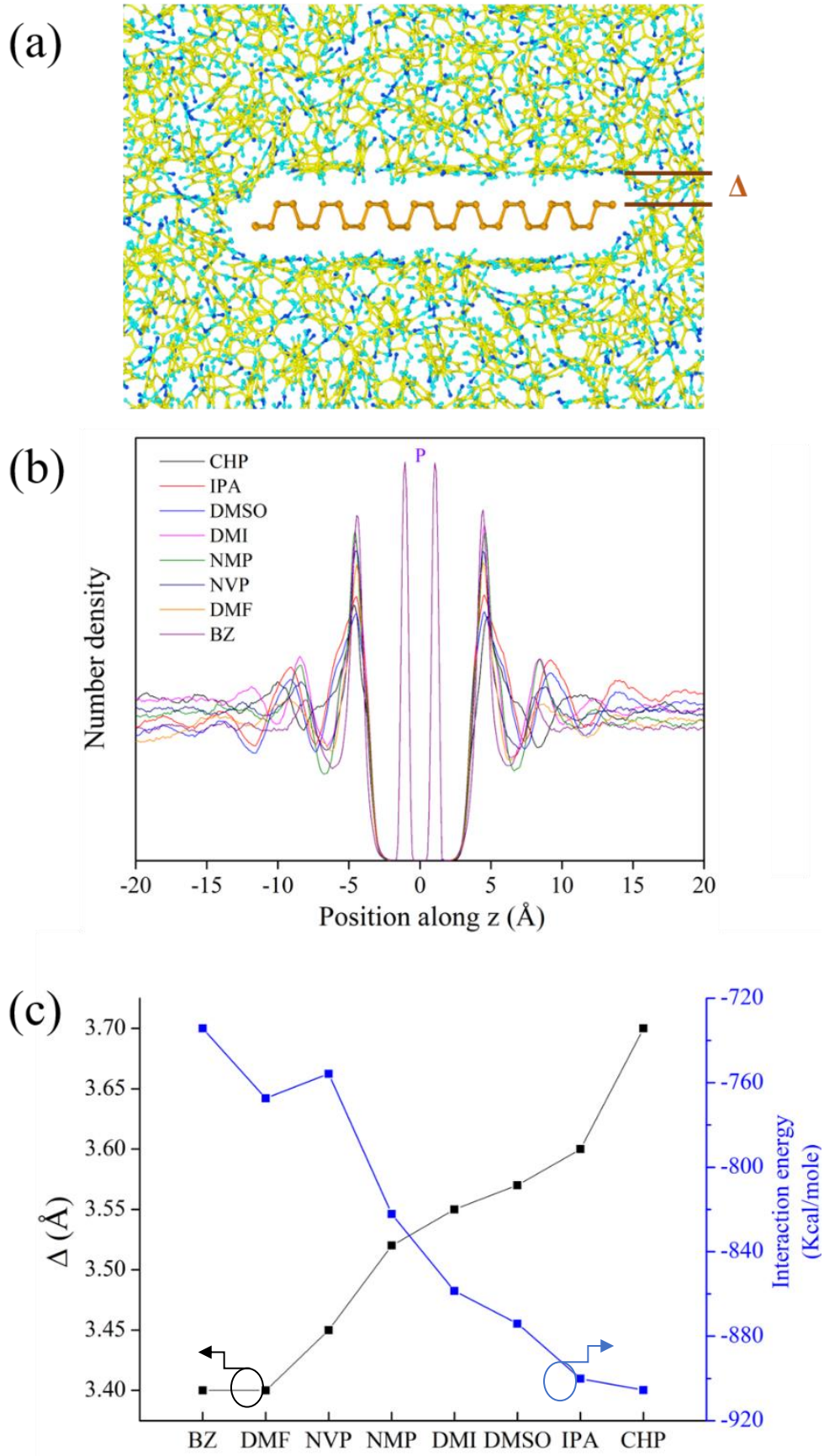

Figure 41. (a) Phosphorene sheet obtained after exfoliation (b) Density profile of molecules along the z-axis (normal to the phosphorene plane) (c) Interaction energy between surfaces molecules and a single phosphorene sheet (blue squares) and their respective di

IV.4.2.3. Mean square displacement of solvents

To get a full picture of the exfoliation process, it is necessary to account for the role of the self-diffusion coefficient of all intercalated molecules. In our study, the self-diffusion coefficient was extracted from the mean square displacement (MSD) in order to describe the dynamics of the solvent. The diffusion coefficient was calculated from Einstein equation at long time interval, which is expressed as follows: $\mathrm{D} = \frac{1}{6}\lim_{\mathrm{t}\to\infty}\frac{\mathrm{d}}{\mathrm{dt}}(\mathrm{MSD(t)})$. Calculation of MSD was given 4 ns to reach equilibrium, before the calculation of self-diffusion coefficient was carried out as shown in Fig. 42.

The study of dynamic properties is of interest to provide significant information about the atomic diffusion and to understand the detailed atomistic mechanism of diffusion transport. The self-diffusion coefficient makes it possible to quantify the dynamics of the species within the system. There are two methods for calculating the self-diffusion coefficient, namely Einstein, who uses the mean square displacement, and that of Green-Kubo, which uses the autocorrelation of velocities. During this study we used Einstein's approach. The average square displacement is defined as:

$$MSD(t) = < \frac{1}{N}\sum_{i=1}^{N}[r_i(t) - r_i(0)]^2 >$$

With < > indicating an ensemble average over all molecules in the simulation, $r_i(t)$ the position of the particle at an instant 't' and $[r_i(t) - r_i(0)]^2$ the distance vector traveled by a given particle over a time interval. The self-diffusion coefficient (D) was calculated based on the Einstein equation at long time interval, which is expressed as.

$$D = \frac{1}{2d}\lim_{t\to\infty}\frac{d}{dt}(MSD(t))$$

With 'D' being the diffusion coefficient, 'd' the dimensionality of the diffusion coefficient (d=1,2 or 3), and 't' the simulation time. The self-diffusion coefficient is obtained by the slope of the linear least square fit of mean square displacement versus time plots.

Fig. 42 shows the MSD of all the molecules versus time. Same trend was observed for the self-diffusion coefficient.

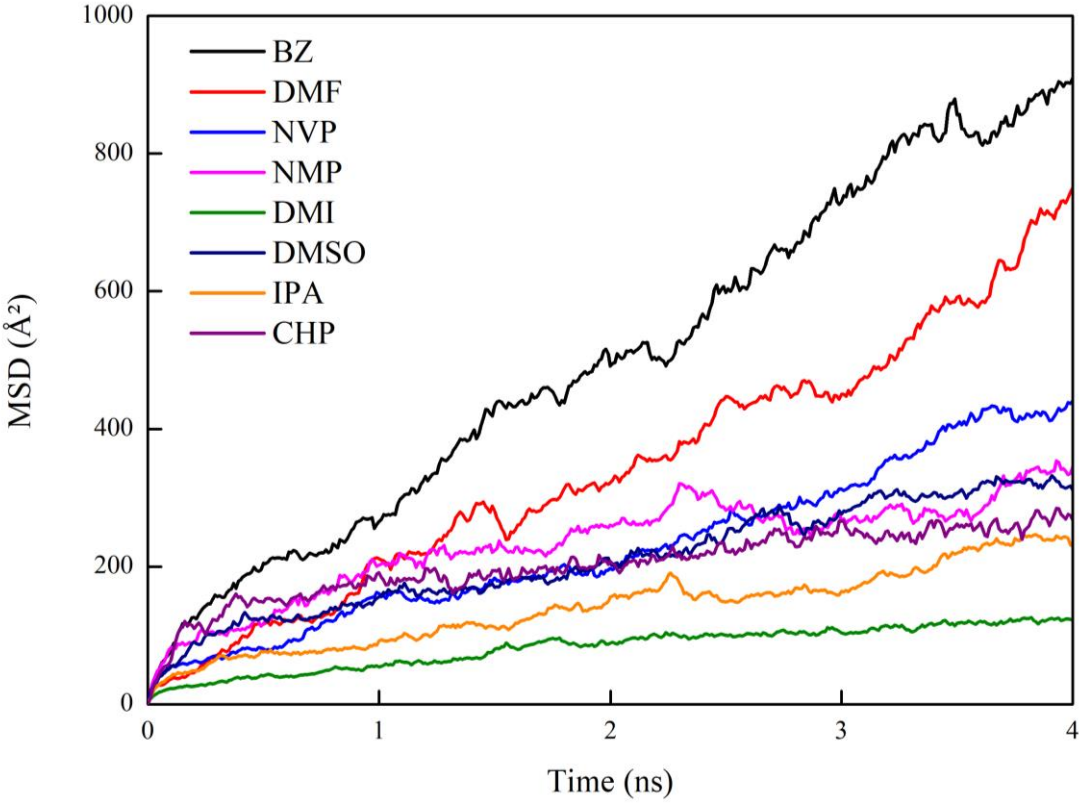

Figure 42. Mean square displacement of molecules between two phosphorene sheets.

IV.4.2.4. Self-diffusion of solvent molecules

Self-diffusion coefficient calculation, shown in Fig. 43, indicates an overall decreasing behavior with increasing δ. The lower is the δ parameter, the higher the self-diffusion is. Therefore, it is interesting to note such a collective action between self-diffusion and progressive detachment of the phosphorene sheet. In the case of BZ for instance, where δ = 0, the molecule diffuses easily and an immediate strong interaction occurs. The latter weakens the interaction between the phosphorene sheets in BP catalyzing therefore the sheet detachment thanks to a low energy contribution (low PMF, Fig. 40c). This partial detachment will allow neighboring molecules to self-diffuse further until the sheet is completely exfoliated. Experimentally speaking, the extra energy needed to fully exfoliate the sheet (equivalent to PMF) would be provided by the ultrasonic action. Therefore, the planar is the solvent molecule, the stronger the interaction of phosphorene with surface molecules is, the higher the self-diffusion is, and the easier the exfoliation process is.

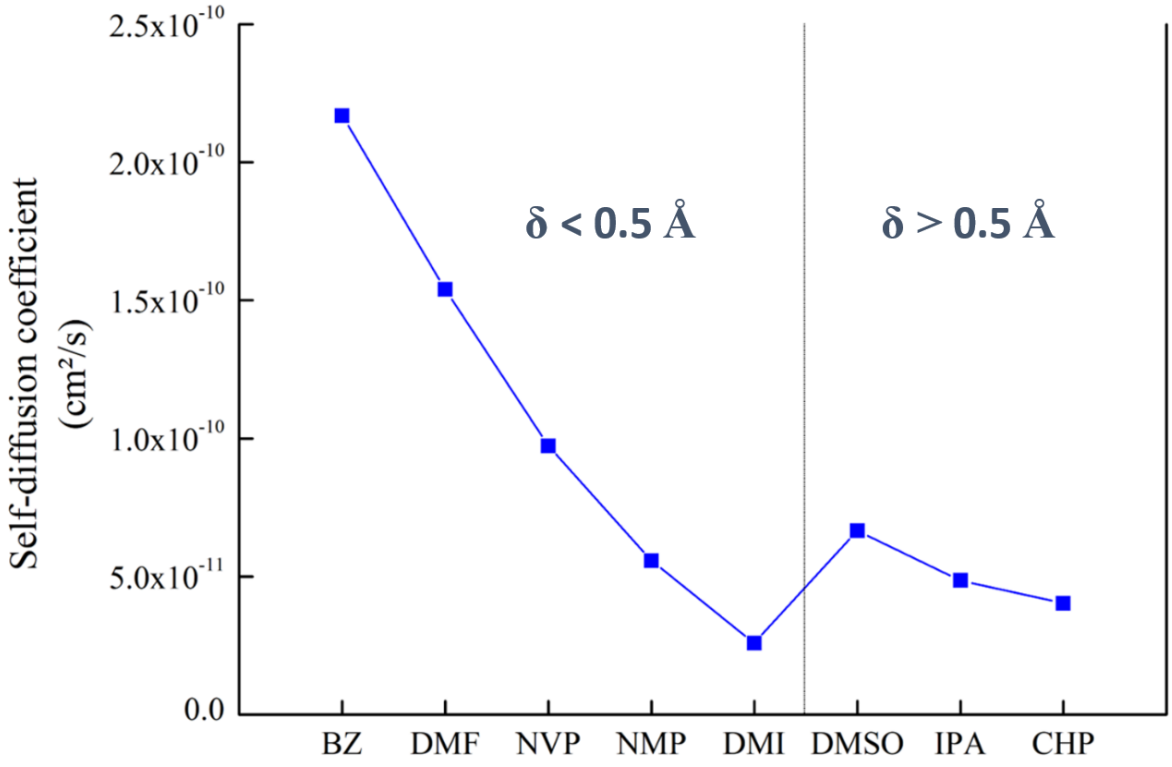

Figure 43. Self-diffusion coefficient of molecules between two phosphorene sheets.

IV.4.3. Re-aggregation process:

IV.4.3.1. Solvent molecules / Phosphorene distances

Let's now focus on the re-aggregation mechanism. Two phosphorene sheets with the same dimensions as those used for the exfoliation process, parallel to each other and separated by about 15Å, solvated in a box of 6 nm × 6 nm × 6 nm, are considered. The number of molecules used in the re-aggregation process is: 1900 for BZ, 1650 for NVP, 1700 for NMP, 1650 for DMI, 2050 for DMF, 2000 for DMSO, 1000 for CHP and 2000 for IPA. After a duration of 5 ns, a final aggregated pack is obtained as shown in Fig. 44a. Two molecular layers seem to surround again the aggregated pack at a distance Δ_1 from the phosphorne outer face (similar to those observed in Fig. 40), in addition to a confined/frozen layer between the two phosphorene sheets at a distance Δ_2 from the phsophorene inner face. This confined molecular layer stays unchanged even after very long calculation runs. Both Δ_1 and Δ_2 values are shown to increase with increasing δ (Fig. 44b).

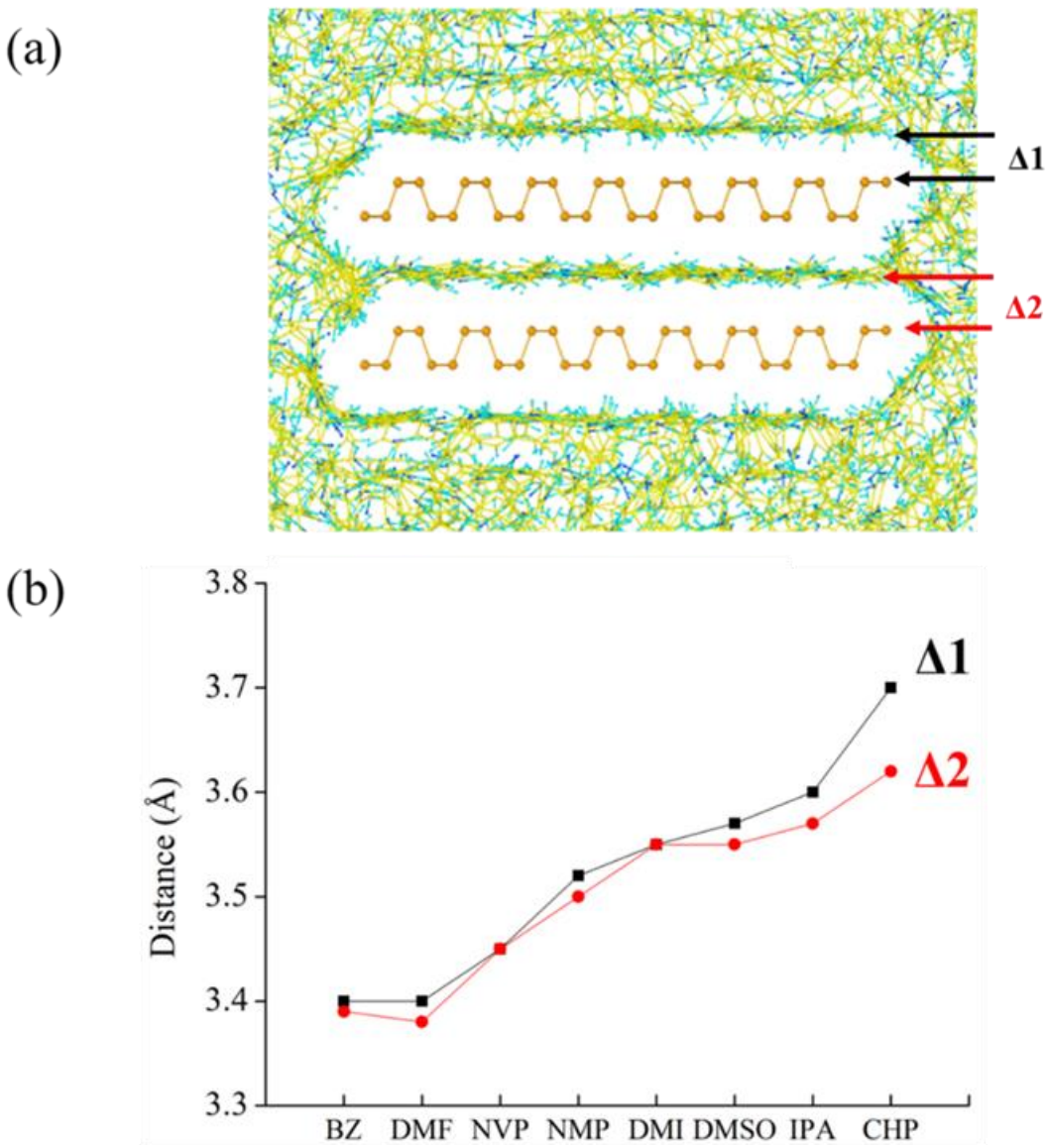

Figure 44. (a) Snapshot of the confined layer for BZ with (b) distances between phosphorene with surface molecules Δ_1, and phosphorene with confined molecules Δ_2

IV.4.3.2. Solvent molecules / Phosphorene Interaction Energy

Calculation of the interaction energy of such a confined molecular layer was performed for all molecules, along with the surface-molecules layer observed in the aggregated case (Fig. 46c). As compared to the surfaces-molecules interaction energy with phosphorene, those of the confined layer with phosphorene look generally higher for all solvents while that of two isolated phosphorene sheets is situated just between them. It is worth noting that planar molecules (**δ** < 0.5Å) behave differently with respect to non-planar molecules (**δ** > 0.5Å). For both molecular layers (surface and confined), the interaction energy decreases with increasing **δ** in the case of planar molecules, while it increases with increasing **δ** in the case of non-planar molecules.

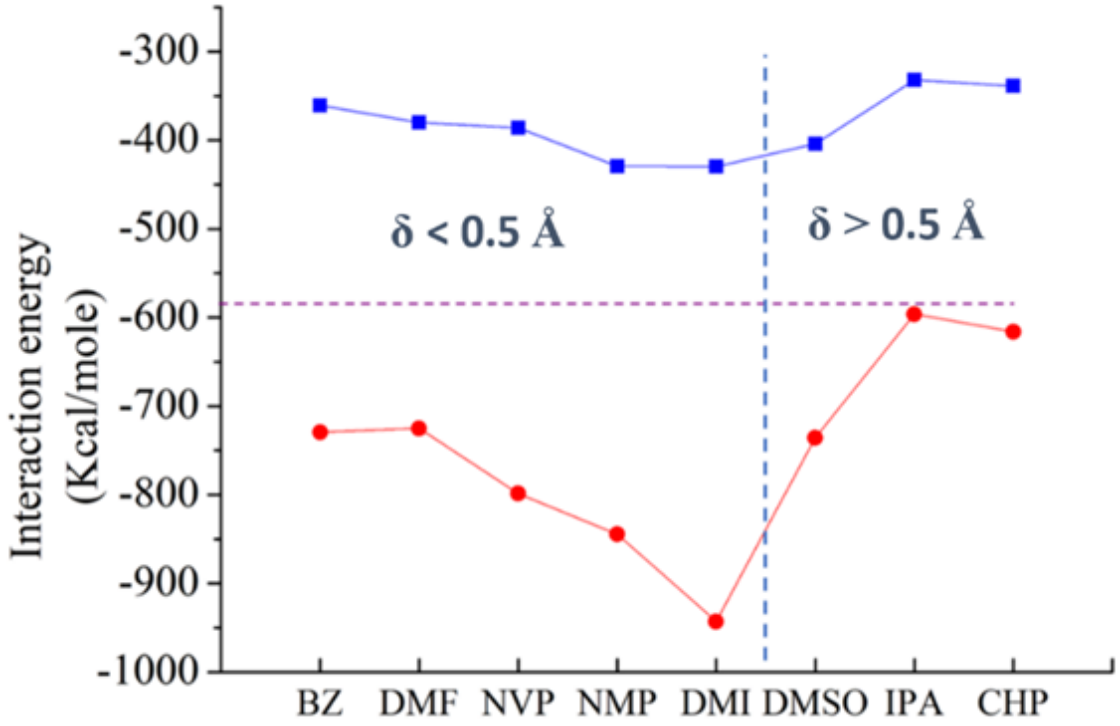

Figure 45. Interaction energy between the confined molecular layer with phosphorene (blue squares), along with that of the surface-molecules layer with phosphorene (red squares). Horizontal dashed line indicates the interaction energy between two isolated phosphorene sheets (-586 Kcal/mol)

IV.4.3.3. Re-aggregation ratio

To better illustrate the role of these interaction energies, we calculated the ratio between the energy interaction of the confined layer and that of the surface-molecules layer, denoted as the R factor, in such a way that the higher is the R factor, the favorable re-aggregation process is. From Fig. 46, this R is clearly higher for non-planar molecules ($\delta > 0.5$A) with respect the one for planar ones suggesting that non-planar molecules readily don't favor neither a stable suspension nor an easy exfoliation (due to their high PMF values). This is very consistent with experiments in which CHP, for example, was found to give chunk of bulk BP without any change of color for 15 hours, sign of no exfoliation.[153] From our findings, a plausible scenario for the re-aggregation mechanism would be a first rapprochement between two phosphorene sheets (surrounded by their respective molecular layers). At a critical distance ($\Delta_1+\Delta_2$), where the solvent molecules cohesion energy (governed by the Hildebrand solubility parameter) becomes weaker with respect to the adhesion energy between phosphorene and molecules, a confined layer is favored then trapped between the two phosphorene sheets forming a stabilized system. Indeed, the calculated total energy of such a system (55623 Kcal/mole) is very close to that of an isolated phosphorene double-sheet (55616 Kcal/mole). This critical distance should be affected by the steric repulsive interactions arising

from atoms in each solvent-molecule due to the non-polar nature of phosphorene.[211,212,213,214,156] Additional sheets can consequently join this nucleus package to form thicker packs. Apparently, it is the systematic formation of this surface-molecular layer which is at the origin of the exfoliation and the re-aggregation processes. In terms of suspension stability, the higher is the surface-molecules interaction energy, the less pronounced the re-aggregation process would be. The collective action between self-diffusion and sheets rapprochement also occurs during the re-aggregation process. The lower is the self-diffusion coefficient, the easy the re-aggregation process is.

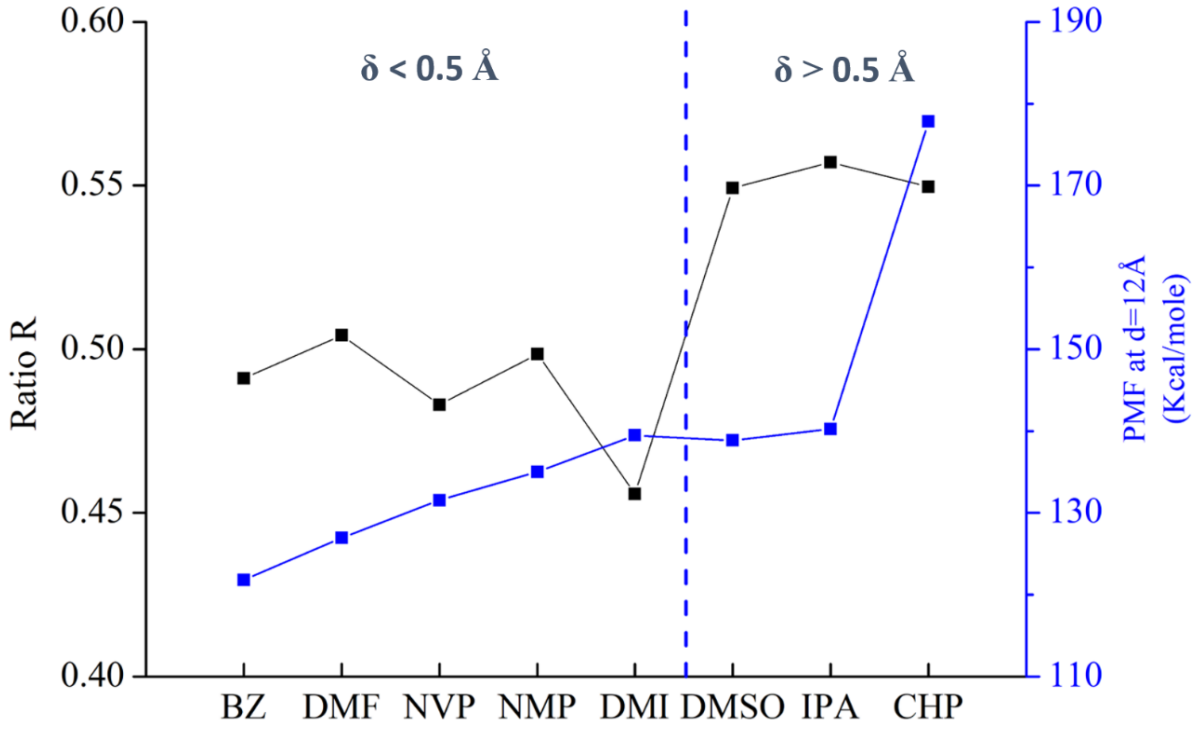

Figure 46. Ratio R (= $\frac{Interaction\ energy\ between\ confined\ molecules\ and\ phosphorene}{(Interaction\ energy\ between\ surface-molecules\ and\ phosphorene}$) as a re-aggregation phenomenon indicator for all molecules along with their respective PMFs at d = 12 Å.

IV.5. Conclusion

In the present study, molecular dynamics simulations were extensively used to elucidate the role of many parameters that contribute to the BP exfoliation/re-aggregation mechanism. Eight solvents were tested for such a purpose. A planarity parameter δ was first designated to classify these molecules from 0 Å (corresponding to BZ) to a value of 2.14 Å (corresponding to CHP). Our modelling of BP exfoliation process showed that, in terms of exfoliation ease, planar molecules (δ < 0.5 Å) seem to require less energy than non-planar ones (δ > 0.5 Å) where the δ parameter

followed the same trend than that of the energy required to exfoliate. Each exfoliated phosphorene was shown to be surrounded by a dense molecular layer, a sign of a significant interaction between the phosphorene sheet and the solvent molecules. The smaller was the δ parameter, the stronger the surface-molecules interaction energy was. In addition, a collective action between self-diffusion and progressive detachment of the phosphorene sheet was observed. Indeed, the planar was the solvent molecule, the stronger the interaction of phosphorene with surface molecules was, the higher the self-diffusion was, and the easier the exfoliation process was. With regards to re-aggregation, the process seemed to be favored by the formation of a confined molecular layer between the phosphorene sheets as the results of the solvent molecules cohesion energy. In this sense, non-planar molecules were shown unfavorable neither for a stable phosphorene suspension nor for an easy exfoliation process. The lower is the surface-molecules interaction energy, the more pronounced the re-aggregation process is.

Chapter V.

Experimental and modelling studies of Structural and optical properties of exfoliated black phosphorus and black phosphorus quantum dots

V.I. Introduction

Generally, size dependent bandgap energy is the most distinguishable feature of quantum confinement in semiconducting nanostructures.[215] In fact, size-dependent quantum confinement effects occurs when the radius of a semiconductor sphere is smaller than the bulk-exciton Bohr radius in a nanocrystal,[216] where the confinement strength weakens to the expected extent by the loss of one confinement dimension.[217] This behavior has long been the topic of several atomistic approaches aiming to describe the electronic properties of quantum structures such as two dimensional (2D), one dimensional (1D) and zero dimensional (0D) nanostructures. The most popular ones are those based on the effective mass approximation (EMA)[218] and quantum transfer matrix methods.[219] Deterministic approaches such as pseudopotential methods,[220] density functional theory (DFT)[221] and DFT-derived EMA[222] provide accurate predictions of the electronic properties; however, these techniques require hardware and time-consuming methods a reason why it always was *computationally* economic to handle the quantum confinement issue using the EMA approach.[223,224,225,226]

It was usually admitted that the quantum confinement signature is the increase of the effective bandgap energy (above the bulk value) in a linear way as a function of the inverse square ($1/d^2$) of the nanostructure diameter d.[215,227] In fact, such a proportionality matter has been shown to depend also on the composition and geometric dimensionality of the confinement as $1/d^n$ with the power parameter "n" is less than 2.[228] Indeed, the bandgap energy of InP quantum dots was found to be proportional to ($1/d^{1.35}$), while that of CdSe quantum wires was proportional to $1/d^{1.36}$.[228,229] In the case of black phosphorous (BP), where the bandgap energy is well known to strongly depends on the phosphorous sheets number,[230] BP nanoribbons bandgap energy was found to scale as a function of $1/d$ for the zigzag orientation and $1/d^2$ for the armchair orientation in BP crystal (d being the thickness of the nanoribbon)[231] depending on the crystal orientation.[231] However, no investigation has up-to-date been performed on the dependency of the power parameter "n" in the case of phosphorene (one phosphorus sheet) and 0D, or quantum dots, BP (BPQDs). Due to their bandgap tunability,[230] high mobility of charge carriers[232] and anisotropic optical properties,[233] a huge interest is nowadays arising on these quantum structures in electronic and optoelectronic applications.[234,235,236,237] For all the above, it is of central importance to investigate the above-mentioned power parameter "n" dependence in the case of phosphorene and BPQDs since its precise determination is crucial for bandgap energy predictions.

In the present study, a detailed structural and spectroscopic investigation is first performed on the as-prepared phosphorene and BPQDs nanostructures, then confronted to DFT and modified-EMA calculations to shed light on the appropriate model describing their electronic and optical properties dependence on the confinement.

V.2. Black phosphorus quantum dots

In this section, a brief review of the synthesis and unique properties of black phosphorus quantum dots is presented. Numerous researchers have already demonstrated that exfoliating graphene samples into quantum dots can be done successfully, allowing black phosphorus researchers to adapt their methodologies. Liquid exfoliation with ultrasonication is the most popular method for exfoliating black phosphorus into QD. This process entails grinding bulk black phosphorus, mixing it with a solvent, and then sonicating it with a variety of sonicators. Depending on the sonication strength and time, this process creates nanoparticles and/or nanoflakes. A review of currently available liquid exfoliation procedures for BP was published. Still many other methods could be used to obtain black phosphorus quantum dots.[238]

Chu and colleagues demonstrated that they required to use both a bath and a probe sonicator to get the tiniest, most consistently formed black phosphorous quantum dots. Drop casting the resulting suspension of black phosphorus material and photographing the samples using TEM and AFM allowed them to reach this conclusion.[239] While the majority of research on BPQDs employs sonication techniques such as those mentioned above, others have proposed using different devices to create enough force to exfoliate BP. Zhu and colleagues synthesized BPQDs with an average size of 5 nm in 0.66 hours using a kitchen mixer.[240] These researchers propose a mechanism for BPQD creation using this method that involves exfoliation into sheets followed by disintegration into QDs, which is backed up by TEM pictures of intermediate samples collected during the blending process. Grinding with a ball mill, on the other hand, produced a BP powder that was made up of large, thin flakes.[241] However, it was discovered that ball-milling had to be done with a LiOH additive, or the BP would create unstable intermediates that would oxidize instantly when exposed to air. Another easy to process method used, is the solvothermal-assisted LPE which consists of providing heat energy after ultrasonication to exfoliate the BP sheets from the edges. This method gave rise to BPQD's with an average size of 2.1 ± 0.9 nm and an excellent nonlinear optical response.[242]

BPQDs have a number of critical qualities that imply they could be useful in a variety of fields and applications. These characteristics are linked to the microstructures of BPQDs giving it unique properties imparted by the quantum confinement effect. These features are discussed, as well as their possible mechanisms. The distinctive qualities of BPQDs, such as their energy spectrum and states, as well as their optical and electrical properties, are of interest in a wide range of study domains. The physicochemical properties of BPQDs from theoretical models are highlighted in this section, along with their empirically observed properties. The BPQDs exhibit a good UV/VIS absorption spectroscopy and excellent memory performance, in addition to having a nonvolatile rewritable memory effect, photoexcitation for cell death with near-infrared light, and cell tracking capability.[226] They also show great near-infrared photothermal performance with a large extinction coefficient of 14.8 $Lg^{-1}cm^{-1}$ at 808 nm, high conversion efficiency (28.4%) and good photostability.[239] Niu et al. used time-dependent density functional theory simulations to investigate the size-dependent electrical, optical absorption, and emission properties of BPQDs.[243] In accordance with quantum confinement phenomena, the electronic and absorption gaps are inversely proportional to the sizes of the BPQDs. Because of structural distortion caused by excited-state relaxation, the emission gap shifts blue with increasing size. In small BPQDs, the unusual size dependence of emission gaps can result in a high Stokes shift; nevertheless, the Stokes shift eventually decays to virtually zero, implying that large BPQDs are good optical materials. Scientists have explored the electrical characteristics of BPQDs in experiments in addition to theoretical models. By varying the size and thickness of BPQDs, the band energy levels and structures can be modified. BPQDs, for example, might be a great addition to organic photovoltaic devices (OPVs).[225] Because of the 2D structure, strong broadband light absorption, and dispersion of the BPQDs, the light absorption of BPQD-based OPVs is improved.

V.3. Quantum Confinement theory

The quantum confinement effect and reduced screening effect caused by thickness reduction typically present themselves in 2D and 0D materials characteristics that are distinct from their bulk counterparts. For that matter, to better understand the properties of black phosphorus, the quantum confinement effect has to be discussed.

It is possible, in a crystal, to spatially quantify the motion of an electron or a hole with E (relative to the bottom of the conduction band or the top of the valence) by restricting its

displacement in at least one of the three directions of space over a distance less than their DeBroglie wavelength defined by the relation

$$\lambda = \frac{h}{p} = \frac{h}{\sqrt{2m^*E}} \qquad (27)$$

The spatial extension of the confinement potential must be such that the confinement energies E are greater than thermal energy k_BT at temperature T so as not to obscure the quantification i.e., it is necessary that:

$$\lambda = \frac{h}{\sqrt{2m^*E}} < \frac{h}{\sqrt{2m^*kT}} = \lambda_{th} \qquad (28)$$

Where λ_{th} is called the thermal wavelength of DeBroglie. Thus, the quantum effects appear for thicknesses less than this characteristic length which is typically on the order of a few tens of nanometers. The electronic properties of structures with confined charges change considerably. Thus, one can confine a charge in one direction of space to form a 2D quantum well, in two directions of space to form a 1D quantum wire or even in the three directions of space to form a 0D quantum dot. One of the consequences of electronic confinement is the discretization of the electronic structure of these materials and the change in the electron density profile. Figure 47 illustrates, by a comparative approach, the density of states and the discretization of the energy levels according to the dimension of the nanomaterial. We also cannot pass without talking about the overspeed effect noticed with the confinement. Indeed, in a nanomaterial the variation of the position Δx of the charge carrier tends towards zero, which results in a trend towards a very large value of its impulse Δp ($\Delta x \Delta p \leq \frac{\hbar}{2}$) and consequently by an overspeed of the charge carrier. The linear and non-linear optical properties of nanomaterials are strongly modified as compared to those of the solid semiconductor having the same chemical composition. The study of these new properties constitutes a vast area of basic and applied research.

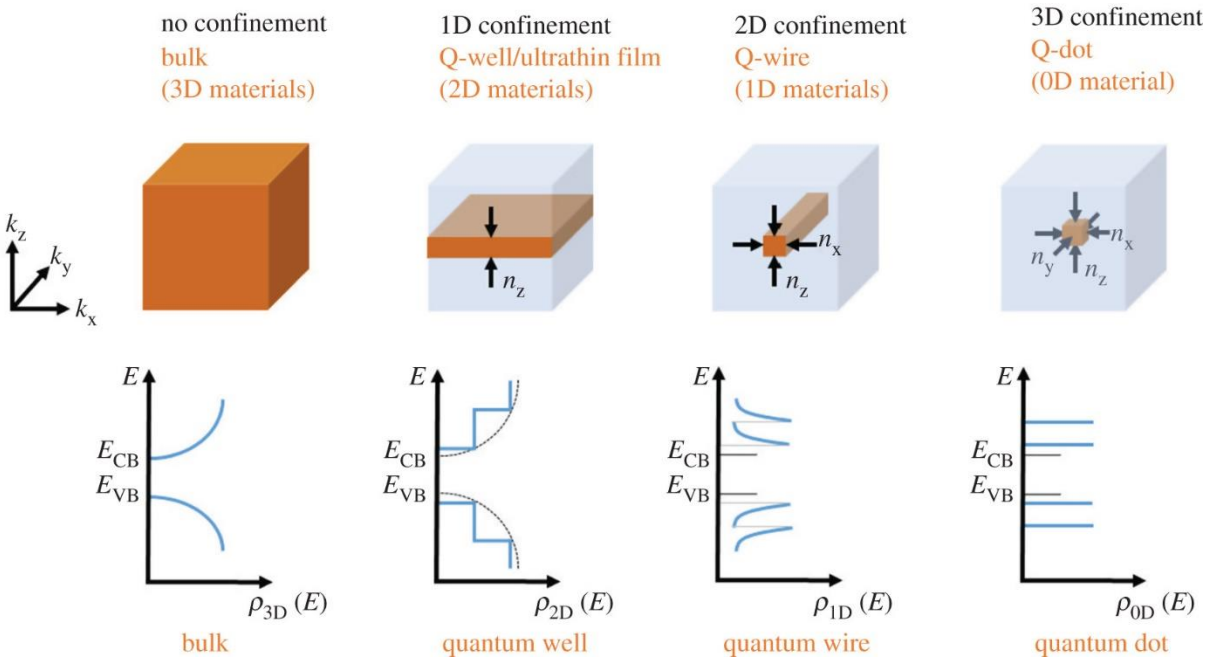

Figure 47. schematic illustration of broken symmetry and functional form of the density of states in a 1D, 2D and 3D confined materials.[244]

V.3.1. Quantum size effect

In the bulk state, an undoped semiconductor exhibits a full valence band and an empty conduction band, separated by a forbidden band, (the bandgap), of a width E_g. By luminous excitation at a frequency ν_{ex} with photons of energy $E_{ex} = h\nu_{ex} > E_g$, an electron of the valence band can pass through the conduction band and thus a hole is created in the conduction band. Fluorescence corresponds to the radiative recombination of this electron-hole pair by emission of a fluorescent energy photon $h\nu_{fluo} = E_g$, the excess energy $h\nu_{ex} - h\nu_{fluo}$ being evacuated under form of heat in phonons. Fluorescence is more likely as the temperature is weak and that the semiconductor contains few structural defects. Under the effect of 0D quantum confinement and with a finite number of atoms, the energy bands of a nanocrystals split into discrete levels, the difference of which increases as the dimension of the nanomaterial decreases.

Because the physical features of semiconductor confined materials, such as the bandgap, are dependent on their size due to charge carrier quantum confinement, having a way to quantify this magnitude is critical. Transmission electron microscopy (TEM) is one of the available technologies for determining the size of nanoparticles. It enables precise measurements of the shape and size of objects on the nanometer scale. Despite its high precision, this methodology is far from ideal for fast measurements in several sets of samples collected on a regular basis. Alternative methods for estimating the size of nanoparticles have been developed based on data obtained from optical

absorption studies. These techniques are dependent on determining the absorption band's edge, which is determined by the nanocrystal's size.

V.3.2. Theoretical approaches to the quantum size effect

V.3.2.1. Effective mass approximation (Brus model)

In the case where the diameter of the crystallites is smaller than the Bohr radius of the exciton of the massive crystal, confinement is very important and the energy levels are widely spaced and the gap becomes very large. The simple formalism of the effective mass approximation (EMA) essentially provides a first qualitative information. Indeed, a clear shift towards the high energies of the absorption threshold optics has been observed.[245,246,247] To explain this phenomenon, Brus proposed a model in the framework of the effective mass approximation where the bands are assumed to be parabolic.[227] The expression of the gap as a function of the size is given by the relation:

$$E_g(D) = E_{g,bulk} + \frac{\hbar^2}{2D^2}\left(\frac{1}{m_e^*} + \frac{1}{m_h^*}\right) \frac{0.992\,\pi^2 e^4}{2(4\pi\varepsilon_0)^2 h^2 \left(\frac{1}{m_e^*} - \frac{1}{m_h^*}\right)} \qquad (29)$$

With $E_g(D)$ being the quantum confined crystal, $E_{g,bulk}$ being the bulk crystal, ħ the Planck constant, D the particle size (radius or thickness), m_e^* and m_h^* are the effective mass of electrons and holes and ε_0 being the vacuum permittivity.

Hence, the bandgap variation, denoted as ΔE_g becomes:

$$\Delta E_g(D) = \frac{\hbar^2}{2D^2}\left(\frac{1}{m_e^*} + \frac{1}{m_h^*}\right) \frac{0.992\,\pi^2 e^4}{2(4\pi\varepsilon_0)^2 h^2 \left(\frac{1}{m_e^*} - \frac{1}{m_h^*}\right)} \qquad (30)$$

This equation shows the increase in the gap with the decrease in crystallite size. The first term of the equation of $\Delta E_g(D)$ represents the kinetic energy, the second term is due to the Coulomb interaction between the electron and the hole and the third term represents the effects of spatial correlation. The latter is very small in absolute value and it is often negligible except for semiconductors of low relative permittivity ε_r. In order to test the applicability of Brus's model, Pejova and Grozdanov,[248] performed an experimental study on ZnSe nanocrystals. The Brus model overestimates the shift in gap for all sizes of ZnSe nanocrystals. For example, for a nanocrystal of 1.4 nm, the shift measured experimentally is 0.52 eV, while with the Brus model gives a value of 1.22 eV. The possible reasons for the inadequacy of the Brus model are:

- The effective mass model ceases to be applicable for very small sizes. Indeed, at as the size decreases, the movements of electrons and holes are not similar to those occurring in solid semiconductor and, therefore, one cannot think of the energy bands as parabolas.
- The second factor concerns the dependence of the Coulomb interaction on the size, which is not well described because of the use of dielectric constants whose values are equal to those of the solid semiconductor. Indeed, we find in the literature of low dielectric constants for crystallites.
- Considering an infinite potential outside of a spherical crystallite contributes to the insufficiency of this model. Indeed, within the framework of this approximation, the electron and the hole do not/cannot penetrate the nanocrystal through its surface.

V.3.2.2. Hyperbolic band model

We saw in the previous paragraph that because of the approximation of the effective mass which suggests parabolic bands, the theoretical model of Brus does not fully reflect the results of the experiment (Figure 48). If the bands are hyperbolic, the gap of a nanocrystal is given by relation:

$$E_g(D) = \sqrt{{E_{g,bulk}}^2 + \frac{h^2 E_g}{D^2}\left(\frac{1}{m_e^*} + \frac{1}{m_h^*}\right)} \qquad (31)$$

In the case of ZnSe nanocrystals, a comparison between the experimental results and those predicted by the hyperbolic band model, allows to conclude that the reason for the inadequacy of the Brus model do not lie solely in the disregard of the parabolic bands.[248]

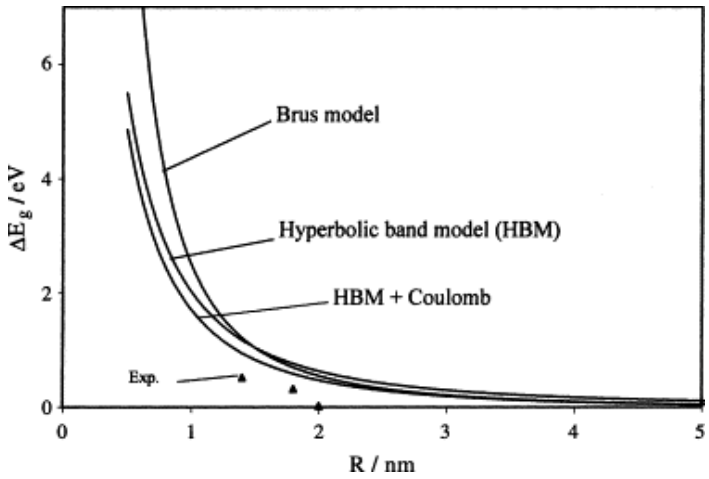

Figure 48. Plot of Eg(R) vs. R according to the Brus model and the hyperbolic band model with the experimental data of ZnSe[248]

V.3.2.3. Nosaka approach

Brus assumes an infinite potential outside the quantum point, if this is the case, the charge carriers cannot cross the surface of the nanocrystal. To remedy this, Nosaka assumed a very great potential but which is not infinite.[249] The excitation energies are therefore given by:

$$E_g(D) = E_g + E_{K,e}(D) + E_{K,h}(D) + E_{K,e-h}(D) \quad (32)$$

Where:

$E_{K,e}(D)$ and $E_{K,h}(D)$ represents the kinetic energies of electrons and holes respectively. Those energies can be calculated by:

$$\frac{E_{K,e(h)}}{E_0} = a + \frac{b}{[\left(E_0 m^*_{e(h)}/m_0\right)^{1/2}\frac{D}{2}+C]^2} \quad (33)$$

The constants a, b and c depend on the effective masses of the charged particles; and E_0 is the energy finite potential (E_0 is equal to infinity in the Brus model)

$$E_{k,e-h}(D) = -\frac{1.786e^2}{2\pi\varepsilon_0\varepsilon_r D} \quad (34)$$

$E_{k,e-h}$ represents the Coulomb interaction energy between electrons and holes. In conclusion, the two models give similar results for nanocrystals of size greater than 3 nm. However, for smaller sizes, Nosaka's approach gives results in better accordance with those of experience.

From these aforementioned models, we used in our study a modified-effective mass approximation model along with DFT to describe the electronic and optical properties of exfoliated BP and BPQD's. The use of the EMA is related to its ease and its good accordance with experiment results for other 2D materials.

V.4. Experimental and theoretical methods

V.4.1. Preparation of the suspensions

In order to experimentally prepare single BP sheets and BPQDs, Liquid Phase Exfoliation[250] (LPE) is very useful with the help a variety of organic solvents such as dimethylformamide (DMF), dimethyl sulfoxide (DMSO), N-cyclohexyl-2-pyrrolidone (CHP), Isopropanol alcohol (IPA) and N-methyl pyrrolidone (NMP).[251,252,253,254] In the case of BPQDs, a solvothermal-assisted LPE method[255] is needed to obtain poly-dispersed QD

suspensions.[256,257,240] The choice of the right solvent remains, however, a key issue to obtain stable suspensions. In the case of phosphorene preparation, we showed[258] very recently that benzonitrile (BN) exhibited a very high performance for exfoliating and for stabilizing BP suspensions, thanks to its surface tension (22.5 $MPa^{1/2}$), which is very close to that of BP (~ 21 $Mpa^{1/2}$), its planar morphology and its high molecular diffusion. Due to all these features, BN gave rise to the highest concentrations of phosphorene (0.11 mg/mL) as compared to other solvents.[251] The image below (Fig. 49) shows the prepared solutions.

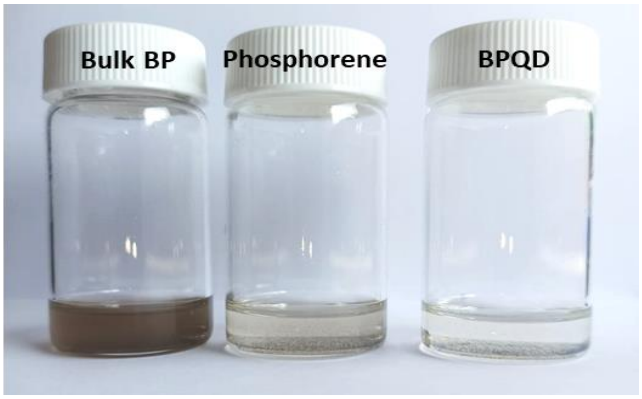

Figure 49. Photograph of as-prepared bulk BP, Phosphorene and BPQD after centrifugation

Due to its easiness and controllable production on a large scale, LPE and solvothermal-assisted LPE were respectively used to prepare our phosphorene and BPQDs solutions. An initial BP solution was first prepared from 1 mg of commercial BP powders (from Smart elements Co.) dispersed in 5 mL of BN solvent (from Honeywell, 99%, BN). The obtained dispersion was then subjected to stirring until solution homogenization. The dispersed BP particles in this first solution are large enough to be assumed as bulk-BP in the following. Exfoliation of the initial BP solution was afterwards obtained through bath ultrasonication in a Branson 8000 for about 1h30, before being subjected to centrifugation at 13000 rpm in a HERMLE Z32 for 15 min, in order to only keep BP monolayers (phosphorene) in the upper part of the solution. These sonication and centrifugation parameters were chosen based on trial test as shown in the TEM image of fig. 50 as shown below for phosphorene and BPQD.

Fig. 50 shows that 1 hour sonication yields exfoliated flakes however not to the phosphorene order and with large diameter, while for the quantum dots, very different sizes along with several aggregation were obtained. Increasing the sonication time to 1h30 showed thinner BP flakes with smaller sizes, and BPQD's solution showed great dispersion of quantum dots with small sizes and no reaggregations. Finally, 2 hours sonication showed a degradation

of the flakes with an increase in the oxidation (60.97% of phosphorus / 39.03% of oxygen) as could be seen from the STEM mapping in Fig. 51.

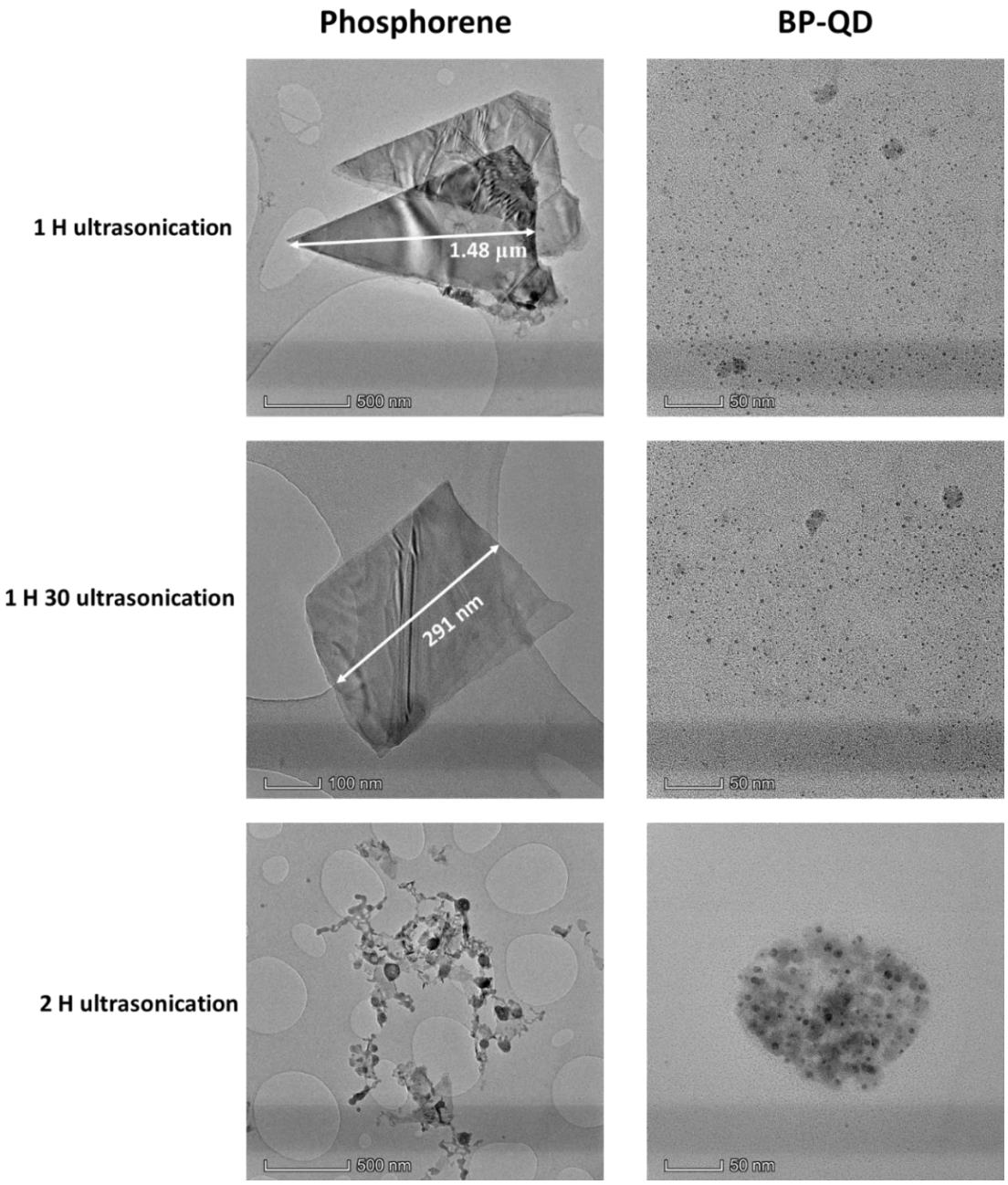

Figure 50. Ultrasonication parameters used for phosphorene and BPQD liquid phase exfoliation

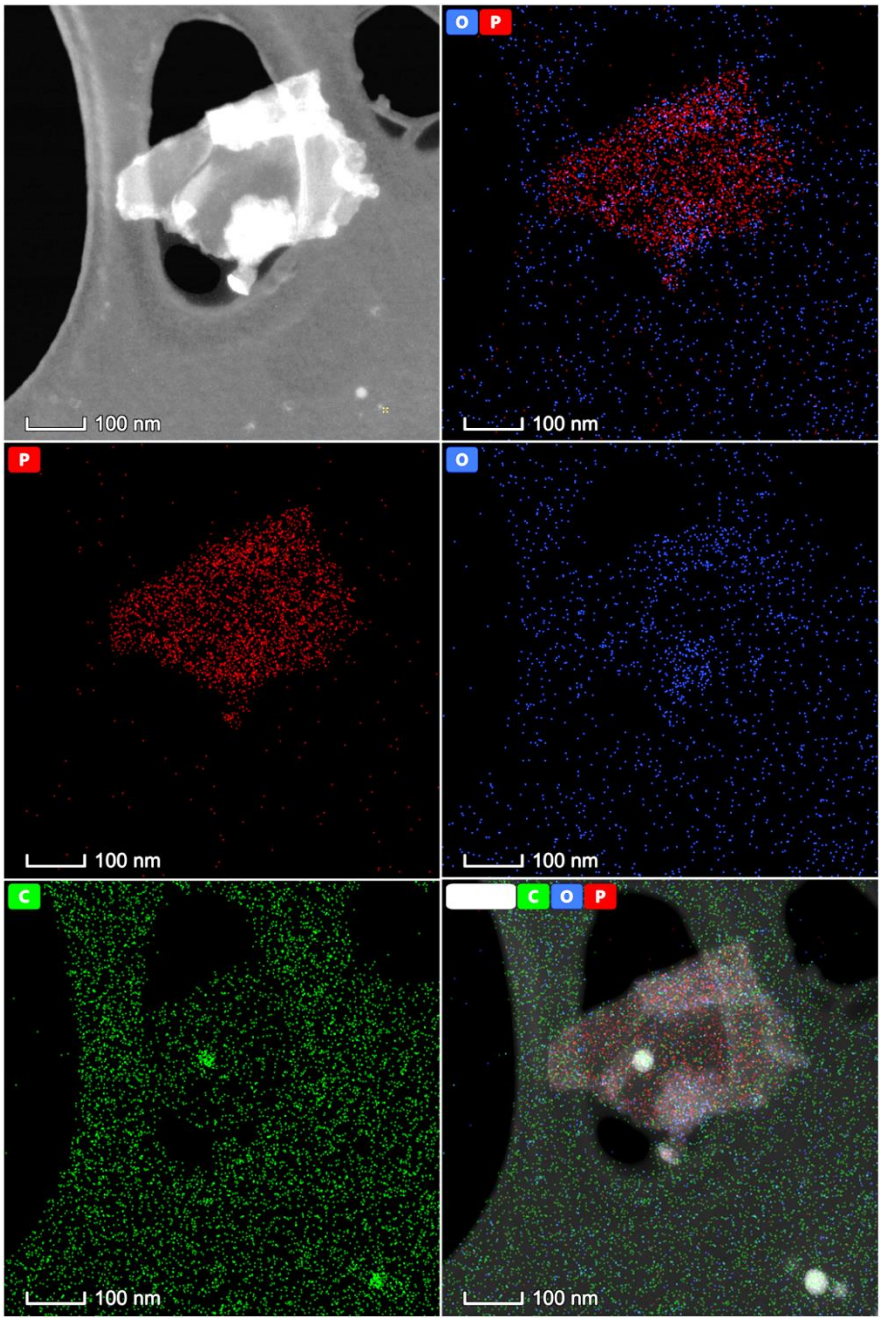

Figure 51. STEM- mapping image of a BP flake after 2 hours sonication and 13k rpm centrifugation.

For QD suspensions, the carbon grid was found to contain agglomerated QD with areas almost devoid of QDs. Hence, the use of 1h30 ultrasonication time. For the centrifugation, we used 13000 rpm (round per minute) to yield the thinnest flakes corresponding to phosphorene. The obtained supernatant is then collected for detailed characterization. Preparation of the BPQDs solution was subjected to the same protocol as for phosphorene, with the addition of a heat treatment at 150°C for 6 hours in an oven, after ultrasonication and prior to centrifugation.

It is worth to mention that other solvents were also tested experimentally such as IPA, NMP, CHP and DMI as shown in the figure below (The optimized ultrasonication and centrifugation

were used to obtain these TEM images). However, BN proved to give better exfoliation efficiency flakes as compared to TEM images with BN.

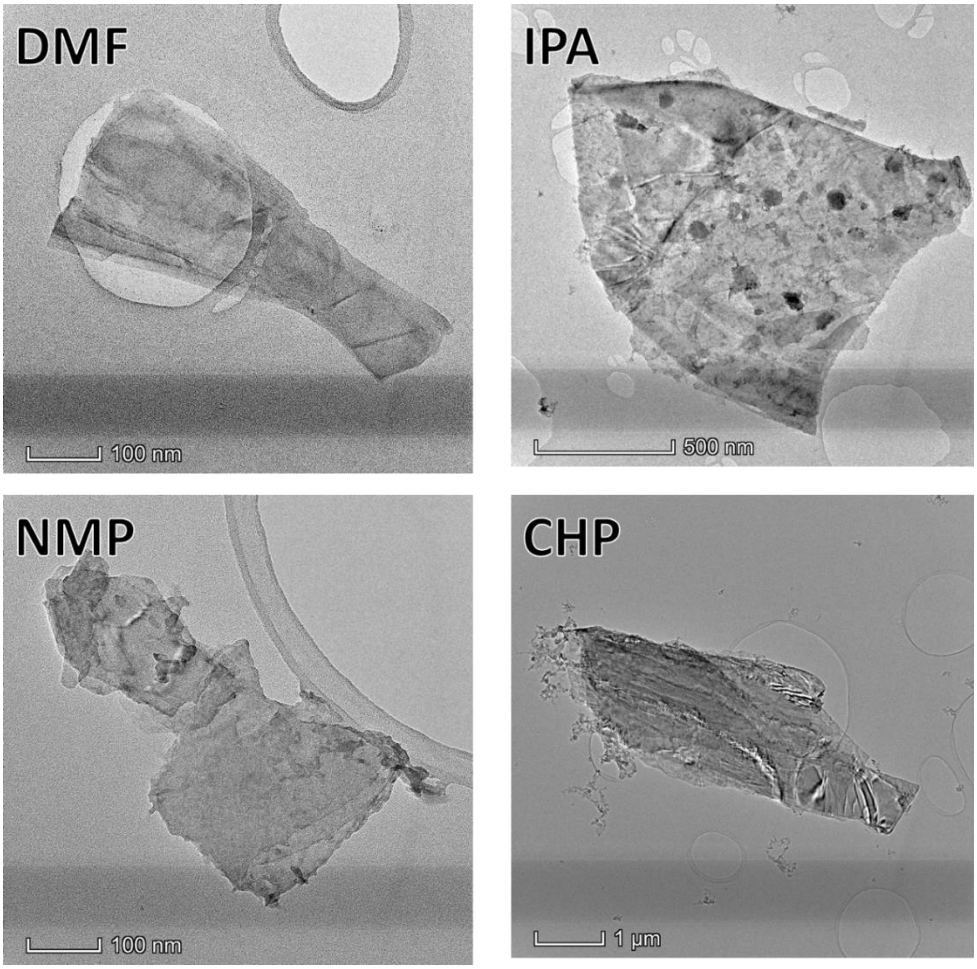

Figure 52. TEM images of BP exfoliated with difference solvents under 1h30 US and 15min centrifugation

V.4.2. Characterization methods

Fourier-transform infrared spectroscopy (FTIR) was used to characterize and identify functional groups of the all dispersions by means of a NICOLET iS50 spectrometer. Raman analysis is performed in a DXR2 Smart Raman by using a 442 nm excitation laser. Bright-field TEM, high-resolution TEM (HRTEM) and electron diffraction experiments were performed using an FEI Talos F200X S/TEM, operated at 200 kV accelerating voltage and with a point-to-point resolution of 1.2 Å. TEM characterization was carried-out using 10µL of the supernatant solution that was drop-cast onto a standard copper-grid. Optical properties were explored using a Perkin Elmer Lambda 900 spectrophotometer in the UV/VIS range.

V.4.3. Computational details

Density functional theory (DFT) was performed using Quantum espresso code.[259] A projector augmented wave (PAW) pseudopotential was employed. The ground state wavefunctions and eigenvalues were calculated using the generalized gradient approximation (GGA-PBE)[260] along the hybrid Heyd-Scuseria-Ernzerhof (HSE06)[261] method on a Monkhorst-Pack[262] k-points grid of 9 x 6 x 1. For this calculation a plane wave cutoff of 80 Ry was used. Long range van der waals interactions were considered. Additionally, a 15 Å vacuum was added in the direction normal to the sheets to avoid interactions between periodic images. Prior to electronic properties calculations, an atomic relaxation was performed with an energy convergence of 10^{-5} Ry and a force convergence of 10^{-4} Ry per Bohr.

V.5. Results and Discussion

V.5.1. Vibrational Properties

V.5.1.1. Infrared spectroscopy

The as-prepared phosphorene and BPQDs are shown in Fig. 53a. A clear change in the solution coloration is observed. First step was to examine the molecular binding in the three solutions along with the respective oxidation state. Results from FT-IR spectroscopy, presented in Fig. 53b, show absorption peaks similar to those of the BN solvent. The peaks observed below 1000 cm^{-1} correspond to unsaturated carbon $C = C$ or aromatic ring $C - H$ wagging vibrations, indicative of a benzene ring in the sample (relative to the benzene ring in BN). Small peaks can be observed between 1000 and 1400 cm^{-1} which correspond to the fingerprint region of BN solvent. The absorption bands at 1440, 1490 and 1597 cm^{-1} are due to the aromatic $C = C$ stretching vibrations. At 2200 cm^{-1}, a strong stretching vibration related to the triple bond $C \equiv C$ is noticed. Additionally, a broad peak associated to $C - H$ stretch is seen at around 3000 cm^{-1}. These observed peaks, correspond solely to the BN solvent. Fig. 53c shows the FT-IR after solvent contribution subtraction. No absorption peaks are observed above 800 cm^{-1}, especially $P{-}O$ and $P{=}O$ stretching vibrations at 1000, 1100 and 1600 cm^{-1}.[263] Thus, suggesting the absence of oxygen in our sample, hence the non-oxidation of BP. Additionally, two small contributions are appearing at 687 and 750 cm^{-1} which corresponds to the P-N vibrations which are arising from the bonding between the P atoms of BP and the nitrogen of Benzonitrile. This result is in accordance with our previous work, stating that a protective solvation shell is formed around the phosphorene sheet as a result of the solvent molecules cohesion energy.[258]

This solvation shell creates a barrier layer against oxidation; thus, preventing degradation of BP. Similar results regarding the solvation shell creation were observed with CHP solvent.[252]

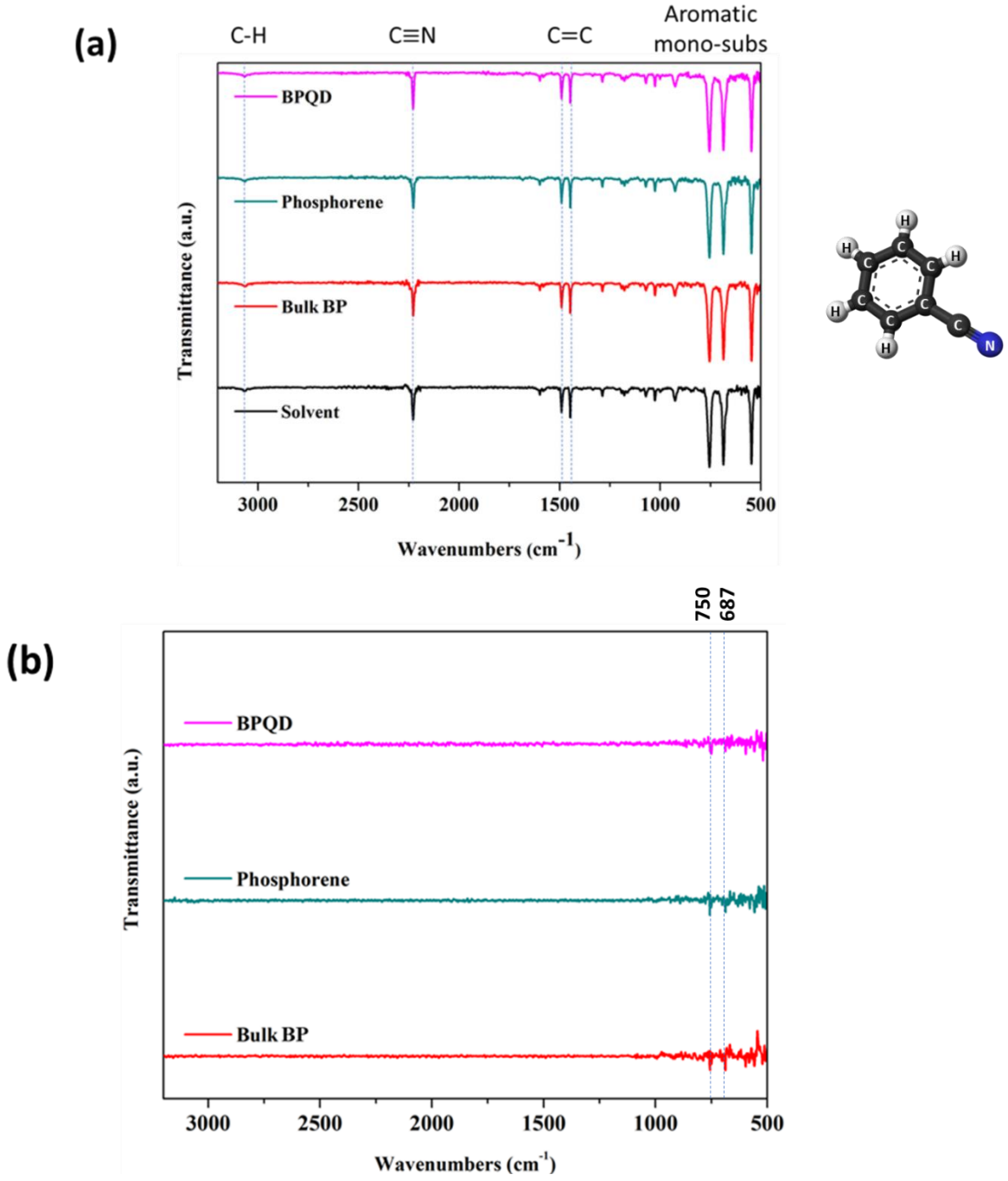

Figure 53. (a) IR spectrums of the as-prepared samples before solvent subtraction and (b) after solvent subtraction.

V.5.1.2. Raman spectroscopy

Further vibrational characterization using Raman spectroscopy was employed. The Raman spectra of bulk BP, phosphorene and BPQDs are depicted in Fig. 54. Three significant peaks can be observed denoted as A_g^1, B_{2g} and A_g^2. Phonon mode A_g^1 is an out-of-plane mode, while B_{2g} and A_g^2

are in-plane modes as shown. For bulk BP, these modes are located at 365 cm^{-1}, 439 cm^{-1} and 465 cm^{-1} for A_g^1, B_{2g} and A_g^2, respectively. These values are in great agreement with reported experimental values.[264,265,266] For the 2D-BP, a shift can be noticed for B_{2g} and A_g^2 modes. However, no apparent shift is seen for A_g^1 mode, which is likely due to the long-range Coulombic interlayer interactions, similar to that observed in exfoliated MoS_2.[267] The B_{2g} mode is also found to be shifted by 0.96 cm^{-1} and the A_g^1 mode by 2.1 cm^{-1}. It should also be mentioned that Raman spectroscopy was previously used to determine the number of layers in other 2D materials.[268,269] Our shift values obtained for phosphorene are found to be coherent with reported values.[270] For Raman spectra of BPQDs, an additional shift of about 0.9 and 3.8 cm^{-1} of the vibrational modes B_{2g} and A_g^2 is obtained as compared to bulk BP, similar to the one observed in reported investigations.[271,272] This shift is attributed to the change of Van der Waals interlayer interaction, as already seen in graphene and MoS_2 quantum dots.[273,274]

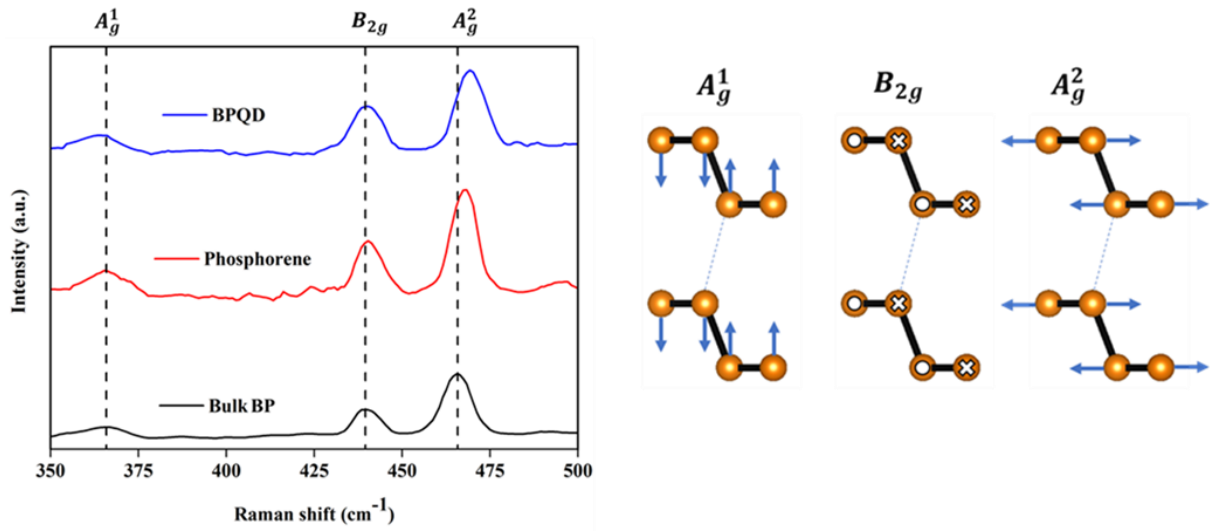

Figure 54. Raman spectrum of bulk BP, Phosphorene and BPQD.

V.5.2. Structural and morphological properties

V.5.2.1. Structural and morphological properties

a. Bulk BP

TEM and HRTEM were performed to investigate the crystallinity, quality and number of layers in each dispersed particle. Fig. 55a shows a typical TEM image of dispersed BP micrometric particles. The selected-area electron diffraction (SAED) performed on the aforementioned BP particles showed diffraction rings (Fig. 55b) the indexation of which reveals the presence of bulk BP planes that are: (020), (021), (040), (041) and (060). Typical HRTEM imaging of different areas viewed along the [001] zone axis is presented in Fig. 55c. In addition to the high degree of crystalline order within the particles, the Fast Fourier

Transform (FFT) of the HRTEM image (inset of Fig. 55c) reveals well identified spots with variable intensity. Those of particular interest are those spots corresponding to (200), (110) and (020) planes due to their direct relation with the BP number of layers.[275] In the case of the FFT pattern shown in Fig. 55c, the intensity distribution of these three spots is illustrated in Fig. 55d. The later clearly shows that the (110) and (200) relative intensity ratio to be equal to 0.50, an indication of the presence of a thick (or multilayers) BP area.[252,275]

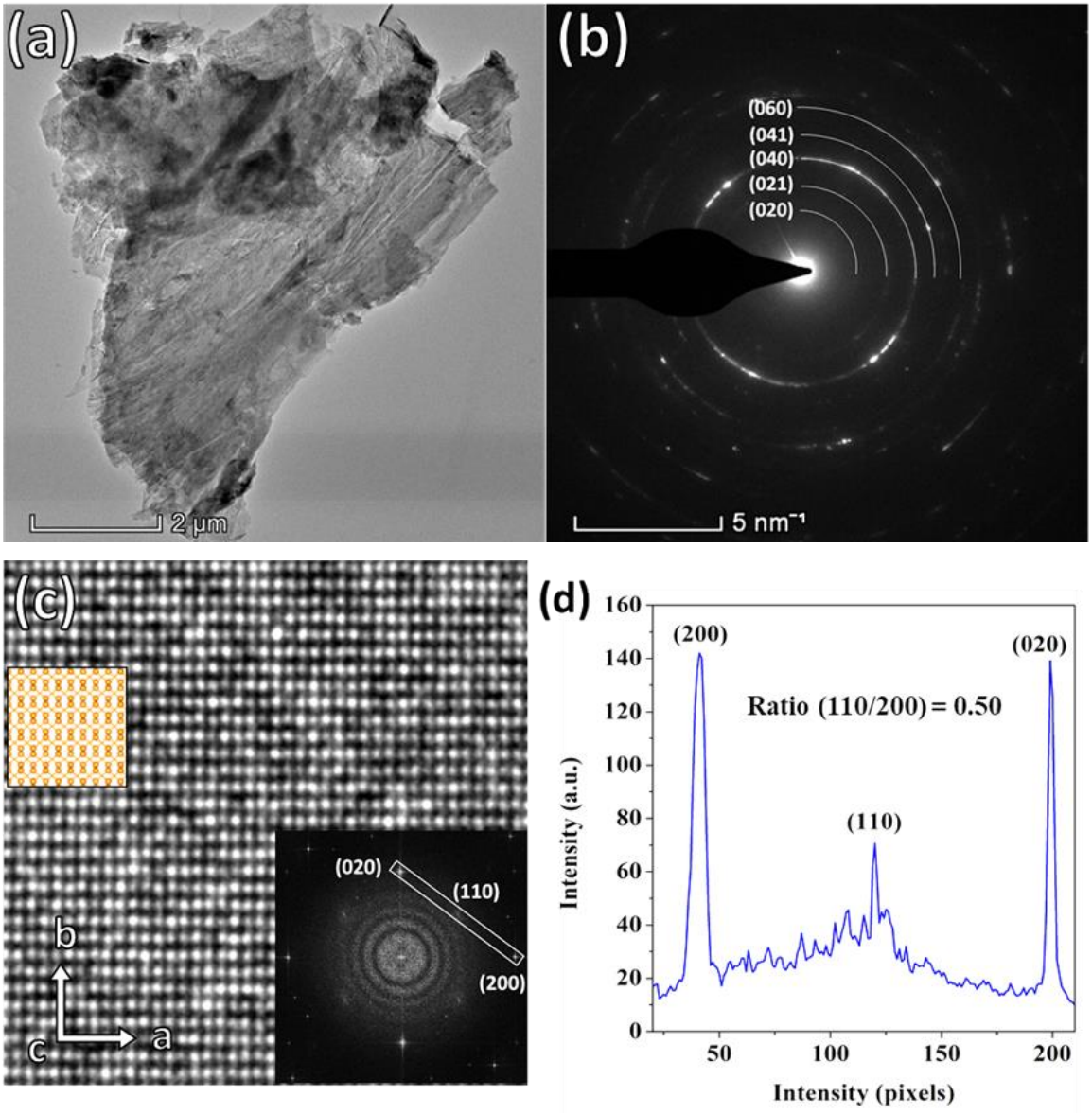

Figure 55. (a) TEM image of bulk BP and (b) its electronic diffraction pattern (c) HRTEM image of the bulk BP flake viewed along [001] direction with its corresponding FFT (inset bottom right) (d) Intensity of the (200) (110) and (020) from the FFT.

b. Phosphorene

A similar TEM analysis was carried out on the single BP sheets solution (Fig. 56). Indeed, Fig. 4a exhibits a typical TEM image of a single phosphorene sheet along with its original thick BP particle from which it was exfoliated. SAED pattern from the thick area (Fig. 56b) gives rise to a pattern similar to the FFT pattern shown in Fig. 55c suggesting the presence of a single crystalline structure viewed along the <001> zone axis. Furthermore, the rectangular area in Fig. 56b also indicates that the (200) and (020) spots are much brighter than the (110) one, thus indicating that this area still contains few layers of BP (>2 layers).[275] HRTEM analyses of the single sheet area, and of a variety of other single BP sheets (as the one shown in Fig. 56c) give rise to the typical image presented in Fig. 56d. On one hand, there is a clear contrast difference in the bi-dimensional array as compared to that of Fig. 56c.

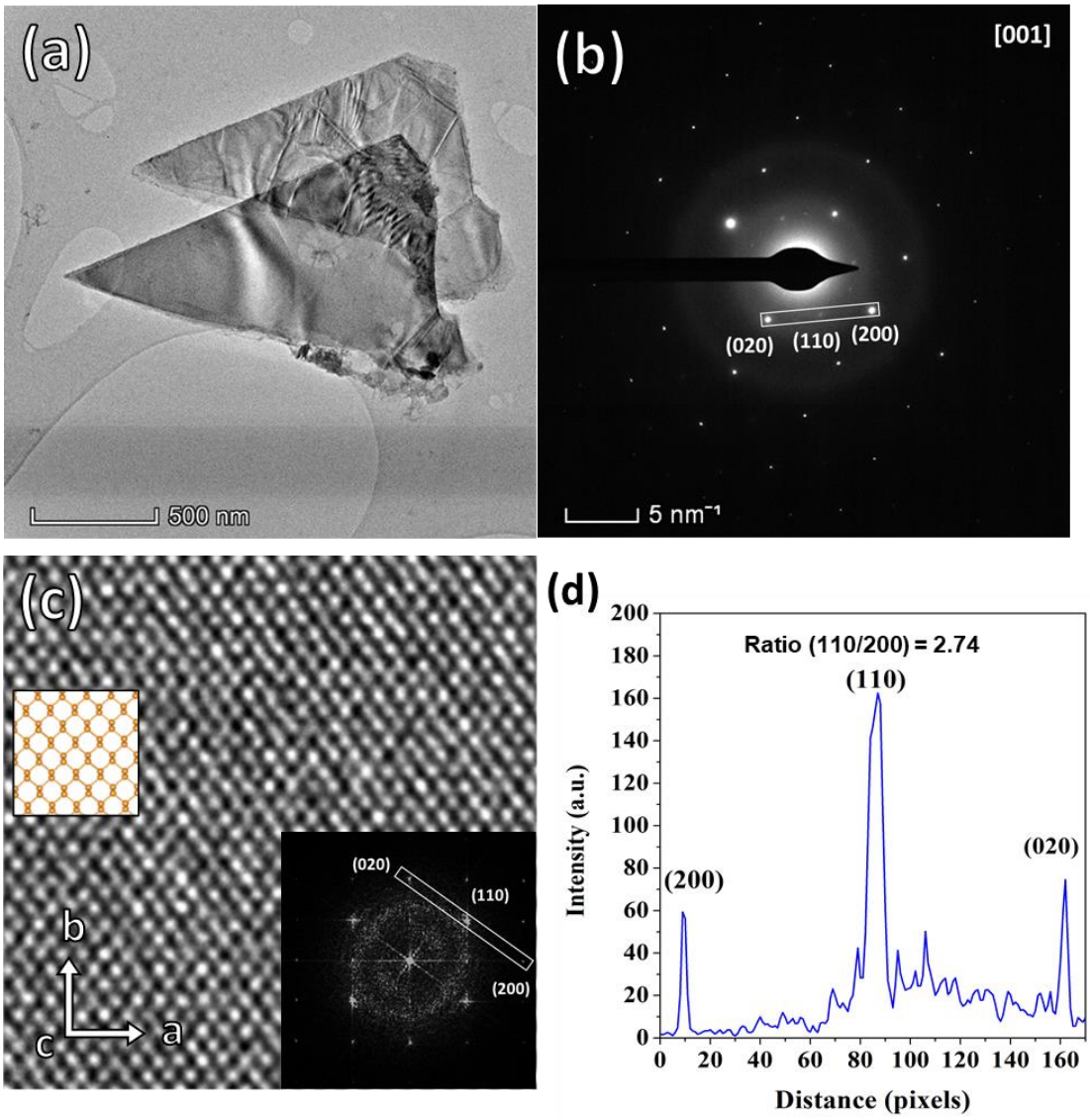

Figure 56. (a) a typical TEM image of a single phosphorene sheet along with its original BP particle from which it was exfoliated, (b) its electronic diffraction pattern (c) HRTEM image of the phosphorene viewed along [001] direction with its corresponding FFT (inset bottom right) (d) Intensity of the (200) (110) and (020) from the FFT.

On the other hand, FFT performed on such an image exhibits a similar pattern as the one shown in Fig. 55c but with completely different intensity ratios as illustrated in Fig. 56d. Contrarily to the few-layers area, the measured intensity ratio I_{110}/I_{200} is found to be 2.74, which is in very good agreement with the computationally (2.55)[275] and experimentally (2.7)[252] measured ones exclusively corresponding to the presence of a single BP sheet.[276,277] This is in fact a powerful method to distinguish few-layers BP particles from phosphorene ones. Indeed, the projected structure (equivalent to an HRTEM image) of phosphorene exhibits a hexagonal like array (inset in Fig. 56c) while that of few-layers BP shows an orthogonal-like array (inset in Fig. 55c). From the above HRTEM analysis, we believe that the dispersed BP particles in the exfoliation solution are mainly of phosphorene type.

c. BPQD

For BPQDs, a qualitative examination was performed by TEM (HRTEM) and SAED, in addition to a statistical size distribution as shown in Fig. 57. The TEM image (Fig. 57a) shows an overview of well dispersed QDs in BN solvent (no aggregated QDs were observed in the whole TEM grid). Fig. 57b shows a SAED ring pattern of the dispersed BPQDs where the diffraction rings and the spots are rather broad due to the small QDs size. For the size distribution, statistical TEM analysis of one thousand (1000) QDs was carried out as shown in Fig. 57c. Three lateral size distributions were found; namely 2.70 ± 0.26, 2.16 ± 0.3 and 1.72 ± 0.6 nm. Strikingly, the average dispersion is much better in our case, suggesting the BN organic solvent is improving the monodispersive character of the BPQDs suspension as compared to reported BPQDs dispersions.[225,278] Additionally, an HRTEM was conducted on an isolated QD as shown in the inset of Fig. 57d and 57e, where interplanar distances corresponding to the (020) planes of orthorhombic BP (of about 0.21 nm) are clearly visible.

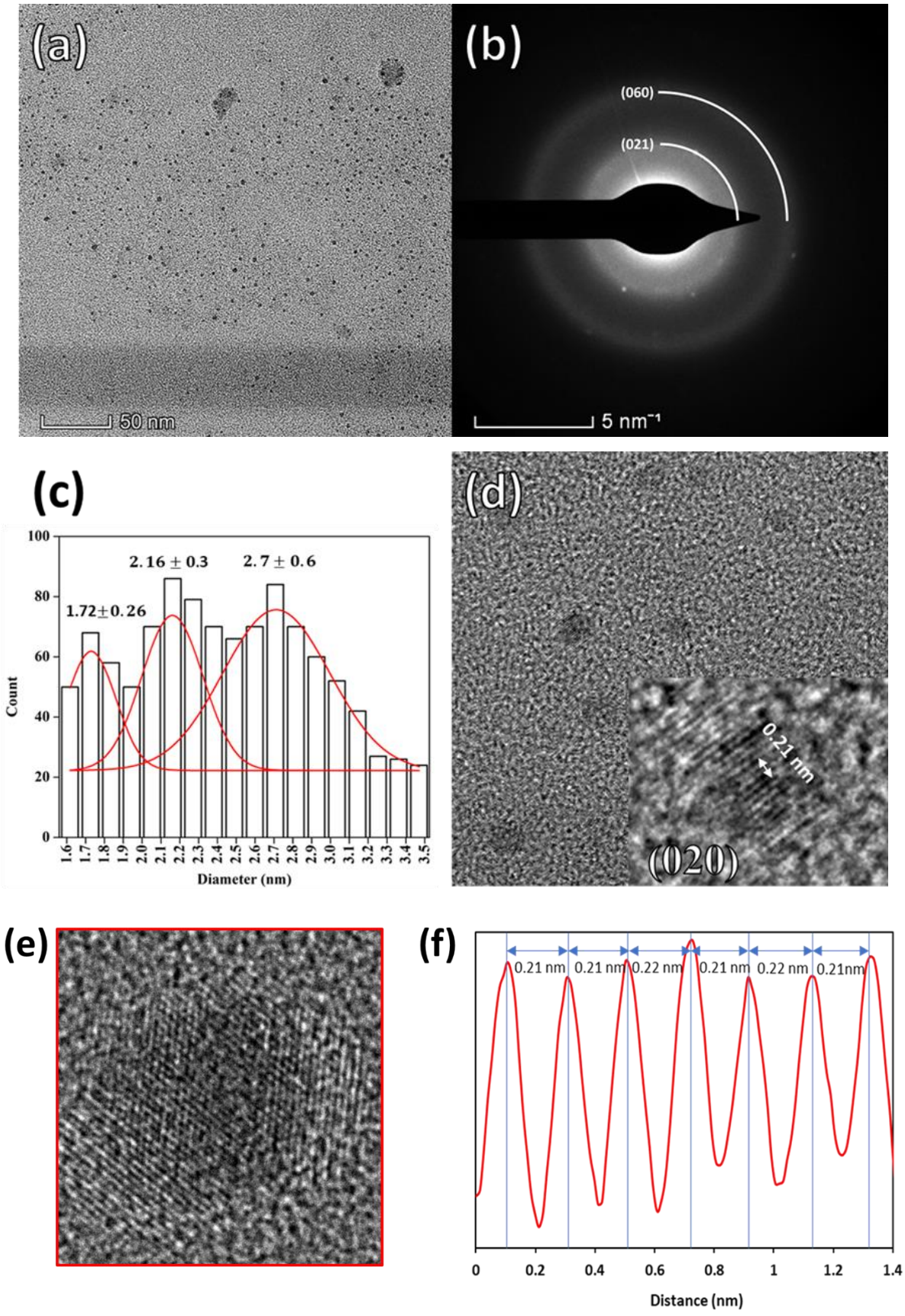

Figure 57. (a) TEM image BPQD's and (b) its electronic diffraction pattern (c) Calculated size distribution for 1000 BPQD (d-e) HRTEM of a BPQD (f) HRTEM line profile intensity.

V.5.3. Optical properties

In order to determine the absorption properties of bulk-BP, phosphorene and BPQDs suspensions in the visible range wavelength (400 - 800 nm), UV-VIS spectrometry was used. With the help of Tauc analysis,[279] $(\alpha hv)^2$ is first plotted as a function of the incident photon energy to extract the allowed direct transition energy which *a priori* corresponds to the bandgap energy value (see Fig. 58). In Fig. 58a, Tauc plot for bulk BP is presented with no evidence of any absorption edge, which is expected since bulk BP absorbs in the infrared region due to its narrow bandgap energy (around 0.3 eV) as we have recently confirmed using a direct electron energy-loss spectroscopy measurement.[280]

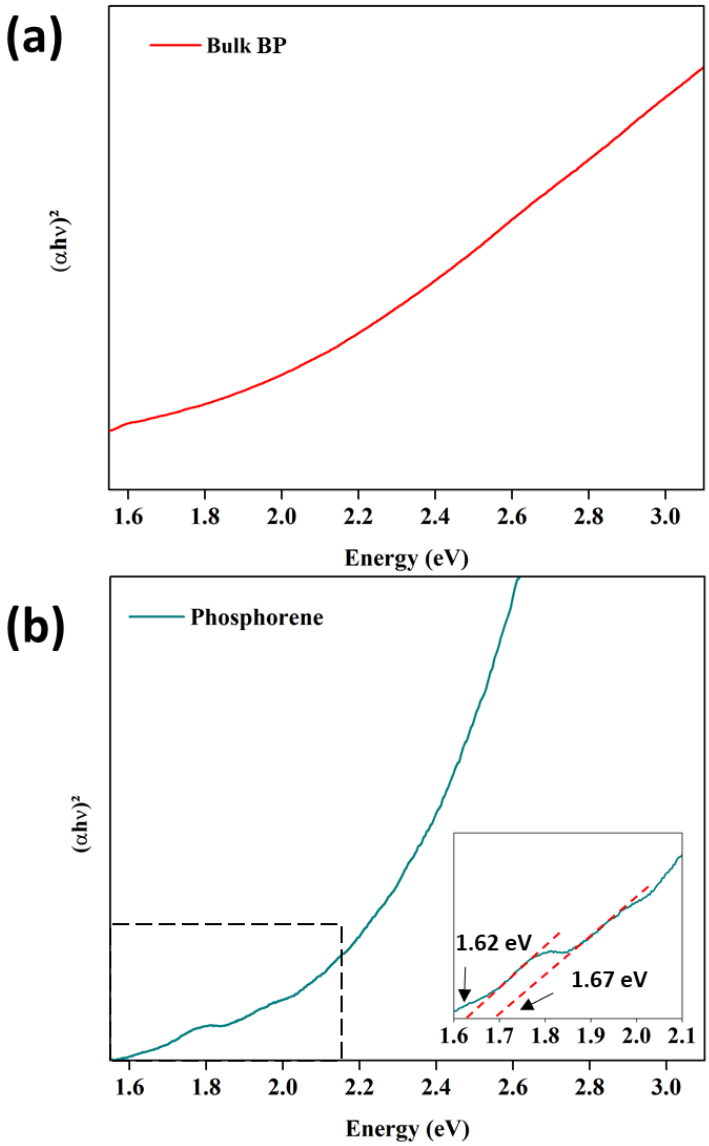

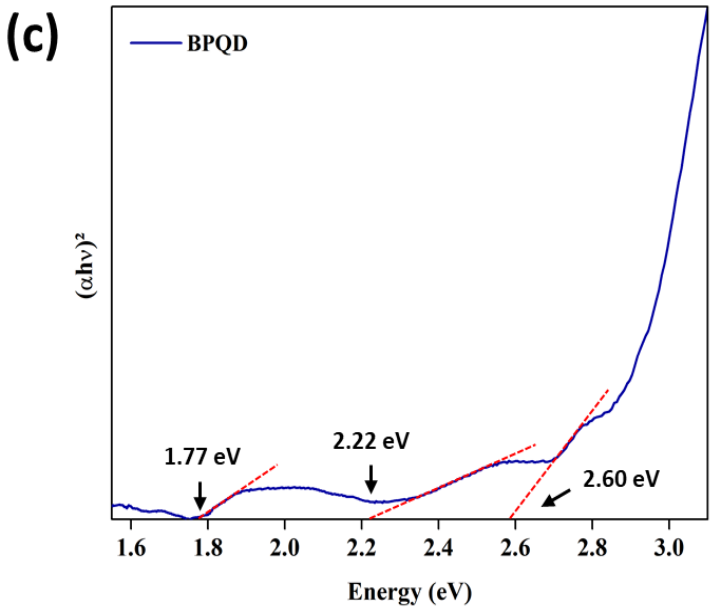

Figure 58. Tauc plot extracted from UV-VIS absorption of (a) bulk BP (b) Phosphorene and (c) BPQD.

However, for the phosphorene suspension (Fig. 58b) two absorptions were detected (dashed lines) indicating bandgap energies at about 1.62 eV and 1.67 eV as can be read from the linear intercept fits. The first bandgap energy value corresponds to that of phosphorene, in great agreement with reported theoretical and experimental bandgap values,[281,282] while for the second, we believe that the fitted energy value corresponds to those phosphorene sheets with a smaller width a fact that increases their bandgap energy. Concerning the BPQDs suspension, the obtained Tauc plot (Fig. 58c) reveals the presence of three absorption edges respectively at about 1.77 eV, 2.22 eV and 2.60 eV, consistent with previous reports on microwave synthesized BPQDs.[283] As will be demonstrated later on, the three energies are in fact linked with the above three size distributions; respectively 2.70 nm, 2.16 nm and 1.72 nm, deduced from HRTEM analyses.

V.5.4. Quantum confinement effect in phosphorene and BPQD

As can be seen, the size-dependent bandgap energies are a fairly obvious indicator of quantum confinement behavior in phosphorene and BPQDs, a finding that is expected since the quantum confinement effect in BP should be observable for sizes below the Bohr radius (~5nm for BP).[284] To investigate such a behavior, DFT and modified-EMA methods were used. Fig. 60 depicts plots of ΔE_g ($= E_g^{qs} - E_g^{bBP}$) as a function of $1/d^2$ for phosphorene and BPQDs where "*bBP*" stands for bulk-BP, "*qs: quantum structure*" stands either for phosphorene or

BPQDs and "*d*" for the size/thickness in these quantum structures. Regarding phosphorene, the bandgap energy was calculated by DFT (HSE06 approximation) as a function of the number of phosphorene layers as shown in Fig. 59 for a monolayer and 2L. A linear fit (red cross) was drawn for 1L, 2L, 3L and 4L (L: phosphorene layer), as shown in Fig. 60a, where our experimental value is indicated with a red empty circle.

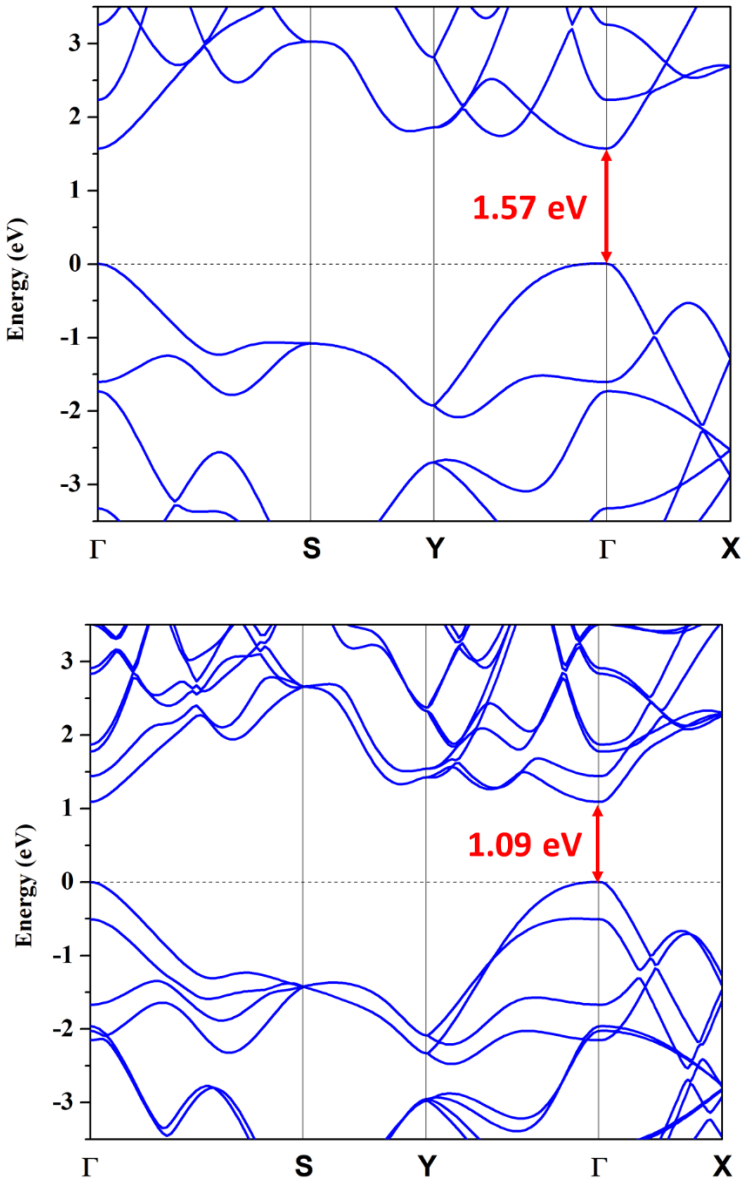

Figure 59. (a) Monolayer and (b) bilayer black phosphorus band structure as calculated with HSE06 approximation.

Comparison with photoluminescence (PL, red plus) data performed by Yang et *al.*[285] is also made for a better appreciation of our findings. For BPQDs, our UV-Vis results (blue empty circles) were confronted to DFT calculations data (blue cross) performed by Niu et *al.*[243] A linear regression is observed with increasing size for both results, although the confinement is seen to be stronger in our experimental data as indicated by the high slope ratio observed.

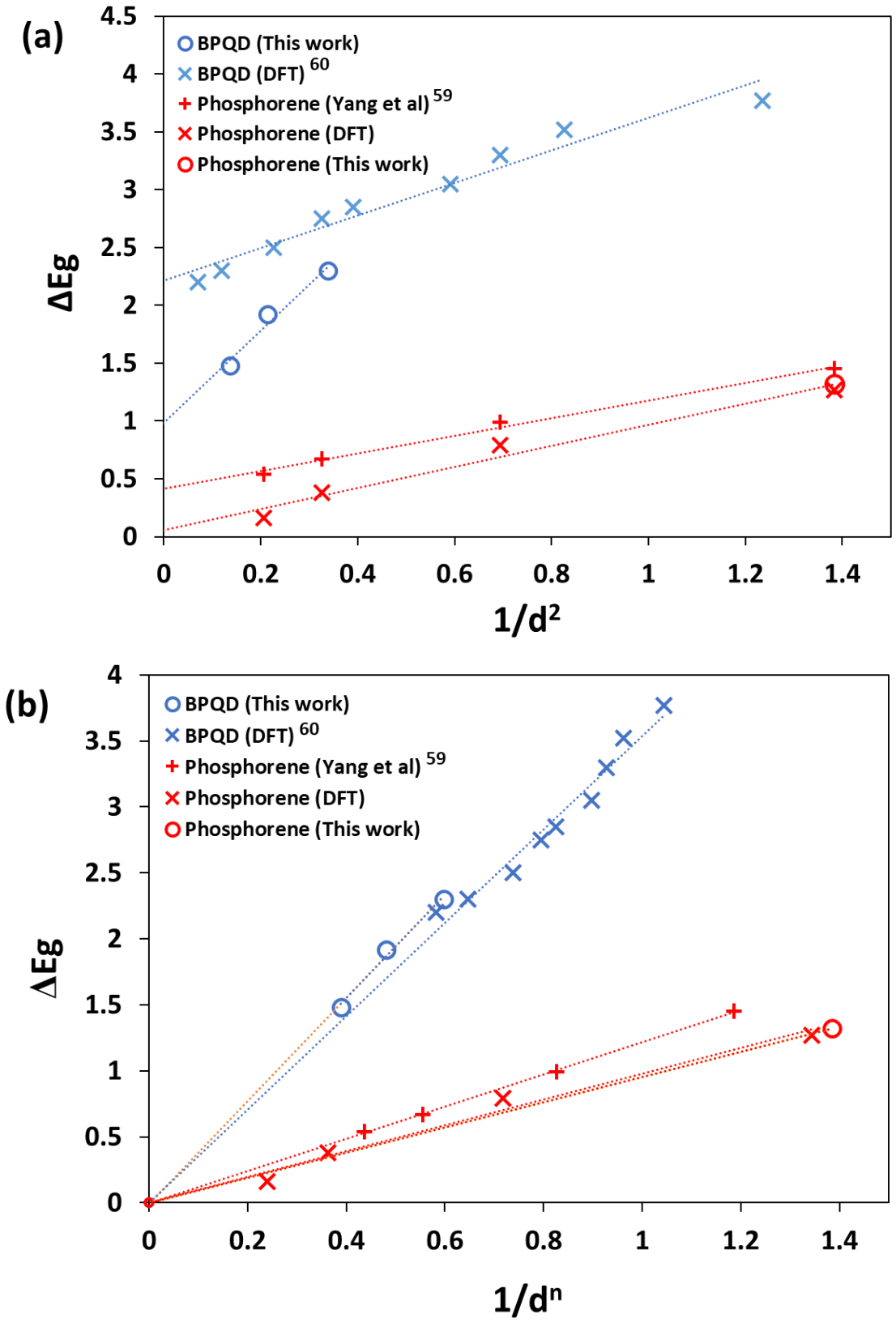

Figure 60. (a) BPQD and Phosphorene data plotted as ΔEg vs 1/d² (b) BPQD and Phosphorene data plotted as ΔEg vs 1/dn. The dotted lines are the data linear fits.

As a first remark, the linear trend of ΔE_g as a function of $1/d^2$ is very obvious in both theoretical and experimental results, in spite of the observed slight difference in the bandgap

energy values in DFT and experimental results. Secondly, and most important, the observed trend does not perfectly scale with $1/d^2$ since the linear fit does not coincide with $\Delta E_g = 0$ for large sizes ($d \to \infty$). This discrepancy is assumed to be due to the parabolic energy bands,[248] as well as to the infinite potential barriers.[248] To overcome such a discrepancy, the ΔE_g is thought to vary as $1/d^n$ as a function of composition and geometric dimensionality of confinement for a finite confinement barrier. In order to shed light on the "n" dependence, different n values for $1/d^n$ were tested as shown in Fig. 60b, for phosphorene and BPQDs quantum structures. In the case of phosphorene, the values obtained for n with an intercept of ΔE_g to 0 is 1.81 for DFT data, which is very close to 2, while for the experimental data it is found to be around 1.05. In the case of BPQDs, intercept to 0 were found for values of "n" around 0.95 and 0.41 for experiment and DFT results, respectively.

From Fig. 60b, it is very clear that the above discrepancies are now hugely reduced where the 3D confinement (BPQDs) and 1D confinement (phosphorene) are well elucidated. As expected, 3D confinement has a larger slope ratio than that in 1D confinement. In this context, the slopes ratio $\mathbf{A}_{1D}/\mathbf{A}_{3D}$ should follow the "rule of thumb"[286] suggesting a value of about 0.25. In our case, the obtained slopes ratio $\mathbf{A}_{phosphorene}/\mathbf{A}_{BPQDs}$ of the linear fit was found to be 0.24, a value that is very close to the predicted one (0.25).

V.5.5. Effective mass calculation in phosphorene and BPQD by EMA

From the aforementioned, we can conclude that our experimental results are in good agreement with the fairly simple modified-EMA model where the quantum confinement in BPQDs is stronger as compared to that in phosphorene due the reduced dimensionality. From such a consistency, the reduced effective mass of phosphorene and BPQDs can be deduced. To assess the reduced effective mass μ, the modified-EMA equation $\Delta E_g = \frac{h^2}{8d^n}\frac{1}{\mu}$ was used, where $\frac{1}{\mu} = (\frac{1}{m_e} + \frac{1}{m_h})$; m_e and m_h are respectively the electron and hole masses. The reduced effective mass of phosphorene ($\mu_{phosphorene}$) and for BPQDs (μ_{BPQDs}) can be deduced from the slope of Fig. 7b, as $\mu = \frac{h^2}{8A}$, where $\mathbf{A} = \Delta E_g d^n$ (**A** being the linear slope fit). Table 7 summarizes the calculated reduced effective masses, $\mu_{phosphorene}$ and μ_{BPQDs}, showing a remarkable accordance between theoretical and experimental data, in addition to the expected increase of μ with increasing the confinement dimensionality. The obtained results demonstrate the great potential in quantum confined materials-based BP for optoelectronic

applications such as solar cells and lasers,[225,287] thanks to their atom-like structure and flexibility in engineering their optical and transport properties.

Table 7. Summary of calculated effective masses

	Bulk	**Phosphorene**			**BPQDs**	
	DFT Ref.[288]	**DFT This work**	**Experimental This work**	**Experimental Ref.[285]**	**Experimental This work**	**DFT Ref.[286]**
μ (m_0)	0.16	0.41	0.33	0.51	1.66	1.51

V.6. Conclusion

In summary, we have demonstrated the performance of BN solvent to synthesize well dispersed and well protected phosphorene and BPQDs. From vibrational characterization, we found that BN solvent tends to protect the as-synthesized phosphorene and BPQD fromj oxidation, as no oxygen peaks around 1000 and 1500 cm^{-1} were visible. Raman spectroscopy showed a shift in B_{2g} and A_g^2 phonon mode in both phosphorene and BPQDs. This Raman shift of 0.96 cm^{-1} for B_{2g} and 2.1 cm^{-1} for A_g^1 further confirms the well dispersed phosphorene layer in the solution with an additional shift for BPQDs. From optical characterization, well-dispersed phosphorene and BPQD were obtained as demonstrated by TEM and electronic diffraction. Optical characterization via UV-VIS showed that the experimental band gap was found to increase as a function of confinement, namely; 1.62 eV for phosphorene to 1.77 eV, 2.22 eV, 2.60 eV for BPQDs. Besides, extensive theoretical studies, by DFT and modified-EMA, reveal that the bandgap variation exhibits a size dependence of $(1/d^n)$ rather than $(1/d^2)$, with n being confinement dimensionality dependent. Phosphorene band gap was found to be $(1/d^{1.05})$ dependent and BPQD $(1/d^{0.95})$. Additionally, the reduced effective mass of such confined materials was calculated from the modified-EMA model, showing an expected increase with increasing the confinement dimensionality.

General conclusion

The objective of this thesis work was twofold: on one hand, it was necessary to achieve good exfoliation and solution stability of exfoliated black phosphorus and BP quantum dots. On the other hand, it was a question of evaluating the electronic and optical properties of these exfoliated-BP and quantum dots at a "nanoscale" using energy loss spectroscopy in a transmission electron microscopy, with the help of UV-Vis spectroscopy and computational methods.

The first part of this study was devoted to perform a detailed structural and electronic study of BP flakes in the low infrared region using monochromated EELS. This study was a pillar to show us the path to optimizing the properties of black phosphorus by exploiting the liquid phase exfoliation. The BP flakes were found to be perpendicular to the analysis axis in core- and low-loss EELS modes. Using core-loss EELS, the characteristic P-$L_{2,3}$ and P-L_1 lines of BP were clearly identified and respectively assigned to $2p^{3/2}\rightarrow 3s$, $2p^{1/2}\rightarrow 3d$ and $2s\rightarrow 3(s+d)$ electronic transitions. In the low-loss EELS zone, the volume plasmon was detected at an energy $E_p = 19.6 \pm 0.1$ eV. With the help of DFT band structure calculations and the highly resolved EELS spectra (20 meV), a fast and direct "lecture" of electronic transitions in the infrared area was possible. Two transitions were respectively assigned along the high symmetry point Z, as the bandgap with an energy of 0.33 ± 0.02 eV and an intraband transition at 0.75 eV. Two more excitations were found to be excitonic in nature as confirmed by the increase of the energy-loss peak intensity with decreasing thickness due to the enhanced screening effect in thick areas. A full description of the imaginary part ($\boldsymbol{\varepsilon}_2$) of the dielectric function was achieved and the dominant critical points assigned to specific IB transitions ($3p\rightarrow 3s$ and $3p\rightarrow 3d_{z^2}$) along Z and Γ high-symmetry points of the Brillouin zone. We finally note that the optical quality of the studied BP flakes may pave the way for optoelectronic and photonic applications. All these findings demonstrate the usefulness of monochromated low-loss EELS in measuring electronic properties of narrow-bandgap semiconductors.

Following the former study, we focused on the exfoliation of the commercialized black phosphorus flakes. Still, for a better understanding of the exfoliation process a study by molecular dynamics simulations was extensively used to elucidate the role of many parameters that contribute to the BP exfoliation/re-aggregation mechanism for a better phosphorene concentration yield. Eight solvents were tested for such a purpose. A planarity parameter δ was first designated to classify these molecules from 0 Å (corresponding to BZ) to a value of 2.14 Å (corresponding to

CHP). Our modeling of BP exfoliation process showed that, in terms of exfoliation ease, planar molecules (δ < 0.5 Å) seem to require less energy than non-planar ones (δ > 0.5 Å) where the δ parameter followed the same trend than that of the energy required to exfoliate. Each exfoliated phosphorene was shown to be surrounded by a dense molecular layer, a sign of a significant interaction between the phosphorene sheet and the solvent molecules. The smaller was the δ parameter, the stronger the surface-molecules interaction energy was. In addition, a collective action between self-diffusion and progressive detachment of the phosphorene sheet was observed. Indeed, the planar was the solvent molecule, the stronger the interaction of phosphorene with surface molecules was, the higher the self-diffusion was, and the easier the exfoliation process was. With regards to re-aggregation, the process seemed to be favored by the formation of a confined molecular layer between the phosphorene sheets as the results of the solvent molecules cohesion energy. In this sense, non-planar molecules were shown unfavorable neither for a stable phosphorene suspension nor for an easy exfoliation process. The lower is the surface-molecules interaction energy, the more pronounced the re-aggregation process is.

The previous molecular dynamics simulation study showed that the BN solvent helped synthesize well dispersed and well protected phosphorene and BPQDs. From vibrational characterization, we found that BN solvent tends to protect the as-synthesized phosphorene and BPQD from oxidation, as no oxygen peaks around 1000 and 1500 cm^{-1} were visible. Raman spectroscopy showed a shift in B_{2g} and A_g^2 phonon mode in both phosphorene and BPQDs. This Raman shift of 0.96 cm^{-1} for B_{2g} and 2.1 cm^{-1} for A_g^1 further confirms the well dispersed phosphorene layer in the solution with an additional shift for BPQDs. From optical characterization, well-dispersed phosphorene and BPQD were obtained as demonstrated by TEM and electronic diffraction. Optical characterization via UV-VIS showed that the experimental band gap was found to increase as a function of confinement, namely; 1.62 eV for phosphorene to 1.77 eV, 2.22 eV, 2.60 eV for BPQDs with respectable sizes of 2.7 nm, 2.16 nm and 1.72 respectively for the BPQDs. In addition, extensive theoretical studies, by DFT and modified-EMA, reveal that the bandgap variation exhibits a size dependence of $(1/d^n)$ rather than $(1/d^2)$, with *n* being confinement dimensionality dependent. Phosphorene band gap was found to be $(1/d^{1.05})$ dependent and BPQD $(1/d^{0.95})$. Additionally, the reduced effective mass of such confined materials was calculated from the modified-EMA model, showing an expected increase with increasing the confinement dimensionality. The obtained results demonstrate the great potential in quantum confined materials-based BP for optoelectronic applications such as solar cells and lasers

thanks to their atom-like structure and flexibility in engineering their optical and transport properties.

References

[1] Novoselov, K. S., Geim, A. K., Morozov, S. V., Jiang, D. E., Zhang, Y., Dubonos, S. V., ... & Firsov, A. A. (2004). Electric field effect in atomically thin carbon films. science, 306(5696), 666-669.

[2] Zhu, F. F., Chen, W. J., Xu, Y., Gao, C. L., Guan, D. D., Liu, C. H., ... & Jia, J. F. (2015). Epitaxial growth of two-dimensional stanene. Nature materials, 14(10), 1020-1025.

[3] Acun, A., Zhang, L., Bampoulis, P., Farmanbar, M. V., van Houselt, A., Rudenko, A. N., ... & Zandvliet, H. J. (2015). Germanene: the germanium analogue of graphene. Journal of physics: Condensed matter, 27(44), 443002.

[4] Splendiani, A., Sun, L., Zhang, Y., Li, T., Kim, J., Chim, C. Y., ... & Wang, F. (2010). Emerging photoluminescence in monolayer MoS2. Nano letters, 10(4), 1271-1275.

[5] Ling, X., Wang, H., Huang, S., Xia, F., & Dresselhaus, M. S. (2015). The renaissance of black phosphorus. Proceedings of the National Academy of Sciences, 112(15), 4523-4530.

[6] Akinwande, D., Brennan, C. J., Bunch, J. S., Egberts, P., Felts, J. R., Gao, H., ... & Zhu, Y. (2017). A review on mechanics and mechanical properties of 2D materials—Graphene and beyond. Extreme Mechanics Letters, 13, 42-77.

[7] Li, X. L., Han, W. P., Wu, J. B., Qiao, X. F., Zhang, J., & Tan, P. H. (2017). Layer-number dependent optical properties of 2D materials and their application for thickness determination. Advanced Functional Materials, 27(19), 1604468.

[8] Li, G., Zhang, Y. Y., Guo, H., Huang, L., Lu, H., Lin, X., ... & Gao, H. J. (2018). Epitaxial growth and physical properties of 2D materials beyond graphene: from monatomic materials to binary compounds. Chemical Society Reviews, 47(16), 6073-6100.

[9] Ma, Q., Ren, G., Xu, K., & Ou, J. Z. (2021). Tunable optical properties of 2D materials and their applications. Advanced Optical Materials, 9(2), 2001313.

[10] Wang, C., Zhang, G., Huang, S., Xie, Y., & Yan, H. (2020). The optical properties and plasmonics of anisotropic 2D materials. Advanced Optical Materials, 8(5), 1900996.

[11] Kim, S. J., Choi, K., Lee, B., Kim, Y., & Hong, B. H. (2015). Materials for flexible, stretchable electronics: graphene and 2D materials. Annual Review of Materials Research, 45, 63-84.

[12] Anichini, C., Czepa, W., Pakulski, D., Aliprandi, A., Ciesielski, A., & Samorì, P. (2018). Chemical sensing with 2D materials. Chemical Society Reviews, 47(13), 4860-4908.

[13] Martín, C., Kostarelos, K., Prato, M., & Bianco, A. (2019). Biocompatibility and biodegradability of 2D materials: graphene and beyond. Chemical Communications, 55(39), 5540-5546.

[14] Zhang, W., Wang, Q., Chen, Y., Wang, Z., & Wee, A. T. (2016). Van der Waals stacked 2D layered materials for optoelectronics. 2D Materials, 3(2), 022001.

[15] Kim, J., Baik, S. S., Ryu, S. H., Sohn, Y., Park, S., Park, B. G., ... & Kim, K. S. (2015). Observation of tunable band gap and anisotropic Dirac semimetal state in black phosphorus. Science, 349(6249), 723-726.

[16] Qiao, J., Kong, X., Hu, Z. X., Yang, F., & Ji, W. (2014). High-mobility transport anisotropy and linear dichroism in few-layer black phosphorus. Nature communications, 5(1), 1-7.

[17] Wang, Y., Wu, F., Liu, X., Lin, J., Chen, J. Y., Wu, W. W., ... & Liao, L. (2019). High on/off ratio black phosphorus based memristor with ultra-thin phosphorus oxide layer. Applied Physics Letters, 115(19), 193503.

[18] Tran, V., Soklaski, R., Liang, Y., & Yang, L. (2014). Tunable band gap and anisotropic optical response in few-layer black phosphorus. arXiv preprint arXiv:1402.4192.

[19] Sotor, J., Sobon, G., Macherzynski, W., Paletko, P., & Abramski, K. M. (2015). Black phosphorus saturable absorber for ultrashort pulse generation. Applied Physics Letters, 107(5), 051108.

[20] Margulis, V. A., Muryumin, E. E., & Gaiduk, E. A. (2018). Optical Kerr effect and two-photon absorption in monolayer black phosphorus. Journal of Optics, 20(5), 055503.

[21] Batmunkh, M., Bat-Erdene, M., & Shapter, J. G. (2018). Black phosphorus: synthesis and application for solar cells. Advanced Energy Materials, 8(5), 1701832.

[22] Li, Y., Liu, Z., Hou, Y., Yang, G., Fei, X., Zhao, H., ... & Guo, Z. (2017). Multifunctional nanoplatform based on black phosphorus quantum dots for bioimaging and photodynamic/photothermal synergistic cancer therapy. ACS applied materials & interfaces, 9(30), 25098-25106.

[23] Qiu, M., Wang, D., Liang, W., Liu, L., Zhang, Y., Chen, X., ... & Cao, Y. (2018). Novel concept of the smart NIR-light–controlled drug release of black phosphorus nanostructure for cancer therapy. Proceedings of the National Academy of Sciences, 115(3), 501-506.

[24] Wang, H., Yang, X., Shao, W., Chen, S., Xie, J., Zhang, X., ... & Xie, Y. (2015). Ultrathin black phosphorus nanosheets for efficient singlet oxygen generation. Journal of the American Chemical Society, 137(35), 11376-11382.

[25] Bridgman, P. W. (1914). TWO NEW MODIFICATIONS OF PHOSPHORUS. Journal of the American Chemical Society, 36(7), 1344-1363.

[26] Li, L., Yu, Y., Ye, G. J., Ge, Q., Ou, X., Wu, H., ... & Zhang, Y. (2014). Black phosphorus field-effect transistors. Nature nanotechnology, 9(5), 372-377.

[27] Brown, A., & Rundqvist, S. (1965). Refinement of the crystal structure of black phosphorus. Acta Crystallographica, 19(4), 684-685.

[28] Maruyama, Y., Suzuki, S., Kobayashi, K., & Tanuma, S. (1981). Synthesis and some properties of black phosphorus single crystals. Physica B+ c, 105(1-3), 99-102.

[29] Lange, S., Schmidt, P., & Nilges, T. (2007). Au3SnP7@ black phosphorus: an easy access to black phosphorus. Inorganic chemistry, 46(10), 4028-4035.

[30] Nilges, T., Kersting, M., & Pfeifer, T. (2008). A fast low-pressure transport route to large black phosphorus single crystals. Journal of solid-state chemistry, 181(8), 1707-1711.

[31] Köpf, M., Eckstein, N., Pfister, D., Grotz, C., Krüger, I., Greiwe, M., ... & Nilges, T. (2014). Access and in situ growth of phosphorene-precursor black phosphorus. Journal of crystal growth, 405, 6-10.

[32] Tiouitchi, G., Hamedoun, M., El Kenz, A., Benyoussef, A., Lachgar, A., Mahmoud, A., ... & Mounkachi, O. (2017). An easy route to synthesis black phosphorus at low pressure and soft conditions.

[33] Guan, L., Xing, B., Niu, X., Wang, D., Yu, Y., Zhang, S., ... & Sha, J. (2018). Metal-assisted exfoliation of few-layer black phosphorus with high yield. Chemical Communications, 54(6), 595-598.

[34] Hernandez, Y., Nicolosi, V., Lotya, M., Blighe, F. M., Sun, Z., De, S., ... & Coleman, J. N. (2008). High-yield production of graphene by liquid-phase exfoliation of graphite. Nature nanotechnology, 3(9), 563-568.

[35] Zhang, X., Xie, H., Liu, Z., Tan, C., Luo, Z., Li, H., ... & Zhang, H. (2015). Black phosphorus quantum dots. Angewandte chemie international edition, 54(12), 3653-3657.

[36] Gui, R., Jin, H., Wang, Z., & Li, J. (2018). Black phosphorus quantum dots: synthesis, properties, functionalized modification and applications. Chemical Society Reviews, 47(17), 6795-6823.

[37] Sun, Z., Xie, H., Tang, S., Yu, X. F., Guo, Z., Shao, J., ... & Chu, P. K. (2015). Ultrasmall black phosphorus quantum dots: synthesis and use as photothermal agents. Angewandte Chemie International Edition, 54(39), 11526-11530.

[38] Zhu, C., Xu, F., Zhang, L., Li, M., Chen, J., Xu, S., ... & Sun, L. (2016). Ultrafast preparation of black phosphorus quantum dots for efficient humidity sensing. Chemistry–A European Journal, 22(22), 7357-7362.

[39] Zhu, C., Xu, F., Zhang, L., Li, M., Chen, J., Xu, S., ... & Sun, L. (2016). Ultrafast preparation of black phosphorus quantum dots for efficient humidity sensing. Chemistry–A European Journal, 22(22), 7357-7362.

[40] Xu, Y., Wang, Z., Guo, Z., Huang, H., Xiao, Q., Zhang, H., & Yu, X. F. (2016). Solvothermal synthesis and ultrafast photonics of black phosphorus quantum dots. Advanced Optical Materials, 4(8), 1223-1229.

[41] Han, S. T., Hu, L., Wang, X., Zhou, Y., Zeng, Y. J., Ruan, S., ... & Peng, Z. (2017). Black phosphorus quantum dots with tunable memory properties and multilevel resistive switching characteristics. Advanced Science, 4(8), 1600435.

[42] Liu, S., Lin, S., You, P., Surya, C., Lau, S. P., & Yan, F. (2017). Black phosphorus quantum dots used for boosting light harvesting in organic photovoltaics. Angewandte Chemie, 129(44), 13905-13909.

[43] Liu, M., Jiang, X. F., Yan, Y. R., Wang, X. D., Luo, A. P., Xu, W. C., & Luo, Z. C. (2018). Black phosphorus quantum dots for femtosecond laser photonics. Optics Communications, 406, 85-90.

[44] Sun, Z., Zhao, Y., Li, Z., Cui, H., Zhou, Y., Li, W., ... & Yu, X. F. (2017). TiL4-Coordinated black phosphorus quantum dots as an efficient contrast agent for in vivo photoacoustic imaging of cancer. Small, 13(11), 1602896.

[45] Zhu, C., Xu, F., Zhang, L., Li, M., Chen, J., Xu, S., ... & Sun, L. (2016). Ultrafast preparation of black phosphorus quantum dots for efficient humidity sensing. Chemistry–A European Journal, 22(22), 7357-7362.

[46] De Broglie, L. (1924). Recherches sur la théorie des quanta (Doctoral dissertation, Migration-université en cours d'affectation).

[47] Schrödinger, E. (1926). An undulatory theory of the mechanics of atoms and molecules. Physical review, 28(6), 1049.

[48] Hohemberg, P. (1965). Physical Reviews 1964, 136, B864; b) W. Kohn, LJ Sham. Physical Reviews, 140, A1133.

[49] Sham, L. J., & Kohn, W. (1966). One-particle properties of an inhomogeneous interacting electron gas. Physical Review, 145(2), 561.

[50] Parr, R. G. (1980). Density functional theory of atoms and molecules. In Horizons of quantum chemistry (pp. 5-15). Springer, Dordrecht.

[51] Perdew, J. P., Burke, K., & Ernzerhof, M. (1996). Generalized gradient approximation made simple. Physical review letters, 77(18), 3865.

[52] Harris, J., & Jones, R. O. (1974). The surface energy of a bounded electron gas. Journal of Physics F: Metal Physics, 4(8), 1170.

[53] Becke, A. D. (1993). A new mixing of Hartree–Fock and local density-functional theories. The Journal of chemical physics, 98(2), 1372-1377.

[54] Ernzerhof, M., & Scuseria, G. E. (1999). Assessment of the Perdew–Burke–Ernzerhof exchange-correlation functional. The Journal of chemical physics, 110(11), 5029-5036.

[55] Adamo, C., & Barone, V. (1999). Toward reliable density functional methods without adjustable

parameters: The PBE0 model. The Journal of chemical physics, 110(13), 6158-6170.

[56] Heyd, J., Scuseria, G. E., & Ernzerhof, M. (2003). Hybrid functionals based on a screened Coulomb potential. The Journal of chemical physics, 118(18), 8207-8215.

[57] Rydberg, H., Lundqvist, B. I., Langreth, D. C., & Dion, M. (2000). Tractable nonlocal correlation density functionals for flat surfaces and slabs. Physical Review B, 62(11), 6997.

[58] Hult, E., Andersson, Y., Lundqvist, B. I., & Langreth, D. C. (1996). Density functional for van der Waals forces at surfaces. Physical review letters, 77(10), 2029.

[59] Andersson, Y., Hult, E., Apell, P., Langreth, D. C., & Lundqvist, B. I. (1998). Density-functional account of van der Waals forces between parallel surfaces. Solid state communications, 106(5), 235-238.

[60] Klimeš, J., Bowler, D. R., & Michaelides, A. (2009). Chemical accuracy for the van der Waals density functional. Journal of Physics: Condensed Matter, 22(2), 022201.

[61] Alder, B. J., & Wainwright, T. E. (1957). Phase transition for a hard sphere system. The Journal of chemical physics, 27(5), 1208-1209.

[62] Rahman, A. (1964). Correlations in the motion of atoms in liquid argon. Physical review, 136(2A), A405.

[63] Verlet, L. (1967). Computer" experiments" on classical fluids. I. Thermodynamical properties of Lennard-Jones molecules. Physical review, 159(1), 98.

[64] Verlet, L. (1968). Computer" experiments" on classical fluids. ii. equilibrium correlation functions. Physical Review, 165(1), 201.

[65] Hansen, J. P., & Verlet, L. (1969). Phase transitions of the Lennard-Jones system. physical Review, 184(1), 151.

[66] Rahman, A., & Stillinger, F. H. (1971). Molecular dynamics study of liquid water. The Journal of Chemical Physics, 55(7), 3336-3359.

[67] Lerbret, A., Bordat, P., Affouard, F., Descamps, M., & Migliardo, F. (2005). How homogeneous are the trehalose, maltose, and sucrose water solutions? An insight from molecular dynamics simulations. The Journal of Physical Chemistry B, 109(21), 11046-11057.

[68] Bordat, P., Lerbret, A., Demaret, J. P., Affouard, F., & Descamps, M. (2004). Comparative study of trehalose, sucrose and maltose in water solutions by molecular modelling. EPL (Europhysics Letters), 65(1), 41.

[69] Avile, F. X.; Gargallo, R.; Hu, P. H.; Oliva, B. Molecular Dynamics Simulation of Highly Charged Proteins: Comparison of the Particle-Particle Particle-Mesh and Reaction Field Methods for the Calculation of Electrostatic Interactions. 2003, 2161–2172.

[70] Jorgensen, W. L., Maxwell, D. S., & Tirado-Rives, J. (1996). Development and testing of the OPLS all-atom force field on conformational energetics and properties of organic liquids. Journal of the American Chemical Society, 118(45), 11225-11236.

[71] Gray, G. W., & Goodby, J. W. (1984). Smectic liquid crystals: Textures and structures. Heyden & son, 247 south 41 street st., Philadelphia, pa 19104, USA, 1984, 256.

[72] Hachtel, J. A., Lupini, A. R., & Idrobo, J. C. (2018). Exploring the capabilities of monochromated electron energy loss spectroscopy in the infrared regime. Scientific reports, 8(1), 1-10.

[73] Woomer, A. H., Farnsworth, T. W., Hu, J., Wells, R. A., Donley, C. L., & Warren, S. C. (2015). Phosphorene: synthesis, scale-up, and quantitative optical spectroscopy. ACS nano, 9(9), 8869-8884.

[74] Yasaei, P., Kumar, B., Foroozan, T., Wang, C., Asadi, M., Tuschel, D., ... & Salehi-Khojin, A. (2015). High-quality black phosphorus atomic layers by liquid-phase exfoliation. Advanced Materials, 27(11), 1887-1892.

[75] Hanlon, D., Backes, C., Doherty, E., Cucinotta, C. S., Berner, N. C., Boland, C., ... & Coleman, J. N. (2015). Liquid exfoliation of solvent-stabilized few-layer black phosphorus for applications beyond electronics. Nature communications, 6(1), 1-11.

[76] Del Rio Castillo, A. E., Pellegrini, V., Sun, H., Buha, J., Dinh, D. A., Lago, E., ... & Bonaccorso, F. (2018). Exfoliation of few-layer black phosphorus in low-boiling-point solvents and its application in Li-ion batteries. Chemistry of Materials, 30(2), 506-516.

[77] Chen, W., Li, K., Wang, Y., Feng, X., Liao, Z., Su, Q., ... & He, Z. (2017). Black phosphorus quantum dots for hole extraction of typical planar hybrid perovskite solar cells. The journal of physical chemistry letters, 8(3), 591-598.

[78] Meng, M., Gan, Z., Zhang, J., Liu, K., Wang, L., Li, S., ... & Li, J. (2017). Hierarchical self-assembly of black phosphorus quantum dots with quantum confinement effects to a centimeter-scale membrane. physica status solidi (b), 254(7), 1700011.

[79] Zhu, C., Xu, F., Zhang, L., Li, M., Chen, J., Xu, S., ... & Sun, L. (2016). Ultrafast preparation of black phosphorus quantum dots for efficient humidity sensing. Chemistry–A European Journal, 22(22), 7357-7362.

[80] Tran V, Soklaski R, Liang Y, Yang L. Layer-controlled band gap and anisotropic excitons in few-layer black phosphorus. Physical Review B. 2014 Jun 26;89(23):235319.

[81] Long G, Maryenko D, Shen J, Xu S, Hou J, Wu Z, Wong WK, Han T, Lin J, Cai Y, Lortz R. Achieving ultrahigh carrier mobility in two-dimensional hole gas of black phosphorus. Nano letters. 2016 Dec 14;16(12):7768-73.

[82] Buscema M, Groenendijk DJ, Blanter SI, Steele GA, Van Der Zant HS, Castellanos-Gomez A. Fast and broadband photoresponse of few-layer black phosphorus field-effect transistors. Nano letters. 2014 Jun 11;14(6):3347-52.

[83] Ge S, Li C, Zhang Z, Zhang C, Zhang Y, Qiu J, Wang Q, Liu J, Jia S, Feng J, Sun D. Dynamical evolution of anisotropic response in black phosphorus under ultrafast photoexcitation. Nano letters. 2015 Jul 8;15(7):4650-6.

[84] Zheng S, Wu E, Feng Z, Zhang R, Xie Y, Yu Y, Zhang R, Li Q, Liu J, Pang W, Zhang H. Acoustically enhanced photodetection by a black phosphorus–MoS 2 van der Waals heterojunction p–n diode. Nanoscale. 2018;10(21):10148-53.

[85] Abbas AN, Liu B, Chen L, Ma Y, Cong S, Aroonyadet N, Köpf M, Nilges T, Zhou C. Black phosphorus gas sensors. ACS nano. 2015 May 26;9(5):5618-24.

[86] Wang Y, Zhang F, Tang X, Chen X, Chen Y, Huang W, Liang Z, Wu L, Ge Y, Song Y, Liu J. All-Optical Phosphorene Phase Modulator with Enhanced Stability Under Ambient Conditions. Laser & Photonics Reviews. 2018 Jun;12(6):1800016.

[87] Wang Q, Yu L, Qi CB, Ding J, He XM, Wang RQ, Feng YQ. Rapid and sensitive serum glucose determination using chemical labeling coupled with black phosphorus-assisted laser desorption/ionization time-of-flight mass spectrometry. Talanta. 2018 Jan 1;176:344-9.

[88] Buscema M, Groenendijk DJ, Steele GA, Van Der Zant HS, Castellanos-Gomez A. Photovoltaic effect in few-layer black phosphorus PN junctions defined by local electrostatic gating. Nature communications. 2014 Aug 28;5(1):1-6.

[89] Li L, Kim J, Jin C, Ye GJ, Qiu DY, Felipe H, Shi Z, Chen L, Zhang Z, Yang F, Watanabe K. Direct observation of the layer-dependent electronic structure in phosphorene. Nature nanotechnology. 2017 Jan;12(1):21.

[90] Li L, Yu Y, Ye GJ, Ge Q, Ou X, Wu H, Feng D, Chen XH, Zhang Y. Black phosphorus field-effect transistors. Nature nanotechnology. 2014 May;9(5):372.

[91] Guo H, Cui X, Zhou W, Han D, Lin C, Cao L, Feng M. Linear scanning tunneling spectroscopy over a large energy range in black phosphorus. Journal of Applied Physics. 2018 Jul 28;124(4):045301.

[92] Zhang CD, Lian JC, Yi W, Jiang YH, Liu LW, Hu H, Xiao WD, Du SX, Sun LL, Gao HJ. Surface structures of black phosphorus investigated with scanning tunneling microscopy. The Journal of Physical Chemistry C. 2009 Oct 29;113(43):18823-6.

[93] Xia F, Wang H, Jia Y. Rediscovering black phosphorus as an anisotropic layered material for optoelectronics and electronics. Nature communications. 2014 Jul 21;5(1):1-6.

[94] Hachtel JA, Lupini AR, Idrobo JC. Exploring the capabilities of monochromated electron energy loss spectroscopy in the infrared regime. Scientific reports. 2018 Apr 4;8(1):1-0.

[95] Varela M, Lupini AR, Benthem KV, Borisevich AY, Chisholm MF, Shibata N, Abe E, Pennycook SJ. Materials characterization in the aberration-corrected scanning transmission electron microscope. Annu. Rev. Mater. Res.. 2005 Aug 4;35:539-69.

[96] De Abajo FG. Optical excitations in electron microscopy. Reviews of modern physics. 2010 Feb 3;82(1):209.

[97] Kimoto K, Kothleitner G, Grogger W, Matsui Y, Hofer F. Advantages of a monochromator for bandgap measurements using electron energy-loss spectroscopy. Micron. 2005 Feb 1;36(2):185-9.

[98] Weeks, M. E. (1932). The discovery of the elements. II. Elements known to the alchemists. Journal of Chemical Education, 9(1), 11.

[99] Bridgman, P. W. (1914). Two new modifications of phosphorus. Journal of the American Chemical Society, 36(7), 1344-1363.

[100] Hultgren, R., Gingrich, N. S., & Warren, B. E. (1935). The atomic distribution in red and black phosphorus and the crystal structure of black phosphorus. The Journal of Chemical Physics, 3(6), 351-355.

[101] Brown, A., & Rundqvist, S. (1965). Refinement of the crystal structure of black phosphorus. Acta Crystallographica, 19(4), 684-685.

[102] Takao, Y., Asahina, H., & Morita, A. (1981). Electronic structure of black phosphorus in tight binding approach. Journal of the Physical Society of Japan, 50(10), 3362-3369.

[103] Zhang, J. L., Zhao, S., Han, C., Wang, Z., Zhong, S., Sun, S., ... & Chen, W. (2016). Epitaxial growth of single layer blue phosphorus: a new phase of two-dimensional phosphorus. Nano letters, 16(8), 4903-4908.

[104] Morita, A. (1986). Semiconducting black phosphorus. Applied Physics A, 39(4), 227-242.

[105] Appalakondaiah, S., Vaitheeswaran, G., Lebegue, S., Christensen, N. E., & Svane, A. (2012). Effect of van der Waals interactions on the structural and elastic properties of black phosphorus. Physical Review B, 86(3), 035105.

[106] Guan, J., Zhu, Z., & Tománek, D. (2014). Phase coexistence and metal-insulator transition in few-layer phosphorene: a computational study. Physical review letters, 113(4), 046804.

[107] Zhu, Z., & Tománek, D. (2014). Semiconducting layered blue phosphorus: a computational study. Physical review letters, 112(17), 176802.

[108] Akhtar, M., Anderson, G., Zhao, R., Alruqi, A., Mroczkowska, J. E., Sumanasekera, G., & Jasinski, J. B. (2017). Recent advances in synthesis, properties, and applications of phosphorene. npj 2D Materials and Applications, 1(1), 1-13.

[109] Castellanos-Gomez, A., Vicarelli, L., Prada, E., Island, J. O., Narasimha-Acharya, K. L., Blanter, S. I., ... & Van Der Zant, H. S. (2014). Isolation and characterization of few-layer black phosphorus. 2D Materials, 1(2), 025001.

[110] Pauling, Linus and Simonetta, Massimo (1952). Bond orbitals and bond energy in elementary phosphorus. The Journal of Chemical Physics, 20 (1), 29–34.

[111] Qiao, J., Kong, X., Hu, Z. X., Yang, F., & Ji, W. (2014). High-mobility transport anisotropy and linear dichroism in few-layer black phosphorus. Nature communications, 5(1), 1-7.

[112] Liu, S., Huo, N., Gan, S., Li, Y., Wei, Z., Huang, B., ... & Chen, H. (2015). Thickness-dependent Raman spectra, transport properties and infrared photoresponse of few-layer black phosphorus. Journal of Materials Chemistry C, 3(42), 10974-10980.

[113] Tiouitchi G, Ali MA, Benyoussef A, Hamedoun M, Lachgar A, Benaissa M, Kara A, Ennaoui A, Mahmoud A, Boschini F, Oughaddou H. An easy route to synthesize high-quality black phosphorus from amorphous red phosphorus. Materials Letters. 2019 Feb 1;236:56-9.

[114] Schwarz K, Blaha P, Madsen GK. Electronic structure calculations of solids using the WIEN2k package for material sciences. Computer physics communications. 2002 Aug 1;147(1-2):71-6.

[115] Perdew, John P., Kieron Burke, and Matthias Ernzerhof. "Generalized gradient approximation made simple." Physical review letters 77.18 (1996):3865.

[116] Tran F, Blaha P. Implementation of screened hybrid functionals based on the Yukawa potential within the LAPW basis set. Physical Review B. 2011 Jun 9;83(23):235118.

[117] Heyd J, Scuseria GE. Efficient hybrid density functional calculations in solids: Assessment of the Heyd–Scuseria–Ernzerhof screened Coulomb hybrid functional. The Journal of chemical physics. 2004 Jul 15;121(3):1187-92.

[118] Klimeš J, Bowler DR, Michaelides A. Chemical accuracy for the van der Waals density functional. Journal of Physics: Condensed Matter. 2009 Dec 10;22(2):022201.

[119] Monkhorst HJ, Pack JD. Special points for Brillouin-zone integrations. Physical review B. 1976 Jun 15;13(12):5188.

[120] Cheng Y, Zhu Y, Han Y, Liu Z, Yang B, Nie A, Huang W, Shahbazian-Yassar R, Mashayek F. Sodium-induced reordering of atomic stacks in black phosphorus. Chemistry of Materials. 2017 Feb 14;29(3):1350-6.

[121] Muller DA, Singh DJ, Silcox J. Connections between the electron-energy-loss spectra, the local electronic structure, and the physical properties of a material: A study of nickel aluminum alloys. Physical Review B. 1998 Apr 1;57(14):8181.

[122] Jürgensen A. The P (1s) and P (2p) XAFS spectra of elemental phosphorus, theory and experiment. Physica Scripta. 2005;2005(T115):548.

[123] Taniguchi M, Suga S, Seki M, Sakamoto H, Kanzaki H, Akahama Y, Terada S, Endo S, Narita S. Valence band and core-level photoemission spectra of black phosphorus single crystals. Solid State Communications. 1983 Jan 1;45(2):59-61.

[124] Taniguchi M, Seki M, Suga S, Mikuni A, Kanzaki H, Akahama Y, Endo S, Narita S. Core-level reflectance spectroscopy of black phosphorus single crystals. Physical Review B. 1983 Jul 15;28(2):1165.

[125] Nicotra G, Politano A, Mio AM, Deretzis I, Hu J, Mao ZQ, Wei J, La Magna A, Spinella C. Absorption edges of black phosphorus: a comparative analysis. physica status solidi (b). 2016 Dec;253(12):2509-14.

[126] Hayes W, Brown FC. Absorption by Some Molecular Gases in the Extreme Ultraviolet. Physical Review A. 1972 Jul 1;6(1):21.

[127] Nicotra G, van Veen E, Deretzis I, Wang L, Hu J, Mao Z, Fabio V, Spinella C, Chiarello G, Rudenko A, Yuan S. Anisotropic ultraviolet-plasmon dispersion in black phosphorus. Nanoscale. 2018;10(46):21918-27.

[128] Wu RJ, Topsakal M, Low T, Robbins MC, Haratipour N, Jeong JS, Wentzcovitch RM, Koester SJ, Mkhoyan KA. Atomic and electronic structure of exfoliated black phosphorus. Journal of Vacuum Science & Technology A: Vacuum, Surfaces, and Films. 2015 Nov 16;33(6):060604.

[129] Egerton RF. Electron energy-loss spectroscopy in the electron microscope. Springer Science & Business Media; 2011 Jul 29.

[130] Egerton RF, Cheng SC. Characterization of an analytical electron microscope with a NiO test specimen. Ultramicroscopy. 1994 Jul 1;55(1):43-54.

[131] Jin Q, Li D. Determining Inelastic Mean Free Path by Electron Energy Loss Spectroscopy. Microscopy and Microanalysis. 2006 Aug;12(S02):1186-7.

[132] Bullock J, Amani M, Cho J, Chen YZ, Ahn GH, Adinolfi V, Shrestha VR, Gao Y, Crozier KB, Chueh YL, Javey A. Polarization-resolved black phosphorus/molybdenum disulfide mid-wave infrared photodiodes with high detectivity at room temperature. Nature Photonics. 2018 Oct;12(10):601-7.

[133] Castellanos-Gomez A. Black phosphorus: narrow gap, wide applications. The journal of physical chemistry letters. 2015 Nov 5;6(21):4280-91.

[134] Tran V, Fei R, Yang L. Quasiparticle energies, excitons, and optical spectra of few-layer black phosphorus. 2D Materials. 2015 Nov 23;2(4):044014.

[135] Li Y, Yang S, Li J. Modulation of the electronic properties of ultrathin black phosphorus by strain and electrical field. The Journal of Physical Chemistry C. 2014 Oct 16;118(41):23970-6.

[136] Schuster R, Trinckauf J, Habenicht C, Knupfer M, Büchner B. Anisotropic particle-hole excitations in black phosphorus. Physical review letters. 2015 Jul 10;115(2):026404.

[137] Jiang Z, Liu Z, Li Y, Duan W. Scaling universality between band gap and exciton binding energy of two-dimensional semiconductors. Physical review letters. 2017 Jun 27;118(26):266401.

[138] Zhang S, Yang J, Xu R, Wang F, Li W, Ghufran M, Zhang YW, Yu Z, Zhang G, Qin Q, Lu Y. Extraordinary photoluminescence and strong temperature/angle-dependent Raman responses in few-layer phosphorene. ACS nano. 2014 Sep 23;8(9):9590-6.

[139] Nerl HC, Winther KT, Hage FS, Thygesen KS, Houben L, Backes C, Coleman JN, Ramasse QM, Nicolosi V. Probing the local nature of excitons and plasmons in few-layer MoS2. npj 2D Materials and Applications. 2017 Apr 11;1(1):1-9.

[140] Rohlfing, M., & Louie, S. G. (2000). Electron-hole excitations and optical spectra from first principles. Physical Review B, 62(8), 4927.

[141] Pines D. Collective energy losses in solids. Reviews of modern physics. 1956 Jul 1;28(3):184.

[142] Tran V, Fei R, Yang L. Quasiparticle energies, excitons, and optical spectra of few-layer black phosphorus. 2D Materials. 2015 Nov 23;2(4):044014.

[143] David DG, Godet C, Johansson FO, Lindblad A. Quantitative analysis of plasmon excitations in hard x-ray photoelectron spectra of bulk black phosphorus. Applied Surface Science. 2020 Mar 1; 505:144385.

[144] Samuel Reich, E. (2014). Phosphorene excites materials scientists. Nature News, 506(7486), 19.

[145] Das, S., Zhang, W., Demarteau, M., Hoffmann, A., Dubey, M., & Roelofs, A. (2014). Tunable transport gap in phosphorene. Nano letters, 14(10), 5733-5739.

[146] Liu, H., Neal, A. T., Zhu, Z., Luo, Z., Xu, X., Tománek, D., & Ye, P. D. (2014). Phosphorene: an unexplored 2D semiconductor with a high hole mobility. ACS nano, 8(4), 4033-4041.

[147] Huang, M., Wang, M., Chen, C., Ma, Z., Li, X., Han, J., & Wu, Y. (2016). Broadband black-phosphorus photodetectors with high responsivity. Advanced Materials, 28(18), 3481-3485.

[148] Li, L., Chen, L., Mukherjee, S., Gao, J., Sun, H., Liu, Z., ... & Koratkar, N. (2017). Phosphorene as a polysulfide immobilizer and catalyst in high-performance lithium–sulfur batteries. Advanced Materials, 29(2), 1602734.

[149] Chen, Y., Ren, R., Pu, H., Chang, J., Mao, S., & Chen, J. (2017). Field-effect transistor biosensors with two-dimensional black phosphorus nanosheets. Biosensors and Bioelectronics, 89, 505-510.

[150] Ciesielski, A., & Samori, P. (2014). Graphene via sonication assisted liquid-phase exfoliation. Chemical Society Reviews, 43(1), 381-398.

[151] Green, A. A., & Hersam, M. C. (2010). Emerging methods for producing monodisperse graphene dispersions. The journal of physical chemistry letters, 1(2), 544-549.

[152] Lu, W., Nan, H., Hong, J., Chen, Y., Zhu, C., Liang, Z., ... & Zhang, Z. (2014). Plasma-assisted fabrication of monolayer phosphorene and its Raman characterization. Nano Research, 7(6), 853-859.

[153] Yasaei, P., Kumar, B., Foroozan, T., Wang, C., Asadi, M., Tuschel, D., ... & Salehi-Khojin, A. (2015). High-quality black phosphorus atomic layers by liquid-phase exfoliation. Advanced Materials, 27(11), 1887-1892.

[154] Guo, Z., Zhang, H., Lu, S., Wang, Z., Tang, S., Shao, J., ... & Chu, P. K. (2015). From black phosphorus to phosphorene: basic solvent exfoliation, evolution of Raman scattering, and applications to ultrafast photonics. Advanced Functional Materials, 25(45), 6996-7002.

[155] Brent, J. R., Savjani, N., Lewis, E. A., Haigh, S. J., Lewis, D. J., & O'Brien, P. (2014). Production of few-layer phosphorene by liquid exfoliation of black phosphorus. Chemical Communications, 50(87), 13338-13341.

[156] Shih, C. J., Lin, S., Strano, M. S., & Blankschtein, D. (2010). Understanding the stabilization of liquid-phase-exfoliated graphene in polar solvents: molecular dynamics simulations and kinetic theory of colloid aggregation. Journal of the American Chemical Society, 132(41), 14638-14648.

[157] Tao, H., Zhang, Y., Gao, Y., Sun, Z., Yan, C., & Texter, J. (2017). Scalable exfoliation and dispersion of two-dimensional materials–an update. Physical Chemistry Chemical Physics, 19(2), 921-960.

[158] Woomer, A. H., Farnsworth, T. W., Hu, J., Wells, R. A., Donley, C. L., & Warren, S. C. (2015). Phosphorene: synthesis, scale-up, and quantitative optical spectroscopy. ACS nano, 9(9), 8869-8884.

[159] Hernandez, Y., Lotya, M., Rickard, D., Bergin, S. D., & Coleman, J. N. (2010). Measurement of multicomponent solubility parameters for graphene facilitates solvent discovery. Langmuir, 26(5), 3208-3213.

[160] Sresht, V., Padua, A. A., & Blankschtein, D. (2015). Liquid-phase exfoliation of phosphorene: design rules from molecular dynamics simulations. ACS nano, 9(8), 8255-8268.

[161] Mukhopadhyay, T. K., & Datta, A. (2017). Deciphering the role of solvents in the liquid phase exfoliation of hexagonal boron nitride: A molecular dynamics simulation study. the Journal of Physical Chemistry C, 121(1), 811-822.

[162] Hanlon, D., Backes, C., Doherty, E., Cucinotta, C. S., Berner, N. C., Boland, C., ... & Coleman, J. N. (2015). Liquid exfoliation of solvent-stabilized few-layer black phosphorus for applications beyond electronics. Nature communications, 6(1), 1-11.

[163] Zhang, Y., Dong, N., Tao, H., Yan, C., Huang, J., Liu, T., ... & Sun, Z. (2017). Exfoliation of stable 2D black phosphorus for device fabrication. Chemistry of Materials, 29(15), 6445-6456.

[164] Coleman, J. N. (2013). Liquid exfoliation of defect-free graphene. Accounts of chemical research, 46(1), 14-22.

[165] Hansen, C. M. (2007). Hansen solubility parameters: a user's handbook. CRC press.

[166] Mukhopadhyay, T. K., & Datta, A. (2018). Design rules for the generation of stable quartet phases of nucleobases over two-dimensional materials. The Journal of Physical Chemistry C, 122(50), 28918-28933.

[167] Mukhopadhyay, T. K., Bhattacharyya, K., & Datta, A. (2018). Gauging the nanotoxicity of h2D-C2N toward single-stranded DNA: an in silico molecular simulation approach. ACS applied materials & interfaces, 10(16), 13805-13818.

[168] Y. Chen, G. Jiang, S. Chen, S. Guo, X. Yu, C. Zhao, Z. Zhang, Q. Bao, S. Wen, W. Tang, D. Fan, mechanically exfoliated black phosphorus as a new saturable absorber for both Q-switching and mode-locking laser operation, Opt. Express. 10 (2015) 12823–12833

[169] M.B. Erande, M.S. Pawar, D.J. Late, Humidity sensing and photodetection behavior of electrochemically exfoliated atomically thin-layered black phosphorus nanosheets, ACS Appl. Mater. Interfaces. 8 (2016) 11548–11556

[170] B. Tian, B. Tian, B. Smith, M.C. Scott, Q. Lei, R. Hua, Y. Tian, Y. Liu, Facile bottom-up synthesis of partially oxidized black phosphorus nanosheets as metal-free photocatalyst for hydrogen evolution, Proc. Natl. Acad. Sci. USA 115 (2018) 4345–4350

[171] Geim, A. K., & Novoselov, K. S. (2010). The rise of graphene. In Nanoscience and technology: a collection of reviews from nature journals (pp. 11-19).

[172] Zhu, X., Zhang, T., Sun, Z., Chen, H., Guan, J., Chen, X., ... & Yang, S. (2017). Black phosphorus revisited: a missing metal-free elemental photocatalyst for visible light hydrogen evolution. Advanced Materials, 29(17), 1605776.

[173] Favron, A., Gaufrès, E., Fossard, F., Phaneuf-L'Heureux, A. L., Tang, N. Y., Lévesque, P. L., ... & Martel, R. (2015). Photooxidation and quantum confinement effects in exfoliated black phosphorus. Nature materials, 14(8), 826-832.

[174] Mason, T. J., Riera, E., Vercet, A., & Lopez-Buesa, P. (2005). Application of ultrasound. In Emerging technologies for food processing (pp. 323-351). Academic Press.

[175] Nascentes, C. C., Korn, M., Sousa, C. S., & Arruda, M. A. (2001). Use of ultrasonic baths for analytical applications: a new approach for optimisation conditions. Journal of the Brazilian Chemical Society, 12(1), 57-63.

[176] Santos, H. M., & Capelo, J. L. (2007). Trends in ultrasonic-based equipment for analytical sample treatment. Talanta, 73(5), 795-802.

[177] Suslick, K. S. (1990). Sonochemistry. science, 247(4949), 1439-1445.

[178] Coleman, J. N., Lotya, M., O'Neill, A., Bergin, S. D., King, P. J., Khan, U., ... & Nicolosi, V. (2011). Two-dimensional nanosheets produced by liquid exfoliation of layered materials. Science, 331(6017), 568-571.

[179] Zhang, Y., Wang, H., Luo, Z., Tan, H. T., Li, B., Sun, S., ... & Yan, Q. (2016). Lithium Storage: An Air-Stable Densely Packed Phosphorene–Graphene Composite Toward Advanced Lithium Storage Properties (Adv. Energy Mater. 12/2016). Advanced Energy Materials, 6(12).

[180] Kang, J., Wood, J. D., Wells, S. A., Lee, J. H., Liu, X., Chen, K. S., & Hersam, M. C. (2015). Solvent exfoliation of electronic-grade, two-dimensional black phosphorus. ACS nano, 9(4), 3596-3604.

[181] Mu, H., Lin, S., Wang, Z., Xiao, S., Li, P., Chen, Y., ... & Bao, Q. (2015). Black phosphorus–polymer composites for pulsed lasers. Advanced Optical Materials, 3(10), 1447-1453.

[182] Kuntz, K. L., Wells, R. A., Hu, J., Yang, T., Dong, B., Guo, H., ... & Warren, S. C. (2017). Control of surface and edge oxidation on phosphorene. ACS applied materials & interfaces, 9(10), 9126-9135.

[183] Kang, J., Wells, S. A., Wood, J. D., Lee, J. H., Liu, X., Ryder, C. R., ... & Hersam, M. C. (2016). Stable aqueous dispersions of optically and electronically active phosphorene. Proceedings of the National Academy of Sciences, 113(42), 11688-11693.

[184] Lin, S., Liu, S., Yang, Z., Li, Y., Ng, T. W., Xu, Z., ... & Lau, S. P. (2016). Solution-processable ultrathin black phosphorus as an effective electron transport layer in organic photovoltaics. Advanced Functional Materials, 26(6), 864-871.

[185] O'Neill, A., Khan, U., Nirmalraj, P. N., Boland, J., & Coleman, J. N. (2011). Graphene dispersion and exfoliation in low boiling point solvents. The Journal of Physical Chemistry C, 115(13), 5422-5428.

[186] Cunningham, G., Lotya, M., Cucinotta, C. S., Sanvito, S., Bergin, S. D., Menzel, R., ... & Coleman, J. N. (2012). Solvent exfoliation of transition metal dichalcogenides: dispersibility of exfoliated nanosheets varies only weakly between compounds. ACS nano, 6(4), 3468-3480.

[187] Lee, M., Roy, A. K., Jo, S., Choi, Y., Chae, A., Kim, B., ... & In, I. (2017). Exfoliation of black phosphorus in ionic liquids. Nanotechnology, 28(12), 125603.

[188] Zhao, W., Xue, Z., Wang, J., Jiang, J., Zhao, X., & Mu, T. (2015). Large-scale, highly efficient, and green liquid-exfoliation of black phosphorus in ionic liquids. ACS applied materials & interfaces, 7(50), 27608-27612.

[189] Chaban, V. V., Fileti, E. E., & Prezhdo, O. V. (2017). Imidazolium Ionic Liquid Mediates Black Phosphorus Exfoliation while Preventing Phosphorene Decomposition. ACS nano, 11(6), 6459-6466.

[190] X. Fan, P. Xu, D. Zhou, Y. Sun, Y.C. Li, M.A.T. Nguyen, M. Terrones, T.E. Mallouk, Fast and efficient preparation of exfoliated 2H MoS_2 nanosheets by sonication assisted lithium intercalation and infrared laser-induced 1T to 2H phase reversion, Nano Lett. 15 (2015) 5956–5960

[191] Y. Wang, B.J. Carey, W. Zhang, A.F. Chrimes, L.X. Chen, K. Kalantar-zadeh, J.Z. Ou, T. Daeneke, Intercalated 2D MoS2 utilizing a simulated sun assisted process: reducing the HER overpotential, J. Phys. Chem. C 120 (2016) 2447–2455.

[192] Wang, M., Liang, Y., Liu, Y., Ren, G., Zhang, Z., Wu, S., & Shen, J. (2018). Ultrasmall black phosphorus quantum dots: synthesis, characterization, and application in cancer treatment. Analyst, 143(23), 5822-5833.

[193] Hughes JM, Aherne D, Coleman JN. Generalizing solubility parameter theory to apply to one- and two-dimensional solutes and to incorporate dipolar interactions. Journal of Applied Polymer Science **127**, 4483-4491 (2013).

[194] Detriche S, Zorzini G, Colomer JF, Fonseca A, Nagy JB. Application of the Hansen Solubility Parameters Theory to Carbon Nanotubes. Journal of nanoscience and nanotechnology **8**, 6082-6092 (2008).

[195] Bergin SD, et al. Towards solutions of single-walled carbon nanotubes in common solvents. Advanced materials **20**, 1876-+ (2008).

[196] Hernandez Y, et al. High-yield production of graphene by liquid-phase exfoliation of graphite. Nature Nanotechnology **3**, 563-568 (2008).

[197] Yi M, Shen ZG, Zhang XJ, Ma SL. Achieving concentrated graphene dispersions in water/acetone mixtures by the strategy of tailoring Hansen solubility parameters. Journal of Physics D-Applied Physics 46, (2013).

[198] Meyer EF. Thermodynamics of "mixing" of ideal gases: A persistent pitfall. Journal of Chemical Education 64, 676 (1987).

[199] Hamaker HC. The London—van der Waals attraction between spherical particles. Physica 4, 1058-1072 (1937).

[200] Plimpton, S. (1995). Fast parallel algorithms for short-range molecular dynamics. Journal of computational physics, 117(1), 1-19.

[201] Fiorin, G., Klein, M. L., & Hénin, J. (2013). Using collective variables to drive molecular dynamics simulations. Molecular Physics, 111(22-23), 3345-3362.

[202] Martínez, L., Andrade, R., Birgin, E. G., & Martínez, J. M. (2009). PACKMOL: a package for building initial configurations for molecular dynamics simulations. Journal of computational chemistry, 30(13), 2157-2164.

[203] Stukowski, A. (2009). Visualization and analysis of atomistic simulation data with OVITO–the Open Visualization Tool. Modelling and Simulation in Materials Science and Engineering, 18(1), 015012.

[204] Jorgensen, W. L., Maxwell, D. S., & Tirado-Rives, J. (1996). Development and testing of the OPLS all-atom force field on conformational energetics and properties of organic liquids. Journal of the American Chemical Society, 118(45), 11225-11236.

[205] Bordes, É., Szala-Bilnik, J., & Pádua, A. A. (2017). Exfoliation of graphene and fluorographene in molecular and ionic liquids. Faraday discussions, 206, 61-75.

[206] Kumar, S., Rosenberg, J. M., Bouzida, D., Swendsen, R. H., & Kollman, P. A. (1992). The weighted histogram analysis method for free-energy calculations on biomolecules. I. The method. Journal of computational chemistry, 13(8), 1011-1021.

[207] Hockney, R. W., & Eastwood, J. W. (2021). Computer simulation using particles. crc Press.

[208] Plutnar, J., Sofer, Z., & Pumera, M. (2018). Products of degradation of black phosphorus in protic solvents. ACS nano, 12(8), 8390-8396.

[209] Qi, Z. H., Hu, Y., Jin, Z., & Ma, J. (2019). Tuning the liquid-phase exfoliation of arsenic nanosheets by interaction with various solvents. Physical Chemistry Chemical Physics, 21(23), 12087-12090.

[210] Mukhopadhyay, T. K., & Datta, A. (2017). Ordering and dynamics for the formation of two-dimensional molecular crystals on black phosphorene. The Journal of Physical Chemistry C, 121(18), 10210-10223.

[211] Lin, S., Shih, C. J., Strano, M. S., & Blankschtein, D. (2011). Molecular insights into the surface morphology, layering structure, and aggregation kinetics of surfactant-stabilized graphene dispersions. Journal of the American Chemical Society, 133(32), 12810-12823.

[212] Yang, D. S., & Zewail, A. H. (2009). Ordered water structure at hydrophobic graphite interfaces observed by 4D, ultrafast electron crystallography. Proceedings of the National Academy of Sciences, 106(11), 4122-4126.

[213] Xu, X., Cai, L., Zheng, X., & Xu, Q. (2017). Molecular dynamics simulations of solvent-exfoliation and stabilization of graphene with the assistance of compressed carbon dioxide and pyrene–polyethylene glycol. Physical Chemistry Chemical Physics, 19(24), 16062-16070.

[214] Sobolewski, E., Makowski, M., Czaplewski, C., Liwo, A., Ołdziej, S., & Scheraga, H. A. (2007). Potential of mean force of hydrophobic association: Dependence on solute size. The Journal of Physical Chemistry B, 111(36), 10765-10774.

[215] Yoffe, A. D. (1993). Low-dimensional systems: quantum size effects and electronic properties of semiconductor microcrystallites (zero-dimensional systems) and some quasi-two-dimensional systems. Advances in Physics, 42(2), 173-262.

[216] Snoke, D. (2020). Solid state physics: Essential concepts. Cambridge University Press.

[217] Efros, A. L.; Efros, A. L. Interband light absorption in a semiconductor sphere. Semiconductors 1982, 16, 1209−1214.

[218] Dresselhaus, G. (1956). Effective mass approximation for excitons. Journal of Physics and Chemistry of Solids, 1(1-2), 14-22.

[219] Dignam, M. M. (1994). Transfer-matrix approach to quantum transport in two-dimensional geometries. Physical Review B, 50(4), 2241.

[220] Rahou, D., Bekhouche, H., Ghezal, E. A., Gueddim, A., Bouarissa, N., & Ziani, H. (2020). Electronic and optical properties of InSb quantum dots from pseudopotential calculation. Chinese Journal of Physics, 66, 206-213.

[221] Choudhary, K., & Tavazza, F. (2020). Predicting Anomalous Quantum Confinement Effect in van der Waals Materials. arXiv preprint arXiv:2011.10139.

[222] Yeo, H., Lee, J. S., Khan, M. E., Kim, H. S., Jeon, D. Y., & Kim, Y. H. (2020). First-principles-derived effective mass approximation for the improved description of quantum nanostructures. Journal of Physics: Materials, 3(3), 034012.

[223] Burt, M. G. (1992). The justification for applying the effective-mass approximation to microstructures. Journal of Physics: Condensed Matter, 4(32), 6651.

[224] Zhao, X., Wei, C. M., Yang, L., & Chou, M. Y. (2004). Quantum confinement and electronic properties of silicon nanowires. Physical review letters, 92(23), 236805.

[225] Fu, N., Huang, C., Lin, P., Zhu, M., Li, T., Ye, M., ... & Ke, S. (2018). Black phosphorus quantum dots as dual-functional electron-selective materials for efficient plastic perovskite solar cells. Journal of Materials Chemistry A, 6(19), 8886-8894.

[226] Zhang, X., Xie, H., Liu, Z., Tan, C., Luo, Z., Li, H., ... & Zhang, H. (2015). Black phosphorus quantum dots. Angewandte chemie international edition, 54(12), 3653-3657.

[227] Brus, L. E. (1984). Electron–electron and electron-hole interactions in small semiconductor crystallites: The size dependence of the lowest excited electronic state. The Journal of chemical physics, 80(9), 4403-4409.

[228] Yu, H., Li, J., Loomis, R. A., Wang, L. W., & Buhro, W. E. (2003). Two-versus three-dimensional quantum confinement in indium phosphide wires and dots. Nature materials, 2(8), 517-520.

[229] Yu, H., Li, J., Loomis, R. A., Gibbons, P. C., Wang, L. W., & Buhro, W. E. (2003). Cadmium selenide quantum wires and the transition from 3D to 2D confinement. Journal of the American Chemical Society, 125(52), 16168-16169.

[230] Zhang, S., Yang, J., Xu, R., Wang, F., Li, W., Ghufran, M., ... & Lu, Y. (2014). Extraordinary photoluminescence and strong temperature/angle-dependent Raman responses in few-layer phosphorene. ACS nano, 8(9), 9590-9596.

[231] De Sousa, D. J. P., De Castro, L. V., Da Costa, D. R., & Pereira Jr, J. M. (2016). Boundary conditions for phosphorene nanoribbons in the continuum approach. Physical Review B, 94(23), 235415.

[232] Liu, H., Neal, A. T., Zhu, Z., Luo, Z., Xu, X., Tománek, D., & Ye, P. D. (2014). Phosphorene: an unexplored 2D semiconductor with a high hole mobility. ACS nano, 8(4), 4033-4041.

[233] Xia, F., Wang, H., & Jia, Y. (2014). Rediscovering black phosphorus as an anisotropic layered material for optoelectronics and electronics. Nature communications, 5(1), 1-6.

[234] Wood, J. D., Wells, S. A., Jariwala, D., Chen, K. S., Cho, E., Sangwan, V. K., ... & Hersam, M. C. (2014). Effective passivation of exfoliated black phosphorus transistors against ambient degradation. Nano letters, 14(12), 6964-6970.

[235] Buscema, M., Groenendijk, D. J., Steele, G. A., Van Der Zant, H. S., & Castellanos-Gomez, A. (2014). Photovoltaic effect in few-layer black phosphorus PN junctions defined by local electrostatic gating. Nature communications, 5(1), 1-6.

[236] Han, S. T., Hu, L., Wang, X., Zhou, Y., Zeng, Y. J., Ruan, S., ... & Peng, Z. (2017). Black phosphorus quantum dots with tunable memory properties and multilevel resistive switching characteristics. Advanced Science, 4(8), 1600435.

[237] Miao, J., Zhang, L., & Wang, C. (2019). Black phosphorus electronic and optoelectronic devices. 2D Materials, 6(3), 032003.

[238] Lin, S., Chui, Y., Li, Y., & Lau, S. P. (2017). Liquid-phase exfoliation of black phosphorus and its applications. *FlatChem*, *2*, 15-37.

[239] Sun, Z., Xie, H., Tang, S., Yu, X. F., Guo, Z., Shao, J., ... & Chu, P. K. (2015). Ultrasmall black phosphorus quantum dots: synthesis and use as photothermal agents. Angewandte Chemie International Edition, 54(39), 11526-11530.

[240] Zhu, C., Xu, F., Zhang, L., Li, M., Chen, J., Xu, S., ... & Sun, L. (2016). Ultrafast preparation of black phosphorus quantum dots for efficient humidity sensing. Chemistry–A European Journal, 22(22), 7357-7362.

[241] Zhu, X.; Zhang, T.; Sun, Z.; Chen, H.; Guan, J.; Chen, X.; Ji, H.; Du, P.; Yang, S. Black Phosphorus Revisited: A Missing Metal-Free Elemental Photocatalyst for Visible Light Hydrogen Evolution. *Adv. Mater.* **2017**, *29*.

[242] Xu, Y., Wang, Z., Guo, Z., Huang, H., Xiao, Q., Zhang, H., & Yu, X. F. (2016). Solvothermal synthesis and ultrafast photonics of black phosphorus quantum dots. Advanced Optical Materials, 4(8), 1223-1229.

[243] Niu, X., Li, Y., Shu, H., & Wang, J. (2016). Anomalous size dependence of optical properties in black phosphorus quantum dots. The journal of physical chemistry letters, 7(3), 370-375.

[244] Edvinsson, T. (2018). Optical quantum confinement and photocatalytic properties in two-, one- and zero-dimensional nanostructures. Royal society open science, 5(9), 180387.

[245] Wei, B., Zheng, K., Ji, Y., Zhang, Y., Zhang, Z., & Han, X. (2012). Size-dependent bandgap modulation of ZnO nanowires by tensile strain. Nano letters, 12(9), 4595-4599.

[246] Lippens, P. E., & Lannoo, M. (1989). Calculation of the band gap for small CdS and ZnS crystallites. Physical Review B, 39(15), 10935.

[247] Li, D., Xu, J. R., Ba, K., Xuan, N., Chen, M., Sun, Z., ... & Zhang, Z. (2017). Tunable bandgap in few-layer black phosphorus by electrical field. 2D Materials, 4(3), 031009.

[248] Pejova, B., & Grozdanov, I. (2005). Three-dimensional confinement effects in semiconducting zinc selenide quantum dots deposited in thin-film form. Materials Chemistry and Physics, 90(1), 35-46.

[249] Nosaka, Y. (1991). Finite depth spherical well model for excited states of ultrasmall semiconductor particles: an application. The Journal of Physical Chemistry, 95(13), 5054-5058.

[250] Brent, J. R., Savjani, N., Lewis, E. A., Haigh, S. J., Lewis, D. J., & O'Brien, P. (2014). Production of few-layer phosphorene by liquid exfoliation of black phosphorus. Chemical Communications, 50(87), 13338-13341.

[251] Woomer, A. H., Farnsworth, T. W., Hu, J., Wells, R. A., Donley, C. L., & Warren, S. C. (2015). Phosphorene: synthesis, scale-up, and quantitative optical spectroscopy. ACS nano, 9(9), 8869-8884.

[252] Yasaei, P., Kumar, B., Foroozan, T., Wang, C., Asadi, M., Tuschel, D., ... & Salehi-Khojin, A. (2015). High-quality black phosphorus atomic layers by liquid-phase exfoliation. Advanced Materials, 27(11), 1887-1892.

[253] Hanlon, D., Backes, C., Doherty, E., Cucinotta, C. S., Berner, N. C., Boland, C., ... & Coleman, J. N. (2015). Liquid exfoliation of solvent-stabilized few-layer black phosphorus for applications beyond electronics. Nature communications, 6(1), 1-11.

[254] Del Rio Castillo, A. E., Pellegrini, V., Sun, H., Buha, J., Dinh, D. A., Lago, E., ... & Bonaccorso, F. (2018). Exfoliation of few-layer black phosphorus in low-boiling-point solvents and its application in Li-ion batteries. Chemistry of Materials, 30(2), 506-516.

[255] Gu, W., Pei, X., Cheng, Y., Zhang, C., Zhang, J., Yan, Y., ... & Xian, Y. (2017). Black phosphorus quantum dots as the ratiometric fluorescence probe for trace mercury ion detection based on inner filter effect. ACS sensors, 2(4), 576-582.

[256] Chen, W., Li, K., Wang, Y., Feng, X., Liao, Z., Su, Q., ... & He, Z. (2017). Black phosphorus quantum dots for hole extraction of typical planar hybrid perovskite solar cells. The journal of physical chemistry letters, 8(3), 591-598.

[257] Meng, M., Gan, Z., Zhang, J., Liu, K., Wang, L., Li, S., ... & Li, J. (2017). Hierarchical self-assembly of black phosphorus quantum dots with quantum confinement effects to a centimeter-scale membrane. physica status solidi (b), 254(7), 1700011.

[258] Benabdallah, I., Kara, A., & Benaissa, M. (2020). Exfoliation and re-aggregation mechanisms of black phosphorus: A molecular dynamics study. Applied Surface Science, 507, 144826.

[259] Giannozzi, P., Baroni, S., Bonini, N., Calandra, M., Car, R., Cavazzoni, C., ... & Wentzcovitch, R. M. (2009). QUANTUM ESPRESSO: a modular and open-source software project for quantum simulations of materials. Journal of physics: Condensed matter, 21(39), 395502.

[260] Perdew, J. P., Burke, K., & Ernzerhof, M. (1996). Generalized gradient approximation made simple. Physical review letters, 77(18), 3865.

[261] Heyd, J., Scuseria, G. E., & Ernzerhof, M. (2003). Hybrid functionals based on a screened Coulomb potential. The Journal of chemical physics, 118(18), 8207-8215.

[262] Monkhorst, H. J., & Pack, J. D. (1976). Special points for Brillouin-zone integrations. Physical review B, 13(12), 5188.

[263] Song, S. J., Raja, I. S., Lee, Y. B., Kang, M. S., Seo, H. J., Lee, H. U., & Han, D. W. (2019). Comparison of cytotoxicity of black phosphorus nanosheets in different types of fibroblasts. Biomaterials research, 23(1), 1-7.

[264] Sugai, S., & Shirotani, I. (1985). Raman and infrared reflection spectroscopy in black phosphorus. Solid state communications, 53(9), 753-755.

[265] Surrente, A., Mitioglu, A. A., Galkowski, K., Tabis, W., Maude, D. K., & Plochocka, P. (2016). Excitons in atomically thin black phosphorus. Physical Review B, 93(12), 121405

[266] Sofer, Z., Bouša, D., Luxa, J., Mazanek, V., & Pumera, M. (2016). Few-layer black phosphorus nanoparticles. Chemical communications, 52(8), 1563-1566.

[267] Lee, C., Yan, H., Brus, L. E., Heinz, T. F., Hone, J., & Ryu, S. (2010). Anomalous lattice vibrations of single-and few-layer MoS2. ACS nano, 4(5), 2695-2700.

[268] Wang, Q. H., Kalantar-Zadeh, K., Kis, A., Coleman, J. N., & Strano, M. S. (2012). Electronics and optoelectronics of two-dimensional transition metal dichalcogenides. Nature nanotechnology, 7(11), 699-712.

[269] Ferrari, A. C., Meyer, J. C., Scardaci, V., Casiraghi, C., Lazzeri, M., Mauri, F., ... & Geim, A. K. (2006). Raman spectrum of graphene and graphene layers. Physical review letters, 97(18), 187401.

[270] Favron A, Gaufrès E, Fossard F, Phaneuf-L'Heureux AL, Tang NY, Lévesque PL, Loiseau A, Leonelli R, Francoeur S, Martel R. Photooxidation and quantum confinement effects in exfoliated black phosphorus. Nature materials. 2015 Aug;14(8):826-32.

[271] Ge, S., Zhang, L., Wang, P., & Fang, Y. (2016). Intense, stable and excitation wavelength-independent photoluminescence emission in the blue-violet region from phosphorene quantum dots. Scientific reports, 6(1), 1-6.

[272] Li, Y., Liu, Z., Hou, Y., Yang, G., Fei, X., Zhao, H., ... & Guo, Z. (2017). Multifunctional nanoplatform based on black phosphorus quantum dots for bioimaging and photodynamic/photothermal synergistic cancer therapy. ACS applied materials & interfaces, 9(30), 25098-25106.

[273] Li, Y., Hu, Y., Zhao, Y., Shi, G., Deng, L., Hou, Y., & Qu, L. (2011). An electrochemical avenue to green-luminescent graphene quantum dots as potential electron-acceptors for photovoltaics. Advanced materials, 23(6), 776-780.

[274] Stengl, V. & Henych, J. Strongly luminescent monolayered MoS2 prepared by effective ultrasound exfoliation. Nanoscale 8, 3387–3394 (2013).

[275] Castellanos-Gomez, A., Vicarelli, L., Prada, E., Island, J. O., Narasimha-Acharya, K. L., Blanter, S. I., ... & Van Der Zant, H. S. (2014). Isolation and characterization of few-layer black phosphorus. 2D Materials, 1(2), 025001

[276] Jia, J., Jang, S. K., Lai, S., Xu, J., Choi, Y. J., Park, J. H., & Lee, S. (2015). Plasma-treated thickness-controlled two-dimensional black phosphorus and its electronic transport properties. ACS nano, 9(9), 8729-8736.

[277] Cheng, J., Gao, L., Li, T., Mei, S., Wang, C., Wen, B., ... & Zhang, H. (2020). Two-dimensional black phosphorus nanomaterials: emerging advances in electrochemical energy storage science. Nano-Micro Letters, 12(1), 1-34.

[278] Amaral, P. E., Hall Jr, D. C., Pai, R., Król, J. E., Kalra, V., Ehrlich, G. D., & Ji, H. F. (2020). Fibrous Phosphorus Quantum Dots for Cell Imaging. ACS Applied Nano Materials, 3(1), 752-759.

[279] Tauc, J. (1968). Optical properties and electronic structure of amorphous Ge and Si. Materials Research Bulletin, 3(1), 37-46.

[280] Benabdallah, I., Auad, Y., Sigle, W., van Aken, P. A., Kociak, M., & Benaissa, M. (2021). Electronic properties of black phosphorus using monochromated low-loss EELS. Materials Science and Engineering: B, 265, 115002.

[281] Rudenko, A. N., & Katsnelson, M. I. (2014). Quasiparticle band structure and tight-binding model for single-and bilayer black phosphorus. Physical Review B, 89(20), 201408.

[282] Guo, G. C., Wei, X. L., Wang, D., Luo, Y., & Liu, L. M. (2015). Pristine and defect-containing phosphorene as promising anode materials for rechargeable Li batteries. Journal of Materials Chemistry A, 3(21), 11246-11252.

[283] Du, K., Yang, W., Deng, S., Li, X., & Yang, P. (2020). High-quality black phosphorus quantum dots fabricated via microwave-tailored technology. Nanomaterials, 10(1), 139

[284] Zhang, G., Chaves, A., Huang, S., Wang, F., Xing, Q., Low, T., & Yan, H. (2018). Determination of layer-dependent exciton binding energies in few-layer black phosphorus. Science advances, 4(3), eaap9977.

[285] Yang, J., Xu, R., Pei, J., Myint, Y. W., Wang, F., Wang, Z., ... & Lu, Y. (2015). Optical tuning of exciton and trion emissions in monolayer phosphorene. Light: Science & Applications, 4(7), e312-e312.

[286] Dong, A., Yu, H., Wang, F., & Buhro, W. E. (2008). Colloidal GaAs quantum wires: solution− liquid− solid synthesis and quantum-confinement studies. Journal of the American Chemical Society, 130(18), 5954-5961.

[287] Liu, M., Jiang, X. F., Yan, Y. R., Wang, X. D., Luo, A. P., Xu, W. C., & Luo, Z. C. (2018). Black phosphorus quantum dots for femtosecond laser photonics. Optics Communications, 406, 85-90.

[288] Qiao, J., Kong, X., Hu, Z. X., Yang, F., & Ji, W. (2014). High-mobility transport anisotropy and linear dichroism in few-layer black phosphorus. Nature communications, 5(1), 1-7.

List of Publications

Articles on the topic of the thesis:

1- **Benabdallah, I.,** Kara, A., & Benaissa, M. (2020). *Exfoliation and re-aggregation mechanisms of black phosphorus: A molecular dynamics study*. Applied Surface Science, 507, 144826. (Impact Factor: 6.612)

2- **Benabdallah, I.**, Auad, Y., Sigle, W., Van Aken, P. A., Kociak, M., & Benaissa, M. (2021). *Electronic properties of black phosphorus using monochromated low-loss EELS*. Materials Science and Engineering: B, 265, 115002. (Impact Factor: 4.051)

3- **Benabdallah, I.,** Sibari, A., El Masaoudi, H., Azouzi, W. Benaissa, M., "*Quantum confinement effect in phosphorene and black phosphorus quantum dots*", Submitted to Materialia. (Impact Factor: 8.203)

Articles in collaboration:

4- El Masaoudi, H., **Benabdallah, I.,** Jaber, B., & Benaissa, M. (2021). Enhanced visible light photocatalytic activity of Cu2+-doped Ag3PO4 nanoparticles. Chemical Physics, 545, 111133.

5- Azouzi, W., **Benabdallah, I.,** Sibari, A., Labrim, H., & Benaissa, M. (2021). Structural and optical properties of LaFe1-xVxO3 as predicted by a DFT study. Materials Today Communications, 26, 101876.

6- Benaissa, M., Sigle, W., **Benabdallah, I.**, ElAfandy, R. T., Ng, T. K., & van Aken, P. A. (2021). Optical properties of freestanding GaN nanomembranes using monochromated valence-EELS. Materials Science and Engineering: B, 272, 115333.

7- Azouzi, W., **Benabdallah, I.**, Essyed. A., Tahri, M., Labrim. H, Benaissa. M. (2021). Structural and optical properties of sol-gel synthesized $LaFe_{1-x}Ag_xO_3$. Materials Science and Engineering: B, 272, 115343.

8- El Masaoudi, H., **Benabdallah, I.,** Jaber, B., Laghzizil, A., & Benaissa, M. (2020). Size Control of Ag3PO4 Nanoparticles Using Monoethanolamine and Oleylamine Chelating Agents. Journal of Nanostructures, 10(2), 362-374.

9- **Benabdallah, I.,** Boujnah, M., El Kenz, A., Benyoussef, A., Abatal, M., & Bassam, A. (2019). Lead-free perovskite-based bismuth for solar cells absorbers. Journal of Alloys and Compounds, 773, 796-801.

Communications and Internship

- Oral Communication at the "1st International Materials Science and Engineering for Green Energy Conference (IMSEGEC2017)" at Al Akhawayn University, Ifrane. May 2017.

- Oral Communication at the "2nd International Materials Science and Engineering for Green Energy Conference (IMSEGEC2017)" at Mohammed V university, Rabat. April 2018.

- 2 Years Internship at Centre National pour la Recherche Scientifique et Technique (CNRST) division d'unité d'appui technique et recherche scientifique (UATRS) 2019-2021.

- 2 Months Internship at « Laboratoire de physique des solides » at the Paris-Saclay University in Paris October 2019-December 2019.

Résumé :

Ce travail de thèse est dédié à l'étude des propriétés électroniques et optiques du phosphore noir exfolié et des boîtes quantiques synthétisés à partir du phosphore noir commercialisé. Pour cela, ce travail a été divisé en trois parties. La première consiste à étudier les propriétés structurales et optiques du phosphore noir commercialisé. Les résultats obtenus par microscopie électronique montrent la pureté du phosphore noir commercialisé. Tandis que la spectroscopie de perte d'énergie électronique a permis une mesure directe du gap ~ 0,3 eV, ainsi que des transitions intrabande électroniques et excitoniques. Après cette première étude, l'accent a été mis sur l'étude de l'effet des propriétés des solvants dans l'exfoliation/réagrégation du phosphore noir par dynamique moléculaire. Cette étude a montré que pour une exfoliation/réagrégation efficace, les molécules planes ayant une haute énergie d'interaction avec le phosphorene sont les plus adaptées pour exfolier et protéger contre la réagrégation. Enfin, l'effet de confinement quantique dans les boîtes quantiques de phosphore et de phosphore noir (BPQD) est étudié. Le Benzonitrile s'avère être le meilleur solvant pour l'exfoliation du BP et la synthèse des BPQD, ainsi que pour la prévention de l'oxydation. De plus, la caractérisation des propriétés optiques a montré une augmentation significative de la valeur du gap des deux structures. Une étude par la théorie de la fonctionnelle de la densité et une approximation de la masse effective modifiée a permis de révéler que variation de la bande interdite présente une dépendance de taille de ($1/d^n$) plutôt que ($1/d^2$), n étant la dimensionnalité du confinement.

Mots-clés : Phosphore noir, Phosphorene, Boîtes quantiques, Exfoliation en phase liquide, Confinement quantique, Calculs ab-initio.

Abstract:

This thesis work is dedicated to the study of the electronic and optical properties of exfoliated black phosphorus and quantum dots synthesized from commercialized black phosphorus. For that purpose, this work was divided into three main parts. The first one consists to investigate the structural and optical properties of the commercialized black phosphorus used in our work. The results obtained by electronic microscopy proved the high purity of the commercialized Black phosphorus used. While the Electron Energy-loss Spectroscopy allowed a direct measurement of the narrow bandgap ~0.3eV, as well as intraband electronic and excitonic transitions. After that first study, the focus was on the investigation of the effect of solvent properties in the exfoliation/reaggregation of black phosphorus by molecular dynamics. This study showed that for an efficient exfoliation/reaggregation planar molecules with a high interaction energy with phosphorene are the most suitable for a smooth exfoliation as well as a better prevention against reaggregation. Finally, the quantum confinement effect in phosphorene and black phosphorus quantum dots (BPQD) is extensively studied. Benzonitrile solvent is found to be the best candidate for exfoliation of BP and for synthesis of BPQD, as well as preventing oxidation. Furthermore, optical properties characterization showed a significant increase in the bandgap value of both structures. Such an increase was supported by theoretical calculations using density functional theory and a modified-effective mass approximation. Thus, revealing that the bandgap variation exhibits a size dependence of ($1/dn$) rather than ($1/d2$), with n being confinement dimensionality.

Keywords : Black phosphorus, Phosphorene, Quantum dots, Liquid Phase Exfoliation, Quantum confinement, ab-initio calculations.